Global and Internal Diffusive Dynamics of Proteins in Solution Studied by Neutron Spectroscopy

Dissertation
der Mathematisch-Naturwissenschaftlichen Fakultät
der Eberhard Karls Universität Tübingen
zur Erlangung des Grades eines
Doktors der Naturwissenschaften
(Dr. rer. nat.)

vorgelegt von
Marco Grimaldo
aus Bozen, Italien

Tübingen
2016

Gedruckt mit Genehmigung der Mathematisch-Naturwissenschaftlichen Fakultät der Eberhard Karls Universität Tübingen.

Tag der mündlichen Qualifikation:	05.07.2016
Dekan:	Prof. Dr. Wolfgang Rosenstiel
1. Berichterstatter:	Prof. Dr. Frank Schreiber
2. Berichterstatter:	Prof. Dr. Martin Oettel

Preamble

This thesis was part of the PhD programme of the Institut Laue-Langevin, Grenoble, France, jointly with the University of Tübingen, Germany, co-founded by the two institutes. The work was supervised by Dr. Tilo Seydel at the Institut Laue-Langevin, and by Prof. Dr. Frank Schreiber and Prof. Dr. Martin Oettel at the University of Tübingen.

List of Papers Being Part of the Thesis

- Grimaldo, M.; Roosen-Runge, F.; Zhang, F.; Seydel, T.; Schreiber, F. Diffusion and Dynamics of γ-Globulin in Crowded Aqueous Solutions. *J. Phys. Chem. B* **2014** *118*, 7203–7209.
- Grimaldo, M.; Roosen-Runge, F.; Jalarvo, N.; Zamponi, M.; Zanini, F.; Hennig, M.; Zhang, F.; Schreiber, F.; Seydel, T. High-resolution Neutron Spectroscopy on Protein Solution Samples in *EPJ Web of Conferences* volume 83 EDP Sciences **2015** page 02005.
- Grimaldo, M.; Roosen-Runge, F.; Hennig, M.; Zanini, F.; Zhang, F.; Jalarvo, N.; Zamponi, M.; Schreiber, F.; Seydel, T. Hierarchical molecular dynamics of bovine serum albumin in concentrated aqueous solution below and above thermal denaturation *Phys. Chem. Chem. Phys.* **2015** *17*, 4645–4655.
- Grimaldo, M.; Roosen-Runge, F.; Hennig, M.; Zanini, F.; Zhang, F.; Zamponi, M.; Jalarvo, N.; Schreiber, F.; Seydel, T. Salt-Induced Universal Slowing Down of the Short-Time Self-Diffusion of a Globular Protein in Aqueous Solution *J. Phys. Chem. Letters* **2015** *6*, 2577–2582.

Other Papers Co-Authored During the Thesis

- Soraruf, D.; Roosen-Runge, F.; Grimaldo, M.; Zanini, F.; Schweins, R.; Seydel, T.; Zhang, F.; Roth, R.; Oettel, M.; Schreiber, F. Protein Cluster Formation in Aqueous Solution in the Presence of Multivalent Metal Ions - a Light Scattering Study *Soft Matter* **2014** *10*, 894–902.
- Lenton, S.; Grimaldo, M.; Roosen-Runge, F.; Schreiber, F.; Nylander, T.; Holt, C.; Garcia Sakai, V.; Haertlein, M.; Zaccai, G.; Seydel, T.; Teixeira, S.C.M. Effect of phosphorylation on the structure and dynamics of a recombinant human-like osteopontin peptide, *in preparation*

Contents

Deutsche Zusammenfassung **1**
- Motivation und Einleitung 1
- Ergebnisse 3
- Schlussfolgerungen und Ausblick 7

Abstract **11**

1 Introduction **13**

2 Theoretical Background **17**
- 2.1 Colloidal Suspensions 17
- 2.2 Diffusion 18
  - 2.2.1 Self-Diffusion 19
  - 2.2.2 Collective Diffusion 22
- 2.3 Proteins as Patchy Colloids 23
- 2.4 Basics of Neutron Scattering 24
- 2.5 Quasi-Elastic Neutron Scattering (QENS) 29
- 2.6 Models for Protein Internal Dynamics in the QENS Analysis 30
  - 2.6.1 Elastic Incoherent Structure Factor 30
  - 2.6.2 Modeling of the Quasi-Elastic Broadening Due to Internal Dynamics 32

3 Literature Review **39**
- 3.1 Dynamics of Hydrated Protein Powders 44
- 3.2 The Importance of Studying Proteins in Solution 44
- 3.3 The Dynamical Transition in Solution 46
- 3.4 Changes of Internal Dynamics on Protein Denaturation 47
- 3.5 The Role of the Structure and the State of Proteins 50
- 3.6 Internal Dynamics of Proteins Under Pressure 51
- 3.7 Adaptation to Physiological and Extreme Temperatures 52
- 3.8 Slow Collective Motions 54
- 3.9 Complementary Use of Neutron Spectroscopy Techniques 55
- 3.10 *In Vivo* Neutron Spectroscopy 56
- 3.11 Protein Diffusion in Crowded Solutions 57

3.12 Dynamics of Protein Clusters, Aggregates, and Glasses 59
3.13 Summary 60

4 Materials and Methods 63
4.1 Materials 64
  4.1.1 D_2O 64
  4.1.2 Bovine Serum Albumin (BSA) 65
  4.1.3 Immunoglobulin G (IgG) 66
  4.1.4 Yttrium Chloride (YCl_3) 67
4.2 Sample Preparation 68
4.3 Methods 70
  4.3.1 Data Reduction 71
  4.3.2 Subtraction of the Contribution of the Sample Holder 72
  4.3.3 Calibration 73
  4.3.4 Backscattering Data Analysis 74
4.4 Instruments 83
  4.4.1 Common Concepts of Neutron Instruments 83
  4.4.2 Principle of a Backscattering Spectrometer 87
  4.4.3 The Backscattering Spectrometer BASIS at the ORNL Spallation Neutron Source 89
  4.4.4 The Backscattering Spectrometer IN16B at the ILL Reactor 92

5 Overview of the Results 95
5.1 The Effect of Self-Crowding on the Dynamics of γ-Globulin 97
5.2 The Dynamics of BSA upon Thermal Denaturation 98
5.3 The Diffusion of BSA in the Presence of the Trivalent Salt YCl_3 100

6 The Effect of Self-Crowding on the Dynamics of IgG 103
6.1 Abstract 103
6.2 Introduction 104
6.3 Experiments and Methods 105
6.4 Results and Discussion 107
  6.4.1 Neutron Spectra 107
  6.4.2 Rotational and Translational Diffusion of the Proteins 107
  6.4.3 Internal Diffusive Molecular Motions 109
  6.4.4 Further Discussion 112
6.5 Conclusions and Outlook 114

7 The Dynamics of BSA upon Thermal Denaturation 115
7.1 Abstract 116
7.2 Introduction 116
7.3 Experimental Section 118
7.4 Results and Discussion 119
  7.4.1 Model-Free Observations 119

7.4.2 Analysis via the Conventional Two-Lorentzian Model Below the Denaturation Temperature . . . 121
7.4.3 Analysis via a Model of Switching Diffusive States at Elevated Temperatures 122
7.4.4 Global Apparent Short-Time Self-Diffusion . . . 123
7.4.5 Translational Short-Time Self-Diffusion Below the Transition Temperature T_d . . . 125
7.4.6 Internal Dynamics . . . 125
7.4.7 Geometry of Confined Motions . . . 126
7.5 Discussion of the General Physical Picture . . . 128
7.6 Conclusions . . . 130

8 The Diffusion of BSA in the Presence of YCl_3 133
8.1 Abstract . . . 134
8.2 Introduction . . . 134
8.3 Results and Discussion . . . 135
8.4 Conclusion . . . 139
8.5 Experimental Methods . . . 140

9 Conclusion 143

Appendices 145

A Supporting Information to Chapter 6 147
A.1 Separation of Rotational and Translational Diffusion. . . . 147
A.2 Fit Results . . . 149
A.3 Alternative Fits of the EISF . . . 150
A.4 Heavy Water (D_2O) Treatment . . . 151
A.5 Additional Examples of Measured Spectra. . . . 152

B Supporting Information to Chapter 7 157
B.1 Effect of an Increase of the Hydrodynamic Radius on the Theoretical and Experimentally Determined Translational Diffusion Coefficients . . . 157
B.2 Alternative Models . . . 158
B.2.1 Single Lorentzian for the Internal Motions . . . 158
B.2.2 Static Distribution of Monomers and Clusters . . . 159
B.2.3 Distribution of Dynamical Clusters and Monomers: Switching Mmodel for the Global Diffusion (2 Alternating Diffusive States) - Homogeneous Internal Dynamics . . . 161
B.2.4 Distribution of Dynamical Clusters and Monomers: Switching Model for the Global Diffusion (2 Alternating Diffusive States) - Heterogeneous Internal Dynamics Modeled by 2 Alternating Diffusive States . . . 162
B.3 Effect of the H/D-Exchange . . . 162

C Supporting Information to Chapter 8 **167**
C.1 Amplitudes of Density Fluctuations 167

D List of Performed Neutron Scattering Experiments **171**

Acknowledgments **191**

List of Abbreviations

Adk Adenylate Kinase

BLA Bovine α-lactalbumin

BR Bacteriorhodopsin

BSA Bovine Serum Albumin

BSS Backscattering Spectrometer

DLS Dynamic Light Scattering

DWF Debye-Waller Factor

EINS Elastic Incoherent Neutron Scattering

EISF Elastic Incoherent Structure Factor

FCS Fluorescence Correlation Spectroscopy

FWHM Full Width at Half Maximum

GDH Glutamate Dehydrogenase

Hb Hemoglobin

HbCO Carbonmonoxyhemoglobin

hHb Human Hemoglobin

HI Hydrodynamic Interactions

HSA Human Serum Albumin

HWHM Half Width at Half Maximum

ILL Institut Max von Laue - Paul Langevin

JCNS Jülich Centre for Neutron Science

linac Linear Accelerator

LLPS Liquid-liquid Phase Separation

MalDH Malate Dehydrogenase

MBLA Molten Bovine α-lactalbumin

MBP Myelin Basic Protein

MD Molecular Dynamics

MSD Mean Square Displacement

NBS Neutron Backscattering

NIST National Institute of Standards and Technology

NMR Nuclear Magnetic Resonance

NSE Neutron Spin-echo

ORNL Oak Ridge National Laboratory

PDB Protein data base

PGK Phosphoglycerate Kinase

PSD Position-sensitive Detector

PST Phase-space transformer

QENS Quasi-Elastic Neutron Scattering

RBC Red Blood Cell

RMSD Root Mean Squared Displacement

RC Reentrant Condensation

SANS Small-angle Neutron Scattering

SD Single Detector

SNS Spallation Neutron Source

TOF Time of Flight

List of Symbols

γ	Half-width at half maximum of the Lorentzian function describing translation and rotation of proteins.
Γ	Half-width at half maximum of the Lorentzian function describing the protein internal motion.
$\delta(\cdot)$	Dirac delta function
φ, ϕ	Stoichiometric (observable) volume fraction
φ_t	Effective volume fraction for comparison with theory
ϑ	Partial specific volume
$2\,\theta$	Scattering angle
θ_c	Critical grazing angle for neutron reflection in a neutron guide
τ	Relaxation time
τ_B	Brownian timescale
τ_I	Interaction timescale
$\rho_H(r)$	Radial density distribution of H-atoms in the protein
ρ_n	Number density of n-clusters
σ_a	Absorption cross-section
σ_s	Scattering cross-section
$\hbar\omega$	Energy transfer
$\mathscr{D}(\mathbf{q})$	Detector efficiency
$\mathscr{L}(\cdots)$	Lorentzian function
$\mathscr{R}(q,\omega)$	Resolution function
$A_0(q)$	Elastic incoherent structure factor
b	Scattering length
c_p	Protein concentration
c_s	Salt concentration
D, d	Global diffusion coefficient
D_0	Dilute limit diffusion coefficient
D_j	Jump-diffusion coefficient
D_r	Rotational diffusion coefficient
D_{r0}	Dilute limit rotational diffusion coefficient
D_t	Translational diffusion coefficient
D_{t0}	Dilute limit translational diffusion coefficient
D_l^s	Long-time self-diffusion coefficient
D_s^s	Short-time self-diffusion coefficient
D_s	Self-diffusion coefficient
E	Energy
$f_r(\phi)$	Reduced rotational diffusion coefficient
$f_t(\phi)$	Reduced translational diffusion coefficient

$G_s(\mathbf{r},t)$	van Hove self-correlation function
$\hbar$	Reduced Planck constant
$I(q,\omega)$	Scattering intensity
$j_l(\cdot)$	lth-order spherical Bessel function of first kind
$\mathbf{k}$	Wavevector
$k_\mathbf{B}$	Boltzmann constant
$\langle k\rangle$,κ	Effective force constant
p_b	Binding probability (in a patchy particle model)
q	Scattering vector
$\mathbf{r}$	Position
R	Radius of the bare protein
R_h	Hydrodynamical radius
$S(q,\omega)$	Scattering function
$S_n(q,\omega)$	Scattering function of an n-cluster
t	Time
T	Temperature
T_d	Denaturation temperature
$\left\langle u^2\right\rangle$	Apparent (internal) mean square displacement
V	Volume
$W(t)$, $\left\langle r^2\right\rangle$	Diffusive mean square displacement

List of Figures

2.1 Sketch of the diffusive MSD as a function of time. 20
2.2 Sketch of the interaction potential between two ion-activated patchy particles [24]. 24
2.3 Schematic representation of a scattering event. 25
2.4 Sketch of the scattering function of elastic, quasi-elastic and inelastic neutron scattering near room temperature. 30
2.5 Comparison of the HWHM γ as a function of q^2 for Fickian diffusion and jump-diffusion. 36

4.1 Surface structure of a BSA molecule. 66
4.2 Surface structure of an IgG molecule. 67
4.3 Schematic representation of the aluminum sample holder. 70
4.4 Comparison of the resolution functions of BASIS and IN16B. 75
4.5 Example spectra and D_2O contribution. 76
4.6 Linewidth γ_{D_2O} of D_2O as a function of the square of the scattering vector q^2 for various temperatures T obtained from time-of-flight data. 78
4.7 Incoherent scattering function $\mathcal{S}_{\mathrm{inc}}^{\mathrm{TR}}(q,\omega)$ of a diffusing hypothetical particle, and the residuals χ resulting from the fit of $\mathcal{S}_{\mathrm{inc}}^{\mathrm{TR}}(q,\omega)$ with a Lorentzian function. . . 80
4.8 General apparent diffusion coefficient $D^{(n)} = D(q, D_t, D_r)$ of a hypothetical diffusing particle with the same parameters as in figure 4.7, and χ^2 of the fit of a Lorentzian function to $\mathcal{S}_{\mathrm{inc}}^{\mathrm{TR}}(q,\omega)$ as a function of q 81
4.9 One of the BASIS choppers with the cover plate underneath. The aluminum (neutron-transparent) window at the position of the neutron guide is visible at the front. Figure from Ref. [174] 85
4.10 Schematic of the principle of a backscattering spectrometer. 88
4.11 Three-dimensional scheme of the Spallation Neutron Source facility. 90
4.12 Photograph of the backscattering spectrometer IN16B at the Institut Laue-Langevin. (Courtesy Serge Claisse, ILL) 93

6.1 Inset: Typical $S(q,\omega)$ (red circles) recorded using cold neutron backscattering for γ-globulin in D_2O ($c_p = 300\,\mathrm{mg/ml}$, $T = 295\,\mathrm{K}$, individual detector at $q = 0.81\,\text{Å}^{-1}$). Main figure: Fitted γ (red circles) vs. q^2 for the full accessible q-range. 108
6.2 Apparent diffusion coefficient D (upper) and reduced translational short-time diffusion coefficient D_t/D_0 (lower) as a function of the protein volume fraction φ. . 109

6.3 Main figure: Elastic incoherent structure factor as a function of q for three γ-globulin concentrations. Inset: Γ as a function of q^2 for three protein concentrations. 110

6.4 Main figure: Fit results for the residence time τ associated with the internal molecular motion of the proteins in terms of the jump diffusion model (Eq. (6.4)) as a function of the protein volume fraction φ in the aqueous solution. Inset: Fit result for the radius R of the impermeable sphere associated with the protein side chain motions in terms of the model for the EISF (Eq. (6.3)) as a function of the protein volume fraction φ. 111

7.1 Example spectra (purple lines) recorded using the backscattering spectrometer BASIS, SNS, ORNL, on bovine serum albumin (BSA) at the scattering vector $q = 0.85\,\text{Å}^{-1}$ for different temperatures T at the protein concentration $c_p = 200\,\text{mg/ml}$ in heavy water (D_2O) subsequent to the subtraction of the empty can spectra. . . 119

7.2 (a) Example spectrum recorded using the neutron backscattering spectrometer BASIS, SNS, ORNL, on bovine serum albumin (BSA) at the concentration $c_p = 200\,\text{mg/ml}$ in heavy water (D_2O) at the temperature $T = 295\,\text{K}$. (b) Linewidth γ of the Lorentzian accounting for the translational and rotational diffusion of the entire protein as a function of q^2 for $c_p = 500\,\text{mg/ml}$ at $T =$ 280, 290 and 310 K. (c) Translational self-diffusion coefficients d_t as a function of temperature for $c_p = 150\,\text{mg/ml}$, $200\,\text{mg/ml}$, and $500\,\text{mg/ml}$. 120

7.3 (a) Apparent self-diffusion coefficient d as a function of T for $c_p = 150$, 200 and 500 mg/ml and fits with equation (7.7). (b) Example spectrum (symbols) of aqueous BSA at $c_p = 500\,\text{mg/ml}$, $T = 370\,\text{K}$ and $q = 0.45\,\text{Å}^{-1}$. (c) D_1 – attributed to the dynamics of the backbone – as a function of T (symbols). (d) Arrhenius plot of the residence time τ_1 between two jumps of the side-chains versus T for three c_p. (e) D_2 – associated with the dynamics of the side-chains – as a function of T for the concentrations reported in the legend. (f) Arrhenius plot of the residence time τ_2 as a function of T. τ_2 is the time a side-chain needs to switch between two conformations during which they are considered immobile with respect to the backbone. 124

7.4 (a) and (b): EISF as a function of q at the temperatures given in the legend for $c_p = 200$ and $500\,\text{mg/ml}$, respectively, and fits following equation (7.8). (c) Radius a (equation (7.11)) as a function of T for $c_p = 500\,\text{mg/ml}$ and fit with equation (7.12). (d) Radius R (equation (7.10)) as a function of T. (e) Fraction of immobile atoms p as a function of T. (f) s as a function of T defining the ratio of side-chains describable with a diffusion in a sphere model to the total amount of mobile side-chains. 127

8.1 Inset: Example backscattering spectrum $I(q, \omega)$ recorded at BASIS for BSA and YCl_3 in D_2O (c_p = 150 mg/ml, c_s = 8 mM, T = 295 K, individual detector at $q = 0.65\mathring{\text{A}}^{-1}$). Main figure: Fitted γ (red circles) vs. q^2 for the full q-range of the example data. 136

8.2 (a) Reduced short-time apparent self-diffusion coefficient $D(c_s, c_p)/D(c_s = 0, c_p)$ as a function of c_s/c_p. (b) Contour plot of the bonding probability p_b as a function of c_p and c_s. Inset: Bonding probability p_b as a function of the number of Y^{3+} ions per protein c_s/c_p as obtained from the experiment under the assumptions explained in the text, using equations (8.2) and (8.6). 137

A.1 Radial density distribution function $\rho(r)$ of hydrogen atoms in IgG monomers, dimers and, for comparison, BSA. 148
A.2 Reduced short-time translational self-diffusion D_t/D_0 as a function of the volume fraction φ of γ-globulin in D_2O (symbols) when assuming dimers for the separation of rotation and translation from the apparent diffusion coefficient D. 148
A.3 Elastic incoherent structure factor (EISF) as a function of q for three γ-globulin concentrations. 151
A.4 Half width at half maximum γ_{D_2O} of the Lorentzian describing the quasi-elastic spectra of D_2O measured at IN6 at several temperatures. 152
A.5 Example spectra and γ as a function of q^2 collected at IN16B for different IgG samples: (A) $c_p = 100\,\mathrm{mg/ml}$, $T = 295\,\mathrm{K}$, (B) $c_p = 150\,\mathrm{mg/ml}$, $T = 295\,\mathrm{K}$ 153
A.6 Example spectra and γ as a function of q^2 collected at IN16B for different IgG samples: (A) $c_p = 200\,\mathrm{mg/ml}$, $T = 295\,\mathrm{K}$, (B) $c_p = 250\,\mathrm{mg/ml}$, $T = 295\,\mathrm{K}$ 153
A.7 Example spectra and γ as a function of q^2 collected at IN16B for different IgG samples: (A) $c_p = 300\,\mathrm{mg/ml}$, $T = 295\,\mathrm{K}$, (B) $c_p = 350\,\mathrm{mg/ml}$, $T = 295\,\mathrm{K}$ 154
A.8 Example spectra and γ as a function of q^2 collected at IN16B for different IgG samples: (A) $c_p = 400\,\mathrm{mg/ml}$, $T = 295\,\mathrm{K}$, (B) $c_p = 450\,\mathrm{mg/ml}$, $T = 295\,\mathrm{K}$ 154
A.9 Example spectrum and γ as a function of q^2 collected at IN16B the IgG sample at $c_p = 500\,\mathrm{mg/ml}$, $T = 295\,\mathrm{K}$ 155
A.10 Example spectra and γ as a function of q^2 collected at IN16B for different IgG samples: (A) $c_p = 150\,\mathrm{mg/ml}$, $T = 280\,\mathrm{K}$, (B) $c_p = 400\,\mathrm{mg/ml}$, $T = 310\,\mathrm{K}$ 155

B.1 Translational diffusion coefficients of BSA solutions as a function of temperature at three protein concentrations. 158
B.2 HWHM Γ of the Lorentzian function describing the internal motions as a function of q^2 for the model in equation (B.1). 159
B.3 Fit parameters d_m, d_c, ϕ_c, τ_m and τ_c from various models as discussed in the captions below the subfigures. 160
B.4 HWHM Γ of the Lorentzian function describing the internal motions as a function of q^2 for the model in equation (B.2) and that in equation (B.3) 161
B.5 Apparent self-diffusion coefficient d as a function of T for $c_p = 150$, 200 and 500 mg/ml (symbols) and fits with the two-state switching diffusion model (see article, lines), assuming an H/D-exchange between the proteins and the solvent water as outlined in Section B.3. 163
B.6 Fit results for the two-state switching diffusion model assuming an H/D-exchange between the proteins and the solvent water as outlined in Section B.3. 164

B.7 Fit results for the EISF associated with the two-state switching diffusion model assuming an H/D-exchange between the proteins and the solvent water as outlined in Section B.3. 165

C.1 (a) Local density $\varphi(x)$ as a function of the position x for a square-well-like fluctuation. (b) Probability density $G(\varphi)$ of local volume fractions φ as a function of φ, in the limiting case of Delta-functions (corresponding to the spatial profile shown in (a)). (c) Amplitude A of density fluctuations as a function of c_s/c_p obtained from the fit of experimental data under the assumption of square-well-like density fluctuations. 169

List of Tables

2.1 Coherent (σ_{coh}), incoherent (σ_{coh}) and absorption (σ_{a}) neutron cross-sections in barns of the elements composing BSA, D_2O and YCl_3, as well as of Aluminum and Vanadium [55]. 28

3.1 Effective force constants (equation (3.1)) of proteins in solution from different studies. 42
3.2 Parameters regarding protein internal dynamics obtained from QENS studies. . . 43

4.1 List of the neutron scattering experiments reported in this thesis in Chapters 6, 7, and 8, already published in peer-reviewed journals. 63
4.2 Selection of properties of H_2O and D_2O [139]. 64
4.3 Coefficients for the calculation of the viscosity of D_2O with equation (4.1) [140]. . 65
4.4 Aluminum alloy composition of the sample holder in mass % [31]. 69

A.1 Parameters of the fit of the EISF by equation (A.2). 149
A.2 Parameters of the fit of Γ by equation (A.3). 150
A.3 Parameters of the fit of the EISF by equation (A.4) with $(1 - P)\,\Phi = 0.22$. 150

D.1 List of all the neutron scattering experiments carried out during the thesis including those not yet published in peer-reviewed journals. DOI denotes the persistent digital object identifier where the raw data, reduced data, log files, and experimental reports are available. 171

Deutsche Zusammenfassung

Motivation und Einleitung

Proteine sind ein bemerkenswertes Forschungsobjekt in vielen Zweigen moderner Wissenschaft und Technik, Kolloidphysik, Chemietechnik und Nanotechnologie, aber auch in der Biologie, Medizin und Pharmazie. Globuläre Proteine sind weiche Makromoleküle mit typischen Durchmessern in der Größenordnung von einigen Nanometern.

Aus biologischer Sicht nehmen Proteine eine wichtige Position ein: sie wirken bei einer Vielzahl von Prozessen, die für jede biologische Zelle lebensnotwendig sind, mit und können, je nach Aufbau, als Enzyme, Antikörper, oder Träger kleinerer Moleküle oder Ionen, sowie zu strukturellen Zwecken dienen [1]. Fehlerhafte Proteine können der Zelle ernsthafte Schäden zufügen [2]. Außerdem wurden durch falsche Proteinfaltung, Denaturierung und Aggregation verursachte Mängel der Proteinaktivität mit einer Vielfalt unterschiedlicher Krankheiten in Verbindung gebracht [3–6].

Die Funktion der Proteine wird durch die Kombination ihrer spezifischen Struktur und Dynamik beeinflusst [7,8]. Infolgedessen ist die quantitative Charakterisierung der internen Dynamik von Proteinen wesentlich für das Verständnis lebender Systeme und möglicherweise gewissener Mechanismen, die zum Funktionsausfall führen. Zudem ermöglicht interne Proteindynamik strukturelle Flexibilität, welche wiederum die Affinität zu Medikamenten verbessern kann. Die Untersuchung solcher Dynamik ist somit fundamental, um besser verstehen zu können, auf welcher Art und Weise Medikamente auf biologische Systeme wirken [9].

Zahlreiche Studien haben sich mit Proteindiffusion in lebenden Zellen [10], im Karyoplasma [11], im mitochondrialen Lumen [12] und im Zytoplasma [13–17] beschäftigt. *In vivo*, wo der makromolekulare Volumenanteil etwa 20 bis 40 % beträgt, ist Proteindynamik in der Regel bedeutend langsamer, als in der verdünnten Proteinlösung (Crowding). Außerdem ist auch die interne Proteindynamik, und dadurch möglicherweise auch die Proteinfunktion, vom makromolekularen Crowding beeinflusst [18].

Weitere *in vivo* Studien haben gezeigt, dass die durchschnittliche effektive Resilienz von Makromolekülen, die in an unterschiedlichen, extremen Temperaturen angepassten Organismen zu finden sind, mit wachsender Anpassungstemperatur größer wird [19–21]. Die Resilienz auf einer Zeiskala von 100 ps ist außerdem so angepasst, dass die mittlere quadratische Verschiebung der Makromolekülwasserstoffatome in den Bakterien stets ca. 1.2 Å bei der entsprechenden Anpassungstemperatur beträgt. Dieses Ergebnis stützt die Hypothese, dass die biologische Aktivität eine optimale interne Makromoleküldynamik auf der Subnanosekundenzeitskala benötigt, die durch biologische Selektion angepasst wurde [19].

Ähnliche Schlussfolgerungen wurden aus einer Neutronenstudie von Haemoglobin (Hb) verschiedener Warmblüter in hochkonzentrierten wässrigen Lösungen [22] und aus einer kombinierten kernmagnetischen Resonanz- und Molekulardynamik-Simulationsstudie auf hyperthermophiler und thermophiler Adenylat-Kinase (AdK) [8] gezogen. Die Pico- zu Nanosekundedynamik könnte außerdem mit der allosterischen Kommunikation zwischen verschiedenen Proteindomänen oder Subdomänen verknüpft sein [23], d.h. schnelle interne Dynamik könnte eine Rolle in der Proteinregulation durch die Bindung spezifischer Moleküle an Stellen, die auch relativ weit vom aktiven Zentrum sein können, spielen [23].

Obwohl das Interesse an Proteinen von einer biologischen Perspektive streng mit ihrer natürlichen Umgebung gekoppelt ist, haben *in vivo* Messungen den offensichtilchen Nachteil, dass systematische Experimente zur Quantifizierung der Wirkung verschiedener Parameter, wie zum Beispiel makromolekulares Crowding oder Salzkonzentration, auf ihr Verhalten nicht durchgeführt werden können. Dafür muss die komplexe zelluläre Umgebung vereinfacht werden, sodass das System in Abhängigkeit von verschiedenen Parametern in zuverlässiger Weise gesteuert werden kann. Eine Art von Protein in der Lösung stellt das einfachste Modell dar, in dem das makromolekulare Crowding durch die hohe Konzentration des selben Proteintyps in Lösung (Self-Crowding) nachgeahmt wird. Ein solches einfaches System ermöglicht beispielsweise die systematische Untersuchung des Einflusses von Self-Crowding auf die Proteindynamik. Selbst dann stellen sowohl die Größe und die Weichheit von globulären Proteinen, als auch das inhomogene Oberflächenladungsmuster eine Herausforderung für die Anwendung von kolloidalen Konzepten und Theorien dar, um ihre translatorische und rotatorische Diffusion in wässriger Lösung zu beschreiben.

In letzer Zeit führte die gegenseitige Inspiration von Proteinuntersuchungen und Kolloidphysik zu der bemerkenswert erfolgreichen Entwicklung und Anwendung der Theorie der “patchy Kolloide” für die Interpretation mehrerer experimenteller Beobachtungen, einschließlich der Bildung von Proteinclustern in Gegenwart von mehrwertigen Salzen [24]. Die Untersuchung von Proteinen in Lösung unter verschiedenen Bedingungen ist demnach ideal, um solche Theorien zu testen und zu verfeinern und ist für das intelligente Engineering von selbstorganisierenden Nanopartikeln vielversprechend. In dieser Hinsicht ist die Möglichkeit des Tunings von Protein-Wechselwirkungen besonders interessant, um Proteinkristallisation, welche für die Bestimmung von Proteinstrukturen über Kristallographietechniken [25] und für Arzneimittelentwicklung [26, 27] nützlich sein kann, auszulösen.

Für die Untersuchung von Proteindynamik in den erwähnten Kontexten ist Neutronenspektroskopie aus mehreren Gründen besonders geeignet. Kalte Neutronen wechselwirken nur schwach mit der Materie, was die Messung von empfindlichen biologischen Proben wie Proteine mit vernachlässigbaren Strahlungsschäden ermöglicht. Zudem können Lösungen mit für Zellumgebungen typisch hohen Konzentrationen und trübe Lösungen mit Neutronenspektroskopie leicht gemessen werden, anders als mit optischen Techniken. Außerdem werden die Neutronen besonders gut von den Wasserstoffatomen im Vergleich zu den anderen Elementen in Proteinen gestreut. Solche Streuung ist hauptsächlich inkohärent, und somit liefert Neutronenspektroskopie Informationen über die Selbst-Korrelationen der relativ homogen verteilten Wasserstoffatome, was die markierungsfreie Messung der durchschnittlichen Proteindynamik ermöglicht.

Allerdings werden Neutronen von den Wasserstoffatomen im H_2O ebenso wie von denen, die in Proteinen sind, gestreut. Eine übliche Abhilfe ist die Verwendung von D_2O als Lösemittel aufgrund des wesentlich geringeren Streuquerschnitts von Deuteriumatomen im Vergleich zu Wasserstoffatomen. Das gleiche Prinzip kann *innerhalb* der Makromoleküle verwendet werden: Proteine können in so einer Weise synthetisiert werden, dass Wasserstoffatome bestimmter Domänen und Subdomänen, gegen Deuteriumatome (D-Markierung) ausgetauscht werden, sodass man Informationen über ausgewählte hydrogenierte Teile erhält.

Typischerweise greift kalte Neutronenstreuung auf Längenskalen von Ångström bis Nanometer, somit im Bereich der Proteingrößen, und auf Zeitskalen von Pikosekunden bis Nanosekunden zu. Bei diesen Zeitskalen tritt, wie erwähnt, eine schnelle lokale Proteindynamik auf. Auf der Nanosekundenzeitskala hat ein mittelgroßes globuleres Protein nicht die Zeit, auf der Länge seines eigenen Radius von seiner Anfangsposition zu diffundieren. In diesem sogenannten Kurzzeitlimes wirken Kontakte zwischen den Teilchen nicht auf die Diffusion, die dennoch durch indirekte hydrodynamische Wechselwirkungen beeinflusst wird. Folglich ist Neutronenspektroskopie auch gut für die Untersuchung hydrodynamischen Wechselwirkungen in dem Kurzzeitlimes geeignet.

In Anbetracht seiner vielfältigen Vorteile wurde Neutronenstreuung in dieser Doktorarbeit zur Untersuchung von Proteinen *in Lösung* verwendet. Das Ziel ist es, die Auswirkungen der Verdrängung, der Temperatur (auch nach thermischer Denaturierung, d.h. die durch die Temperatur verursachte Entfaltung eines Proteins aus seiner nativen Struktur), als auch die Auswirkung der Anwesenheit von Ladungen in der Lösung auf die Proteindynamik besser zu verstehen. Die untersuchte Proteindynamik schließt globale Schwerpunktsdiffusion und innere Dynamik auf der Pikosekunden- bis Nanosekundenzeitskala mit ein.

Zu diesem Zweck haben wir eine systematische Studie von hochwertigen Daten, die während mehrerer Streuexperimente gesammelt wurden, durchgeführt. Solche Experimente wurden dafür aufgewendet, nur wenige einfache und leicht steuerbare Systeme, aber mit Variationen des Proteinvolumenanteils, der Lösungstemperatur und der Salzkonzentration in einem erheblich breiten Bereich zu untersuchen. Die gesammelten Daten ermöglichten den quantitativen Vergleich mit theoretischen Konzepten der Kolloidphysik, welche anschließend als Grundlage für die konsistente Extraktion und quantitative Analyse von internen Proteindynamik dient.

Ergebnisse

In dieser Arbeit wurde Proteindynamik als Funktion von den drei Parametern Proteinkonzentration, Temperatur und Konzentration eines mehrwertigen Salzes (YCl_3) untersucht. Im Folgenden fassen wir die in dieser Arbeit erzielten Ergebnisse, über den Einfluß der vorgenannten Parameter auf die Dynamik von Proteinen, zusammen.

Selbstverdrängungseffekte auf die Dynamik von γ-Globulin

Der Einfluss der Konzentration von γ-Globulin (IgG) sowohl auf seine Diffusion, als auch auf seine innere Dynamik wurde durch Neutronenrückstreuung (NBS) untersucht. Die Ergebnisse eines der ersten auf dem neuen Rückstreuspektrometer IN16B durchgeführten Experimente werden in Kapitel 6 auf Englisch dargestellt und wurden in Ref. [28] veröffentlicht.

Eine systematische Untersuchung wurde durch die Messung quasielastischer Spektra von Lösungen von IgG an Volumenanteilen φ von ~ 6 % bis ~ 27 % durchgeführt. Zwei Lorentz-Funtkionen wurden verwendet, um die von der Translation und der Drehung des Proteins, und von den internen Bewegungen entstehende quasielastische Verbreiterung, zu modellieren.

Unsere Experimente zeigen, dass der translatorische Diffusionskoeffizient D_t mit zunehmender Proteinkonzentration abnimmt. Nach der erfolgreichen Anwendung der Theorie der Diffusion von kolloidalen harten Kugeln zur Beschreibung einer solchen Verlangsamung in Rinderserumalbumin (BSA) Suspensionen [29] wurde die Studie in Kapitel 6 konzipiert, um zu testen, ob der gleiche Ansatz für IgG, das durch eine stark verzweigte Struktur charakterisiert ist, angenommen werden könnte. Der Vergleich zwischen Experiment und Theorie erfordert die Berechnung des effektiven Volumenanteils $\varphi_t = \alpha^3 \cdot \varphi$, wobei der Skalierungsfaktor $\alpha = R_h/R$ (R_h: hydrodynamischer Radius, R: Radius des trockenen Proteins) in Ref. [29] verwendet wurde, um das effektive hydrodynamische Proteinvolumen zu berücksichtigen. Für IgG, stimmt D_t quantitativ mit der kolloidalen Theorie überein, wenn $\alpha = 1.4$, d.h. wenn $\alpha = R_{\text{eff}}/R$, mit $R \leqslant R_{\text{eff}} \leqslant R_h$. Aus physikalischer Sicht könnte ein effektiver Radius beispielsweise wegen der Weichheit der Proteine, wegen einer zusätzlichen Mobilität der Domäne von IgG, oder wegen der Anisotropie seiner Struktur erforderlich sein.

Zusätzlich zu der Proteinselbstdiffusion wurden Informationen über die innere Dynamik selbstkonsistent aus der Streufunktion extrahiert. Der sogenannte Elastic Incoherent Structure Factor (EISF) liefert Informationen über die geometrische Einschränkung der diffusiven Bewegung der Atome im Protein. Der EISF wurde durch eine Kombination von zwei unterschiedlich eingeschränkten Geometrien und einem Anteil immobiler Atome modelliert. Ein erster Beitrag beschreibt die Geometrie der H-Atome in Methylgruppen (CH_3) und wurde durch Sprünge zwischen drei Standorten, die auf die bekannten Atomabstände in der chemischen Gruppe gesetzt wurden, modelliert.

Der zweite Beitrag beschreibt den Durchschnitt der Diffusionsgeometrien der übrigen mobilen H-Atome und wurde durch ein Modell, in dem ein Atom innerhalb einer undurchlässigen Kugel diffundiert, beschrieben. Nach unseren Ergebnissen ist der Radius R der Kugel sowie der Anteil an immobilen Atomen innerhalb der Fehlerbalken unabhängig von φ.

Die quasielastische Verbreiterung, die der inneren Dynamik zuzuschreiben ist, wurde durch ein Sprung-Diffusions-Modell mit einem Sprung-Diffusionskoeffizient D_j und einer Verweilzeit τ beschrieben. Während D_j, sowie die geometrischen Parameter aus dem EISF, innerhalb der Fehlerbalken konstant waren, nimmt τ mit steigendem Volumenanteil zu. Diese Beobachtung legt eine durch Verdrängung induzierte Stabilisierung der Proteinkonformation nahe.

Die Dynamik von BSA während der Wärmedenaturierung

Um ein besseres Verständnis des Unterschieds der Dynamik von BSA vor und nach der Denaturierung, zu erhalten, wurden mit BASIS wässrige (D_2O) Lösunge bei drei Proteinkonzentrationen (150, 200, und 500 mg/ml), bei Temperaturen unterhalb und oberhalb der Denaturierungstemperatur gemessen.

Nah an Raumtemperatur wurden die Daten über das konventionelle Zwei-Lorentz-Modell ausgewertet. Die beobachtete q-Abhängigkeit der halben Halbwertsbreite (HWHM) Γ_{int} für die interne Dynamik ist im Einklang mit dem Sprung-Diffusions-Modell, das auch in der Studie über

IgG verwendet wurde. Die am BASIS gemessenen Daten weisen bei Temperaturen nahe genug an der Denaturierung ein ungewöhnliches nicht-monotones Verhalten von $\Gamma_{\text{int}}(q)$ auf. Bezugnehmend auf die Eigendynamik, würde ein solches Verhalten suggerieren, dass ein Atom mehr Zeit braucht ein kleines Volumen als ein großes Volumen zu erkunden, was eindeutig widersprüchlich ist. Infolgedessen ist unsere Beobachtung mit einem einzigen internen Prozess nicht konsistent. Daher zeigen die Daten das Auftreten von dynamischen Prozessen auf mindestens drei Zeitskalen .

Wir haben vorgeschlagen, dass diese drei Prozesse der globalen Diffusion des gesamten Proteins, der Rückgratdynamik (“Backbone”) und der Seitenkettendynamik entsprechen. Wir haben daher ein Modell angewandt, bei dem die mobilen Seitenketten kontinuierlich zwischen zwei Diffusionszuständen wechseln. In einem Zustand wird die Seitenkette bezüglich des Backbones beispielsweise aufgrund sterischer Wechselwirkungen mit anderen Seitenketten blockiert. Das Backbone schwankt jedoch, wenn auch mit einer niedrigeren Rate, und damit auch die gebundene Seitenkette. Folglich erfährt die Seitenkette in diesem Zustand eine Diffusionsbewegung, welche die Bewegung des Backbones reflektiert. Im laufe der Zeit finden eine zunehmende Zahl von lokalen Umlagerungen statt, und schließlich kann sich die Seitenkette relativ frei mit einer höheren Rate bewegen. Daher wird die Backbonedynamik nur indirekt gemessen, wenn die Seitenketten im blokierten Zustand sind, da die Mehrheit des Signals von den Seitenketten stammt.

Das oben beschriebene Modell liefert ein konsistentes physikalisches Bild der Wirkung der Temperatur und der Wärmedenaturierung, sowohl im Bereich der Diffusion, als auch der inneren Dynamik. Es wurde bestätigt, dass die Kurzzeit-Selbstdiffusion von BSA bei Temperaturen unterhalb der Denaturierung mit der Kolloidtheorie übereinstimmt. Nach dem Entfalten nahm der Diffusionskoeffizient, im Einklang mit der Vorstellung eines vernetzten Proteinnetzwerkes, das die Diffusion unterdrückt, drastisch ab.

In der Dynamik der Backboneatome wurde einen Übergang in der Nähe der Denaturierungstemperatur beobachtet, oberhalb deren der zugeordnete Diffusionskoeffizient schneller mit steigender Temperatur zunimmt. Dies spiegelt wahrscheinlich die Entfaltung der Sekundärstruktur wider. Der den Seitenketten zugeordnete Diffusionskoeffizient zeigte stattdessen nur bei der höchsten Konzentration eine Änderung bei der Denaturierung, während bei niedrigeren Konzentrationen kein klarer Übergang beobachtet wurde. Dagegen wurde die verstrichene Zeit, bevor die Seitenketten von einem Zustand zum anderen wechseln an der Denaturierungstemperatur abrupt erhöht.

In Bezug auf die eingeschränkte Diffusionsgeometrie wurde ein Radius a, zusätzlich zu dem von den Seitenketten zugänglichem effektiven Radius R, vom EISF abgeleitet und mit den Backboneschwankungen assoziiert. Innerhalb der Fehlerbalken blieb R in den gesamten Temperaturbereich konstant. Dies ist konsistent mit einer Vorstellung, in der die kovalenten Bindungen zwischen Seitenkettenatomen das zugängliche Volumen stark beeinflussen. Stattdessen konnte die Temperaturabhängigkeit des mit den Backboneschwankungen verbundenen Radius, in Bezug auf Atome, die in einer effektiven elastischen Potentiallandschaft sitzen, interpretiert werden. Unter dieser Annahme wurde eine effektive Kraft erhalten, die konsistent mit Literaturwerten ist. Schließlich wurde beobachtet, dass die Anzahl der immobilen Atome mit wachsender Temperatur kleiner wird und der Anteil der Atome, die mit einer “Diffusion in einer Kugel” beschrieben werden wird an der Denaturierungstemperatur deutlich erhöht, was mit einer höheren Anzahl von Seitenketten, die nach der Entfaltung ein größeres Volumen erkunden dürfen, konsistent ist.

Mehrere andere Hypothesen wurden getestet, um die Daten zu interpretieren, einschließlich der Anwesenheit von Populationen von Monomeren und statischen Clusters oder Monomeren und dynamisches Clusters, doch lieferten keine dieser Hypothesen konsistente Ergebnisse.

Zusammenfassend konnten wir eine Änderung der Dynamik von BSA auf der Piko- bis Nanosekundenzeitskala bei thermischer Denaturierung beobachten, und wir haben eine quantitative Modellierung der Dynamik des Entfaltens von Proteinen in Lösung eingeführt. Die steile Abnahme des globalen Diffusionskoeffizienten wurde als Folge der Bildung eines vernetzten Proteinnetzwerkes, welche die Schwerpunktsmobilität drastisch reduziert, interpretiert. Zur Berücksichtigung der internen Dynamik wurde ein Modell, das Seitenkettenatome beschreibt, die alternierend zwischen einer langsamen und einer schnellen Diffusionsbewegung umtauschen, vorgeschlagen. Die erste wurde spekulativ mit den zugrunde liegenden Backboneschwankungen identifiziert. Gemäß einem solchen Bild kann das hier zum ersten Mal angewandete Modell den Zugang und die Einsicht sowohl in die Seitenketten- als auch in die Backbonedynamik gewähren.

Die Diffusion von BSA in Gegenwart des dreiwertigen Salzes YCl_3

Um ein besseres Verständnis der Wirkung von YCl_3 auf die Dynamik von BSA zu gewinnen, haben wir systematische quasielastische Neutronenstreu- (QENS) Messungen am Time-of-Flight-Rückstreuspektrometer BASIS am Oak Ridge National Laboratory (ORNL) durchgeführt. Dafür wurden die apparente Diffusionskoeffizienten $D(c_s, c_p)$ von Serien von Proben bei mehreren festen Proteinkonzentrationen c_p und steigender Salzkonzentration c_s (Salzserie), gemessen. Es wurde beobachtet, dass $D(c_s, c_p)$ bei jeder Salzserie mit steigenden c_s abfällt. Darüber hinaus wurde $D(c_s, c_p)$ von jeder Salzserie durch den jeweiligen Koeffizient $D(c_s = 0, c_p)$ normiert, und als Funktion von c_s/c_p geplottet. Somit wurde ein bemerkenswert universelles Verhalten gefunden. Mathematisch ausgedrückt, haben wir beobachtet, dass $D(c_s, c_p) = D(c_s = 0, c_p)\, g(c_s/c_p)$, wobei $g(c_s/c_p)$ eine skalare Funktion ist, die nur von der Anzahl von Y^{3+} Ionen pro Protein in der Lösung abhängt.

Folglich werden die Kurzzeit diffusiven Eigenschaften des Systems vollständig durch $g(c_s/c_p)$ kombiniert mit den Ausdrücken aus der Kolloidtheorie charakterisiert, innerhalb des untersuchten Bereichs von c_p und c_s/c_p.

Um das Ergebnis zu interpretieren, haben wir uns von der Theorie der kolloidalen Suspensionen von “patchy” harten Kugeln [24] inspirieren lassen. In diesem Bild binden Y^{3+} Ionen an spezifische Stellen auf der Oberfläche von Proteinen, wo sie als Brücke zwischen den Makromolekülen wirken. In diesem Fall liefert die Flory-Stockmeyer-Theorie eine Abschätzung der Anzahldichteverteilung von n-Clusters, welche von der Bindungswahrscheinlichkeit p_b abhängt. Daher wird eine Verschiebung der Clustergrößeverteilung zu größeren Ausdehnungen von der Zugabe von Salz verursacht. Die Anwesenheit größerer Clusters ergibt sich dann in einer Verlangsamung der durch NBS gemessenen durchschnittlichen apparenten Diffusion. Unsere Auswertung zeigt, dass eine solche Vorstellung die Universalität des Abnehmens von $D(c_s, c_p)/D(c_s = 0, c_p)$ als Funktion von c_s/c_p konsistent erklären könnte, nur wenn auch p_b innerhalb der experimentellen Genauigkeit universell mit c_s/c_p skaliert, was im Enklang mit einer quantitativen Bindung von Y^{3+} Ionen an der Oberfläche von BSA stünde.

Dieses Ergebnis zeigt das Potential von Patchy-Teilchen-Theorien zur Beschreibung von Proteinen. In ferner Zukunft könnte das Resultat der intelligenten Herstellung von selbstorganisierenden Teilchen dienen.

Schlussfolgerungen und Ausblick

Im Folgenden werden die wichtigsten Ergebnisse dieser Doktorarbeit zusammengefasst und mögliche Auswirkungen der Ergebnisse und Entwicklungen werden kurz diskutiert.

Das Ziel dieser Arbeit war die Untersuchung der Diffusion und der inneren Dynamik von Proteinen in Lösung als Funktion dreier Parameter: der Proteinkonzentration, der Lösungstemperatur und der Konzentration von mehrwertigen Ionen. Die Auswirkung dieser Parameter auf die Dynamik von Proteinen kann für Biologie, Kolloidphysik, Chemie und Pharmazie wichtig sein. Um Informationen über Pikosekunden- bis Nanosekundendynamik auf der Nanometerskala zu erhalten, führten wir quasielastische Neutronenstreuexperimente, bestehend in der systematischen Variation verschiedener Parameter auf vereinfachte Modellsysteme, durch. Alle Proben waren wässrige Lösungen.

Die Untersuchung eines Proteins mit einer stark verzweigten Struktur, γ-Globulin (IgG), bei verschiedenen Konzentrationen wurde durchgeführt, um ein besseres Verständnis der Auswirkung der Verdrängungseffekte auf die Proteindiffusion und innere Proteindynamik zu gewinnen. Unsere Ergebnisse zeigen, dass makromolekulares Crowding einen signifikanten Einfluss auf beides hat: es verursacht sowohl eine Verlangsamung der Diffusion des ganzen Proteins, als auch eine Zunahme der Korrelationszeiten, die der Seitenkettebewegung zugeschrieben werden, was auf eine Stabilisierung der Proteinstruktur hinweist, die für biologische Prozesse wichtig sein könnten. Darüber hinaus haben wir gezeigt, dass Konzepte der Physik der kolloidalen Suspensionen von harten Kugeln aufgebracht werden können, um die Diffusion des stark anisotropen IgGs auf der Nanosekundenzeitskala zu beschreiben, angenommen dass der Volumenanteil für den theoretischen translatorischen Kurzzeitdiffusionskoeffizienten mit einem effektiven Partikelradius berechnet wird, welcher größer als der des trockenen Proteins, aber kleiner als der von einer starren Struktur berechneten hydrodynamischen Radius ist. Eine offene Herausforderung für zukünftige Studien ist die Entwicklung eines verbesserten Modells dieses Ergebnis mit den neuen Ergebnissen von Neutronenspinechospletroskopie (NSE) Kombination in Bezug auf die Dynamik der Domänen von IgG [30].

Die durchgeführte Studie ist, zusammen mit anderen, ein wichtiger Schritt zum Verständnis der Auswirkungen der Zellumgebung auf die Dynamik von Proteinen. In dieser Hinsicht könnten Neutronenstreuungstudien von hydratisierten Proteinen in deuteriertem Lysat [1] zusätzliche Informationen liefern. Ein solches System ist zweifellos komplexer als die wässrige Lösung aus einer einzigen Art von Protein, aber es stellt auch ein realistischeres Modell für die zelluläre Umgebung dar. Außerdem ermöglicht es, im Gegensatz zu Messungen in lebenden Zellen, eine systematische und kontrollierte Variation von verschiedenen Parametern (insbesondere die Verdrängung), ähnlich zu den hier vorgestellten Experimenten.

Lösungen des globulären Proteins BSA bei drei Konzentrationen wurden verwendet, um die Auswirkungen der Temperatur und der thermischen Denaturierung der Proteindynamik zu untersuchen. Die Diffusion von BSA wurde wiederum konsistent mit früheren Studien und Kolloid

---

[1] Lysate ist das Produkt des Zerbrechens einer Zelle durch den Bruch der Zellmembran.

Theorien gefunden, bis aufgrund des thermisch induzierten Entfaltens des Proteins ein gelartiges Netzwerk gebildet wurde und die Proteinmobilität drastisch abfiel. Insbesondere zeigen die Daten das Auftreten von zwei internen Prozessen bei hohen Temperaturen. Um die Ergebnisse zu interpretieren, wurde ein Modell entwickelt, das ein Atom der Seitenkette beschreibt, das zwischen zwei diffusiven Zuständen umschaltet. Damit wurde ein in sich konsistentes physikalisches Bild der inneren Dynamik vor und nach der Denaturierung erhalten. Unterhalb der Denaturierungstemperatur hat die Temperatur wenig oder keinen Einfluss auf den mit dem Backbonebewegung verbundenen Diffusionskoeffizienten, während der den Seitenketten zugeordnete Diffusionskoeffizient sowie die Anzahl von mobilen Atomen mit steigender Temperatur erhöht werden. Nach der Denaturierung wird die Anzahl von mobilen Atomen sowie der Anteil an Seitenketten, die sich ziemlich frei bewegen können, deutlich erhöht. Zudem erhöhte sich außerdem der Diffusionskoeffizient, der auf die Backboneschwankungen zurückzuführen ist, stärker, während jener der beweglichen Seitenketten nur bei der höchsten Konzentration signifikant beeinflusst wurde, vermutlich wegen der Nähe von mehr Seitenketten anderer Proteine in dem vernetzten Netzwerk.

Die Unterscheidung der Backbone- und Seitenkettendynamik könnte beispielsweise interessant sein, um das Verständnis der allosterischen Regulation zu verbessern.

Schließlich wurde die Wirkung des dreiwertigen Salzes YCl_3 auf die Diffusion von BSA in wässriger Lösung untersucht. Messungen bei mehreren Protein- und Salzkonzentrationen wurden durchgeführt, und eine Dämpfung der Diffusion wurde sowohl bei steigender Protein- als auch Salzkonzentration beobachtet. Der Einfluß der Konzentration von BSA auf seine Selbstdiffusion wurde in einer früheren Rückstreustudie von Roosen-Runge et al. [29] gründlich untersucht. Interessanterweise haben wir zusätzlich zu diesen Ergebnissen festgestellt, dass bei allen gemessenen Proteinkonzentrationen c_p die Erhöhung der Anzahl der Y^{3+} Ionen pro Protein in Lösung, innerhalb der Fehlerbalken eine universelle Verlangsamung relativ zu der Diffusion bei dem gleichen c_p jedoch in Abwesenheit von Salz, verursacht. Inspiriert von Roosen-Runge et al. [24] wurde die Beobachtung in Bezug auf kolloidale Suspensionen von durch Ionen aktivierten patchy harte Kugeln, bei welchen die Bildung von Proteinclusters durch Ionenbrücken mit einer gut definierten Größenverteilung erwartet ist, interpretiert.

Eine vereinfachte Streufunktion für dieses Szenario wurde abgeleitet und an die Daten angepasst, um eine Bindungswahrscheinlichkeit p_b zu erhalten. Wir fanden, dass, innerhalb der Fehlerbalken, p_b selbst eine Funktion von nur c_s/s_p ist, was auf eine nahezu quantitative Bindung der Kationen an spezifischen Stellen auf der Proteinoberfläche hinweist. Daher kann die beobachtete Verlangsamung von der Anwesenheit von Ionen in der Lösung verursacht werden, indem diese zur Clusterbildung führen, wobei die Clustergrößenverteilung lediglich durch das Verhältnis der Salzkonzentration und Proteinkonzentration gesteuert werden könnte.

Eine interessante Folge des vorgeschlagenen Bildes ist die Möglichkeit, die Größenverteilung der Cluster auch durch die Veränderung der Temperatur des Systems zu steuern, ohne die Probenzusammensetzung zu modifizieren. Die Beobachtung und das Verständnis eines solchen Verhaltens könnte erhebliche Auswirkungen sowohl in theoretischen als auch in angewandten Bereichen, wie Kolloidphysik und quantitative Biologie, haben. Zum Beispiel könnte es ein guter Test für Theorien der patchy Kolloidphysik sein, könnte zu einer rationalen Wahl der Parameter für die Herstellung von selbstorganisierenden Clusters führen, oder könnte auch wichtig zum Verständnis der Proteinaggregation in biologischen Zellen sein, die in mehreren neurodegenerativen

Erkrankungen, wo auch mehrwertige Salze scheinen eine zu Rolle spielen scheinen, beobachtet wird.

Abstract

Proteins are macromolecules naturally occurring in living cells and organisms, involved in a great number of processes essential for life. Their structural and dynamical properties are strictly related to their function, which is optimized in the temperature range in which the respective organisms live. The cellular environment in which globular proteins are found consists of an aqueous solution of several types of macromolecules occupying large volume fractions (molecular crowding) and larger assembled structures, together with different kinds of sugars and ions. Such an environment crucially affects the physico-chemical properties of these molecular machines. For instance, in the simple case of one single type of negatively charged protein in solution, the presence of multivalent cations results in a very rich phase behavior, characterized, amongst others, by protein aggregation – often related to neurodegenerative diseases –, liquid–liquid phase separation, and crystallization. Recently, it was demonstrated that such a phase behavior can be rationalized by theories of colloidal suspensions of patchy particles, which renders protein systems interesting not only from a biomedical perspective, but also for colloid physics, chemical engineering and nanotechnology, especially in the prospect of the smart production of self-assembling structures.

In this thesis, the results of experiments carried out at the Institut Laue-Langevin, Grenoble, France, and at the Spallation Neutron Source at the Oak Ridge National Laboratory, Tennessee, USA, are presented after an extensive review of the literature concerning the dynamics of proteins in solution studied by neutron spectroscopy. In order to progressively improve the understanding of the effect of different parameters on the dynamics of proteins, the picosecond to nanosecond (short-time) self-diffusion and internal dynamics of two model proteins in aqueous (D_2O) solution is studied by neutron backscattering as a function protein concentration, temperature and multivalent salt concentration. Hence, the cellular environment is simplified to an aqueous solution of a single protein, such that a systematic investigation can be carried out.

First, a change of diffusion and internal dynamics of the antibody γ-globulin as a function of its concentration (self-crowding) is observed. The concentration dependence of the protein translational diffusion is rationalized in the context of colloid physics, provided that a volume fraction accounting for the bare protein and additional water molecules diffusing with it is inserted in the theoretical expression. The protein internal dynamics is observed to slow down with increasing self-crowding.

Second, temperature effects are studied on both the diffusion and the internal dynamics of the globular protein bovine serum albumin (BSA), below and above the denaturation temperature. A novel model is proposed to describe the dynamics of the protein side-chains, yielding a rather

complete and consistent physical picture of the pico- to nanosecond dynamical changes occurring upon protein denaturation.

Third, the change of the diffusion of BSA as a function of the concentration of the trivalent salt YCl_3 is investigated, and a remarkably universal slowing down of the apparent diffusion coefficient of BSA molecules as a function of the number of cations per protein c_s/c_p in solution is found. The result is interpreted in terms of the theory of colloidal suspensions of patchy particles as a result of the semi-quantitative binding of Y^{3+} ions to specific sites on the protein surface leading to the formation of protein clusters with a cluster size distribution easily tunable by c_s/c_p.

Chapter 1

Introduction

Proteins are a formidable subject of study for several branches of modern science and technology, from colloid physics to chemical engineering and nanotechnology, from biology to medicine and pharmacy. Globular proteins are soft and floppy macromolecules with typical diameters on the order of a few nanometers.

Obviously, proteins were first studied because of their biological relevance: they take part in a large variety of processes of vital importance for all biological cells, and, depending on their composition, they can serve for instance as enzymes, antibodies or carriers of smaller molecules or ions, as well as for structural purposes [1]. When defective, proteins can cause serious disorders in the life cycle of a cell [2]. Moreover, deficiencies in protein activity resulting e.g. from misfolding, denaturation, and aggregation have been associated to a variety of different diseases [3–6].

The function of proteins is granted by a combination of their specific structure and dynamics [7,8], which renders a quantitative characterization of protein internal dynamics essential for the understanding of living systems and possibly of some mechanisms leading to malfunction. Moreover, protein internal dynamics allowing structural flexibility can increase the affinity to be achieved between a drug and its target and is therefore fundamental to understanding the ways in which drugs exert biological effects [9].

Numerous studies have addressed protein diffusion in living cells [10], in the nucleoplasm [11], in the mitochondrial lumen [12], and in the cytoplasm [13–17]. Generally, protein dynamics *in vivo*, where the macromolecular volume fraction is 20-40% (roughly equivalent to a concentration of 200 - 400 mg/ml), is found to be significantly slower than in dilute protein solutions. In addition to this, also protein internal dynamics, and thus potentially protein function, is expected to be affected by macromolecular crowding, i.e. the high concentrations found in physiological environments [18].

Further *in vivo* studies regarding protein internal dynamics have shown that the mean effective resilience of macromolecules present in living bacteria adapted to live at different, extreme temperatures, increases with their adaptation temperature [19–21]. Even more, the resilience is such that the average root mean square fluctuation of the hydrogen atoms in the macromolecules within the bacteria at a 100 ps time scale is always about 1.2 Å at the respective adaptation temperature. Such a result corroborates the hypothesis that biological activity requires internal macromolecular fluctuations on the subnanosecond time scale to be maintained within a narrow limit, which is ensured by evolutionary selection of macromolecular structures yielding the appropriate resilience [19].

Similar results were obtained by a neutron study of hemoglobin (Hb) from different endotherm species in highly concentrated aqueous solutions [22] and by a combined nuclear magnetic resonance (NMR) and molecular dynamics (MD) simulations study on a hyperthermophilic and a mesophilic adenylate kinase (Adk) [8]. In the former research, the resilience of Hb was found to be higher for species adapted to higher temperatures, and the root mean square displacement of hydrogen atoms within Hb is about 1.2 Å at the corresponding average body temperature [22]. The latter study reports that on the ps-ns timescale, even though at the same temperature local protein motions differ between a mesophilic and a hyperthermophilic Adk, they are markedly similar at temperatures at which enzymatic activity and free energy of folding are matched [8]. Since the enzymatic activity of Adk requires the opening and closing of a “lid” occurring on the µs-ms time scale, these results suggest that fast local motions within a limited range of correlation times and amplitudes are key for facilitating motions of large sub-units of proteins on longer time scales [8]. The ps-ns dynamics may also be related to allosteric signaling between different parts of the biomacromolecule [23]. In other words, fast internal dynamics may contribute in the regulation of a protein by the binding of specific molecules at a site other than the active site of the protein, in a way that cannot be predicted on the basis of the ground-state structure of the protein [23].

Although the biological interest of proteins is strictly coupled to its natural environment, *in vivo* measurements have the clear disadvantage that systematic experiments to quantify the effect of various parameters such as macromolecular crowding or salt concentration on their behavior cannot be performed. In order to do so, the complex cellular environment must be first simplified so that the system can be controlled as a function of different parameters in a reliable manner. One type of protein in solution constitutes the simplest model, where the macromolecular crowding is mimicked by the high concentration of the single protein type in solution (self-crowding). Such a simple system allows, for instance, for the systematic investigation of the effect of self-crowding on protein dynamics.

Even so, the size and softness of globular proteins poses a challenge for the application of colloidal concepts and theories in order to describe their translational and rotational diffusion in aqueous solution. Moreover, the inhomogeneous surface charge pattern of proteins and their tendency, under certain conditions, to form clusters constitutes an additional challenge to colloid physics.

Recently, mutual inspiration from protein studies and colloid physics lead to the remarkably successful development and application of the theory of “patchy colloids” for the interpretation of a number of experimental observations, including the formation of protein clusters in the presence of multivalent salts [24]. Thus, the study of proteins in solution under different conditions is ideal for testing and refining such theories, and is promising for smart engineering of self-assembling nano-particles. In this respect, the possibility of tuning protein interactions is particularly interesting in order to trigger their crystallization, which may be useful for the determination of protein structures via crystallography techniques [25] and drug discovery [26, 27].

As an experimental tool to study protein dynamics in these contexts, neutron spectroscopy is a remarkable technique for a series of reasons. Cold neutrons interact only weakly with matter, which allows the measurement of fragile biological samples such as proteins with negligible radiation damage. Also, generally, high protein concentrations typical of cell environments and turbid solutions can be easily measured, other than with optical techniques. Moreover, the neutrons are scattered particularly well by the hydrogen atoms compared to the other elements in proteins. Such a scattering is mainly incoherent, meaning ultimately that neutron spectroscopy can provide information on the self-correlations of the rather homogeneously distributed hydrogen atoms, which allows for a label-free measurement of the average protein dynamics.

Unsurprisingly, however, the hydrogen atoms in H_2O scatter neutrons just as well as those in proteins. A common workaround is the use of D_2O as a solvent, due to the much lower scattering cross Section of deuterium atoms compared to hydrogen atoms. The same principle can be used *within* the macromolecules: proteins can be synthesized in such a way that the hydrogen atoms in specific domains and sub-domains are exchanged with deuterium atoms (D-labeling), thus information on selected parts can be obtained.

Typically, cold neutron scattering accesses length scales from Ångströms to nanometers – precisely in the range of protein sizes –, and dynamics from picoseconds to nanoseconds. At this time scale, as mentioned, fast local dynamics occurs. On the nanosecond time scale, a medium sized globular protein has not the time to diffuse the length of its own radius from its initial position. In this so-called short-time limit, contacts between particles do not affect the diffusion, which will nevertheless be influenced by indirect hydrodynamic interactions (HI). Consequently, neutron spectroscopy is well suited for the study of effects of HI occurring in the short-time limit.

In the light of its multiple advantages, we thus employ neutron scattering for the study of proteins *in solution*. Our aim was to understand the impact of crowding, temperature – also throughout thermal denaturation, that is the unfolding of a protein from its native structure due to temperature – as well as that of the presence of charges in solution on protein dynamics, from global center-of-mass diffusion to internal dynamics, on the pico- to nanosecond time scale.

To this end, we performed a very systematic study by exploiting high-quality data gathered during an unprecedented amount of beam time dedicated to just a few simple and easily controllable systems, but with variations of the protein volume fraction, solution temperature and salt concentration in a considerably broad range. The experiments allowed for a quantitative comparison with theoretical concepts of colloid physics, which subsequently served as a basis for consistent extraction and quantitative analysis of protein internal dynamics.

This thesis is organized as follows. In Chapter 2, the theory and concepts of colloid physics, protein dynamics and neutron scattering, which will be employed in the ensuing Chapters, will be explained. Chapter 3 presents a review of pre-existing neutron studies on the dynamics of proteins in solution. Chapter 4 contains information on the employed materials (proteins, salts, etc.), sample preparation, established analysis procedures of neutron scattering data, as well as on the instruments on which experiments were performed. In Chapter 5, an overview of the results of this work will be given, preceding the Chapters 6, 7, and 8 reporting the results and interpretation of the studies of protein dynamics as a function of crowding, temperature, and the concentration of a trivalent salt, respectively.

Chapter 2

Theoretical Background

Proteins are rather soft particles which, in many cases, can be considered as nanometer scale colloids. In this thesis, the global diffusion typical of all kinds of colloids, as well as the internal dynamics of these macromolecules is explored by employing quasi-elastic neutron scattering (QENS). This Chapter provides the main necessary theoretical notions. The topics will be approached in a rather heuristic and intuitive manner. For more a more rigorous treatment, the reader is invited to refer to the references cited below and to the PhD thesis of Marcus Hennig [31].

In Section 2.1 we introduce the concept of colloidal particles and colloidal suspensions, following mainly the approach found in the text book by Dhont [32] and the lecture notes by Nägele [33]. Section 2.2 is focused on diffusion and is again largely based on the lecture notes by Nägele [33] and the text book by Dhont [32]. In a first part, self-diffusion is introduced, followed by a part on collective diffusion. In Section 2.3, the concept of patchy colloids is presented, mostly referring to the article by Roosen-Runge et al. [24]. Sections 2.4 to 2.5 give an introduction to basic concepts of neutron scattering and in particular QENS, mainly based on the text books by Bee [34], and Squires [35], as well as on the article by Schober [36]. Finally, in Section 2.6, models commonly used for the description of internal protein motion as seen by QENS are reviewed, and a model applied here for the first time is explained.

2.1 Colloidal Suspensions

In the following, the concept of “colloids” will be explained. This Section is inspired by the text book by Dhont [32] and the lecture notes by Nägele [33].

The first systematic studies on colloidal systems started 1861 and were carried out by Thomas Graham, who also first defined “colloids” as those species dissolved in solutions which are not able to diffuse through a membrane. This definition obviously depends on the size characteristics of the membrane, since the particles not diffusing through it are larger than the size of the pores. A more modern definition considers colloids those species dissolved in solution, which exhibit Brownian motion, i.e. the irregular motion caused by random collisions (induced by thermal motion) of solvent molecules on the colloidal particle first observed on pollen grains in water. Clearly, also this definition is not particularly sharp, since it simply requires colloidal particles to be large compared to the solvent molecules, but sufficiently small to exhibit Brownian motion [32].

In an attempt to estimate the lower and upper limits for the size of a colloidal particle some heuristic considerations can be done. Colloidal particles must be sufficiently large to allow a description of the interaction between them and the solvent molecules by macroscopic equations of motion for the fluid with boundary conditions for the solvent flow on the surface of the particles. In this way, Brownian motion is characterized through macroscopic properties of the solvent, such as viscosity and temperature. These requirements are fulfilled when (i) the structure of the solvent molecules enters the interaction of the colloidal particle with the solvent molecules only in an averaged way, and (ii) many solvent molecules interact simultaneously with the surface of a single colloidal particle. Therefore, the radius of the colloidal particle must be at least about a factor ten larger than that of the solvent molecule. Hence, the effective radius of water commonly being approximated to 1.4 Å, the radius of a colloidal particle in suspension in water should be at least on the order of nanometers [32].

On the other hand, a colloidal particle must still show Brownian motion (thermal motion), which is relevant only when thermal displacements are a measurable fraction of the linear size of the particle on typical timescales accessible during experiments. As soon as thermal motion is of importance to determine the displacements of a "large object", this object is classified as colloidal particle. If the particle is too big, displacements due to other forces (e.g. gravity or Archimedes' principle) will be much larger than thermal displacements, which will therefore be negligible. Typically, thermal motion becomes significant when the radius of the particle is less than approximately 10 µm [32].

We can generally distinguish between three kinds of colloidal particles: (i) rigid particles such as gold nanoparticles, (ii) macromolecules, i.e. very large molecules with a rather flexible structure, and (iii) assemblies of small molecules in thermodynamic equilibrium with their environment, such as micro-emulsions, usually consisting of droplets of oil in water or of water in oil stabilized by surfactant molecules [32].

Examples of macromolecules which can be considered as colloidal particles are compact polymer particles and proteins. Particularly, the latter are at the lower limit for the size of a colloid, since typical protein radii are on the order of nanometers [32].

Particles in colloidal suspensions, including proteins, can be subject to strong local correlations and the system may be characterized by a rich phase diagram depending on the relative strength of interparticle interactions, including "gas", liquid, solid, glass, gel, and crystallized phases. A detailed description of the physics regarding such phenomena is however beyond the purpose of this thesis.

In this thesis, notions and theories of the physics of colloidal suspensions are applied in an attempt to describe the diffusion of proteins in solution. After having introduced here the concept of "colloidal particle", in the next Section the basic principles of diffusion of colloidal particles are presented.

2.2 Diffusion

Two fundamental types of diffusion processes can be distinguished in suspensions of monodisperse colloids: self-diffusion and collective diffusion. The former refers to the diffusion of a tagged colloidal particle (or tracer particle) in suspension with other particles, while the latter refers to the isothermal relaxation of density inhomogeneities through correlated and collective motions of many particles. In the limit of infinite dilution, collective and self-diffusion converge to the same value [33].

This Section, based on the text book by Dhont [32] and the lecture notes by Nägele [33], will be concerned with the diffusion theory of colloidal particles. A rather heuristic approach will be followed, and many of the derivations of the laws will not be presented, as they can be easily found in the aforementioned references and references therein.

2.2.1 Self-Diffusion

In the following, we will consider a tracer particle diffusing in a solution with other particles of the same type, i.e. we will focus on self-diffusion of monodisperse colloidal particles. In a very dilute colloidal suspension, diffusion can be simply understood in terms of a particle undergoing a random motion, as the molecules of the solvent colliding with the surface of the diffusing particle, act as a Gaussian distributed fluctuating force $\xi(t)$ such that

$$\langle \xi(t) \rangle = 0\,, \qquad \left\langle \xi(t) \cdot \xi(t') \right\rangle = 2d\,B\,\delta(t - t')\ , \tag{2.1}$$

where d is the dimension of the system, and the brackets represent an average over the fast solvent collisions. $B = k_B T \gamma$ is a measure of the strength of the fluctuating force, with the friction coefficient γ, which for a sphere is given by $\gamma = 6\pi\eta\,R$ [33]. At higher particle concentrations, additional direct and indirect interactions between the particles become important, as explained below.

In order to characterize the translational displacement of a tracer colloidal particle it is convenient to consider the diffusive mean-square displacement (MSD):

$$W(t) \equiv \frac{1}{2d} \left\langle |\mathbf{r}(t) - \mathbf{r}(t=0)|^2 \right\rangle\ , \tag{2.2}$$

where $\mathbf{r}(t)$ denotes the position vector of the center of mass of the tracer particle at time t, and d is the system dimension (in the systems considered in this thesis, $d = 3$). The brackets $\langle ... \rangle$ denote an ensemble average.

Analyzing the evolution of $W(t)$ as a function of time, different characteristic times for the dynamics of a colloidal particle can be identified (cf. Figure 4.12). If a particle is moving at the time $t = 0$ with a velocity $\mathbf{v}_0$, the velocity will not change significantly under the impact of the solvent molecules for very short times, that is $\mathbf{r}(t) - \mathbf{r}(0) \simeq \mathbf{v}_0\,t$. Hence, a momentum relaxation time τ_B can be defined, with

$$W(t) \sim t^2 \qquad t \ll \tau_B\,. \tag{2.3}$$

For times much larger than τ_B but well before collisions between particles occur, the colloidal particle has experienced several collisions with the solvent molecules and its trajectory can be described by a Brownian random motion (see Equation (2.1)). Hence,

$$W(t) \sim D_s^s\,t \qquad \tau_B \ll t \ll \tau_I\ , \tag{2.4}$$

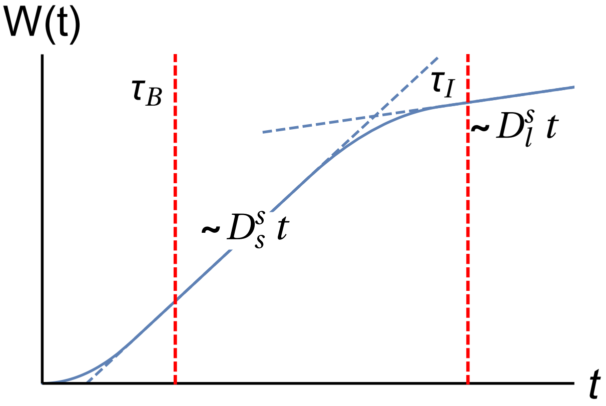

Figure 2.1: Sketch of the diffusive MSD $W(t)$ as a function of time. For very short times, $W(t) \sim t^2$. For $\tau_B \ll t \ll \tau_I$, $W(t) \sim D_s^s\,t$, and for $t \gg \tau_I$ $W(t) \sim D_l^s\,t$.

with the short-time self-diffusion coefficient D_s^s and the interaction time scale τ_I after which a particle experiences a substantial change of the potential interactions through a perceptible change in its next neighbor particle configuration [33].

For a diffusive process, the MSD $W(t)$ can be related to the probability of finding a tracer particle in the position $\mathbf{r}$ at the time t given that at the time $t = 0$ it was in $\mathbf{r}_0$ by a Gaussian probability distribution:

$$P(\mathbf{r}, t|\mathbf{r}_0) = \frac{1}{(4\pi\, W(t))^{\frac{d}{2}}} \exp\left(-\frac{(\mathbf{r}-\mathbf{r}_0)^2}{4\, W(t)}\right)\,, \tag{2.5}$$

where d is the dimension of the system [33]. We anticipate that equation (2.5) is key to model the energy spectra measured by quasi-elastic neutron scattering, as explained in Sections 2.4 and 2.5.

In general, $D_s^s = D_s^s(\varphi)$, where φ is the so-called particle volume fraction, i.e. the fraction of the total volume of a suspension which is occupied by the colloidal particles. In a very dilute solution, where both direct and indirect interactions between particles are negligible, $\lim_{\varphi\to 0} D_s^s(\varphi) = D_{t0} = k_{\mathrm{B}}\,T/\gamma$ is the Stokes-Einstein dilute limit diffusion coefficient. As mentioned above, for a sphere of radius R suspended in a solvent with viscosity η, $\gamma = 6\pi\eta R$, hence

$$D_{t0} = \frac{k_{\mathrm{B}}\,T}{6\pi\eta R}\,, \tag{2.6}$$

where k_{B} is the Boltzmann constant and T denotes the temperature.

In more concentrated solutions, indirect, hydrodynamic interactions (HI) between colloidal particles caused by the solvent flow field become important already in the short-time limit, and cause a slowing down of the particle self-diffusion that can be described by the monotonically decreasing function $f_t(\varphi)$

$$D_s^s(\varphi) = D_{t0}\, f_t(\varphi)\,. \tag{2.7}$$

Theoretical expressions of $f_t(\varphi)$ for neutral and charged hard spheres can be found in Refs. [37, 38].

On the interaction timescale τ_I, a significant change of the direct interaction potential due to e.g. excluded volume, van der Waals and screened electrostatic forces results in a subdiffusive dynamics, that is $W(t) \propto t^{\alpha}$, $\alpha < 1$ [33].

For $t \gg \tau_I$, instead, the tracer particle has experienced numerous independent collisions with the neighbors which leads again to a linear time dependence of $W(t)$

$$W(t) \sim D_l^s \, t \qquad\qquad t \gg \tau_I \, , \tag{2.8}$$

with the long-time self-diffusion coefficient $D_l^s \leqslant D_s^s \leqslant D_{t0}$. As in the short-time limit, D_l^s can be factorized to:

$$D_l^s(\varphi) = D_{t0} \, f_{t,l}(\varphi) \, , \tag{2.9}$$

with the monotonically decreasing function $f_{t,l}(\varphi)$ accounting for the slowing down of the long-time diffusion due to interactions between particles [33].

It is important to note that, if the particle has a finite size, also the random rotations induced by the collisions of the water molecules with the particle surface can be described by a diffusive process, with the random torque $\xi_r(t)$ defined analogous to $\xi(t)$ in equation (2.1) by

$$\langle \xi_r(t) \rangle = 0 \, , \qquad\qquad \left\langle \xi_r(t) \cdot \xi_r(t') \right\rangle = 6 \, k_\mathrm{B} T \, \gamma_r \, \delta(t - t') \, , \tag{2.10}$$

where γ_r is the Stokes-Debye rotational friction coefficient, which for a sphere of radius R rotating in a solvent of viscosity η is given by $\gamma_r = 8\pi\eta R^3$. Thereby, the dilute limit rotational diffusion coefficient of a sphere is given by:

$$D_{r0} = \frac{k_\mathrm{B} T}{8\pi\eta R^3} \, , \tag{2.11}$$

and in general the short-time rotational self-diffusion coefficient $D_r = D_r(\varphi) = D_{r0} f_r(\varphi)$. The probability density for a sphere to have orientation $\hat{\mathbf{u}}(t)$ at time t given that it had orientation $\hat{\mathbf{u}}_0$ at time $t = 0$ is described by

$$P(\hat{\mathbf{u}}, t | \hat{\mathbf{u}}_0) = \sum_{l=1}^{\infty} \sum_{m=-l}^{l} Y_{l,m}(\hat{\mathbf{u}}) \, Y_{l,-m}(\hat{\mathbf{u}}_0) \exp(-l \, (l+1) D_r \, t) \tag{2.12}$$

where $Y_{l,m}$ are spherical harmonic functions [33].

Other than for translation, a true long-time rotational self-diffusion coefficient does not exist for monodisperse suspensions, although an orientational self-diffusion coefficient averaged over all times from 0 to infinity can be defined and can be shown to be only slightly different from D_r in the short-time limit [33].

Quasi-elastic neutron backscattering accesses the short-time limit of the diffusion of proteins in solution and therefore, in the analysis and interpretation of backscattering data, we will employ the reduced short-time translational self-diffusion $f_t(\varphi)$ from the study of Tokuyama and Oppenheim [37] and the rotational analogous $f_r(\varphi) = 1 - 1.3 \, \varphi^2$ from Ref [38].

Both $f_t(\varphi)$ and $f_r(\varphi)$ start at one in the dilute limit, such that the dilute limit diffusion coefficient is found for self-diffusion. In fact, as already mentioned, in the dilute limit there is no distinction between short- and long-time limit and between self- and collective diffusion [33]. At higher concentrations, however, collective diffusion significantly differs from self-diffusion, as explained in the next Section.

2.2.2 Collective Diffusion

In the previous Section, self-diffusion, that is the diffusion of a tagged particle in a sea of others, was discussed. A different kind of diffusion, known as collective diffusion, can be defined to describe the collective motion of many colloidal particles leading to the isothermal relaxation of density fluctuations.

Density fluctuations can be generally described by a sum of sine functions in space, with different wavelengths. Without loss of generality, let us consider at time $t = 0$ a sinusoidal density wave $\rho_q(\mathbf{r}, t = 0)$ with wavelength $\Lambda = 2\pi/q$ around the average density ρ_0, i.e. a fluctuation in the local density of the particles such that

$$\rho_q(\mathbf{r}, t = 0) = \rho_0 + \rho(\mathbf{q}, t = 0)\,\sin(\mathbf{q} \cdot \mathbf{r})\,. \tag{2.13}$$

Such a wave will relax to the homogeneous state due to the so-called collective diffusion, that is the coordinated motion of particles [32, 33].

Similar to the case of self-diffusion, also for collective diffusion different regimes can be identified depending on the observation time. For $\tau_B \ll t \ll \tau_I$ and $t \gg \tau_I$ the density wave relaxation may be described by a single exponential in time [1]:

$$\rho_q(\mathbf{r}, t) = \rho_0 + \exp(-q^2\, D^c(q)\, t)\,\rho(\mathbf{q}, t = 0)\,\sin(\mathbf{q} \cdot \mathbf{r})\,, \tag{2.14}$$

with $D^c(q)$ denoting the short- or long-time collective diffusion coefficient depending on the time regime, the latter being usually smaller than the former. In an intermediate stage, for $t \approx \tau_I$, the decay becomes slower than that in the short-time limit as a result of interactions between the colloidal particles and cannot be described by an exponential function [33].

As a last remark, we note that, in equation (2.14), the diffusion coefficient depends on q and hence on the wavelength Λ, meaning that the density relaxations depend on the length scales on which the fluctuations occur. In fact, a minimum of $D^c(q)$ occurs for repulsive systems at $q_m = 2\pi/r_m$, where r_m is the nearest neighbor distance. Furthermore, it can be shown that in repulsive systems for $q \gg q_m$ and sufficiently short times (for any particle i, $\mathbf{r_i}(t) - \mathbf{r_i}(0) \ll r_m$), $D^c(q)$ tends to the q-independent self-diffusion coefficient D^s [33].

In neutron spectroscopy on protein solutions, collective diffusion is generally measured by neutron spin-echo. The interpretation of $D^c(q)$ on the entire accessible q-range (which typically contains also $q \sim q_m$) is however non-trivial. Therefore, NSE is routinely employed to measure the diffusion coefficient in the incoherent approximation, that is $D^c(q \gg q_m)$.

For further deepening on the theory of diffusion, the reader is invited to refer to the text book by Dhont [32] or the lecture notes by Nägele [33].

---

[1] As a phenomenological approach, one can consider the continuity equation $\frac{\partial}{\partial t}\rho(\mathbf{r}, t) = -\nabla \cdot \mathbf{j}(\mathbf{r}, t)$ and Fick's local law of macroscopic gradient diffusion $\mathbf{j}(\mathbf{r}, t) = -D^c\,\nabla\,\rho(\mathbf{r}, t)$ and obtain the Fick's second law $\frac{\partial}{\partial t}\rho(\mathbf{r}, t) = D^c\,\nabla^2\rho(\mathbf{r}, t)$, for which the fluctuation in equation (2.14) is a solution.

2.3 Proteins as Patchy Colloids

As mentioned in Section 2.1, proteins are at the lower limit for being considered colloidal particles. For this reason, concepts of colloid theories with isotropic potentials were successfully employed to describe both static (see e.g. Refs. [39–42] and references therein) and dynamic (see e.g. Refs [29, 41, 43]) properties of proteins in solution under various conditions. However, considering the macromolecular structure and the highly inhomogeneous surface charge patterns, theories accounting for anisotropic interactions are supposedly a better description of protein systems. In the last years, models of colloidal particles with attractive surface patches resulting in anisotropic potentials have aroused a growing interest, and were shown to be appropriate for explaining several observed phenomena regarding protein solutions [24, 44–52].

In Chapter 8, the results of a study on the diffusion of a protein in the presence of a trivalent salt are reported. The physical interpretation of the result was inspired by the work by Roosen-Runge et al. [24], in which proteins are described as hard spheres with ion-activated attractive patches. Such a model was successfully employed to explain the phase diagram of the protein bovine serum albumin (BSA) in the presence of $\mathrm{YCl_3}$, which features phenomena such as reentrant condensation and liquid-liquid phase separation [24]. Roosen-Runge and co-workers considered a solution of colloidal hard spheres with m surface patches. Ions dissolved in solution bind to the patches, which are considered as binding sites independent from each other and with binding energy ε_b. The average occupancy Θ of each binding site is given by the statistics of a two-state system in the grand canonical ensemble [24]:

$$\Theta = \frac{1}{\exp\left(\frac{\varepsilon_b - \mu_s}{k_\mathrm{B}T}\right) + 1} \tag{2.15}$$

where μ_s is the chemical potential of the salt cations. In the model, two patchy colloidal spheres interact via a hard-sphere potential, unless two patches come into contact, in which case the interaction between them is modeled by a square-well attractive potential, that is [24]:

$$V(1,2) = V_{HS}(R_{12}) + \sum_{i=1}^{m}\sum_{j=1}^{m} V_{pp}\left(r_{12}^{ij}\right) , \tag{2.16}$$

$$V_{pp}\left(r_{12}^{ij}\right) = \begin{cases} -\varepsilon_{pp} & \text{for } r_{12}^{ij} < r_c \\ 0 & \text{for } r_c \leqslant r_{12}^{ij} \end{cases} , \tag{2.17}$$

where V_{HS} denotes the hard-sphere potential, R_{12} is the center-to-center distance of the particles, and r_{12}^{ij} represents the distance between the centers of patch i of particle 1 and patch j of particle 2. Regarding the square well potential, r_c denotes the range of the interaction and $\varepsilon_{pp} = \Theta\,(1-\Theta)\,\varepsilon_{uo}$ is an effective attraction strength between two patches accounting for the probability $\Theta\,(1-\Theta)$ that an occupied and an unoccupied patch come across and are subject to the attraction strength ε_{uo} (see Figure 2.2). ε_{pp} then, together with the size of the patches, determines the probability p_b for an ion-bridge between particles to occur [24].

As a consequence of the model, the addition of ions to the suspension of the patchy hard spheres activates an increasing number of patches and promotes the formation of clusters. In

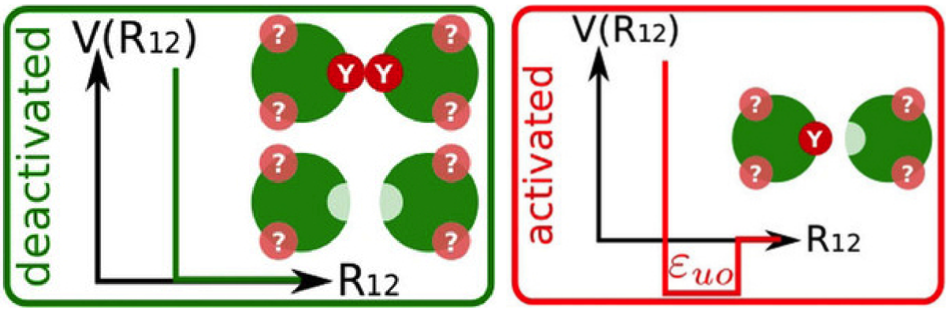

Figure 2.2: Sketch of the interaction potential between two ion-activated patchy particles. Figure from Ref. [24].

this picture, the Flory-Stockmeyer theory [53, 54] can be applied to estimate the number density ρ_n of n-clusters

$$\rho_n = \rho\,(1-p_b)^m \left[p_b(1-p_b)^{m-2}\right]^{n-1} \frac{m(m\,n-n)!}{(m\,n-2n+2)!n!}\,, \tag{2.18}$$

where the number density ρ is related to the protein volume fraction $\varphi = \frac{4}{3}\pi R_p^3\,\rho$. Rather intuitively, if the number of patches is fixed, p_b is expected to increase upon addition of ions, until $\Theta = 1/2$. This is consistent with experimental observations regarding the structure and the dynamics of proteins in solution in the presence of multivalent salts [24].

In fact, the success of this theory in reproducing in a semi-quantitative way the main features of the phase diagram of BSA dissolved in the electrolyte solution $YCl_3 + H_2O$ also inspired the analysis of QENS data on BSA diffusion reported in Chapter 8. There, the diffusion of BSA was estimated from the experimental data along with the patchy-particle model, and it was found consistent with an increase of p_b upon the addition of YCl_3.

This Section concludes the first part of this Chapter concerning colloidal suspensions. The second part will be concerned with the basis of neutron scattering and modeling of neutron scattering data regarding protein internal dynamics.

2.4 Basics of Neutron Scattering

In the following, a short introduction to the theory of neutron scattering will be given. For a comprehensive treatment of neutron scattering, the reader is invited to consult for instance the article by Schober [36] and the text books by Squires [35] and Bee [34], on which this Section is based.

Neutrons are spin-$\frac{1}{2}$ subatomic particles having a mass $m \simeq 1.67 \times 10^{-27}$ kg, and carrying no charge. Together with protons, they are usually found in atomic nuclei, where they are stable. Instead, free neutrons, which can be produced by fission or spallation nuclear reactions (cf. Sections 4.4.1), are unstable and decay to a proton, an electron and an antineutrino with a mean lifetime of about 15 minutes. Their energy after moderation is simply equal to their

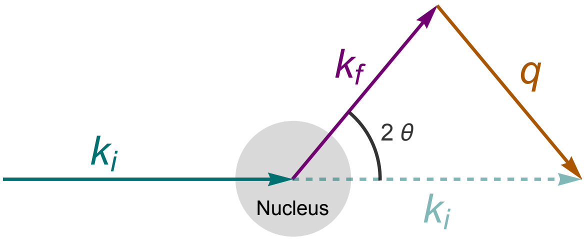

Figure 2.3: Schematic representation of a scattering event. An incoming neutron with initial wavevector $\mathbf{k}_i$ interacts with an atomic nucleus and is scattered at an angle 2θ. After the event, its wavevector is $\mathbf{k}_f$. The scattering vector q is defined as the difference between $\mathbf{k}_f$ and $\mathbf{k}_i$.

non-relativistic kinetic energy:

$$E_{\text{kin}} = \frac{1}{2}\, m\, v^2 = \frac{\hbar^2 k^2}{2m}\,, \tag{2.19}$$

where the first equality is valid for sufficiently low velocities, and the last equality follows from the wave-particle duality with the wavevector $\mathbf{k} = \frac{m}{\hbar}\mathbf{v}$ [34].

When a neutron is directed towards a sample material, it can interact with its atomic nuclei and either be absorbed or be scattered and may thereby change, in addition to its spin orientation, its energy and its wavevector.

Two basic quantities can be thus measured in a scattering experiment, that is, the energy transfer

$$\hbar\omega = E - E_0 = \frac{\hbar^2}{2m}(k^2 - k_0^2) \tag{2.20}$$

between the energy of the neutron before, E_0, and after, E, the scattering event, and the so-called scattering vector

$$\mathbf{q} = \mathbf{k} - \mathbf{k_0}\,. \tag{2.21}$$

A schematic representation of a scattering event is depicted in Figure 2.3.

The neutron-nucleus scattering is characterized by the scattering length b, which is independent of the neutron energy and can be a complex number. The imaginary part of b represents absorption, while the real part is related to scattering and can be either positive or negative, depending on the nature of the interaction. For a repulsive potential, b is positive, while a negative and very large b indicates the imminent appearance of a bound state. However, an attractive potential does not necessarily require a negative b [35, 36].

Since b characterizes the interaction between a neutron and a nucleus, its value is different not only for different elements, but also for different isotopes and spin states. In general, a sample is composed of several atomic species i, all with a given b_i. The coherent b_i^{coh} and the incoherent b_i^{inc} scattering lengths of the i species are defined as the average of b_i over all isotopes and spin states

$$b_i^{\text{coh}} = \langle b_i \rangle \tag{2.22}$$

and as the mean square deviation of b_i from $\langle b_i \rangle$

$$b_i^{\mathrm{inc}} = \left[\langle b_i^2 \rangle - \langle b_i \rangle^2 \right]^{1/2} , \tag{2.23}$$

respectively [34].

The scattering length can be related to the probability that a neutron with incident energy E_0 leaves the sample in the solid angle element $\mathrm{d}\mathbf{\Omega}$ about the direction $\mathbf{\Omega}$ and with an energy transfer between $\hbar\omega$ and $\hbar(\omega + \mathrm{d}\omega)$, that is the double-differential cross-section

$$\frac{\partial^2 \sigma_s}{\partial \mathbf{\Omega} \partial E} = \frac{1}{\hbar} \frac{\partial^2 \sigma_s}{\partial \mathbf{\Omega} \partial \omega} . \tag{2.24}$$

The integral in Ω and E of the double-differential cross-section is the scattering cross-section σ_s. Let I_0 be the number of incoming neutrons per unit of time and area, then the number I_s of scattering events per unit of time is given by

$$I_s = I_0 \, \sigma_s = I_0 \int \mathrm{d}E \int \mathrm{d}\Omega \, \frac{\partial^2 \sigma_s}{\partial \mathbf{\Omega} \partial E} , \tag{2.25}$$

with

$$\sigma_s = \sigma_{\mathrm{inc}} + \sigma_{\mathrm{coh}} = 4\pi (b_{\mathrm{inc}}^2 + b_{\mathrm{coh}}^2) . \tag{2.26}$$

We note that, similarly to the scattering cross-section in equation (2.25), an absorption cross-section can be defined such that

$$I_a = I_0 \, \sigma_a = I_0 \int \mathrm{d}E \int \mathrm{d}\Omega \, \frac{\partial^2 \sigma_a}{\partial \mathbf{\Omega} \partial E} , \tag{2.27}$$

where I_a denotes the number of absorption events per unit of time [34].

In general, a sample can be composed of n different types of atoms such as H, D, C. It can be shown that, if there is no coupling between the values of the scattering lengths for different isotopes, the double-differential scattering cross-section can be written as

$$\frac{\partial^2 \sigma_s}{\partial \mathbf{\Omega} \partial \omega} = \left(\frac{\partial^2 \sigma_s}{\partial \mathbf{\Omega} \partial \omega} \right)_{\mathrm{coh}} + \left(\frac{\partial^2 \sigma_s}{\partial \mathbf{\Omega} \partial \omega} \right)_{\mathrm{inc}} , \tag{2.28}$$

with

$$\left(\frac{\partial^2 \sigma_s}{\partial \mathbf{\Omega} \partial \omega} \right)_{\mathrm{coh}} = \frac{1}{N} \frac{k}{k_0} \sum_{\alpha=1}^{n} \sum_{\beta=1}^{n} b_\alpha^{\mathrm{coh}} b_\beta^{\mathrm{coh}} \sqrt{N_\alpha N_\beta} \; S^{\alpha\beta}(\mathbf{q}, \omega) , \tag{2.29}$$

and

$$\left(\frac{\partial^2 \sigma_s}{\partial \mathbf{\Omega} \partial \omega} \right)_{\mathrm{inc}} = \frac{1}{N} \frac{k}{k_0} \sum_{\alpha=1}^{n} \left(b_\alpha^{\mathrm{inc}} \right)^2 \; S_{\mathrm{inc}}^{\alpha}(\mathbf{q}, \omega) , \tag{2.30}$$

where N_α, and N_β denote the number of atoms of type α and β, and b^{coh} and b^{inc} were defined in equations (2.22) and (2.23), respectively [34].

The function $S^{\alpha\beta}(\mathbf{q},\omega)$ is the so-called coherent scattering function relative to the components α and β, while $S^{\alpha}_{\text{inc}}(\mathbf{q},\omega)$ is the incoherent scattering function. They are defined as:

$$S^{\alpha\beta}(\mathbf{q},\omega) = \frac{1}{2\pi\sqrt{N_\alpha N_\beta}} \int_{-\infty}^{+\infty} \sum_{i_\alpha=1}^{N_\alpha} \sum_{j_\beta=1}^{N_\beta} \big\langle \exp(i\,\mathbf{q}\cdot\mathbf{R}_{i_\alpha}(t)) \times \exp(i\,\mathbf{q}\cdot\mathbf{R}_{j_\beta}(0))\big\rangle \exp(-i\omega\,t)\,\mathrm{d}t\,, \tag{2.31}$$

and

$$S^{\alpha}_{\text{inc}}(\mathbf{q},\omega) = \frac{1}{2\pi N_\alpha} \int_{-\infty}^{+\infty} \sum_{i_\alpha=1}^{N_\alpha} \langle \exp(i\,\mathbf{q}\cdot\mathbf{R}_{i_\alpha}(t)) \times \exp(i\,\mathbf{q}\cdot\mathbf{R}_{i_\alpha}(0))\rangle \exp(-i\omega\,t)\,\mathrm{d}t\,, \tag{2.32}$$

respectively.

Importantly, by applying the inverse Fourier transform twice to $S^{\alpha\beta}_{\text{coh}}(\mathbf{q},\omega)$, from ω to t, and from q to r, the time-dependent pair-correlation function also known as the van Hove function

$$G(\mathbf{r},t) = \frac{1}{N}\int \big\langle \rho(\mathbf{r}'-\mathbf{r},0)\,\rho(\mathbf{r}',t)\big\rangle\,\mathrm{d}\mathbf{r}' \tag{2.33}$$

is obtained, with the microscopic particle density operator

$$\rho(\mathbf{r},t) = \sum_i \delta(\mathbf{r}-\mathbf{R}_i(t))\,, \tag{2.34}$$

where $\mathbf{R}_i(t)$ is the position of particle i at time t. The same can be obtained from $S^{\alpha}_{\text{inc}}(\mathbf{q},\omega)$, but without cross-correlation terms between different atoms. Consequently, $S^{\alpha\beta}_{\text{coh}}(\mathbf{q},\omega)$ provides information on the correlation between a particle at time $t = 0$ and another particle at time t' (cross-correlation), while $S^{\alpha}_{\text{inc}}(\mathbf{q},\omega)$ provides information on the correlation between the position of a particle at a time $t = 0$ and its position at time t' (autocorrelation) [34].

To explain these two types of correlation in a more intuitive way, let us imagine many particles in suspension, where they can diffuse freely. At a given time $t = 0$, the particle i is at the position $R_i(0)$. The presence of the particle in that site at that time may influence the behavior of the close-by particles at subsequent times, which may in turn influence other particles and so on. Let one of these be particle j. The cross-correlation between particle i and j gives information on how large of an influence the position, $R_i(t = 0)$, of particle i at time 0 has on particle j at a time $t > 0$. The same concept can be applied to a single particle: at time 0, the particle i is at position $R_i(0)$. For sufficiently small times, the particle cannot move considerably, and therefore its position at time $t > 0$ will be related to its initial location. After a sufficiently long time, however, the particle being at $R_i(t)$ could have arrived from several other points and therefore the correlation between the position of the particle i at time 0 and that of the same particle at a later time will be lost and tend to zero. This type of correlation is the so-called self-correlation or autocorrelation.

In the case of diffusion, the coherent scattering function provides information on collective diffusion, while the incoherent scattering function yields information on the particles self-diffusion.

In aqueous solutions of proteins, the nucleus with the highest neutron scattering cross-section is the incoherent scattering cross-section of hydrogen, as reported in Table 2.1.

Table 2.1: Coherent (σ_{coh}), incoherent (σ_{coh}) and absorption (σ_{a}) neutron cross-sections in barns of the elements composing BSA, D_2O and YCl_3, as well as of Aluminum and Vanadium [55].

	H	^{2}D	C	N	O
σ_{coh}	1.7583(10)	5.592(7)	5.550(2)	11.01(5)	4.232(6)
σ_{inc}	80.27(6)	2.05(3)	0.001(4)	0.50(12)	0.000(8)
σ_{a}	0.00019(2)	0.3326(7)	0.000519(7)	0.00350(7)	1.90(3)

	Al	S	Cl	V	Y
σ_{coh}	1.495(4)	1.0186(7)	11.526(2)	0.01838(12)	7.55(4)
σ_{inc}	0.0082(6)	0.007(5)	5.3(5)	5.08(6)	0.15(8)
σ_{a}	0.231(3)	0.53(1)	33.5(3)	5.08(4)	1.28(2)

Since proteins are largely composed of hydrogen, their main contribution to the neutron scattering function is incoherent, at least at scattering vectors q sufficiently far from correlation peaks. Moreover, given that deuterium (D) atoms have a much smaller cross-section than H-atoms, one can dissolve proteins in D_2O rather than in H_2O, thereby significantly reducing the signal of the solvent. Therefore, although the impact of the replacement of H_2O with D_2O on the protein dynamics should be considered (see Section 3.2), neutron scattering is well-suited to access the self-dynamics of proteins in solution.

Importantly, considering a colloidal particle undergoing free translational diffusion, the van Hove self-correlation function $G_s(\mathbf{r}, t)$ is given by the probability density function seen in equation (2.5):

$$G_s(\mathbf{r}, t) = \frac{1}{(4\pi\, D^s\, t)^{\frac{d}{2}}} \exp\left(-\frac{(\mathbf{r}-\mathbf{r}_0)^2}{4\, D^s\, t}\right) , \tag{2.35}$$

with the self-diffusion coefficient D^s. Note that the equation above is valid both in the short- and long-time limit of diffusion, with the respective diffusion coefficients (cf. Section 2.2). The double Fourier transform of $G_s(\mathbf{r}, t)$ yields a Lorentzian function

$$S(q, \omega) = \frac{1}{\pi}\, \frac{\gamma}{\gamma^2 + \omega^2} , \tag{2.36}$$

with half width at half maximum (HWHM) $\gamma = D^s\, q^2$. For proteins, typical time-scales for short-time diffusion are on the order of nanoseconds, which correspond to $\gamma \sim 1\,\mu\mathrm{eV}$ at $q \sim 1\,\text{Å}^{-1}$, that are energy transfer and scattering vector ranges accessible by quasi-elastic neutron backscattering.

Summarizing, neutron scattering experiments on protein solutions measure in general the number of neutrons scattered by a sample as a function of the scattering vector $\mathbf{q}$ and an energy transfer $\hbar\omega$, that is the scattering function $S(q, \omega)$. Importantly, $S(q, \omega)$ is the sum of a coherent and an incoherent part, providing information on collective and self-dynamics, respectively. The main advantages of neutron scattering on proteins are the low radiation damage, and the high contrast between hydrogen atoms and other atoms typically present in such systems, as a consequence of the large incoherent neutron scattering cross Section of hydrogen. Moreover, QENS being a scattering technique, the quantities obtained are an average over a large number of proteins which do not need to be labeled. Finally, we have seen that the scattering function of a freely diffusing particle can be easily modeled by a Lorentzian function centered at $\hbar\omega = 0$ (see equation (2.36)). This last result naturally leads to the use of QENS techniques to study protein diffusion, as explained in the next Section.

2.5 Quasi-Elastic Neutron Scattering (QENS)

As mentioned in the previous Section, a neutron scattering experiment measures the function $S(\mathbf{q}, \omega)$, that is the probability density of neutrons to be scattered with a scattering vector $\mathbf{q}$ and an energy transfer $\hbar\omega$. Depending on the energy transfer spectrum, three types of scattering can be identified, as shown in Figure 2.4: (i) elastic scattering occurs when the spectrum is, ideally, a delta function centered at $\hbar\omega = 0$. This happens when there is no dynamics in the sample. Note that, in practice, the delta function is always convoluted with a resolution function, specific for every instrument, which in combination with a given statistics also limits the longest observable correlation time (cf. Section 4.3.3). (ii) Quasi-elastic scattering corresponds to a broadening of the elastic spectrum due to the movement of the scattering centers in the sample. Hence, the spectrum is broader than in the elastic case, but it still presents a peak centered at zero. For instance, in the case of diffusion, quasi-elastic scattering resulting in a scattering function with a Lorentzian profile centered at $\hbar\omega = 0$ is expected, as seen in equation (2.36). Typical broadenings γ due to protein diffusion in solution are on the order of µeV for $0.2\,\text{Å}^{-1} \lesssim q \lesssim 2\,\text{Å}^{-1}$. (iii) If the spectrum presents peaks centered at $\hbar\omega \neq 0$, the scattering is inelastic (quasi-elastic scattering is also inelastic, but, as mentioned, with the peak centered at $\hbar\omega = 0$). Inelastic scattering is due to e.g. phonons or magnons, typically centered at energies of some meV.

In the case of elastic scattering, the magnitude of the wavevectors of the incoming $\mathbf{k}_i$ and outgoing $\mathbf{k}_f$ neutron is the same, and

$$q \equiv |\mathbf{q}| = \frac{4\pi}{\lambda}\sin(\theta)\,, \tag{2.37}$$

where 2θ is the angle between $\mathbf{k}_i$ and $\mathbf{k}_f$ (see Figure 2.3). Equation (2.37) is also true within the experimental accuracy for QENS.

Techniques based on quasi-elastic neutron scattering are neutron spin-echo, time-of-flight, and backscattering (NBS) spectroscopy. The latter was extensively used in this work. Typically, backscattering spectrometers access a q-range between $0.2\,\text{Å}^{-1}$ and $2\,\text{Å}^{-1}$ corresponding to length scales $l = 2\pi/q$ between $\sim 30\,\text{Å}$ and $\sim 3\,\text{Å}$. Typical energy resolutions and dynamic ranges of NBS spectrometers allow to access a time scale comprised between several tens of ps and some nanoseconds. Typical sizes of globular proteins are on the order of nanometers, and typical timescales for their short-time diffusion and fast internal dynamics are on the order of nanoseconds and picoseconds, respectively. Hence, both the length scale and the timescale accessible by NBS spectrometers are relevant for protein dynamics.

The principles of backscattering are explained in Section 4.4.2. The following Section gives a brief overview on the most employed models for protein internal dynamics studied by QENS.

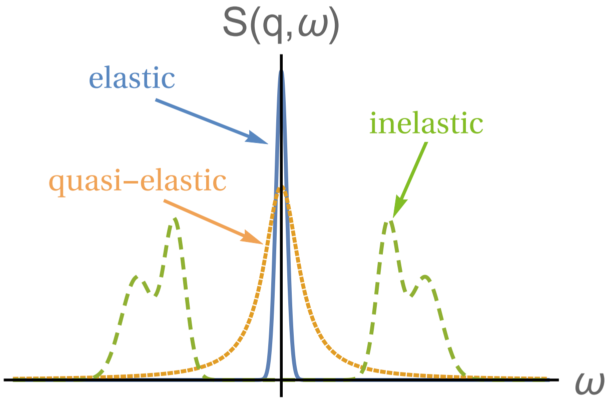

Figure 2.4: Sketch of the scattering function of elastic, quasi-elastic and inelastic neutron scattering near room temperature, in the absence of so-called detailed-balance effects. Elastic scattering gives a very sharp peak centered at $\omega = 0$. QENS yields a broader peak centered at $\omega = 0$, while the scattering function of inelastic scattering is characterized by peaks centered at $\omega \neq 0$.

2.6 Models for Protein Internal Dynamics in the Analysis of QENS Data

In the previous Sections, it was explained that $S(q, \omega)$ from QENS provides information on the dynamics of proteins by quantifying the broadening of the elastic line. In particular, it was shown that the diffusion of the center-of-mass of the protein results in a Lorentzian scattering function (cf. equations (2.35) and (2.36)). However, as seen in Section 2.2.1, also the rotation of the protein can be described in terms of a diffusive process. This process results in an additional broadening of the quasi-elastic spectrum, which is practically indistinguishable from that due to translational diffusion [29, 56]. In fact, the apparent diffusion coefficient measured by QENS includes a contribution from translational and rotational diffusion. On top of the dynamics of the "rigid protein", also internal dynamics of atoms with respect to the center-of-mass occurs, and results in an additional broadening of the quasi-elastic spectrum.

In the following, a non-exhaustive list of models for the internal dynamics of atoms in the side-chains employed to analyze neutron scattering data is given.

2.6.1 Elastic Incoherent Structure Factor

The details of the modeling of the scattering function including translational and rotational diffusion as well as internal atomic motion are given in Section 4.3.4. Here, we anticipate that, concerning the internal protein dynamics, the scattering function can be modeled as [29]:

$$S_{\text{int}}(q, \omega) = A_0(q)\, \delta(\omega) + \, (1 - A_0(q))\, \mathscr{L}(\Gamma, \omega) \tag{2.38}$$

where the first term arises from the Fourier transform of the equilibrium position distribution of confined atoms, which is to be expected for the internal dynamics of atoms in proteins, and the second term with the Lorentzian function $\mathscr{L}(\Gamma, \omega)$ models the broadening caused by the motion of atoms with respect to the protein seen as a rigid body. The q-dependent factor $A_0(q)$, the so-called elastic incoherent structure factor (EISF), provides therefore information on the geometry of confinement of the atoms within the protein.

The most common models employed to describe the experimental EISF include those for an atom diffusing in an (effective) impermeable sphere and in a Gaussian potential, as well as that for an atom jumping between three fixed sites. The latter is often used to describe the geometry of confinement of hydrogen atoms part of a methyl group.

Diffusion in a Sphere

The model developed by Volino and Dianoux [57] describes an atom diffusing freely inside an impermeable sphere of radius R. The following expression was obtained for the EISF [57]:

$$A_{\mathrm{sph}}(q\,,R) = \left|\frac{3j_1(qR)}{qR}\right|^2 \tag{2.39}$$

where

$$j_1(x) = \frac{\sin(x)}{x^2} - \frac{\cos(x)}{x}$$

denotes the first order spherical Bessel function of the first kind.

Such a model can be applied to estimate the volume accessible by the hydrogen atoms in a protein, although there are no obvious reasons for this volume to be spherical. Nonetheless, the radius obtained from the model is easily compared between different proteins and may be used as a rough indicator of the local structural flexibility and the ability of the protein to explore different conformations.

Gaussian Model for Localized Diffusion

Following the diffusion in a sphere model, Volino et al. [58] proposed a model describing an atom confined in a region quantified by the variance $\langle u^2 \rangle$ of its displacement u from the origin, under the assumption that u is a Gaussian random variable. Compared to the diffusion in a sphere model, the Gaussian model may often be a more physical description of confinement, since it accounts for soft boundaries [58]. The EISF for such a model is given by an exponential function [58]:

$$A_{\mathrm{G}}(q) = \exp\left(-q^2 \langle u^2 \rangle\right) \ . \tag{2.40}$$

It was shown by Volino et al. [58] that this expression for the EISF can be almost superimposed to that in equation (2.39), if $\langle u^2 \rangle = R^2/5$, for $(q\,R)^2 \lesssim 5$.

Jumps Between Three Equivalent Sites Equally Spaced on a Circle

In order to describe the geometrical confinement of the H-atoms in a methyl group, a model describing an atom jumping between three equivalent sites on the vertices of an equilateral triangle is commonly used [34, 56, 59]. The expression for the EISF is given by [34, 56, 59]:

$$A_{\text{3-j}}(q\,,a) = \frac{1}{3}\left[1 + 2\,j_0(qa)\right] \ , \tag{2.41}$$

where $j_0(x) = \sin(x)/x$ is the zeroth order spherical Bessel function of the first kind and a denotes the jump-distance between two sites.

The three models presented above or, in some cases, a combination of them, are the most often used to describe the entire EISF. In most cases the total EISF is modeled as

$$A_0(q) = p + (1 - p)\, A_{\mathrm{model}}(q)\,, \tag{2.42}$$

where p denotes the number of atoms which remain immobile on the timescale accessible by the instrument, and $A_{\mathrm{model}}(q)$ is one or a combination of the models presented above. It should be emphasized that these models provide a very simplified description of the complexity of the local confinement of atoms in a protein. Nevertheless, these simple models were successfully applied in previous studies to obtain valuable information on the confinement of the internal dynamics, and its dependence on several parameters, as reported in Chapter 3.

The three models presented above for different geometries of confinement will be used in later Chapters. For further information on the topic, the reader may consult the text book by Bee [34]. In the following Section, two models will be presented to describe the quasi-elastic signal produced by the internal protein motion.

2.6.2 Modeling of the Quasi-Elastic Broadening Due to Internal Dynamics

The fast, local motion of atoms with respect to the protein center-of-mass causes a quasi-elastic broadening which is convoluted to that arising from the translation and rotation of the entire protein.

The internal self-dynamics as measured by QENS is usually modeled by one or more Lorentzian functions. As already seen in Section 2.4 (see in particular equation (2.36)), the free diffusion of an atom results in a HWHM of the quasi-elastic broadening $\gamma \propto q^2$. Even if mobile, however, atoms composing the proteins are located in a very complex potential, characterized by several minima, corresponding to preferred spatial configurations. Under such conditions, the motion of atoms can be thought of as a sequence of effective jumps from one preferred position to the other. Consequently, a behavior resembling free diffusion may be expected only on a length scale sufficiently large compared to the distance of these minima (or the length of the jumps) and, sufficiently small to be below that corresponding to the geometrical constraints due to e.g. steric interactions or chemical bond lengths.

Often, for the analysis of QENS data on the internal dynamics of proteins, a jump-diffusion model was used. In the following, we first derive the model of jump-diffusion by Singwi and Sjölander [60] as originally done by the authors. Subsequently, little variations to such a procedure are applied to obtain a novel model used in this study describing an atom switching between two diffusive states characterized by different diffusive rates.

Jump-Diffusion Model

The jump-diffusion model by Singwi and Sjölander describes a particle switching between a state in which it is oscillating in an equilibrium position, and one in which it performs a diffusive motion while moving towards a new equilibrium position, where it will start oscillating again.

In their work, Singwi and Sjölander used a step-by-step approach to calculate the scattering function corresponding to this type of motion. More recently, Bicout and Roosen-Runge [61] derived the scattering function for the more general case, in which a particle alternates between two dynamical states. Jump-diffusion as modeled by Singwi and Sjölander is a special case of such a situation. The calculation by Bicout and Roosen-Runge is more direct than that by Singwi and Sjölander. However, it may be instructive to present the original reasoning and derivation by Singwi and Sjölander [60].

In order to calculate the scattering function, let us divide the motion of the atom into steps 0, 1, 2, ..., 2N, ... , where the even steps correspond to the oscillatory motion, and the odd steps to the diffusive motion. Moreover, let us define the following quantities [60]:

- $g(\mathbf{r}, t)$ is the probability of finding a particle at the position $\mathbf{r}$ at time t, when it is performing an oscillatory motion about an equilibrium position, starting from the origin at time $t = 0$; for an oscillatory motion, $g(\mathbf{r}, t) = [2\pi\gamma(t)]^{-3/2} \exp(-\mathbf{r}^2/(2\gamma(t)))$.

- $p(t)$ is defined as the probability that the particle remains in the initial oscillatory state at a later time t; it will be assumed that $p(t) = \exp(-t/\tau_0)$.

- $h(\mathbf{r}, t)$ denotes the probability for a particle to be at the position $\mathbf{r}$ at time t while performing a diffusive motion between two equilibrium positions, starting from the origin at time $t = 0$; as seen before, for diffusion $h(\mathbf{r}, t) = (4\pi D_1 t)^{-1} \exp(-\mathbf{r}^2/(4D_1 t))$.

- $s(t)$ gives the probability that a particle starting from a state of diffusive motion remains in the initial state at a later time t; it will be assumed that $s(t) = \exp(-t/\tau_1)$.

- $p'(t)\mathrm{d}t = p(t) - p(t + \mathrm{d}t)$ is the probability that the particle has left the oscillatory state during the time interval t and $t + \mathrm{d}t$, and has gone into the diffusive state;

- $s'(t)\mathrm{d}t = s(t) - s(t + \mathrm{d}t)$ gives the probability that the particle has left the diffusive state during the time interval t and $t + \mathrm{d}t$, and has gone into the oscillatory state.

Then, the van Hove self-correlation function of an atom starting with the oscillatory motion can be written as a sum over the different steps [60]:

$$G_s(\mathbf{r}, t) = \sum_i F_i(\mathbf{r}, t) \ , \qquad t > 0 \, , \tag{2.43}$$

where

$$
\begin{aligned}
&\text{Step 0:} \quad F_0(\mathbf{r},t) = g(\mathbf{r},t)\,p(t)\,,\\
&\text{Step 1:} \quad F_1(\mathbf{r},t) = -\int_0^t \mathrm{d}t_1 \int \mathrm{d}\mathbf{r}_1\; s(t-t_1)\,h(\mathbf{r}-\mathbf{r}_1,t-t_1)\,p'(t_1)\,g(\mathbf{r}_1,t_1)\,,\\
&\text{Step 2:} \quad F_2(\mathbf{r},t) = (-1)^2 \int_0^t \mathrm{d}t_2 \int_0^{t_2} \mathrm{d}t_1 \int \mathrm{d}\mathbf{r}_2\mathrm{d}\mathbf{r}_1\; p(t-t_2)\,g(\mathbf{r}-\mathbf{r}_2,t-t_2)\,s'(t_2-t_1)\\
&\qquad\qquad \times h(\mathbf{r}_2-\mathbf{r}_1,t_2-t_1)\,p'(t_1)\,g(\mathbf{r}_1,t_1)\,,\\
&\text{Step 2N:} \quad F_{2N}(\mathbf{r},t) = (-1)^{2N} \int_0^t \mathrm{d}t_{2N} \int_0^{t_{2N}} \mathrm{d}t_{2N-1}\ldots \int_0^{t_2} \mathrm{d}t_1 \int\ldots\int \mathrm{d}\mathbf{r}_{2N} d\mathbf{r}_{2N-1}\ldots \mathrm{d}\mathbf{r}_1\\
&\qquad\qquad \times p(t-t_{2N})\,g(\mathbf{r}-\mathbf{r}_{2N},t-t_{2N})\,s'(t_{2N}-t_{2N-1})\\
&\qquad\qquad \times h(\mathbf{r}_{2N}-\mathbf{r}_{2N-1},t_{2N}-t_{2N-1})\,p'(t_1)\ldots g(\mathbf{r}_1,t_1)\,.
\end{aligned}
\tag{2.44}
$$

It can be shown that for the $2N$ state [60]:

$$\int_0^\infty \mathrm{d}t \int \mathrm{d}\mathbf{r}\; F_{2N}(\mathbf{r},t)\exp(i(\mathbf{q}\cdot\mathbf{r}-\omega t)) = A\,(C\,D)^N\,, \tag{2.45}$$

and for the $2N+1$ state:

$$\int_0^\infty \mathrm{d}t \int \mathrm{d}\mathbf{r}\; F_{2N+1}(\mathbf{r},t)\exp(i(\mathbf{q}\cdot\mathbf{r}-\omega t)) = B\,C^{N+1}\,D^N\,, \tag{2.46}$$

where

$$A = \int_0^\infty \mathrm{d}t \int \mathrm{d}\mathbf{r}\;\; \exp(i(\mathbf{q}\cdot\mathbf{r}-\omega t))\;\, p(t)\,g(\mathbf{r},t)\,, \tag{2.47}$$

$$B = \int_0^\infty \mathrm{d}t \int \mathrm{d}\mathbf{r}\;\; \exp(i(\mathbf{q}\cdot\mathbf{r}-\omega t))\;\, s(t)\,h(\mathbf{r},t)\,, \tag{2.48}$$

$$C = -\int_0^\infty \mathrm{d}t \int \mathrm{d}\mathbf{r}\;\; \exp(i(\mathbf{q}\cdot\mathbf{r}-\omega t))\;\, p'(t)\,g(\mathbf{r},t)\,, \tag{2.49}$$

$$D = -\int_0^\infty \mathrm{d}t \int \mathrm{d}\mathbf{r}\;\; \exp(i(\mathbf{q}\cdot\mathbf{r}-\omega t))\;\, s'(t)\,h(\mathbf{r},t)\,. \tag{2.50}$$

$$\tag{2.51}$$

Therefore, the scattering function describing an atom switching between an oscillatory state and a diffusive state, starting at $t=0$ with the oscillation is given by [60]:

$$
\begin{aligned}
S^{(0)}_{\text{inc}}(q,\omega) &= \int_{-\infty}^{+\infty} \mathrm{d}t \int \mathrm{d}\mathbf{r} \sum_{N=0}^{\infty} F_N(\mathbf{r},t)\exp(i(\mathbf{q}\cdot\mathbf{r}-\omega t)) = \frac{1}{2\pi}\,\Re\left[A\sum_{N=0}^{\infty}(C\,D)^N + BC\sum_{N=0}^{\infty}(C\,D)^N\right]\\
&= \frac{1}{2\pi}\,\Re\left[\frac{A+BC}{1-CD}\right]
\end{aligned}
\tag{2.52}
$$

If at $t = 0$ the particle is diffusing, the same approach yields [60]:

$$S_{\text{inc}}^{(1)}(q,\omega) = \int_{-\infty}^{+\infty} \mathrm{d}t \int \mathrm{d}\mathbf{r} \sum_{N=0}^{\infty} F_N(\mathbf{r},t) \exp(i(\mathbf{q}\cdot\mathbf{r} - \omega t)) = \frac{1}{2\pi} \Re \left[\frac{B + AD}{1 - CD} \right] \tag{2.53}$$

Hence, the scattering function accounting both for those atoms starting with an oscillation and those starting with a diffusive motion is given by [60]:

$$\begin{aligned} S_{\text{inc}}(q,\omega) &= \frac{\tau_0}{\tau_0 + \tau_1} S_{\text{inc}}^{(0)}(q,\omega) + \frac{\tau_1}{\tau_0 + \tau_1} S_{\text{inc}}^{(1)}(q,\omega) \\ &= \frac{1}{2\pi} \left(\frac{\tau_0}{\tau_0 + \tau_1} \Re \left[\frac{A + BC}{1 - CD} \right] + \frac{\tau_1}{\tau_0 + \tau_1} \Re \left[\frac{B + AD}{1 - CD} \right] \right) , \end{aligned} \tag{2.54}$$

where τ_0 is the residence time of the atom in the oscillatory state, τ_1 denotes the residence time of the atom in the diffusive state, and $\tau_0/(\tau_0 + \tau_1)$ and $\tau_1/(\tau_0 + \tau_1)$ give the fractions of particles performing an oscillatory motion and that of particles performing a diffusive motion, respectively.

Using the assumptions for $p(t)$, $s(t)$, $g(\mathbf{r},t)$ and $h(\mathbf{r},t)$ mentioned in the beginning of this paragraph in equations (2.48) to (2.51) yields [60]:

$$A = \exp\left(-\frac{1}{2} q^2 \gamma(\infty) \right) \frac{\tau_0}{1 + i\omega\tau_0} , \tag{2.55}$$

$$B = \frac{\tau_1}{(1 + D_1 \tau_1 q^2) + i\,\omega\tau_1} , \tag{2.56}$$

$$C = \tau_0^{-1} A , \tag{2.57}$$

$$D = \tau_1^{-1} B . \tag{2.58}$$

$$\tag{2.59}$$

In order for the model to describe jump-diffusion, first the limiting case of $\tau_0 \gg \tau_1$ and very small oscillation amplitude is done, yielding [60]

$$S(q,\omega) = \frac{1}{\pi} \frac{\dfrac{D_1 q^2}{1 + D_1 \tau_0 q^2}}{\omega^2 + \left(\dfrac{D_1 q^2}{1 + D_1 \tau_0 q^2} \right)^2} \tag{2.60}$$

which is a Lorentzian function with HWHM $\Gamma = D_1 q^2/(1 + D_1 \tau_0 q^2)$. As shown in Figure 2.5, $\Gamma = D_1 q^2$ for $q \to 0$, and it tends to an asymptotic value, $\Gamma = 1/\tau_0$, for $q \to \infty$. This characteristic is typical for random jump-diffusion models, such as the one presented here or e.g. that by Hall and Ross [62].

Although simple models are usually preferable in QENS data analysis, and $\Gamma(q)$ following the behavior expected for jump diffusion was indeed measured in some cases, in Chapter 7 we observed that at high temperatures QENS data were not consistent with simple jump-diffusion. Therefore, a slightly more complex model based on a similar idea will be developed in the next Section.

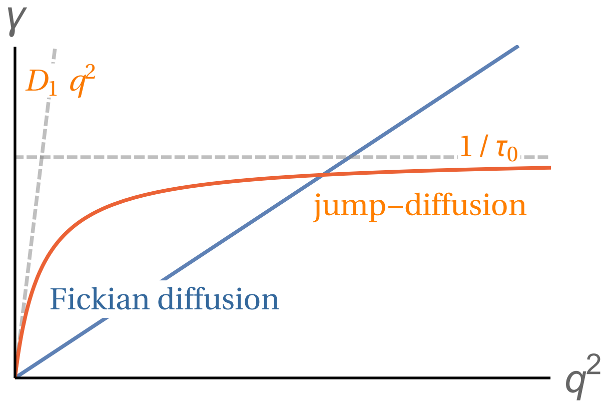

Figure 2.5: Comparison of the HWHM γ as a function of q^2 for Fickian diffusion and jump-diffusion. For Fickian diffusion $\gamma = Dq^2$: a straight line is obtained and the slope gives the diffusion coefficient D. For unrestricted jump-diffusion, the slope at low q gives the jump-diffusion coefficient D_1, and the asymptote at high q gives the inverse of the residence time τ_0.

Two-Diffusive States Model

In the previous paragraph, we have reported the derivation of the jump-diffusion model by Singwi and Sjölander, describing an atom alternating between an oscillatory motion around an equilibrium position characterized by a residence time τ_0 and a diffusive motion with a diffusion coefficient D_1 to a new equilibrium position, in the limiting case of small oscillation amplitudes and long residence times compared to the diffusion time. This model was often used to describe the internal dynamics of atoms within a protein as measured by QENS.

In the study presented in Chapter 7, a model accounting for an atom switching between two diffusive states characterized by the respective diffusion coefficients D_1 and D_2 and residence times τ_1 and τ_2 is used to describe the motion of side-chain atoms. Such a model is therefore similar to that by Singwi and Sjölander, but for the fact that, here, in both states the atom is diffusing, although with different diffusion coefficients. A possible way to calculate the scattering function for such a model can be found in Ref. [61]. The same result can be obtained following the approach by Singwi and Sjölander for jump-diffusion. In fact, if one assumes

- $g(\mathbf{r}, t) = (4\pi D_1\, t)^{-1} \exp(-\mathbf{r}^2/4D_1 t)$,
- $p(t) = \exp(-t/\tau_1)$,
- $h(\mathbf{r}, t) = (4\pi D_2\, t)^{-1} \exp(-\mathbf{r}^2/4D_2 t)$, and
- $s(t) = \exp(-t/\tau_2)$,

the reasoning presented in the previous paragraph can be used in this slightly different scenario.

Rearranging the resulting scattering function in an appropriate manner yields [61]:

$$S_{\mathrm{sw}}(q,\omega) = \alpha\,\mathscr{L}_{\lambda_1}(\omega) + (1-\alpha)\,\mathscr{L}_{\lambda_2}(\omega) \tag{2.61}$$

where $\mathscr{L}_{\lambda_1}$ and $\mathscr{L}_{\lambda_2}$ are Lorentzian functions with HWHM λ_1 and λ_2, respectively, and

$$\begin{aligned}\alpha =&(\lambda_2-\lambda_1)^{-1}\biggl[\frac{\tau_1}{\tau_1+\tau_2}\,\bigl(\Gamma_2+\tau_1^{-1}+\tau_2^{-1}-\lambda_1\bigr)\ldots\\ &\qquad\cdots+\frac{\tau_2}{\tau_1+\tau_2}\,\bigl(\Gamma_1+\tau_1^{-1}+\tau_2^{-1}-\lambda_1\bigr)\biggr]\end{aligned} \tag{2.62}$$

$$\lambda_{1,2} = \frac{\Gamma_1+\tau_1^{-1}+\Gamma_2+\tau_2^{-1}\pm\Lambda}{2} \tag{2.63}$$

$$\Lambda = \left[(\Gamma_1-\Gamma_2+\tau_1^{-1}-\tau_2^{-1})^2+4\,(\tau_1\,\tau_2)^{-1}\right]^{1/2}\,. \tag{2.64}$$

Hence, this model accounting for a particle or an atom alternating between two diffusive states results in a more complicated scattering function than that of jump-diffusion. However, the physical situation described by the function may be expected in some cases for internal dynamics (and also in other systems). Moreover, the fact that it can be written as a sum of two Lorentzian functions renders its application rather uncomplicated, although a simultaneous fit over the entire accessible (q,ω)-space may be needed due to the large number of parameters. A first application of this model is reported in Chapter 7.

This Section concludes Chapter 2. In this Chapter, the main theoretical notions of colloid physics and the concept of ion-activated patchy particles were introduced. Subsequently, the basics of neutron scattering were presented, including the definitions of the energy transfer $\hbar\omega$, the scattering vector $\mathbf{q}$ and the scattering lengths b and cross Sections σ. Also, the coherent and incoherent scattering functions were discussed together with their relation to the van Hove correlation function. Finally, quasi-elastic neutron scattering was addressed, and some selected models concerning internal dynamics of proteins measured by QENS were considered.

In the following Chapter, previous neutron spectroscopy studies on protein dynamics will be reviewed.

Chapter 3

Literature Review: Dynamics of Proteins in Solution Using Neutron Spectroscopy

Neutron scattering, as seen in the previous Chapters, is well suited for the study of protein dynamics (see also [63,64]). Three classes of neutron scattering can be used to obtain dynamical information on proteins: elastic, quasi-elastic and inelastic neutron scattering.

A significant difference between quasi-elastic neutron scattering (QENS) and elastic incoherent neutron scattering (EINS) (cf. Sections 2.4 and 2.5) is the amount of information provided by the two techniques. In general, a QENS spectrum contains much more information than that provided by EINS, since the former measures the scattering function $S(q, \omega)$ for a given *range* of energy transfers $\hbar\omega$ around zero, as opposed to EINS, where only $S(q, \omega = 0)$ (within resolution) is recorded. One of the consequences is that EINS experiments generally require much shorter measuring times on NBS spectrometers at continuous sources, and are therefore frequently applied to save beam time to allow for parameter scans such as temperature ramps. However, extracting and analyzing the additional information of QENS requires more modeling, and therefore more interpretation. Nevertheless, EINS has been employed less frequently in the recent years, due to the improvement of sources and instrumental efficiency as well as to the establishment of appropriate frameworks for QENS data analysis.

From EINS, the average apparent mean square displacement $\left\langle u^2 \right\rangle$ (MSD) of the hydrogen atoms in the sample can be obtained almost model-free, on a time scale defined by the instrument resolution. We emphasize that the vibrational MSD $\left\langle u^2 \right\rangle$ is not the same as the one presented in Section 2.2, i.e. the diffusive MSD $\left\langle r^2 \right\rangle (t)$ referring to the protein center-of-mass diffusion. $\left\langle u^2 \right\rangle$ rather refers to the motions of atoms within the protein. The apparent MSD is obtained from the elastic signal in the limit of small q, with the Gaussian approximation $S(q, \omega = 0) \approx \exp\left(-\frac{q^2}{3}\left\langle u^2 \right\rangle\right)$ [65,66]. In principle, for proteins in solution, not only vibrations, but also molecular subunit diffusion and the diffusion of the entire protein contribute to $\left\langle u^2 \right\rangle$ [67]. However, most of the EISF studies accessed a timescale of about 100 ps, on which displacements due to global diffusion are expected to be small, while only a limited number of them accessed timescales up to a few nanoseconds (depending on the instrument employed). Therefore, contributions not originating from vibrations are often neglected. In protein samples, an effective force constant can be obtained from the temperature dependence of the MSD, as explained in the next Section.

QENS techniques include time-of-flight (TOF) and backscattering (NBS), as well as neutron spin-echo (NSE). When probing protein samples, the former two techniques rely on the large incoherent scattering cross-section of H-atoms to measure the self-dynamics of the atoms in the macromolecule. While TOF spectroscopy typically reveals motions in a range from some picoseconds to some hundreds of picoseconds, NBS instruments access dynamics on the order of ∼100 ps to some nanoseconds. Other than TOF and NBS, NSE is typically used to measure the coherent scattering of proteins, meaning that information on collective dynamics is obtained. The broad time-range accessible, from some hundreds of picoseconds to about one microsecond, allows to study the center-of-mass diffusion and slow movements of entire protein subdomains. TOF, NBS and NSE are therefore highly complementary QENS techniques accessing a broad range of time scales and types of dynamics.

In solution, protein internal dynamics was in the past mostly investigated with TOF instruments, since the contribution of center-of-mass diffusion is often considered negligible at the time scales accessible by TOF. Although in the last ten years several NSE studies addressed internal, slow collective motions of protein domains, NSE and quasi-elastic NBS were mostly employed to determine the protein center-of-mass diffusion. On this regard, it is important to realize that there are different regimes of diffusion. Assuming the observation time τ is sufficiently long to observe Brownian diffusion, the limiting short-time and long-time cases are defined by the size of τ relative to the interaction time τ_I after which diffusing proteins collide: in the former case $\tau \ll \tau_I$, while in the latter case $\tau \gg \tau_I$. However, in the experiment, it is not always simple to make the distinction and to ensure that the result falls into one or the other limiting case.

Finally, inelastic neutron scattering reveals atomic vibrations and the so-called protein boson peak. The boson peak is related to low-frequency vibrational modes observed at low temperatures for globular proteins where it is coupled to the protein hydration water, but is also found in several glassy materials [68–72]. Its origin was found to be related to an energy landscape rich of local minima [71] and could be explained in terms of a mechanical instability of the system [72]. Inelastic scattering is however not in the focus of this thesis, and therefore related studies will not be reviewed.

In the following, we report on previous neutron scattering studies of protein dynamics, starting with those focusing on internal motions and concluding with investigations of the entire-protein center-of-mass diffusion. Parameters regarding internal dynamics of proteins in solution from several studies are reported in Table 3.1 (effective forces, see Section 3.1), and Table 3 (parameters from analysis of QENS spectra). The list of parameters does not claim to be exhaustive, although it contains a representative number of studies. We note that certain observations may be influenced by the resolution functions of the instruments as well as by the specific data treatment and models used to describe the data. Effective parameters may therefore depend on these models and results may be difficult to compare. The respective instrument resolution is also listed in the tables.

As a general remark on the parameters measured by EINS (cf. Table 3.1), we notice that all the effective force constants of proteins in *in vitro* solution are on the order of 10^{-2} to 10^{-1} N/m, with the exception of *Methanococcus jannaschii* malate dehydrogenase (Mj MalDH), having $\langle k \rangle = 1.5\,\mathrm{N/m}$ [20]. In particular, force constants measured on the 40 ps timescale are mostly on the order of 10^{-2} N/m, while those measured on a 500 ps timescale are predominantly on the order of some 10^{-1} N/m.

QENS studies (cf. Table 3) suggest that the radius of the effective sphere accessible by H-atoms within a protein vary from ~ 2 to ~ 7 Å, whereas the internal relaxation times τ are more heterogeneous, but seem to be predominantly either on the order of some picoseconds or on the order of 100 ps, depending predominantly on the instrument resolution. In addition to this, the fraction of atoms seen as immobile on the 10 to 100 ps time is generally about 0.6, while it ranges from ~ 0.1 to ~ 0.2 on the nanosecond timescale.

Before reviewing the main studies pointing out differences of protein internal dynamics in hydrated powders and solutions (Section 3.2), a brief summary of the results obtained on the dynamics of hydrated protein powders will be given in Section 3.1. Subsequently, studies regarding a temperature-dependent dynamical transition in solution will be reviewed in Section 3.3, followed by studies on the influence of the protein conformation on the internal macromolecular motions in Sections 3.4 and 3.5. In Section 3.6 pressure experiments on protein solutions are reported. In Section 3.7, investigation of the molecular basis of thermal adaptation will be reviewed, part of which were performed *in vivo*. Studies on slow, collective dynamics of domains and subdomains are presented in Section 3.8, and in Section 3.9, the characterization of the internal dynamics of alcohol dehydrogenase from the fast self-dynamics, to the slow collective dynamics is reviewed. Finally, further *in vivo* studies are presented in Section 3.10, followed by a review of results regarding protein diffusion, in Sections 3.11 and 3.12.

Table 3.1: Effective force constants (equation (3.1)) of proteins in solution from different studies.

Sample	c_p [mg/ml]	T [°C]	$\langle k \rangle$ [N/m]	Instrument	Resolution*
Ribonuclease A [73]	200	~ 7 - 47	0.04 ± 0.01	IN13	8 µeV / 100 ps
HmMalDH in D_2O [74]	200	~ 7 - 47	0.505 ± 0.049	IN13	8 µeV
HmMalDH in 2 M $NaCl{\cdot}D_2O$ [75]	200	~ 7 - 47	0.505 ± 0.049	IN13	8 µeV / 100 ps
HmMalDH in 2 M $KCl{\cdot}D_2O$ [75]	200	~ 7 - 47	0.205 ± 0.04	IN13	8 µeV / 00 ps
HmMalDH in 2 M $NaCl{\cdot}H_2O$ [75]	200	~ 7 - 47	0.113 ± 0.007	IN13	8 µeV / 100 ps
Mj MalDH [20]	200	~ 7 - 47	1.5	IN13	8 µeV / 100 ps
Oc LDH [20]	200	~ 7 - 37	0.15	IN13	8 µeV / 100 ps
BSA in D_2O [75]	200	~ 7 - 47	0.085 ± 0.012	IN13	8 µeV / 100 ps
BSA in D_2O [67]	$174^\dagger$	~ 7 - 70	0.04	IN10/IN16	0.9 µeV / 5 ns
BSA in D_2O [67]	$174^\dagger$	~ 70 - 98	0.007	IN10/IN16	0.9 µeV / 5 ns
BSA in 2 M $NaCl{\cdot}D_2O$ [75]	200	~ 7 - 47	0.125 ± 0.008	IN13	8 µeV / 100 ps
BSA in H_2O [75]	200	~ 7 - 47	0.55 ± 0.246	IN13	8 µeV / 100 ps
platypus Hb [22]	$570^\ddagger$	~ 5 - 40	0.11 ± 0.01	IN13	8 µeV / 100 ps
platypus Hb [76]	$570^\ddagger$	~ 7 - 33	0.038 ± 0.004	IN6/TOFTOF/FOCUS	100 µeV
platypus Hb [76]	$570^\ddagger$	~ 33 - 70	0.017 ± 0.001	IN6/TOFTOF/FOCUS	100 µeV
human Hb [22]	$570^\ddagger$	~ 5 - 40	0.15 ± 0.02	IN13	8 µeV / 100 ps
chicken Hb [22]	$570^\ddagger$	~ 5 - 40	0.23 ± 0.03	IN13	8 µeV / 100 ps
chicken Hb [76]	$570^\ddagger$	~ 7 - 40	0.048 ± 0.002	IN6/TOFTOF/FOCUS	100 µeV
chicken Hb [76]	$570^\ddagger$	~ 40 - 70	0.016 ± 0.001	IN6/TOFTOF/FOCUS	100 µeV
crocodile Hb [22]	$570^\ddagger$	~ 5 - 40	0.18 ± 0.02	IN13	8 µeV / 100 ps
crocodile Hb [76]	$570^\ddagger$	~ 5 - 70	0.11 ± 0.01	IN6/TOFTOF/FOCUS	100 µeV
A. arcticum [19]	living cell	~ 5 - 30	0.21 ± 0.03	IN13	8 µeV / 100 ps
A. arcticum [19]	living cell	~ 5 - 37	0.42 ± 0.01	IN13	8 µeV / 100 ps
P. mirabilis [19]	living cell	~ 5 - 35	0.39 ± 0.01	IN13	8 µeV / 100 ps
T. thermophilus [19]	living cell	~ 6 - 36	0.67 ± 0.11	IN13	8 µeV / 100 ps
A. pyrophilus [19]	living cell	~ 7 - 37	0.60 ± 0.01	IN13	8 µeV / 100 ps

* Intended as the FWHM of the resolution function; the resolution in time is reported when estimated in the respective reference.

† Calculated with the specific volume of BSA, $\vartheta = 0.735\,\mathrm{ml/g}$, from a nominal concentration of 200 mg/ml.

‡ Calculated with the specific volume of Hb, $\vartheta = 0.75\,\mathrm{ml/g}$ from a hydration level of 1.1 g D_2O/1 g protein.

Table 3.2: Parameters regarding protein internal dynamics obtained from QENS studies.

Sample	c_p [mg/ml]	T [°C]	Γ_{int} [μeV]	D_{int} [Å^2/ns]	τ [ps]	a [Å]	p	Instrument	Resolution*
Np [77]	50	25	-	-	-	5.82 ± 0.46	0.11 ± 0.03	NG2	1 μeV / 8 ns
Np [77]	50	25	-	-	1	3.92 ± 0.29	0.67 ± 0.03	NG4	57 μeV / 145 ps
Np [77]	100	25	-	-	-	5.04 ± 0.24	0.16 ± 0.02	NG2	1 μeV / 8 ns
Np [77]	100	25	-	-	3	4.21 ± 0.25	0.79 ± 0.01	NG4	57 μeV / 145 ps
NpP [77]	100	25	-	-	-	4.98 ± 0.25	0.15 ± 0.02	NG2	1 μeV / 8 ns
NpP [77]	100	25	-	-	3	3.32 ± 0.16	0.70 ± 0.02	NG4	57 μeV / 145 ps
Ip [77]	50	25	-	-	-	6.63 ± 0.25	0.13 ± 0.01	NG2	1 μeV / 8 ns
Ip [77]	50	25	-	-	1.2	3.39 ± 0.35	0.56 ± 0.07	NG4	57 μeV / 145 ps
Rp [77]	50	25	-	-	-	-	-	NG2	1 μeV / 8 ns
Rp [77]	50	25	-	-	2	3.53 ± 0.24	0.56 ± 0.04	NG4	57 μeV / 145 ps
native PGK [78]	50	15	∼60	64 ± 10	11.4 ± 0.8	1.78 ± 0.10	0.40 ± 0.05	MiBeMol	96 μeV / 30 ps
denat. PGK [78]	50	15	∼60	90 ± 10	11.8 ± 0.8	2.15 ± 0.15	0.18 ± 0.05		
native DHFR [79]	∼ 300†	12	∼50	47 ± 9	7.95 ± 1.02	2.47 ± 0.20	0.61 ± 0.02	IN6	100 μeV
immob. DHFR [79]	–	12	∼50	34 ± 7	20.36 ± 1.80	2.59 ± 0.20	0.60 ± 0.01		
ConA [80]	100	20	∼150	-	4	-	-	TOFTOF	30 μeV / 22 ps
Myo [80]	100	20	∼150	-	4	-	-	TOFTOF	30 μeV / 22 ps
Myo [56]	60	20	150 - 250	-	4.4	5.19 ± 0.03	0.64 ± 0.01	IN5	100 μeV
Lys [80]	100	20	∼150	-	4	-	-	TOFTOF	30 μeV / 22 ps
Lys [56]	60	20	150 - 250	-	4.4	5.54 ± 0.03	0.65 ± 0.01	IN5	100 μeV
α-Cas [80]	100	20	∼150	-	4	-	-	TOFTOF	30 μeV / 22 ps
β-Cas [80]	100	20	∼150	-	4	-	-	TOFTOF	30 μeV / 22 ps
κ-Cas [80]	100	20	∼150	-	4	-	-	TOFTOF	30 μeV / 22 ps
ADH [81]	52	5	-	78 or 65(15)	140 - 160	7.5 or 7.1 (-1.5+3)	0.42(5) to 0.63(5)	IN5, SPHERES	4 and 0.7μeV
WTsnase [82]	82	27	-	-	20-40	5.48, 1.1, 0.49	0.5	IN5	100 μeV / 50 ps
FRsnase [82]	78.8	27	-	-	20-40	5.48, 1.1, 0.60	0.5		
Rb. sphaer. RC [83]	0-30μM	11	∼100	-	6.5	-	-	MiBeMol	∼ 60 μeV
platypus Hb [76]	∼570†	∼5 - 70	100 - 200	220 - 605	3.5 - 2.5	3 - 4	0.6 - 0.5	IN6/ TOFTOF/ FOCUS	100 μeV
chicken Hb [76]				285 - 605	3.5 - 2.5	3 - 3.8	0.625 - 0.5		
crocodile Hb [76]				500 - 780	2.7 - 2	2.3 - 3.7	0.675 - 0.525		
hHb [84]	320	27	∼200	-	3.4 ± 0.8	-	-	TOFTOF	∼ 20 ps
hHb in RBCs [85]	330‡	∼10 - 40	5.5 to 4.2	-	120 to 157	-	-	IN10	1 μeV / ∼ 1 ns
			5.8 ± 1.4 to 6.2 ± 1.0	-	113 to 106	-	-	IN16	0.9 μeV / ∼ 1 ns
			-	-	∼ 4	2.8 to 3.3 ± 0.1	0.67	IRIS	17μeV / 40 ps
Living E. coli [17]	300-400‡	7	100 - 150	-	4 - 6	3.11	0.61	IN6	90 μeV / 15 ps
		27	100 - 200	-	3 - 6	3.4	0.56		
		7	100 - 150	-	4 - 6	-	-	IRIS	17 μeV / 75 ps
			∼ 14	-	47	-	-		
		27	100 - 200	-	3 - 6	-	-		
			∼ 14	-	47	-	-		
		11	7	-	94	-	-	IN16	0.9 μeV / ∼ 1 ns
		30	7	-	94	-	-		

* Intended as the FWHM of the resolution function; the resolution in time is reported when estimated in the respective reference.

† Calculated with the specific volume of Hb, $\vartheta = 0.75\,\text{ml/g}$ from a hydration level of 1.1 g D_2O/1 g protein.

‡ Estimated.

3.1 Dynamics of Hydrated Protein Powders

Several neutron studies have investigated protein internal dynamics on subnanosecond time scale by comparing dry and hydrated protein powders, i.e. with a layer of hydration on the protein surface (for extensive reviews see Refs. [64, 86]). Notably, such studies have observed that the presence of one hydration water layer activates specific internal motions above a transition temperature T_d that are not visible in dry samples, thereby confirming Mössbauer spectroscopy results [87]. Such an activation is indicated in EINS experiments by the change of the slope of the MSD as a function of temperature (cf. Section 3.3). This dynamical transition, in some cases, could be correlated with the activation of the protein activity [7, 63, 88–90]. Moreover, it was found to be correlated with an increased mobility of water above T_d [91] and, interestingly, it does not require amino acids, the building blocks of proteins, to be connected in a chain [92, 93].

Zaccai [7] proposed to model proteins in a simplified picture of atoms connected by effective springs. In that way the apparent vibrational mean square displacements $\langle u^2 \rangle$ measured by elastic neutron scattering could be interpreted in terms of the spring equation, yielding the mean force constant [7]:

$$\langle k \rangle = 2\, k_{\mathrm{B}} \left(\frac{\mathrm{d} \langle u^2 \rangle}{\mathrm{d}T} \right)^{-1} . \tag{3.1}$$

The force constant was associated with the resilience of the protein, and was calculated in a number of studies to compare in a quantitative manner EINS results from different proteins in various conditions [64].

In summary, studies on proteins in hydrated powders highlighted the presence of a temperature-activated dynamical transition in the sub-nanosecond internal dynamics. The transition was found to be coupled to the dynamics of the hydration water, and, in some cases, it was possible to associate the onset of the fast dynamics with the activation of the protein function.

3.2 The importance of Studying Proteins in Solution

In this Section, studies focusing on the subnanosecond internal dynamics of protein powders under different hydration conditions and in solution will be reviewed. In the last part, results on the influence of the specific solvent (use of H_2O vs. D_2O, presence of salts) on protein dynamics will be presented.

In 1999, Pérez and co-workers performed the first systematic neutron scattering experiments on the picosecond internal dynamics of proteins as a function of hydration, from dry powders to solutions [56]. Measurements of two proteins, myoglobin and lysozyme, demonstrated that, from dry powder to coverage by one water layer, the surface side chains progressively participate in local diffusive motions. Further increasing the level of hydration, the rate of the local proton diffusion is enhanced. In a solution with $\sim 60\,\mathrm{mg/ml}$ protein, motions were found to occur with an average amplitude larger than in the fully hydrated powder by about a factor three. Also, the calculated average relaxation time decreased from $\sim 9.4\,\mathrm{ps}$ in powders with one hydration layer to $\sim 4.5\,\mathrm{ps}$ in solution. The authors also noticed that, in solution, a component of the total scattering characterized by a quasi-elastic broadening proportional to q^2 (typical for Fickian diffusion) could be attributed to the global diffusion of the entire proteins, including both a translational and a rotational contribution, in good agreement with the theory of colloidal suspensions. Importantly, the contribution of rotational diffusion to the apparent diffusion coefficient measured by QENS was calculated and the translational coefficient could be consistently extracted from the data [56].

In a comparative neutron scattering study of the dynamics of lysozyme in hydrated powders and in solutions at approximately 100 mg/ml, a two-power law of the quasi-elastic contribution to the spectra was identified, with a ballistic Gaussian decrease above $\sim 2\,\mathrm{meV}$ (Marconi et al. [94]). The most significant difference between the powder and the solution sample was the much larger intensity of the quasi-elastic contribution, which was attributed by the authors to the increase of both the number and the amplitudes of the confined diffusive processes related to protein side-chain motions at the protein surface [94]. The comparison confirmed thus that proteins in solution exhibit enhanced dynamics.

Two additional investigations focused on the difference between the dynamics in powders and solution [95, 96]. Russo et al. [95, 97] measured the internal dynamics of hydrophobic side chains of small peptides as a function of the level of hydration and of temperature. Hydrated powders were measured from 50 K to 300 K, whereas the solutions were measured between 275 K and 310 K. An evolution of the dynamics was observed: for low levels of hydration, only rotational motions, mostly due to methyl group rotations were observed, whereas at high hydration levels also translational internal diffusive motions were detected above 250 K. Importantly, the experiments revealed that only long side chains could trigger the diffusive motion, while short side chains were found to undergo only rotational motions. Therefore, both the interfacial water and the side chain length play a major role in the dynamical transition [95]. Surprisingly, the internal translational motions were not observed in highly concentrated solutions at room temperature [97], but were only measured in hydrated powders [95]. This discrepancy was explained as a consequence of the structural and dynamical properties of the specific interfacial water network, since the hydration water network around hydrophobic side-chains in hydrated powders is less structured [95]. Therefore, the outcome of the experiment corroborated the hypothesis of the authors that protein dynamics is strongly influenced by the structural and dynamical properties of interfacial water [95]. No significant differences between different hydration levels were reported at low temperatures ($T < 250\,\mathrm{K}$) [95].

Stadler et al. [22, 96] focused on the internal picosecond dynamics of human hemoglobin (Hb), as well as platypus and chicken Hb, as a function of hydration and temperature. The rates of the diffusive motion were found to increase with increasing hydration up to highly concentrated solutions (approximately 570 mg/ml). Moreover, the data showed a substantial difference between powders and solutions: in solution, the volume accessible by the amino acid side chains above body temperature was larger than that expected from a linear extrapolation from lower temperatures. The same was not observed in fully hydrated powders, suggesting that the investigation of fully hydrated protein powders may not be sufficient to accurately describe all aspects of protein picosecond dynamics that might be relevant for biological function [96].

Before concluding this Section we note that the amplitude of fast molecular motions depends on whether the protein is dissolved in H_2O or in D_2O, as reported in Section 4.1.1, and on the presence of different kinds of salts. This phenomenon was measured with elastic neutron scattering by Tehei and co-workers in solutions of halophilic malate dehydrogenase (MalDH), and bovine serum albumin (BSA) at $\sim 200\,\mathrm{mg/ml}$ [75]. The values of resilience measured in the study [75] can be found in Table 3.1. It was noted by the authors that BSA must be stabilized predominantly by entropic effects, since its resilience is higher in H_2O, even though its thermostability is higher in D_2O. On the contrary, the higher resilience of MalDH in D_2O, where the protein is more stable, suggests that enthalpic terms dominate its stability. The ion-dependent changes of $\langle k \rangle$ in MalDH were interpreted as a consequence of a significant contribution of the protein-ion interactions in the hydration shell. Hence, the solvent affects protein dynamics in a non-trivial way [75].

In conclusion, a general outcome of the reported experiments is that additional molecular dynamics is present when proteins are in solution, compared to hydrated powders. Such a dynamics may be relevant for biological function (for more general information on the hydration-function relation, see Ref [98]). Therefore, a full picture of the dynamical properties of proteins requires studies in solution. In this context, it was established that, after appropriate sample preparation, information on the internal dynamics can be detected by neutron scattering experiments also in bulk solutions composed of membrane proteins in detergent microemulsions (Gall et al. [83]). Finally, it should be kept in mind that marked differences in the amplitude of protein fluctuations occur depending on the solvent, although no general trend could be identified.

3.3 The Dynamical Transition in Solution

A dynamical transition at low T far below physiological temperature, often related to protein activity, was observed in protein hydrated powders in numerous studies, as briefly mentioned in Section 3.1 (for a review see those by Gabel et al. [64], and Daniel et al. [86]). In aqueous solutions, similar measurements are limited by the crystallization of water. Nevertheless, a few experiments, mostly on proteins dissolved in antifreeze solvents (cryoprotectants), revealed a dynamical transition also in solution. Such studies are presented below.

Neutron scattering experiments probing two different time scales, namely below 100 ps (on IN6 at the ILL) and below 5 ns (on IN16 at the ILL) were performed on solutions of the enzyme glutamate dehydrogenase (GDH) in 70% v/v CD_3OD/D_2O for $70\,\mathrm{K} < T < 320\,\mathrm{K}$ (Daniel et al. [99]). The obtained temperature dependence of the MSD was found to be markedly dependent on the instrument resolution: at the nanosecond timescale, several inflections of the MSD were identified, at $\sim 140\,\mathrm{K}$, $\sim 210\,\mathrm{K}$ and $280\,\mathrm{K}$, while on the picosecond timescale only the well-known dynamical transition at $\sim 220\,\mathrm{K}$ was observed. Moreover, none of these temperatures could be associated with an activity loss. It was therefore concluded that anharmonic fast motions are not necessarily coupled to the much slower motions required for the enzyme activity. However, as noted by the same authors, it cannot be excluded that functionally important fast motions may occur locally in the protein at the active site, even though these are not detectable in the average dynamics [99].

A second investigation regarding the dynamical transition in protein solutions was carried out by Réat et al. [100]. The study focused on the solvent dependence of the picosecond dynamic transition of solutions of xylanase, a simple single-subunit enzyme. The elastic intensity of the protein in dry powder, in D_2O, and in four two-component perdeuterated single-phase cryosolvents in which the protein is active and stable was measured on IN6, with a resolution of 50 μeV. It was found that the dynamic transitions of the protein solutions are partially coupled to those of the respective solvents. In D_2O a very sharp transition is observed at approximately 280 K, i.e. much above the transition temperature of hydrated powders (200-220 K), but very close to the melting temperature of D_2O, $T_m = 277\,\mathrm{K}$. In the cryosolvents used in the performed experiment, instead, the transition is much more gradual and starts at $\sim 230\,\mathrm{K}$, independent of the cryosolvent composition. In particular, the transition temperature remains the same not only in the cryosolvent with a melting temperature of $\approx 230\,\mathrm{K}$, but also in that with melting temperature below 190 K [100].

An at least apparent decoupling of the dynamics of a protein (lysozyme) in solution from the dynamics of its solvent (7.6 M LiCl D_2O) was observed also in a more recent QENS study on BASIS at the ORNL [101]. Other than the cryosolvent used in the aforementioned study, which was characterized by a melting point below 190 K [100], the LiCl solution undergoes a dynamical crossover at about 220 K. Nevertheless, no transition is visible in the protein dynamics at this temperature. The authors argued that there may be two ways to explain the observations: (i) there is a real decoupling of the dynamics of the solvent from that of the protein, or (ii) the transition observed for the solvent does not reflect a transition in its α-relaxation, which is believed to drive the dynamical transition in proteins [101].

Hence, experiments show that the dynamical transition is not restricted to protein hydrated powders, but can be observed also in D_2O and cryosolvents. Nonetheless, unlike for hydrated powders, the coupling of the protein dynamics and the dynamics of the solvent at low temperature (when using cryosolvents) does not appear obvious.

3.4 Differences of the Internal Dynamics of Proteins in Native, Molten and Denatured States

Several studies have attempted to identify general differences of the internal dynamics of proteins in solution between well-folded conformations and molten (i.e. an intermediate equilibrium state between native and fully denatured) or unfolded states [67, 78, 82, 102–108]. In the following, we summarize the results of such investigations.

The comparison of TOF data of yeast phosphoglycerate kinase in the native from and denatured in 1.5 M guanidinium chloride revealed a clear increase of the fraction of hydrogen atoms undergoing picosecond diffusive motions upon denaturation [78]. The same experiment evidenced that the H-atoms can access a larger volume in the denatured state, as reflected by the increase of the radius of the effective accessible sphere from 1.8 Å to 2.2 Å (cf. Section 2.6).

Partial denaturation through C-terminal truncation of staphylococcal nuclease (snase) was studied in solutions at a concentration $c_p \sim 80\,\mathrm{mg/ml}$ by TOF spectroscopy [82]. An increase in the amplitude of the ps-timescale average local fluctuations $\langle u^2 \rangle$ on truncation of the 13 C-terminal residues of snase was detected, from 0.49±0.02 Å in the native state to 0.60±0.02 Å in the denatured form. Furthermore, molecular dynamics simulations suggested that these differences are related to an increased solvent accessibility of the protein chain, accompanied by a decrease of the number of internal hydrogen bonds [82].

Picosecond dynamics differences were also measured between the native bovine α-lactalbumin

(BLA) and its molten globules (MBLA) at $\sim 75\,\mathrm{mg/ml}$ by Bu et al. [102]. They observed that spatially restricted long-range diffusive motions and local jump motions (cf. Section 2.6) of H-atoms within the proteins are less restricted in the molten globules than in the native BLA. It was found that H-atoms in BLA and MBLA diffuse at $T = 303\,\mathrm{K}$ with diffusion coefficients $D_{\mathrm{BLA}} = 42 \pm 0.5\,\mathrm{Å}^2/\mathrm{ns}$ and $D_{\mathrm{MBLA}} = 73 \pm 0.5\,\mathrm{Å}^2/\mathrm{ns}$, in effective spheres of radii $R_{\mathrm{BLA}} = 4.1 \pm 0.1\,\mathrm{Å}$ and $R_{\mathrm{MBLA}} = 5.4 \pm 0.1\,\mathrm{Å}$, respectively. A jump-diffusion was identified, with a residence time $\tau_{\mathrm{BLA}} = 56 \pm 7\,\mathrm{ps}$ in native BLA, reducing to $\tau_{\mathrm{MBLA}} = 23 \pm 2\,\mathrm{ps}$ in MBLA. Notwithstanding that, root mean square jump distances did not change significantly ($\sqrt{\langle r^2 \rangle}_{\mathrm{BLA}} = 3.7 \pm 0.3\,\mathrm{Å}$, $\sqrt{\langle r^2 \rangle}_{\mathrm{MBLA}} = 3.2 \pm 0.3\,\mathrm{Å}$), which may indicate switching between different rotamers [102]. In addition to the self-dynamics, Bu and co-workers [102] extracted information on collective diffusive motions within the protein, by concluding on coherent scattering effects, which suggested that atoms at a distance $d_{\mathrm{BLA}} = 4.4 \pm 1.3\,\mathrm{Å}$ and $d_{\mathrm{MBLA}} = 5.6 \pm 0.1\,\mathrm{Å}$ from each other move in a correlated manner with correlation lengths $\xi_{\mathrm{BLA}} = 18 \pm 4\,\mathrm{Å}$ and $\xi_{\mathrm{MBLA}} = 6.9 \pm 1.2\,\mathrm{Å}$, respectively. Therefore, the dynamics of the native protein is characterized by more localized motions of atoms correlated up to relatively long distances, as opposed to that of the molten globule presenting less localized motions of less strongly correlated atoms.

In a later study, Bu and co-workers [103] compared the nanosecond and picosecond dynamics of native, molten and denatured BLA in solution at 60 mg/ml and ∼15 to 20 mg/ml, respectively. Two dynamical contributions (two Lorentzian functions) were used to describe the time-of-flight data. The fast contribution was identified with the motion of the side-chains, whereas the other one was attributed to the center-of-mass motion of the protein and was not discussed. The picosecond dynamics showed reduced potential barrier to side-chain torsional motion in the molten globule and in the denatured protein. Importantly, although a faster internal dynamics may be expected also because of the lower concentration of the molten and denatured protein samples compared to that of the native protein solution, the urea-denatured BLA showed a less restricted long-range motion than both the native protein and the molten globule, the latter being at a comparable concentration. Other than the TOF data, the NBS data were interpreted in terms of one single dynamical contribution, under the assumption that the center-of-mass diffusion was too fast to be detected. The obtained results suggested the presence of dynamic regimes and strongly correlated density fluctuations within the native protein and the denatured states, based on coherent scattering intensity: an unusual dynamic behavior that is not observed for chain-like polymers was reported, which was suggested to be imputable to strongly non-local, attractive forces within the proteins. Finally, the analysis of the q-dependence of the scattering intensity suggested that both a residual secondary structure and long-range interactions on the scale of the tertiary structure fluctuate over several hundred picoseconds in both the native protein and in the highly denatured states α-lactalbumin [103].

BLA in native and molten state was further studied combining QENS and MD simulations [105]. The protein concentrations were $\sim 60\,\mathrm{mg/ml}$ for the native and $\sim 20\,\mathrm{mg/ml}$ for the molten globule. The study confirmed the increase of the average internal motion of the molten state, and showed that such a motion is characterized by a high degree of heterogeneity, which is more pronounced in MBLA compared to BLA. The simulations evidenced differences by up to an order of magnitude between the amplitude of motions in highly structured parts of the protein, and in unstructured regions (loops connecting secondary structural elements, termini, unfolded chain segments of the molten globule). Thereby, it was demonstrated that the increased average sub-nanosecond dynamics of the molten globule was mainly due to additional motions in the region of the protein that unfolds upon formation of the molten globule [105].

The same conclusion was drawn beforehand by Russo et al. [104] in a study on the temperature dependence of the picosecond internal dynamics of an all-β protein, neocarzinostatin (NCS), in solutions at 58 and 42 mg/ml [104]. The authors observed that the number of protons undergoing detectable diffusive motions increased from 33% at 20°C to $\sim$ 90% upon heat-induced partial unfolding at 71°C. Furthermore, a decrease of the *average* volume accessible to the atoms upon unfolding was reported. It was pointed out by the authors of this study that 33% is very close to the fraction of protons contained in the side-chains of random coil structures and it was suggested that, at room temperature, the only detectable diffusive movements are those involving the side chains of random coil structures. Thus, the increased fraction of mobile atoms at higher temperature could be explained by the onset of picosecond dynamics in the fraction of backbone and β-sheet side-chain hydrogen atoms, which were seen as immobile at room temperature. These atoms would still be in a very confined environment until the protein is fully unfolded, which would account for the decrease of the average accessible volume, as most of the additional motion would have to be very restricted [104].

Also a later study by Gibrat and colleagues [108] on apo-calmodulin reported the observation of a dynamical transition upon protein thermal denaturation. The transition was characterized by a decrease of the confinement of hydrogen atoms, and a decrease of the fraction of immobile protons. Moreover, the data analysis revealed an increase of dynamical heterogeneity, but also a decrease of the "most probable volume explored" [108]. It was proposed that this finding could indicate that the distance of atom to protein backbone plays a more important role than the solvent exposure to the residue, or the fact that the residue belongs to protein surface or interior in determining atom dynamics in proteins. In fact, if the exposure of the residue to the solvent determined dynamics, this should be less homogeneous in the folded state, where only a fraction of side-chains is solvent-exposed, than in the unfolded state, where all residues get exposed to the solvent [108].

An increase of the radius from the diffusion in a sphere model (cf. Section 2.6) was observed instead for α-amylase by Fitter et al. [106] at 30 mg/ml from the folded (R = 1.2 Å) to a pH-induced unfolded conformation (R = 1.8 Å). In both states, at 30°C, an average correlation time of approximately 4.4 ps and a mean square displacement $\langle u^2 \rangle = 0.15 \pm 0.03\,\text{Å}^2$ were found [106].

At higher temperatures, while no variation within the experimental error of the correlation time was observed, an increase of R was detected (Fitter et al. [107]). Such a change was more pronounced in the unfolded conformation, the radius of which increased from $R \simeq 1.8\,\text{Å}$ at 30°C to $R \simeq 2.4\,\text{Å}$ at 70°C, as opposed to that of the native protein, which increased from $R \simeq 1.2\,\text{Å}$ at 30°C to $R \simeq 1.4\,\text{Å}$ at 70°C. The conformational entropy change between the two states upon heating was also estimated on the basis of the neutron scattering data and a significant increase upon heating was demonstrated. As a consequence, it was concluded that, since an increasingly larger part of the conformational space can be explored by confined motions with increasing temperature, the conformational entropy change contributes significantly to thermal unfolding [107].

Recently, a combined QENS and EINS study was performed on the thermal denaturation of bovine serum albumin in highly concentrated aqueous solution (Hennig et al. [67]). The apparent mean square displacement $\left\langle u^2 \right\rangle$ was decomposed into the global diffusive contribution $\left\langle u^2_{\text{diff}} \right\rangle$ and the internal part $\left\langle u^2 \right\rangle - \left\langle u^2_{\text{diff}} \right\rangle$ comprising the vibrations and the subunit diffusive motions. Upon increasing T, $\left\langle u^2 \right\rangle$ was characterized by a linear increase up to $T = 325\,\text{K}$, followed by a sharp decrease in the range $331\,\text{K} < T < 354\,\text{K}$ and a second linear increase up to $370\,\text{K}$. This observation was interpreted as a result of the transition from a liquid solution to a cross-linked gel-like state: as long as the proteins are free, they diffuse increasingly fast with rising temperature. When denaturation starts, the diffusion is hindered by the formation of a growing network. When the building of the cross-linked network of denatured proteins is complete, a further temperature increase enhances the dynamics of the subunits of the proteins, while their center-of-mass diffusion is restrained. The MSD of the internal dynamics $\left\langle u^2 \right\rangle - \left\langle u^2_{\text{diff}} \right\rangle$, instead, showed a slow linear increase up to the denaturation temperature $T = 343\,\text{K}$, after which it increased linearly with a higher slope, indicating an enhanced flexibility after denaturation. The force constants were calculated in the two regimes: before denaturation, $\langle k_1 \rangle = 4.1 \times 10^{-2}\,\text{N/m}$, consistent with the force constant measured by Wood et al. [73] in a solution of ribonuclease A, while after denaturation $\langle k_2 \rangle = 0.1 \times 10^{-2}\,\text{N/m}$ [67].

In summary, neutron scattering revealed that proteins become more flexible upon molten globule formation and denaturation. A larger fraction of mobile atoms and a loss of local confinement were also observed in most cases. In combination with simulations, the experiments suggest that changes are related to the increased solvent-accessibility, and to the decrease of internal hydrogen bonds. In addition to this, some observations suggest that the distance of atoms to the protein backbone is more important than the solvent exposure or the distance from the surface when determining average dynamics. Finally, evidence was found suggesting that the conformational entropy change significantly contributes to thermal unfolding.

3.5 The Role of the Structure and the State of Proteins

A reasonable question to ask on protein dynamics is whether the specific hierarchical structure of different proteins has an impact on their subnanosecond dynamics.

In an attempt to answer this question, Gaspar et al. [80] investigated the picosecond dynamics of well-folded and intrinsically disordered proteins, and found that the rigidity, as obtained from the fraction of mobile atoms, changes depending on the secondary structure. The most rigid protein was concanavalin A, composed of β-sheets. Myoglobin, the structure of which is made of α-helices was found less rigid than concanavalin A, but more rigid than the α/β-protein lysozyme. Finally, the intrinsically disordered casein proteins were associated with the smallest rigidity. In addition to this, intrinsically disordered proteins appeared to undergo additional motions, compared to well-folded proteins [80].

In order to understand the influence of the quaternary structure on the nanosecond and subnanosecond protein dynamics, neutron scattering experiments were performed on hemoglobin solutions in two states, namely deoxyhemoglobin (deoxyHb) in T quaternary conformation, and carbonmonoxyhemoglobin (HbCO) in R quaternary conformation [109]. As a solvent, 65% glycerolD_8/D_2O was used. EINS showed no differences in the sub-nanosecond MSD (measured on IN13) on the entire temperature range from 20 to $300\,\text{K}$. Similarly, the MSD shows no difference up to $\sim 250\,\mathrm{K}$ on the nanosecond timescale. Above that temperature, deoxyHb is characterized by a MSD approximately 15% smaller than that of HbCO. It was concluded that the quaternary structure does not affect the sub-nanosecond dynamics, but it does influence the nanosecond dynamics. The q-averaged QENS spectra at room temperature showed a stronger quasi-elastic broadening for deoxyHb than HbCO, indicating a faster dynamics of the former conformation [109].

Four forms of pepsin – a kinetically stable (Np), a thermodynamically stable (Rp), a partially unfolded (Ip), and an inhibitor-bound (NpP) states – were investigated by neutron time-of-flight and backscattering. The aim of the study was to determine whether different states of the same enzyme are characterized by different picosecond to nanosecond internal dynamics [77]. By comparing solutions at 50 mg/ml of Np, Rp, and Ip, and at 100 mg/ml of Np and NpP, differences between the different states could indeed be identified. In particular, the authors found increasing flexibility in the order Rp < Np < Ip, and therefore concluded that kinetic stabilization does not necessarily correspond to a reduction in picosecond diffusive motions. The TOF measurements yielded, especially at high q, significant differences between quasi-elastic broadening of Rp and Np. More subtle were the variations between Np, and Ip on the picosecond timescale. However, at the nanosecond timescale Ip was characterized by faster dynamics, especially at short length scales. By contrast, no significant variations were observed between Np and NpP [77].

The experiments reported above give a clear indication that average fast internal motions are affected by changes in the protein structure, in some cases even small ones. Regarding the secondary structure, β-sheets seem to be the most rigid conformation, followed by α-helices, and combinations of α and β structures. Unstructured chains, such as those found in intrinsically disordered proteins, are the most flexible ones. Moreover, differences in the quaternary structure appear to affect the dynamics on the nanosecond but not on the picosecond time scale. Consistently, state-related conformational changes were also correlated with dynamical changes in the pico- to nanosecond timescale.

3.6 Internal Dynamics of Proteins Under Pressure

Life developed on Earth under various conditions. Particular interest is drawn by organisms adapted to extreme conditions such as high temperatures and pressure.

Due also to the difficulty of high-pressure experiments, only relatively recently a few neutron scattering experiments focusing on the influence of pressure on protein dynamics could be carried out [84, 110, 111].

The investigation of the influence of pressure on the dynamics of human hemoglobin at $\sim 320\,\mathrm{mg/ml}$ by Appavou et al. [84] demonstrated a subtle pressure-induced slowing down of the protein fluctuations, as evinced by a slight increase of the proton relaxation time, from 3.36 ps at atmospheric pressure to 3.71 ps at 2 kbar. The authors speculated that the change may be attributed to the rearrangement of water molecules in the hydration shell of the protein leading to stronger geometrical constraints for the motions of lateral chain residues. Besides this, the global diffusion was observed to slow down with increasing pressure, which was tentatively explained by the authors as due to the increase of solvent viscosity and to the formation of hemoglobin pentamers and hexamers [84].

Recent experiments combined small-angle neutron scattering (SANS) and EINS to investigate the effects of pressure on $\sim 400\,\mathrm{mg/ml}$ human acetylcholinesterase (hAChE) in D_2O (Marion et al. [110]). A four-step model was proposed, based on different regimes of the 100 ps dynamics.
(i) From 1 bar to 1 kbar, only minor changes are visible in the measured MSD, even though a clear compression of the enzyme structure by about 11% was detected by SANS up to a pressure of 900 bar [110].
(ii) In the range 1-3 kbar, a marked decrease of the MSD is observed, indicating that local degrees of freedom are strongly reduced. This was attributed to both Le Châtelier's principle and the reduction of the cavities inside the inner parts of the proteins, as a consequence of pressure [110].
(iii) Along the decrease in the second regime, the MSD at 1750 bar clearly deviates from the trend defined by the points at lower and higher pressure. In particular, the MSD was found to increase at that pressure, where the formation of a molten globule was expected. The deviation was therefore associated with an increased flexibility caused to the formation of the molten globule, defining the third step [110].
(iv) In the range 3-6 kbar, the slope of the MSD as a function of pressure was found to decrease again. This was interpreted by the occurrence of two competing effects: on the one hand, after Le Châtelier's principle the degrees of freedom at the atomic scale are decreased. On the other hand, large parts of the protein are exposed to water as a consequence of the unfolding. An increasing amount of inner cavities are invaded by water, leading to an increase in the degrees of freedom [110].

EINS was also employed very recently to investigate the influence of high pressure (up to 4 kbar) on the internal subnanosecond dynamics of lysozyme in solution at 80 and 160 mg/ml [111]. At 80 mg/ml, the MSD was found to decrease from ~ 1.4 to $\sim 1.0\,\text{Å}^2$ in the range 1-2000 bar, indicating that pressure induces a loss of protein mobility. No further change was observed from 2 to 4 kbar. At 160 mg/ml, instead, no changes in the MSD are observed up to 1000 bar. Above this pressure, up to 4 kbar, a slow decrease of the MSD occurs, from ~ 0.9 to $\sim 0.75\,\text{Å}^2$. These results demonstrate therefore that (i) crowding reduces the protein sub-nanosecond dynamics, and (ii) the crowding condition stabilizes the protein against pressure changes [111].

In summary, neutron scattering measurements probed a damping of the dynamics of proteins at high pressures. In one case, the formation of a molten globule and denaturation, both induced by pressure, could be associated with changes in subnanosecond dynamics. Even though the pressure reached here is beyond deep-sea limits, these results may help understanding the molecular mechanisms of adaptation of organisms living under high pressure, such as deep-sea bacteria. Evidence for the adaptation of organisms to hostile conditions on a macromolecular level were found in the case of extreme temperatures and are presented in the next Section.

3.7 Adaptation to Physiological and Extreme Temperatures

Below, we will review the main outcomes of experiments attempting to understand the molecular basis of thermal adaptation. In the first half, we will focus on adaptation to extreme temperatures, while in the second part findings on the correlation of hemoglobin dynamics with body temperature will be reported.

The first neutron scattering studies on thermal adaptation were performed on living bacteria adapted to low temperature (psychrophile), room temperature (mesophile), high (thermophile), and very high temperature (hyperthermophile) by Tehei and co-workers [19]. Even if in such systems a very large number of different types of macromolecules contribute to the overall scattering, EINS was successfully employed to determine the root mean square atomic fluctuation amplitudes averaged over all these cellular constituents. Interestingly, it was found that, on the 100 ps time scale accessible by the backscattering spectrometer IN13 at the ILL, $\sqrt{\langle u^2 \rangle} \simeq 1\,\text{Å}$ for each organism at its physiological temperature. The authors could also calculate the effective force constants determining the mean macromolecular resilience, and observed that they increase with rising physiological temperature: for the measured psychrophiles $\langle k \rangle = (0.21 \pm 0.03)\,\text{N/m}$, for the mesophiles $\langle k \rangle = (0.39 \pm 0.01)\,\text{N/m}$, for the thermophiles $\langle k \rangle = (0.67 \pm 0.11)\,\text{N/m}$, and for the hyperthermophiles $\langle k \rangle = (0.60 \pm 0.01)\,\text{N/m}$. This result indicated that the increase in stabilization free energy is dominated by enthalpic rather than entropic terms, and it was suggested by the authors that larger resilience allows for macromolecular stability at high temperatures, while maintaining flexibility within acceptable limits for biological activity [19].

In a subsequent study, Tehei et al. [20] measured $\langle u^2 \rangle$ and $\langle k \rangle$ of two homologue enzymes in solution at 200 mg/ml. The enzymes were extracted from a mesophilic and a hyperthermophilic organism, and once again the root mean square fluctuations were approximately the same, $\sqrt{\langle u^2 \rangle} \simeq 1.5\,\text{Å}$ for both enzymes at their optimal activity temperature. Furthermore, $\langle k \rangle \simeq 0.15\,\text{N/m}$ for the enzyme of the mesophile organism, while $\langle k \rangle \simeq 1.5\,\text{N/m}$ for the enzyme of the hyperthermophilic organism, consistent with the earlier *in vivo* measurements [19–21].

Following these findings, a correlation between dynamics and body temperature was discovered also for human hemoglobin (Hb), both in solution [96] and in red blood cells (RBCs) [112]. The investigation of the dynamics of human hemoglobin in RBCs revealed a change in the geometry of confinement of the protein protons at 36.9°C [112]: above that temperature, the volume accessible by the side-chain atoms was larger than expected from normal temperature dependence. As mentioned in Section 3.2, the same was observed for hemoglobin in highly concentrated solution [96]. The coincidence of the changes in molecular dynamics in the picosecond time range and Ångstrom length scale with macroscopic effects on whole RBCs that occurs at body temperature, namely the ability of RBCs to deform and pass through small capillaries, may suggest a causal link [112]. In addition to the internal dynamics, the global diffusion of Hb was found rather consistent with theoretical predictions for the short-time self-diffusion of effective hard-sphere suspensions [112].

Finally, also Hb from platypus and chicken exhibit a resilience correlated with the respective physiological temperatures (the higher the body temperature, the stronger the resilience) [22, 76], and a RMSD at the body temperature of approximately $1.2\,\text{Å}$ [22]. Hb from salt water crocodile, instead, does not undergo any similar change in the dynamics, presumably because of the much larger body temperature range of reptiles [22, 76]. Activation energies calculated from the temperature dependence of the residence times and diffusion coefficients associated with the side-chain motions were found to be similar for all species, namely $\sim 4\,\text{kJ/mol}$ and $\sim 10\,\text{kJ/mol}$, respectively [76].

3.8 Slow Collective Motions

The results presented above provide a picture of the local self-dynamics of atoms on timescales ranging from picoseconds to a few nanoseconds. Obviously, the movement of large parts of the protein requires at least some of these fast motions. However, the motion of entire domains and subdomains takes place on timescales from tens of nanoseconds to microseconds. Such movements can be directly observed at rather low protein concentrations by employing neutron spin-echo spectroscopy combined with normal mode analysis of the protein crystal structure, as explained in detail in Refs. [113–115].

In 2005, Bu and colleagues, measured coupled motion of domains separated by 70 Å of DNA polymerase I from *Thermus aquaticus* [116]. This motion is essential to coordinate nucleotide synthesis and cleavage during DNA synthesis and repair. In particular, at low concentration, the deviation of the effective diffusion coefficients from the diffusion coefficient measured by dynamic light scattering was attributed to large-scale internal dynamics. These experimentally determined deviations were compared with those calculated assuming domain motions based on normal mode analysis. Thereby, it was shown that the motion of DNA polymerase I can be well approximated by few normal modes of three coupled domains.

Following the study on DNA polymerase, NSE revealed that catalytic activity of phosphoglycerate kinase (PGK) is enabled by large domain fluctuations on 50 ns timescale. [117]. Structural analysis of small-angle scattering data indicated that the protein in solution has a more compact structure than that of the crystal structure. However the function of the protein could not be fulfilled, if this structure was static. Correlation functions measured with NSE were characterized, above $q \sim 0.08\,\text{Å}^{-1}$, by two decays. The slower of these was ascribable to the long-time translational and rotational diffusion, while the fastest decay was attributed to internal dynamics. Data analysis indicated that domain movements facilitate a close encounter of the key residues in the active center to build the active configuration. Furthermore, the measurements showed that substrate binding induces faster domain motion, but with a simultaneous reduction of its amplitude. Hence, it was shown that the binding of a substrate leads to an increased rigidity of PGK. The results of this study were later compared with MD simulations, which confirmed that a significant component of NSE signal arises from internal dynamics. The comparison also evidenced that the amplitudes of the motions derived by MD are smaller than those derived from the experimental analysis [118].

In order to understand the domain motion of complex proteins, selective deuteration can be employed. This was the case for NHERF1, a multidomain protein assembling protein complexes after being allosterically[1] triggered by the binding of another protein, ezrin, 11 nm away from the active domains [119]. NSE measurements of selectively deuterated NHERF1 highlighted the activation of interdomain collective dynamics on nanometer length-scales and on submicrosecond timescales after the formation of a complex with ezrin. The results demonstrated therefore that allosteric regulation can involve changes in long-range submicrosecond domain motions [119].

Recently, the method was successfully employed also to determine the internal dynamics of intrinsically disordered myelin basic protein (MBP) [120]. First, small-angle scattering revealed that the protein compactness lies between that of a globular protein and that of a random coil polymer. Instead, the large contribution of the internal motions of the peptide chain to the overall diffusion measured by NSE indicated a high structural flexibility with relaxation rate of 8.4 ns. Collective stretching and bending motions, especially pronounced at the termini, were identified by normal mode analysis as the prominent contribution to the internal dynamics. Moreover, the data were found inconsistent with the Zimm model with internal friction derived from polymer theory. The inconsistency was interpreted by the authors as a result of the presence of a compact core and of a secondary structure content of 44%.

---

[1] Allosteric regulation is the process through which the activity of an enzyme is altered by means of a conformational and dynamical change induced by a different molecule

In summary, studies have shown that the coherent scattering function measured by neutron spin-echo spectroscopy contains important information regarding collective motions of domains and subdomains. This information could be extracted after a careful analysis of the q-dependence of the effective diffusion coefficients and, with the aid of normal mode analysis on the protein crystal structure, large-scale internal fluctuations critical for the activity of the investigated proteins could be identified. With complex proteins, deuterium labeling can be used to gain a more clear picture of the dynamics of different domains.

3.9 Complementary Use of Neutron Spectroscopy Techniques: Alcohol Dehydrogenase

Both the internal and center-of-mass dynamics of alcohol dehydrogenase (ADH), a protein responsible for the interconversion between alcohol and ketones, was investigated with NSE, TOF and NBS, on a broad range of timescales [81, 121, 122].

NSE revealed two main domain motions, one of which corresponds to the opening and closing of a cleft in the protein structure, between the binding and the catalytic domains [121]. This motion enables the binding and release of the cofactor required for the conversion of ethanol to acetaldehyde. Moreover, the analysis indicated that, when the cofactor is bound, the mode related to the opening and closing of the cleft is reduced, denoting a stiffening of the concerned domains.

The diffusion coefficient and the slow internal relaxation obtained with NSE were fixed in a global fit of TOF and NBS data [81]. The fitted model considered atoms to belong to one of three classes of motions occurring on top of rotation and translation of the entire protein: (i) atoms immobile with respect to the protein as a rigid body; (ii) atoms undergoing large scale domain motions; (iii) atoms participating in fast localized motions. Additionally, atoms belonging to each of the three classes were free to distribute over 10 concentric shells composing the protein. Approximately 34 to 37% of the atoms were found to undergo fast diffusive motions with the diffusion coefficient D_s ranging between 78 and 65 Å^2/ns in a confined volume with effective radius $\sim$ 7.5 to 7.1 Å, depending on whether class (ii) was taken into account or not. It was noted by the authors that the results are consistent with a more simple analysis combining NSE and TOF, but not NBS data on ADH, yielding a fraction of mobile atoms $\sim$ 35%, and a radius $R \sim 8$ Å [122], and with the results presented in Chapter 6, where $R \sim 6.7$ Å. A further outcome of the model is that most H-atoms undergoing fast movements seemed to be close to the surface, while those being immobile seem to be located mainly in the center. It was therefore speculated that the fast motions result from direct interaction of amino acids at the surface with the surrounding water.

In conclusion, the analysis of NSE, TOF and NBS data proposed by Monkenbusch et al. [81] to model the dynamics of ADH suggested the occurrence of three distinct dynamical processes: one due to the translation and rotation of the protein, the second, occurring on tens of nanoseconds, due to domain motion, the third, occurring on hundreds of picoseconds, related to fast localized motions at the amino acid level. Moreover, the model suggested that the third component is mainly arising from motions of amino acids in the outer shells, close to the solvent, whereas those in the inner parts appeared immobile.

3.10 *In Vivo* Neutron Spectroscopy

In addition to the EINS measurements of living bacteria and red blood cells (RBCs) presented in Section 3.7, other neutron spectroscopy studies have been performed in living *E. coli* and human RBCs, exploiting instruments accessing different time scales.

Hemoglobin diffusion in RBCs was first studied by Doster and Longeville with neutron spin-echo spectroscopy [123]. The measured time and wave vector behavior suggested the crossover of self- and collective diffusion in the accessible time and q-range. The data revealed features characteristic of hydrodynamic interactions between the proteins, and the diffusion coefficients (in RBC containing H_2O, at 20°C $D = 1.1\,\text{Å}^2/\text{ns}$) agreed quantitatively with long-time self-diffusion coefficients from the theory of hard-sphere suspensions, after adjusting the volume fraction of Hb by including the volume of the hydration layer to the dry protein volume. The results suggested therefore the applicability of concepts of colloid physics, developed for much larger particles, to proteins. Also, it was concluded from these results that hydrodynamic interactions dominate long-range molecular transport at physiological concentration.

A later study on Hb dynamics in RBC was performed with two backscattering spectrometers with different energy resolutions [85]. The scattering function of both spectrometers was modeled with two dynamical contributions, one arising from the protein global diffusion (translation and rotation of the whole protein), the other due to internal motions. Different apparent global diffusion coefficients were obtained from each instrument. The translational diffusion coefficient was extracted from the apparent coefficient, and compared to the values expected from the theory of colloidal suspensions. As Doster and Longeville [123], Stadler and co-workers [85] added the volume of the hydration layer to that of the bare protein in calculating the volume fraction. In this way, the two translational diffusion coefficients were found to agree quantitatively with the expected short- and long-time self-diffusion coefficients. Regarding the internal Hb dynamics, the faster contribution was attributed to localized jump-diffusion with $D \sim 300\,\text{Å}^2/\text{ns}$ and $\tau_0 \sim 4\,\text{ps}$ at 20°C. The slow internal contribution was rather q-independent and its correlation time at 27°C was $\sim 100\,\text{ps}$. While the fast internal dynamics was higher than in fully hydrated Hb powder, the slow component was found to be rather similar to that of fully hydrated protein powders, solutions and *E. coli* cells reported in other studies [85].

Jasnin et al. [17] carried out measurements of *E. coli* on three different spectrometers providing access to dynamics in a wide range of timescales. Several types of motions were identified and associated with contributions from diverse dynamical classes. Three types of motion were associated with internal processes. A fast relaxation was attributed to confined jump-diffusion motions with correlation times of 4.7 ps and 3.6 ps at 280 and 300 K, respectively. A slower process characterized by a q-independent quasi-elastic broadening was assigned to rotational motions occurring on characteristic times of $\sim$ 40 ps. It was noted by the authors that this process may arise from stochastic reorientations of large molecular subunits, such as polypeptide side chains, fatty acid chains, or other molecular subunits, as well as rotational motions of smaller groups such as protons in methyl groups. The slowest dynamical contribution associated with internal dynamics was also characterized by a q-independent quasi-elastic broadening and was therefore ascribed to rotational motions, the correlation times being approximately 94 ps and 90 ps at 284 and 303 K, respectively. The authors interpreted this contribution as due, for example, to librations of buried groups, relative displacements of globular domains, sugar conformational changes, or RNA global bending. A comparison of the results of this study with those in hydrated powders lead Jasnin and co-workers to the conclusion that the cellular environment induces a significant enhancement of internal dynamics. Instead, the *in vivo* dynamics appeared limited compared to that measured in solutions. It was therefore inferred that macromolecular interactions and confinement typical of physiological environments is not mimicked accurately by protein solutions, and it was suggested that intracellular complexity may participate in functional dynamics necessary for biological activity [17]. Finally, an even slower dynamical contribution showing typical features of jump-diffusion was attributed to the average macromolecular self-diffusion with diffusion coefficients $D = (0.85 \pm 0.15)\,\text{Å}^2/\text{ns}= (0.85 \pm 0.15) \times 10^{-7}\text{cm}^2/\text{s}$ and $D = (1.06 \pm 0.11)\,\text{Å}^2/\text{ns}$ at 284 and 303 K, consistent with the measurements of self-diffusion in RBCs [123]. The respective residence times were $\tau_0 = 0.97 \pm 0.08\,\text{ns}$ and $\tau_0 = 0.59 \pm 0.04\,\text{ns}$.

The studies above demonstrate that, although in living cells a great variety of macromolecules are present and several processes are active, valuable information on the dynamics on the nanosecond timescale can be carried out *in vivo* with neutron scattering. In particular, concepts of colloid physics were applied to understand the diffusive properties of the macromolecules, and three types of motions could be observed and attributed to internal dynamics of macromolecules inside *E. coli.*

3.11 Protein Diffusion in Crowded Solutions

One of the strengths of high-resolution neutron scattering spectroscopy is the possibility to investigate the translational and rotational diffusion of proteins on a nanosecond timescale and a nanometer length scale at high concentrations. The study of proteins at high concentrations is motivated by the fact that the environment in which most proteins occur in living cells is crowded, i.e. it is filled with several types of macromolecules at volume fractions between 20 and 40%. A number of studies has been carried out in such a condition. In the following, we review the results of experiments where the crowded environment of the cell is mimicked simply by the increased concentration of one single type of protein (see Section 3.10 for measurements of diffusion *in vivo*).

Myoglobin dynamics at high concentrations was investigated with NSE by Longeville and co-workers [124, 125] and by Le Coeur and Longeville [126]. At $q = 0.3\,\text{Å}^{-1}$, collective diffusion was identified with the self-diffusion. The self-diffusion coefficient D_s was found to decrease with concentration [124], as reported later by Wood et al. [73] on the diffusion of ribonuclease A.

Between dilute solution and 32 mM myoglobin, D_s was reduced by a factor 15 [125]. After the volume of one hydration layer on the surface was added to that of the bare protein to calculate the volume fraction – as done by Doster et al. [123] for Hb in RBCs – the measured diffusion coefficients were found to agree remarkably well with the long-time self-diffusion coefficient predicted by the theory of colloidal hard spheres [126]. The collective diffusion at low q, instead, was shown to grow with concentration as a result of increasing direct interactions [125].

In an attempt to measure also the short-time limit of the diffusion coefficient by NSE, hemoglobin was measured at 350 mg/ml in H_2O [126]. Two relaxations were observed at $1\,\text{Å}^{-1}$, one of which arising from water diffusion. The second component with relaxation time $\tau = 67 \pm 15$ ps was too fast to be due to short-time diffusion and it was not possible to determine the related process.

Myoglobin diffusion up to a volume fraction of 40% was measured also by neutron backscattering spectroscopy [127]. Two components of the scattering function were identified: the slow relaxation was attributed to translational diffusion (thus neglecting rotational diffusion), the fast process was assigned to internal dynamics. The narrow quasi-elastic broadening was found to follow a q-behavior typical of subdiffusive processes. The data were fitted with the jump-diffusion model by Singwi and Sjölander (see Section 2.6), and the diffusion coefficients were found to decrease with increasing protein concentration, whereas the residence times increased.

Similar results were observed in solutions of ferritin, a complex consisting of protein units responsible for iron storage [128]. At low concentrations and high ionic strength, the diffusion measured by NSE approaches the dilute limit. Increasing the concentration, as expected, slows down the diffusion. The study examined also solutions with low-salt content. In these samples, a structure factor peak appeared as a consequence of the ordering of the ferritin molecules. In the vicinity of the peak, only an approximate analysis was possible, because the q-averaged intermediate scattering function is affected by the slope of the structure factor. Nevertheless, the data indicated that in low-salt samples both direct electrostatic and indirect interactions influence the ferritin dynamics, especially close to the structure factor. These results essentially confirmed those by Häusler and Farago on apoferritin (ferritin without the iron core) suggesting that, at the structure factor peak, dynamics is slowed down by strong spatial correlations, while at lower scattering vectors (larger length scales), dynamics is hindered by hydrodynamic interactions [129].

The effect of crowding and the presence of NaCl on the diffusion of bovine serum albumin (BSA) was investigated with both NBS and NSE [29, 130]. A crowding-induced decrease of the apparent self-diffusion coefficient D was observed with both techniques. Instead, the addition of NaCl was found to affect the diffusion only at low protein concentration [130]. Roosen-Runge et al. established an analytical framework for separating the rotational D_r and the translational D_t contributions to the experimentally determined D, requiring knowledge of D_r [29]. Using the short-time limit of D_r from the theory of colloids, D_t could be extracted from the data at 280 and 300 K and its value as a function of the protein volume fraction φ, calculated with the hydrodynamic radius rather than the bare protein radius, was found to agree quantitatively with the corresponding theoretical short-time translational diffusion coefficients. Therefore, hydrodynamic interactions arising from self-crowding at physiological volume fractions were shown to slow down short-time self-diffusion by a factor 5 compared to the dilute limit [29].

A general outcome of the studies above is that the diffusion of proteins is slowed down by crowding. The application of concepts from the theory of colloids suggests that such a damping of the dynamics is mainly due to hydrodynamic interactions. In addition to that, close to the structure peak appearing at high concentrations of charged proteins at low salt concentrations, collective dynamics is hindered by strong spatial correlations.

Before concluding, two critical points for the interpretation of the measured self-diffusion in terms of colloid physics should be noticed. (i) In all cases, an agreement between experimental data and theories for effective hard-spheres is observed only after an appropriate renormalization of the volume fraction of the bare proteins to an effective, larger volume fraction. This renormalization requires a calibration based on accurate information on the volume, dilute limit dynamics (e.g. from DLS or HYDROPRO), and structure of the proteins (e.g. from the specific volume, SAXS/SANS measurements, or PDB files). In addition to this, assumptions must be done regarding the physical origin of the volume fraction renormalization, in particular concerning the relevant radius for the hydrodynamic interactions. The sensitivity of the result to the precise calibration of the volumes occupied by the proteins and hydration layers will inevitably lead to different conclusions under different assumptions. In particular, it should be mentioned that non-sphericity in general leads to a larger effective volume and it is thus in principle insufficient to increase the volume only by the geometric volume of the hydration layer. (ii) The application of the aforementioned colloid theories implies that the measurement must account for either the long or the short-time diffusion limit. However, this is in practice not always simple to ensure.

3.12 Dynamics of Protein Clusters, Aggregates, and Glasses

In the previous Sections, solutions of protein monomers were studied. Proteins, however, under specific conditions, can form different types of clusters, aggregates, gels and glasses. In this Section, we review neutron scattering studies regarding these phenomena.

Porcar et al. [131] investigated solutions of lysozyme at concentrations in the range ~ 50 to $\sim 250\,\mathrm{mg/ml}$. Prior to that study, small-angle scattering had not provided a conclusive picture on whether proteins were forming clusters or rather strongly repulsive, individual lysozyme proteins were present in solution at high concentrations (see Ref. [131] and references therein). The self-diffusion coefficients measured by neutron spin-eco spectroscopy were found to decrease with increasing concentration more than predicted by colloid theory, assuming proteins are diffusing as monomers and dimers, as at low concentrations [131]. It was therefore concluded that protein clusters form at high lysozyme concentrations, with a lifetime larger than 25 ns, since the data were consistent with static clusters in the timescale accessible by the instrument (25 ns). Moreover, at a volume fraction $\varphi \equiv 0.2$, the effective cluster radius was found to increase from 2.5 to 3.6 times that of a monomer when temperature was decreased from 25 to 5°C, in agreement with small-angle scattering [131]. In a subsequent study, the short- and long-time diffusion properties of lysozyme samples at different concentrations were obtained from NSE and nuclear magnetic resonance (NMR) (Liu et al. [132]). The comparison yielded, within the error bars, the same diffusion coefficients, even though the long-time diffusion coefficient is expected to be smaller than in the short-time limit. The result was interpreted as a result of the diffusion of clusters with a finite lifetime, larger than the NSE timescale, but shorter than that probed by NMR. In other words, while on the timescale of NSE clusters are still static, at a timescale of $\sim 200\,\mathrm{ms}$

proteins can escape from the cluster, which is thus a dynamic cluster [132].

For the same system, lysozyme in aqueous solutions, Douglas Godfrin et al. [133] noticed that, while viscosity measurements show a behavior typical for Newtonian liquids, at high concentration the short-time dynamics measured by NSE is characterized by features typical of glassy colloid systems. Also, with increasing protein concentration, a correlation peak grows in the SANS data, the so-called intermediate range order peak (IRO, observed first by Stradner and colleagues [134]). This behavior was explained by Douglas Godfrin and co-workers as a consequence of localized heterogeneous density distributions occurring at the same length-scale at which the IRO peak is detected, due in turn to competing short-range attraction and long-range repulsion interactions [133].

Recently, Yearley and co-workers [135] observed by NSE the formation of protein clusters in solutions of monoclonal antibodies (mAbs) at high concentrations. In the study, two model mAbs in solution were compared, one of which was characterized by a steep increase of the viscosity of solutions at high concentration (mAb1), the other showing a less pronounced increase (mAb2). The combination of NSE and small-angle scattering demonstrated that in the solutions with high viscosity the mAb1 molecules formed dimers, whereas the mAb2 molecules retained their monomer structure. The high viscosity, which is undesirable for pharmaceutical applications, was therefore related to the formation of such dimers at high concentrations [135].

Understanding protein aggregation is fundamental also because it often leads to the formation of so-called amyloid fibrils, which are related to numerous diseases. In this context, Erlkamp et al. [136] performed a combined SAXS-NSE study of insulin under two solvent conditions, one promoting, the other inhibiting amyloid fibril formation. In the former case, no collective diffusion (density fluctuations) was observed in the range of time and length scales experimentally accessible, and only self-diffusion could be measured. In the former case, collective diffusion was visible, as expected from the appearance of a correlation peak in the SAXS profiles. The results suggested therefore that a lack of repulsive interactions reducing collective effects promotes the fibril formation [136].

Summarizing, the results above demonstrate the power of neutron spectroscopy for measuring nanoscale diffusion of proteins, even of rather complex solutions, which was shown to provide important information on microscopic properties such as clustering and glass transitions useful to understand the basis of macroscopic properties of the system. From the perspective of colloid physics, proteins represent a fascinating model system and an opportunity for the study of new phenomena related to the interplay of repulsive and attractive interactions.

3.13 Summary

Neutron scattering spectroscopy was employed in a multitude of investigations of protein dynamics – from fast, localized motion with TOF and NBS to slow domain motion with NSE, as well as center-of-mass diffusion with NBS and NSE. Experiments have shown that the internal motion of proteins in hydrated powders differs from that in solution, where generally additional dynamics was observed. Protein internal dynamics does not only depend on the hydration level, but also on the characteristics of the solvent, e.g. if H_2O or D_2O are used. EINS studies revealed the existence of a dynamical transition in solution similar to that observed in powders. Other than in powders, some results suggested an apparent decoupling of water and protein dynamics. Furthermore, numerous studies have demonstrated an effect of the structure and state of proteins, as well as an influence of pressure, temperature and crowding, on their dynamic behavior. Finally, in addition to studies on highly concentrated protein solutions, investigations of entire living cells demonstrated the occurrence of different dynamical processes *in vivo*, and provided evidence for a molecular mechanism of adaptation of organisms to the temperature at which they live.

This Section concludes the review on quasi-elastic neutron scattering studies of proteins in solution. In the following Chapter, the materials and the methods employed in this work will be presented.

Chapter 4

Materials and Methods

In this Chapter, the materials (Section 4.1) and the experimental procedure for the preparation of the samples (Section 4.2) are presented, along with some previously established methods employed for the neutron data analysis (Sections 4.3) and the instruments used for the experiments (Section 4.4). Table 4.1 lists the experiments in which the data analyzed and published in this thesis were recorded.

Table 4.1: List of the neutron scattering experiments reported in this thesis in Chapters 6, 7, and 8, already published in peer-reviewed journals.

Experiment Number / DOI	Year	Instruments	Experimentalists
IPTS-2782	2010	BASIS (NBS)	M. Hennig, F. Zanini, T. Seydel
IPTS-4625	2011	BASIS (NBS)	M. Hennig, F. Zanini, T. Seydel
IPTS-7787	2012	BASIS (NBS)	V. Glenisson, M. Grimaldo M. Hennig, T. Seydel
IPTS-9987	2014	BASIS (NBS)	M. Grimaldo, T. Seydel
doi:10.5291/ILL-DATA.9-13-477	2013	IN16B (NBS)	M. Grimaldo, T. Seydel
9-13-276	2009/ 2010	IN6 (TOF)	M. Hennig, M. Koza, F. Roosen-Runge, T. Seydel, F. Schreiber

Further experiments carried out during this thesis, the result of which have not yet been published in peer-reviewed journals are listed in the Appendix D along with their persistent digital object identifier (DOI). Even if no DOI is assigned, all data are permanently curated by the respective neutron facilities.

Table 4.2: Selection of properties of H_2O and D_2O [139].

	H_2O	D_2O
Molar mass [g/mol]	18.01528	20.02748
Melting point (101.325 kPa) [°C]	0.00	3.82
Boiling point (101.325 kPa) [°C]	100.00	101.42
Maximum density [g/cm^3]	0.99995	1.1053
Temperature of maximum density [°C]	4.0	11.2
Ionization constant (20°) -log K_W	14.163	15.132

4.1 Materials

This Section presents the main characteristics of the materials composing the measured samples – solvent, proteins and salts –, focusing on the properties relevant for this work.

4.1.1 D_2O

As seen in Section 2.4, neutrons are scattered particularly well by hydrogen atoms, which are present to a large extent in proteins. Obviously, scattering of neutrons by H-atoms of water molecules would also greatly contribute to the total scattering, if H_2O was used as a solvent. As a consequence, the discernment of the signal from the proteins and from water would not be an easy task. Therefore, in order to reduce the scattering from the solvent and increase the contrast with the proteins, heavy water (D_2O) is used in place of H_2O, because of the much smaller neutron cross Section of deuterium compared with hydrogen atoms (cf. Table2.1). In other words, the hydrogen atoms of the proteins are seen much better than all the other atoms in the system, including the deuterium atoms in heavy water.

D_2O is water, where the two hydrogen atoms are replaced by two deuterium atoms, that is atoms with a nucleus composed of one proton and one neutron. The addition of the two neutrons to the H_2O molecules results in significantly different vibrational and librational frequencies [137, 138], as well as other physico-chemical properties, as partially summarized in Table 4.2.

A key parameter of the solvent when studying colloidal suspensions is the viscosity (c.f. Section 2.2). In our analysis, we calculated the viscosity of D_2O with the formula [140].

$$\eta(T) = A\,[\Delta T + a\,\Delta T^2 + b\,\Delta T^3 + c\,\Delta T^4]^{-\gamma}\,, \tag{4.1}$$

where $\Delta T = T - T_0$, and T_0, A, a, b, c, and γ are listed in Table 4.3.

Although the use of D_2O is common praxis for neutron scattering, NMR, and other spectroscopic techniques, it should be kept in mind that the quantitative determination of some parameters related to the protein structure and dynamics may differ depending on whether the protein is dissolved in H_2O or in D_2O [64]. For example, D_2O leads to stronger hydrogen-bond interactions as well as to stronger hydrophobic interaction due to the lower solubility of apolar groups [64, 137]. The stability of proteins in D_2O is generally higher than in H_2O [141], and also

Table 4.3: Coefficients for the calculation of the viscosity of D_2O with equation (4.1) [140].

A [cP K^γ]	885.60402
a[K^{-1}]	2.7990×10^3
b [K^{-2}]	1.6342×10^5
c[K^{-3}]	2.9067×10^8
γ	1.55255
T_0 [K]	231.832

the subnanosecond internal dynamics and stiffness of proteins is significantly different in the two solvents [64, 75].

Even if measurable, such variations do not affect the conclusions of this work, the purpose of which is not the mere determination of the physical quantities of one or the other specific protein, but rather the attempt to identify and understand universal natural phenomena, and test the applicability of theoretical models and concepts.

4.1.2 Bovine Serum Albumin (BSA)

One of the model proteins used in this work, is bovine serum albumin (BSA).

BSA is the most abundant soluble protein in the body of cows [142] and is, after water, the main component of cow blood serum, where it acts as a transporter of hormones such as thyroid hormones, of fatty acids and of various cations such as Cu(ii) and Ni(II), Ca(II), and Mg(II) [142]. BSA also acts as an antioxidant [143], it helps maintaining the blood pH [143,144], and its typical concentration of 35-50 mg/ml results in a contribution of 80% [142, 143] to the overall osmotic blood pressure.

Bovine serum albumin was chosen for our studies because of its compact, ellipsoidal structure [145, 146], good stability, high solubility, and wide availability at a relatively low cost.

Serum albumin is a highly helical protein: about 70% of the polypeptide chain is folded in α-helices, about 10% is composed of β-sheets, and the rest is a less structured peptide chain [142]. A surface plot of a BSA molecule is illustrated in Figure 4.1. The parts of the surface highlighted in red and blue are acidic, basic residues, respectively. In solution, at neutral pH, the alkaline residues (colored in blue) are assumed to be positively charged and analogously the acidic residues (highlighted in red) are negatively charged. Thus, the surface charge distribution of BSA, as that of all proteins, is an inhomogeneous pattern of positive and negative charges. In aqueous solution at pH=6.8, the net charge of BSA is -11e and its effective charge is -8.4e [148, 149].

The chemical formula is $C_{2935}H_{4617}N_{781}O_{898}S_{39}$ [145, 146, 150] and its molecular weight amounts to 66.4 kDa [142]. The hydrodynamic radius calculated by HYDROPRO [151] is 3.6 Å and the partial specific volume is $\vartheta = 0.7348\,\mathrm{ml/g}$ [152].

As explained in Section 4.2, for the preparation of the BSA aqueous solutions, we dissolve lyophilized BSA in D_2O. Although pure serum albumin is colorless the lyophilized BSA is in the form of a white or light yellow powder, because of low concentration impurities due to its

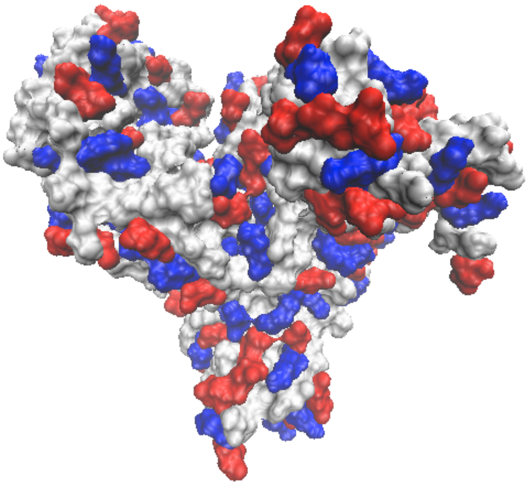

Figure 4.1: Surface structure of a BSA molecule [145]. The acidic and basic residues are highlighted in red and blue, respectively. DOI: 10.2210/pdb4f5s/pdb The figure was rendered using VMD [147].

particularly marked affinity for substances such as hematin and bilirubin, which in turn appear yellow [142].

4.1.3 Immunoglobulin G (IgG)

With the aim of investigating the role of the shape of protein on their short-time diffusion (cf. Chapter 2.2), bovine *gamma*-globulin, consisting essentially of bovine immunoglobulin G (IgG), was chosen as a model protein with an irregular shape, strongly deviating from a sphere (see Figure 4.2).

IgG is the most abundant antibody in the blood plasma, representing 75% to 85% of the all the immunoglobulins in blood [153]. Immunoglobulin G, as all the antibodies, is a glycoprotein that interacts specifically with an antigen. IgG is secreted by plasma cells and accumulate in the blood plasma and interstitial fluid of tissues [153].

The chemical formula of a typical mouse IgG is $C_{6440}H_{9962}N_{1704}O_{2011}S_{56}$ [150,154]. IgGs are Y-shaped molecules, with a molecular mass of approximately 150 kDa, and consist of two identical light chains (molecular weight of ∼25 kDa each) and two identical heavy chains (molecular weight of ∼50 kDa each) bound by disulfide bonds [153,155].

Most of the secondary structure of immunoglobulin G consists of β-sheets [156]. A surface plot of an IgG molecule is illustrated in Figure 4.2, in which the acidic and basic residues are highlighted in red and blue, respectively.

Each IgG molecule has two antigen-binding sites, both for the same antigen. A peculiarity of IgG is the ability of penetrating the placental barrier into the fetal circulation, which confers the newborn passive immunity against certain infections [153].

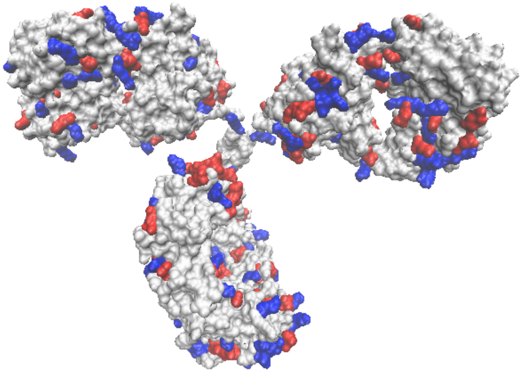

Figure 4.2: Surface structure of an IgG molecule [154]. The acidic and basic residues are highlighted in red and blue, respectively. DOI: 10.2210/pdb1igt/pdb The figure was rendered using VMD [147].

IgG is highly soluble, and remarkably stable (half-life > 3 weeks in solution [153]), although less than BSA. Its hydrodynamic radius determined with HYDROPRO [151] is $\sim 55\,\text{Å}$ and the partial specific volume is $\vartheta = 0.739\,\text{ml/g}$ [157].

As BSA, IgG can be purchased as a lyophilized powder of a white color, which can be dissolved in D_2O at the desired concentration.

4.1.4 Yttrium Chloride (YCl_3)

One of the main scientific questions of this thesis is how the presence of multivalent salts in solution affects protein dynamics. To this end, yttrium chloride (YCl_3) was employed for the reasons explained below.

YCl_3 is a trivalent salt dissociating in water in Y^{3+} with an ionic radius of 104 pm and 3 Cl^- with an ionic radius of 167 pm [158]. Its molecular weight is $M_{YCl_3} = 195.26$ Da [159]. Importantly, when dissolved in water, the pH of the solution remains between ~6 and 7 on the wide concentration range $c_{YCl_3} = 0$ to 100 mM [160].

Highly purified YCl_3 is widely available at a reasonably low cost. At room temperature, yttrium chloride is an odorless, white solid. It is highly soluble in water (82 g/100 ml), and it was found by our group that its cation Y^{3+} strongly binds on specific sites on BSA in aqueous solutions.

The particularly rich phase behavior of negatively charged proteins in the presence of multivalent cations was first observed with aqueous BSA solutions in the presence of YCl_3 [161]. After this discovery, several studies were performed on this kind of system [161–164]. Therefore, YCl_3 was chosen for this work for historical reasons because of the good pre-characterization of the system, as well as because of its reasonable cost and rather neutral pH in water, avoiding the fast corrosion of the aluminum sample holders employed in neutron backscattering (see Section 4.2).

4.2 Sample Preparation

In this Section, all the information and procedures required for the preparation of the samples are reported. As the preparation procedure is the same as that employed in Ref. [165], some parts of the description will be inevitably unchanged.

The products employed for the sample preparation are listed below and were used without further purification.

D_2O Deuterium oxide from the *Acros Organics* company. Purity: $\geqslant 99.75\%$. Code: 166301000. Deuterium oxide from the *Sigma Aldrich* company. Purity: 99.9%. Code: 151882.

BSA Lyophilized powder, essentially globulin and protease free from the *Sigma-Aldrich* company. Purity: $\geqslant 98\%$. Code: A3059.

Bovine γ-globulins Lyophilized powder, essentially globulin and protease free from the *Sigma-Aldrich* company. Purity: $\geqslant 98\%$. Code: A3059.

YCl_3 Anhydrous beads and powder from the *Sigma-Aldrich* company. Purity: 99.99%. Codes: 450103 and 451363.

The salt stock solutions were prepared as follows.

1. A vial together with its cap was weighted using an analytical balance with precision of ± 0.1mg.
2. The mass m_s of salt to be weighted for the desired volume $V_{\mathrm{D_2O}}$ of stock solution at the molar concentration c_{stock} was calculated through the formula $m_s = V_{\mathrm{D_2O}}\, c_{\mathrm{stock}}\, M_s$, where M_s is the salt molecular weight. Approximately the calculated mass was inserted into the vial.
3. Subsequently, the closed vial containing the salt was weighted again and the weight of the empty vial was subtracted to this value to determine the exact mass of salt in the vial m_s.
4. To obtain the wanted salt concentration c_{stock}[mM] a volume $V_{\mathrm{D_2O}} = m_s/(c_{\mathrm{stock}}\, M_s)$ of D_2O was pipetted into the vial.
5. The vial was closed, sealed with Parafilm, and put on a roller mixer for several hours.

The procedure for the preparation of the samples is described in the following.

1. A vial was weighted together with its cap.
2. Since the sample holders contain a volume of approximately 1.3 ml, a mass $m_p \simeq c_p \cdot 1.5\,\mathrm{ml}$, where c_p is the desired nominal protein concentration, was put into the vial.
3. The closed vial containing the protein was weighted to obtain the exact mass of protein m_p in the vial (filled minus empty vial mass).

4. The total volume of heavy water and salt stock solution $V = V_{\mathrm{D_2O}} + V_{\mathrm{stock}}$ to be added to the protein powder to obtain the wanted nominal protein concentration c_p[mg/ml] was determined by the formula
$$V = \frac{m_p}{c_p} \; . \tag{4.2}$$
The volume of D_2O
$$V_{\mathrm{D_2O}} = V - V_{\mathrm{stock}} = V - V\frac{c_s}{c_{\mathrm{stock}}} \tag{4.3}$$
was pipetted into the vial. In the equation above, c_s is the salt concentration of the sample.

5. Finally, the volume $V_{\mathrm{stock}} = V\frac{c_s}{c_{\mathrm{stock}}}$ of salt stock solution was added to the solution. The vial was closed with its cap, sealed with Parafilm and put on the roller mixer for some hours, until the entire content was completely dissolved (in general, the higher c_p and c_s, the more time was needed).

Once the sample was ready, it was filled into the sample holder for the neutron measurements. For all the backscattering experiments a double cylindrical aluminum sample holders as the one illustrated in Figure 4.3 was used. The cell has an outer diameter of 23 mm, and a gap width between the cylinders of 0.15 mm. The gap was chosen such that a solution of BSA in heavy water at a concentration $c_p = 500\,\mathrm{mg/ml}$ scatters neutrons with an less than 10% probability, which decreases the probability that a neutron is scattered twice to less than 1% [31]. Aluminum was chosen to manufacture the cell because it is a weak elastic coherent scatterer within the quasi-elastic energy range of the employed instruments (see Table 2.1). The composition of the aluminum alloy of the sample holder is shown in Table 4.4.

Table 4.4: Aluminum alloy composition of the sample holder in mass % [31].

Si	Fe	Cu	Mn	Mg	Cr	Zn	Ti	Al
0.3 - 0.6	0.1 - 0.3	0.1	0.1	0.35 - 0.6	0.05	0.15	0.1	98 - 98.75

After filling the outer cylinder, the inner cylinder was slowly inserted and sealed against vacuum by screwing the two cylinders together at the top. Thereby, an Indium wire was squeezed between the top surfaces of the cylinders sealing possible leaks (see Figure 4.3).

Finally, the sample holder was screwed to a stick, which went inside the sample environment of the spectrometer. The stick serves also to house the cables necessary to determine and regulate the temperature of the sample thanks to a sensor placed in the tip of the stick. An additional temperature-sensor is located close to the heating point and cold valve of the sample environment.

Before concluding this Section we note that the nominal protein concentration c_p differs from the real protein concentration $c_{p,\mathrm{real}}$. In fact, the total volume of the solution is not $V_{\mathrm{D_2O}} + V_{\mathrm{stock}}$, since in that sum the volume of the proteins is neglected. The real concentration can be easily obtained from c_p and the known partial specific volume ϑ by the formula
$$c_{p,\mathrm{real}} = \frac{c_p}{1 + c_p\,\vartheta} \; . \tag{4.4}$$

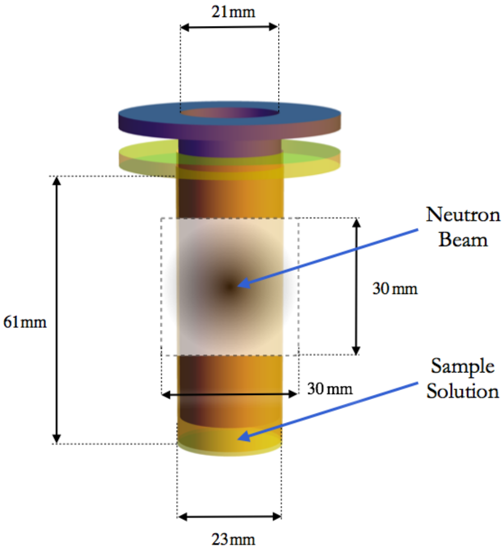

Figure 4.3: Aluminum sample holder consisting in an inner and an outer cylinder. The sample solution is filled into the outer cylinder. Subsequently the smaller cylinder is inserted in the outer cylinder and screwed on the top plateau with 12 screws. In this way, when the cell is closed, the sample is homogeneously distributed on the entire cell height in the gap between the two cylinders. While screwing, an Indium placed in a thin groove (not shown) on the top of the outer cylinder is squeezed between the two plateaus, ensuring sealing against vacuum. Figure from Ref. [31].

In this work, the concentrations reported are nominal concentrations unless specified otherwise.

Analogously, the protein volume fraction φ, i.e. the volume occupied by the proteins to the total volume of the solution is given by:

$$\varphi = \frac{c_p\,\vartheta}{1 + c_p\vartheta}\;. \tag{4.5}$$

This Section concludes the part of the Chapter concerned with the sample materials and preparation. In the next Section, previously established methods for the data treatment are presented.

4.3 Methods

In this Section, the main steps performed during the data treatment and analysis are explained: Sections 4.3.1 to 4.3.3 deal with the neutron data treatment at a very general level, while in Section 4.3.4 more a specific analysis protocol developed within our group is discussed.

4.3.1 Data Reduction

When measuring a quasi-elastic spectrum, both on BASIS and IN16B (see Sections 4.4.3, and 4.4.4), very large arrays containing the counts from every detector are recorded together with the time when each neutron was detected. As explained in Section 4.4 the time information is essential to determine the energy of the neutrons.

In order to obtain a spectrum, before any data analysis can be performed, the data must be reduced to a treatable form: every count collected from different time channels and detectors is associated with a neutron energy transfer $\hbar\omega$ by means of equation (4.35) in Section 4.4.3, and with a scattering vector q as in equation (2.37), respectively (cf. Section 2.4). Subsequently, the data are grouped and integrated with the desired binning of both energy and scattering vectors.

The Mantid routines provided by the SNS facility were used to reduce BASIS data, while the reduction of IN16B data was performed with self-written Matlab code, inspired by the octave code written for the same purpose by Markus Appel [166]. The subsequent analysis and fitting was done in both cases, BASIS and IN16B, by self-written MATLAB code involving a few compiled subroutines written in C++ based on the predecessor code by Marcus Hennig [31].

The reduction of BASIS data was done such to obtain spectra in an energy range from -100 µeV to 100 μeV with 0.4 µeV wide bins, for q ranging from 0.25 to 1.95 $\mathring{A}^{-1}$ with bin width 0.1 $\mathring{A}^{-1}$, i.e. 18 bins.

IN16B data, instead, is limited to a dynamic range of -30 µeV to 30 µeV with 0.25 µeV wide bins. The scattering vector ranges from $\sim$ 0.15 to 1.95 $\mathring{A}^{-1}$ with a bin width of approximately 0.1µeV.

These untreated QENS spectra are a complicated superposition of different contributions such as:

- Background from the sample environment (e.g. cryofurnace), possibly q, ω and intensity dependent (mainly at BASIS, where the instrumental background is higher than at IN16B);
- Scattering from the aluminum sample holder;
- Scattering from the bulk water;
- Scattering from the water on the protein surface (hydrodynamic shell);
- Scattering from the atoms in the protein.

The latter is the contribution in which we are interested, and is in turn a superposition of contributions due to the self-diffusion of the entire protein, composed of a translational and a rotational part, and to the internal motions of the protein atoms (e.g. side chains movements).

In the following Sections, the data treatment performed to obtain, to the best of our efforts, the protein signal only, is discussed.

4.3.2 Subtraction of the Contribution of the Sample Holder

As mentioned in Section 4.3.1, despite the low neutron scattering cross-section of aluminum (see Table 2.1), one of the contributions to the raw spectra arises from the cell containing the sample.

In order to subtract such a contribution from the total scattering function, the spectrum of the empty sample holder is measured in addition to the samples.

For the data collected on IN16B and presented in Chapter 6, the empty cell spectrum was subtracted directly from the raw spectra. Thereby, it is neglected that, when the gap between the cell walls is filled with the sample, the spectrum of the cell is slightly different from that of the empty sample holder. In fact, both the incident and the scattered beams are subject to absorption not only within the walls of the sample cell, but also within the sample. Moreover, the absorption is a function of the scattering vector [167].

To account for these effects, a more sophisticated treatment was applied to the data recorded on BASIS and presented in Chapters 7 and 8, where the instrumental background from the sample environment is higher, the resolution function less symmetric, and the accessible energy range is larger. This procedure is the Paalman-Pings [167] numerical correction presented below.

In the following, the superscript refers to the scattering object, while the subscript indicates the absorbing object. In both the super- and the subscript

c indicates the cell;

s indicates the sample.

The scattering intensity of the bare sample I^s, without the contribution of the empty cell is given by [167]

$$I^s(\mathbf{q},\omega) = \alpha_{sc}(\mathbf{q}) I_{sc}^{sc}(\mathbf{q},\omega) - \beta_{sc}(\mathbf{q}) I_c^c(\mathbf{q},\omega) \ , \tag{4.6}$$

where I_{sc}^{sc} indicates the scattering intensity after scattering and absorption from both the sample and the cell and I_c^c represents the scattering intensity of the empty cell. α and β are defined as follows:

$$\begin{aligned} \alpha_{sc} &= \frac{1}{A_{sc}^s} \\ \beta_{sc} &= \frac{1}{A_{sc}^s} \frac{A_{sc}^c}{A_c^c} \ . \end{aligned} \tag{4.7}$$

Therein A_{sc}^s, A_{sc}^c, A_c^c denote q-dependent cylindrical absorption factors, the so called Paalman-Pings coefficients. They are defined as the integral [31]

$$A_{\Sigma}^V(\mathbf{q}) = \frac{1}{V} \int_V \exp\left[- \int_{\gamma(\mathbf{x})} \Sigma(\mathbf{x}') \mathrm{d}s(\mathbf{x}') \right] \mathrm{d}^3\mathbf{x} \ , \tag{4.8}$$

where V indicates the scattering volume (either of the sample, or of the cell), γ is the path of a scattered neutron, $\Sigma(\mathbf{x})$ denotes the linear attenuation coefficient at position $\mathbf{x}$ and $\mathrm{d}s(\mathbf{x})$ is the infinitesimal line element of the line integral. The values of the attenuation coefficients have been calculated using the utility of National Institute of Standards and Technology (NIST) [168].

As in Ref. [165], the density ρ used in the calculation of the linear attenuation coefficient of the BSA solutions was obtained for a concentration $c_p = 200\text{mg/ml}$ as follows:

$$\rho = (1-\varphi)\rho_{\mathrm{D_2O}} + \varphi\ \rho_{BSA}\ , \tag{4.9}$$

where $\varphi = 0.128$ is the protein volume fraction (equation (4.5)), $\rho_{BSA} = 1.36\,\mathrm{g\ cm^{-3}}$ (see Section 4.1.2), and $\rho_{\mathrm{D_2O}} = 1.1050\,\mathrm{g\ cm^{-3}}$ (see Section 4.1.1). The density of the solution is then $\rho = 1.14\,\mathrm{g\ cm^{-3}}$. This value has been used for the calculation of the Paalman-Pings coefficients used for the BSA samples at all the measured concentrations, since the density differences result in variations of the linear attenuation coefficient on the order of a few percent, therefore of acceptable magnitude.

Two example spectra measured at BASIS (dark blue squares) and IN16B (red circles), after the subtraction of the spectrum of the empty cell are superimposed in Figure 4.5.

After the contribution to the spectra due to the sample holder is removed, the spectrum ideally contains only information about the contained sample. However, before further quantitative analysis can be performed, a calibration accounting for instrumental characteristics must be carried out. The steps required for this calibration are presented in the next Section.

4.3.3 Calibration

The accurate analysis of the neutron spectra requires an instrument-dependent calibration accounting for the different efficiency of different detectors and the instrument resolution. The procedure employed for the calibration is explained in the next paragraphs.

The Detector Efficiency

The measured intensity of the quasi-elastic spectra depends, practically, on the efficiency of each detector, that is to say that the recorded intensity $I(\mathbf{q},\omega)$ can be described by

$$I(\mathbf{q},\omega) = \mathscr{D}(\mathbf{q})\,S(\mathbf{q},\omega)\,, \tag{4.10}$$

where $S(\mathbf{q},\omega) = I(\mathbf{q},\omega)$ in the ideal case of perfect detector efficiency $\mathscr{D}(\mathbf{q})$. For incoherent QENS, $\mathscr{D}(\mathbf{q})$ can be estimated by integrating $I_{\mathrm{V}}(\mathbf{q},\omega)$ of Vanadium (V):

$$\mathscr{D}(\mathbf{q}) = \int I_{\mathrm{V}}(\mathbf{q},\omega)\,\mathrm{d}\omega\,. \tag{4.11}$$

Vanadium is chosen because of its large incoherent neutron scattering cross-section, and its purely elastic peak (modulated by the Debye-Waller factor, see below) over the observable energy transfer range, meaning that ideally all the incoherent scattering intensity is detected. Therefore, all the measured spectra are corrected for the detector efficiency by the q-wise normalization

$$S(\mathbf{q},\omega) = \frac{I(\mathbf{q},\omega)}{\int I_{\mathrm{V}}(\mathbf{q},\omega)\,\mathrm{d}\omega}\,. \tag{4.12}$$

The Resolution Function

Besides the detector efficiency, another instrument-dependent characteristic unavoidably affects every measurement: the instrument resolution.
As a matter of fact, equation (4.10) can be written as

$$I(\mathbf{q},\omega) = \mathscr{D}(\mathbf{q})\,\mathscr{R}(\mathbf{q},\omega) \otimes \mathscr{S}(\mathbf{q},\omega)\,, \tag{4.13}$$

where the scattering function $\mathscr{S}(\mathbf{q},\omega)$ of the sample is "smeared" by the convolution with the resolution function $\mathscr{R}(\mathbf{q},\omega)$. As for the determination of the detector efficiency, measuring the scattering of Vanadium is ideal for determining the resolution function, since

$$S_{\mathrm{V}}(\mathbf{q},\omega) = \mathscr{R}(\mathbf{q},\omega) \otimes \mathscr{S}_{\mathrm{V}}(\mathbf{q},\omega) = \mathscr{R}(\mathbf{q},\omega) \otimes \exp[-\left\langle u^2\right\rangle_T q^2]\,\delta(\omega) \simeq \mathscr{R}(\mathbf{q},\omega)\,, \tag{4.14}$$

with the Dirac delta function $\delta(\omega)$, and the Debye-Waller factor (DWF) $\exp[-\left\langle u^2\right\rangle_T q^2]$ accounting for the lattice vibrations of Vanadium. The temperature dependent mean-squared displacement $\left\langle u^2\right\rangle_T$ of Vanadium at $T = 296$ K is $\left\langle u^2\right\rangle_T = (6.7 \pm 0.6) \times 10^{-3}$ Å [169]. Hence, the DWF is very close to one in the accessible q-range ($0.2\ \text{Å}^{-1} \leqslant q \leqslant 2\ \text{Å}^{-1}$).

Since in our case $S(q,\omega)$ is modeled by a sum of Lorentzian functions, and the convolution of a Lorentzian with a Gaussian, the Voigt function, can be easily expressed analytically to obtain a full analytical expression of $\mathscr{R}(\mathbf{q},\omega) \otimes S(\mathbf{q},\omega)$, we fitted the Vanadium spectra with the following model function:

$$I_V = \sum_{i=1}^{4}(A_i(\mathbf{q})R_i(\mathbf{q},\omega)) + B(\mathbf{q})\ . \tag{4.15}$$

The sum $\sum_{i=1}^{4}(A_i(\mathbf{q})R_i(\mathbf{q},\omega))$ describes the resolution function, while $B(\mathbf{q})$ accounts for a flat background. $R_i(\mathbf{q},\omega)$ are Gaussian functions

$$R_i(\mathbf{q},\omega) = \frac{1}{\sqrt{2\pi}\Delta\omega_i(\mathbf{q})}\exp\left[-\frac{\omega^2}{2\Delta\omega_i^2(\mathbf{q})}\right]\ . \tag{4.16}$$

A comparison of the resolution functions of BASIS and IN16B (cf. Sections 4.4.3 and 4.4.4) is shown in Figure 4.4.

Once all the steps of the treatment above are completed, the spectra of the samples can be quantitatively analyzed. The general approach for the analysis of our data is discussed in the next Section.

4.3.4 Backscattering Data Analysis

This Section is based on the article M. Grimaldo et al. [1], High-resolution neutron spectroscopy on protein solution samples, *EPJ Web of Conferences* **2015**, page 02005 [170].

Backscattering data, after the accurate treatment presented above, is used to gain quantitative information on the dynamics of the atoms within the samples. To this end, a rather elaborate analysis is required, the details of which are discussed in the next Sections.

---

[1] Author contributions: M. G., F. R.-R., M. H., T. S., F. S. designed research; M. G., F. R.-R., M. H., T. S., F. Z., M. H. performed research; N. J. and M. Z. provided technical assistance; M. G., F. R.-R. and M. H. analyzed data; M. G., F. R.-R., T. S., F. Z. and F. S. wrote the paper.

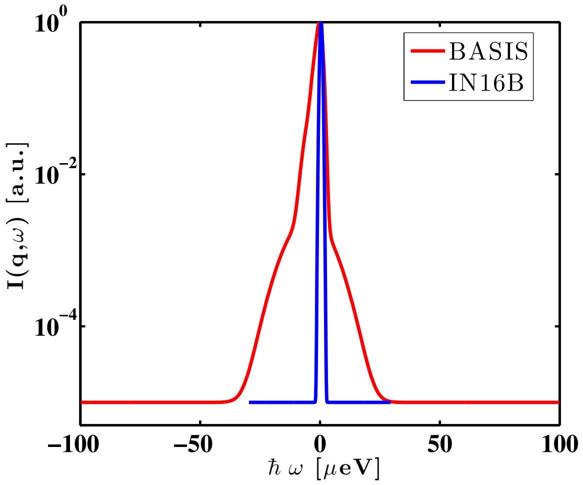

Figure 4.4: Comparison of the resolution functions of BASIS and IN16B. The red line illustrates the fit with four Gaussian functions of a Vanadium spectrum measured at BASIS. The blue line is the fit of a Vanadium spectrum measured at IN16B. Note that the y-scale is logarithmic.

New Opportunities with High-Flux Spectrometers

Very recently, significant progress has been made with the advent of new cold neutron backscattering spectrometers. Amongst those, the most recently commissioned IN16B impresses with its significantly enhanced flux at the sample compared to its predecessor instrument IN16 (figure 4.5, top), both using the same reactor neutron source. The flux increase in this case has been achieved solely by fundamentally redesigning the neutron optics [171] based amongst other concepts on the phase space transformation [172], since the source flux remains constant.

The scattering function obtained from protonated proteins in aqueous (D_2O) solution using a high-resolution neutron spectrometer can be modeled as

$$\begin{aligned} S(q,\omega) = & \mathscr{R} \otimes \{\, \beta \, [A_0(q)\, \mathscr{L}(\gamma,\omega) \; \ldots \\ & + \; (1 - A_0(q))\, \mathscr{L}(\gamma + \Gamma, \omega)\,] \ldots \\ & + \; \beta_{\mathrm{D_2O}}\, \mathscr{L}(\gamma_{\mathrm{D_2O}}, \omega) \,\} \,. \end{aligned} \tag{4.17}$$

Therein, $\mathscr{R}$ denotes the energy resolution function and $\mathscr{L}(\ldots,\omega)$ stand for Lorentzian functions with the respective linewidth given by the first parameter associated with different contributions from the sample. γ describes the global diffusion of the proteins, consisting of both translational and rotational contributions. Γ represents the internal relaxations accessed by the dynamic window of the respective spectrometer, and $\gamma_{\mathrm{D_2O}}$ the contribution of the solvent. β, $\beta_{\mathrm{D_2O}}$, and A_0 are scalars, and $A_0 = A_0(q)$ can be identified with the elastic incoherent structure factor (EISF) which contains information on the geometry of confinement of the internal fluctuations [59].

Example spectra (symbols) recorded on IN16 [173], IN16B [171], and BASIS [174] are depicted in figure 4.5 (top and bottom, respectively). In all experiments, the samples were held in identical double-walled cylindrical Al cells with outer radius 23 mm and annular gap 0.15 mm. Please note

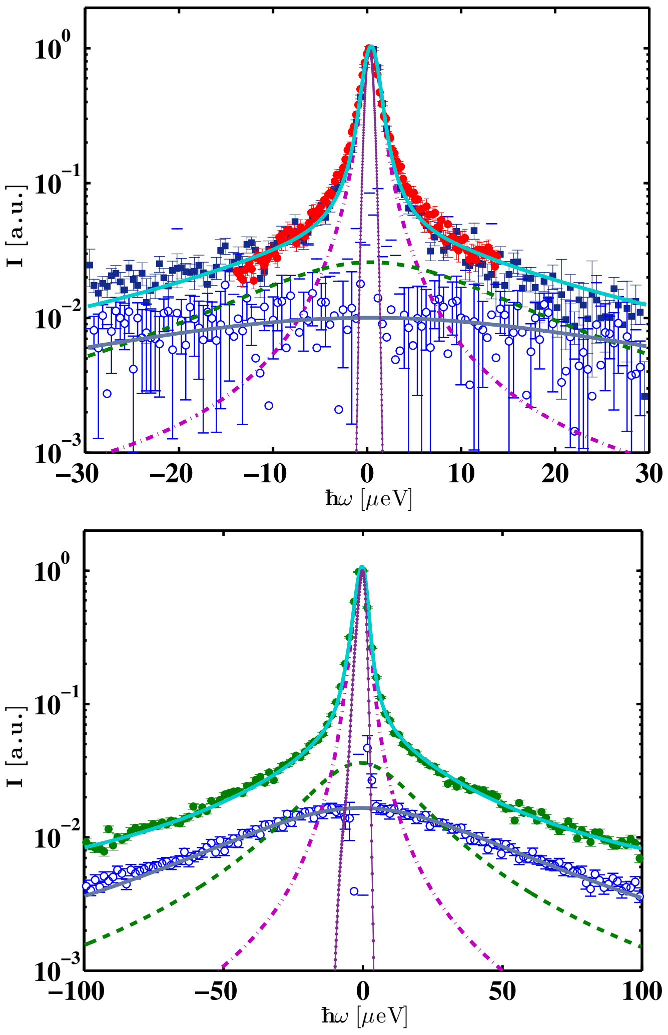

Figure 4.5: Top: Comparison of spectra recorded using the former spectrometer IN16 (red circles, narrow spectrum, 256 channels with width 0.12μeV) and the new spectrometer IN16B (blue squares, broad spectrum, 256 channels with width 0.24μeV) on BSA proteins in D_2O solution (same BSA concentration 200 mg/ml and $T = 295$ K for both spectra) at the same scattering vector $q = 0.6\,\text{Å}^{-1}$, subsequent to the empty can subtraction, illustrating the progress made with IN16B. The IN16 data have been recorded during 24 hours, the IN16B data during only 4 hours. The solid line superimposed on the data denotes the fit to the IN16B data according to equation (4.17) and the dashed and dash-dotted lines denote the Lorentzians $\mathscr{L}(\Gamma+\gamma)$ and $\mathscr{L}(\gamma)$, respectively. The narrow line with dot symbols indicates the resolution determined for both instruments by a fit to a Vanadium measurement. While on IN16 the D_2O-solvent contribution can be approximated by a constant background, this contribution becomes weakly ω-dependent within the energy-range of IN16B (open circle symbols modeled by the Lorentzian-shaped solid line, see also Section 4.3.4). All Lorentzians are displayed subsequent to the convolution with the resolution function. Bottom: Example spectrum (symbols) recorded on BASIS at $q = 0.65\,\text{Å}^{-1}$ on a BSA solution in D_2O (concentration 200 mg/ml, $T = 295$ K, counting time $\approx$ 4 hours, 500 channels with width 0.4μeV), subsequent to the empty can subtraction. The attribution of the lines is as in the top figure. The resolution function of BASIS is approximately 3.5 μeV FWHM wide.

that the statistical errors of the IN16B and BASIS spectra do not allow for a direct comparison, because the channel width in energy as well as the flux per energy interval are different, given the different design principles of these instruments. Furthermore, we note that the fast solvent water contributes differently to the signal and errors on all three spectrometers due to the different dynamic ranges. The three Lorentzians included in equation (4.17) are denoted by dashed, dash-dotted, and solid lines lines, respectively. BASIS achieves an energy resolution of approximately $3.5\,\mu$eV FWHM. By contrast, IN16B [171] operates in exact backscattering and therefore achieves a higher energy resolution of $0.9\,\mu$eV FWHM. Also on IN16B, which covers a smaller energy range associated with the higher energy resolution compared to BASIS, a significant energy-dependent contribution of the D_2O solvent is visible.

Importantly, given the good quality of the data that can now be obtained, the spectra at the individual scattering vectors can be fitted by equation (4.17) with free parameters $0 \leqslant \beta \leqslant \infty$, $0 \leqslant A_0 \leqslant 1$, $0 \leqslant \gamma \leqslant \infty$, and $0 \leqslant \Gamma \leqslant \infty$. The prerequisite for such a fit without imposing further constraints is an accurate description of the solvent contribution. In this way, $\beta_{\mathrm{D_2O}}$ and $\gamma_{\mathrm{D_2O}}$ can be fixed, as explained in the following Section. Further, the resolution function $\mathscr{R} = \mathscr{R}(\omega)$ has to be accurately taken into account by describing it analytically as a sum of Gaussian functions. In the numerical implementation of the fit, the expressions $\mathscr{R} \otimes \mathscr{L}(\ldots, \omega)$ are subsequently calculated using Voigt functions. The resolution function of IN16B can be well approximated by a single and even better by a sum of two Gaussians centered at $\omega = 0$ (the latter is the case for the fits in figure 4.5, top). The resolution of BASIS is modeled by a sum of 4 Gaussians centered at $\omega \neq 0$ (figure 4.5, bottom).

The Contribution from the Solvent Water

The scattering function of the solvent water can be modeled as [176]

$$S_{\mathrm{D_2O}}(q,\omega) = A_\gamma \mathscr{L}(\gamma_{\mathrm{D_2O}},\omega) + A_\Gamma \mathscr{L}(\Gamma_{\mathrm{D_2O}},\omega) + B(q) \ , \tag{4.18}$$

where $\mathscr{L}(\gamma_{\mathrm{D_2O}},\omega)$ denotes the Lorentzian function describing the dynamics of the entire water molecule, and $\mathscr{L}(\Gamma_{\mathrm{D_2O}},\omega)$ accounts for faster movements, the width $\Gamma_{\mathrm{D_2O}}$ being a factor 3 or more larger than $\gamma_{\mathrm{D_2O}}$. A_γ and A_Γ are scalars. $B(q)$ denotes a q-dependent background [176] which we find to be always smaller by at least a factor of 10^{-3} than the maximum of the spectrum. A slight curvature due to $\mathscr{L}(\gamma_{\mathrm{D_2O}},\omega)$ is detectable within the dynamic range of IN16B and BASIS (figure 4.5), whilst $\mathscr{L}(\Gamma_{\mathrm{D_2O}},\omega)$ is too broad to be visible on these instruments. $\gamma_{\mathrm{D_2O}}(q,T)$ is depicted in figure 4.6, as experimentally determined using the time-of-flight spectrometer IN6. The model in equation (4.18) has originally been developed for H_2O. We note that due to the use of D_2O as a solvent, a de Gennes-narrowing becomes visible at the highest q (figure 4.6), and the q-dependence of the spectral intensity is modulated by the structure factor due to the coherent scattering contribution. However, since the D_2O-contribution to the scattering from the protein solution samples is treated individually for each q, the latter fact is of no importance in the present context, and the polynomial interpolation in figure 4.6 naturally also includes the modulation of the q-dependence of $\gamma_{\mathrm{D_2O}}$ due to coherent scattering effects. We note that the fit results displayed in figure 4.6 may at some q-values and temperatures be inaccurate due to a possible cross-talking of the two Lorentzians in equation (4.18) and the resolution of IN6, as

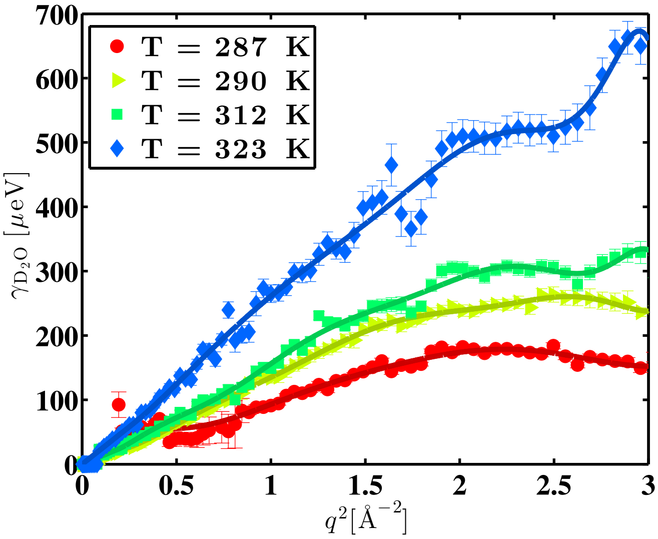

Figure 4.6: Linewidth γ_{D_2O} of D_2O (equation (4.18)) as a function of the square of the scattering vector q^2 for various temperatures T obtained from time-of-flight data recorded on IN6, ILL (symbols) [175], using the incident wavelength 5.1 Å corresponding to a resolution of $\approx 90\mu$eV FWHM. The lines are polynomial fits. Note that at the lowest temperature, the fit becomes unstable for $q^2 < 0.5\,\text{Å}^{-2}$. (Figure from the supplementary material of Ref. [28].)

reflected by large error bars. Nevertheless, the spline fits over the entire q-range appear to be sufficiently robust. The resulting Lorentzian line shape $\mathscr{L}(\gamma_{D_2O}, \omega)$ obtained from IN6 for the solvent contribution to the protein solution spectra is therefore included in equation (4.17). The amplitude β_{D_2O} of this contribution is determined by weighting the intensity of pure D_2O-spectra recorded on IN16B or BASIS, respectively, according to the D_2O-volume $(1-\varphi)$ in the sample,

$$I^{(\varphi)}_{D_2O}(q,\omega) = (1-\varphi) I_{D_2O}(q,\omega). \tag{4.19}$$

Subsequently equation (4.18) is fitted to $I^{(\varphi)}_{D_2O}(q,\omega)$ with γ_{D_2O} fixed from the IN6 results and $A_\Gamma = 0$ in equation (4.18). Finally,

$$I^{(\varphi)}_{D_2O}(q,\omega) = \beta_{D_2O} \mathscr{L}_{D_2O}(\Gamma_{D_2O}, \omega) \tag{4.20}$$

at $\omega = 0$ determines β_{D_2O} in this fit result. In figure 4.5, we include both the water spectra measured on IN16B and BASIS, respectively (open circles), as well as the model for the D_2O solvent contribution obtained from the above method (Lorentzian shaped solid line) to illustrate the validity of the method.

The Separation of the Rotational and Translational Diffusion

In equation (4.17), γ is associated with the observable apparent diffusion coefficient D via $\gamma(q) = D\,q^2$. D consists of contributions from the translational diffusion D_t and rotational diffusion D_r

through an implicit relation $D(\varphi) = D(D_t(\varphi), D_r(\varphi))$. In general, $D > D_t$ [56], and D_r thus causes an additional line broadening of $\mathscr{L}(\gamma, \omega)$ compared to a hypothetical situation without rotational diffusion (figure 4.7). The scattering function due to translational diffusion of a rigid sphere can be written as a Lorentzian with width $D_t\, q^2$,

$$\mathcal{S}_{\text{inc}}^{\text{T}}(q,\omega) = \mathscr{L}(D_t\, q^2, \omega), \tag{4.21}$$

and the scattering function due to the rotation of a rigid sphere reads

$$\mathcal{S}_{\text{inc}}^{\text{R}}(q,\omega) = \sum_{l=0}^{\infty} B_l(q)\, \mathscr{L}\left[l\,(l+1)\, D_r, \omega\right], \tag{4.22}$$

with the Lorentzian $\mathscr{L}$ with width $l\,(l+1)\, D_r$ and

$$B_l(q) = (2\,l+1) \int \rho_H(r)\, j_l^2(q\, r)\, \mathrm{d}r. \tag{4.23}$$

Therein, $j_l(x)$ denotes the lth-order spherical Bessel function of first kind and $\rho_H(r)$ the hydrogen density at radius r. The scattering function of the superposition of the rotational and translational diffusion is the convolution

$$\begin{aligned} \mathcal{S}_{\text{inc}}^{\text{TR}}(q,\omega) =& \mathcal{S}_{\text{inc}}^{\text{R}}(q,\omega) \otimes \mathcal{S}_{\text{inc}}^{\text{T}}(q,\omega) \\ =& \sum_{l=0}^{\infty} B_l\,(q)\, \mathscr{L}\,(\Gamma_l, \omega) \end{aligned} \tag{4.24}$$

with the width $\Gamma_l = l\,(l+1)\, D_r + q^2\, D_t$. Perez et al. [56] have shown that the superposition of the rotational and translational diffusion of proteins in solution can be accurately described by a single Lorentzian function with the dependence $\gamma = Dq^2$, which is in agreement with our experimental observations [29]. Therefore, the fit of this single Lorentzian to the data $\mathcal{S}_{\text{inc}}^{\text{TR}}(q,\omega)$ can be written as

$$\min_{\alpha,\gamma} \left\{ \int \left[\mathcal{S}_{\text{inc}}^{\text{TR}}(q,\omega) - \alpha\, \mathscr{L}(\gamma,\omega)\right]^2 \mathrm{d}\omega \right\}. \tag{4.25}$$

Solving equation (4.25) results in two coupled nonlinear equations determining the parameters α and γ [31]:

$$\alpha = 2\,\gamma \sum_{l=0}^{\infty} \frac{B_l}{\Gamma_l + \gamma}, \tag{4.26}$$

$$0 = \sum_{l=0}^{\infty} \frac{B_l}{\Gamma_l + \gamma} \left(\frac{1}{\Gamma_l + \gamma} - \frac{1}{2\,\gamma} \right). \tag{4.27}$$

Assuming $\gamma = D\, q^2$ and rearranging equation (4.27) yields:

$$\sum_{l=0}^{\infty} B_l(q)\, \frac{l\,(l+1)\, D_r + q^2\, (D_t - D)}{\left[l\,(l+1)\, D_r + q^2\, (D_t + D)\right]^2} = 0. \tag{4.28}$$

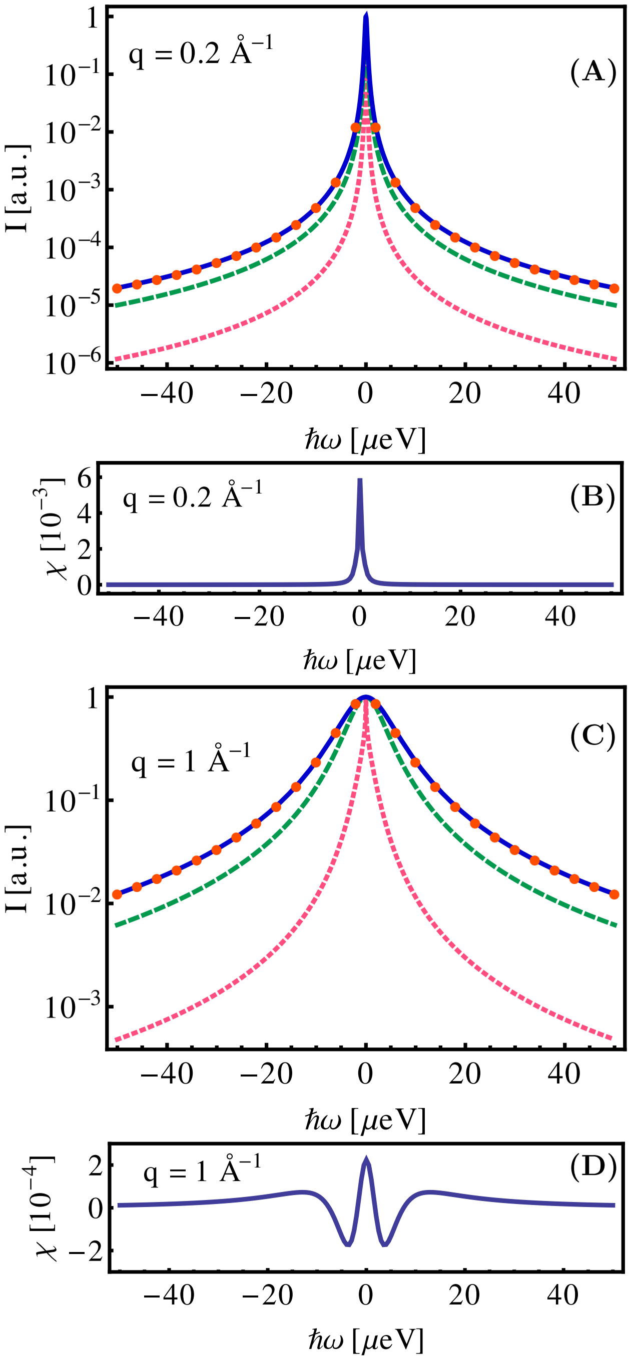

Figure 4.7: (A) and (C): Incoherent scattering function $\mathcal{S}_{\mathrm{inc}}^{\mathrm{TR}}(q,\omega)$ of a hypothetical diffusing particle of radius $r = 36\,\text{Å}$ at $q = 0.2\,\text{Å}^{-1}$ (A) and $q = 1\,\text{Å}^{-1}$ (C), respectively (circles). The translational and rotational diffusion coefficients are $D_t = 6\,\text{Å}^2/\mathrm{ns}$ and $D_r = 3.1 \cdot 10^{-3}\,\mathrm{ns}^{-1}$, respectively, for both (A) and (C), corresponding to BSA at room temperature in water. The dark blue solid line is a Lorentzian function fitted to $\mathcal{S}_{\mathrm{inc}}^{\mathrm{TR}}(q,\omega)$. The green dashed line and the pink short-dashed line are the incoherent scattering functions $\mathcal{S}_{\mathrm{inc}}^{\mathrm{T}}(q,\omega)$ and $\mathcal{S}_{\mathrm{inc}}^{\mathrm{R}}(q,\omega)$ respectively. Note that the three functions were normalized to the respective maxima. The residuals χ resulting from the fit are shown below the spectra ((B) and (D), respectively). (Figure rendered by Dr. Felix Roosen-Runge using *Mathematica*.)

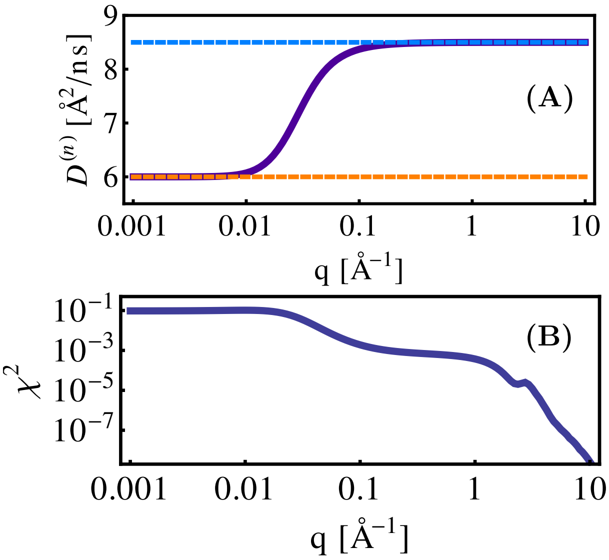

Figure 4.8: (A): General apparent diffusion coefficient $D^{(n)} = D(q, D_t, D_r)$ of a hypothetical diffusing particle with the same parameters as in figure 4.7 (solid line). For the calculation the sum in equation (4.31) has been truncated at $n = 550$, since convergence was sufficient. We observe that for $q \to 0$, $D \approx D_t$ (lower dashed line) and for $q \to \infty$, $D_r = \text{const.}$, and, thus, $D = \text{const.}$ (upper dashed line). (B): χ^2 of the fit of a Lorentzian function to $\mathcal{S}_{\text{inc}}^{\text{TR}}(q,\omega)$ as a function of q. (Figure rendered by Dr. Felix Roosen-Runge using *Mathematica*, part (A) from [31].)

We now notice that $B_l(q)$ strongly decays for $l > q\,R$, with $R = \sup\{r, \rho_H(r) \neq 0\}$, and therefore approximate equation (4.28) by a finite sum, thereby introducing the sequence $D^{(n)}\,(q, D_t, D_r)$ [31]:

$$\sum_{l=0}^{n} B_l(q)\,\frac{l\,(l+1)\,D_r + q^2\,\left(D_t - D^{(n)}\right)}{\left[l\,(l+1)\,D_r + q^2\,\left(D_t + D^{(n)}\right)\right]^2} = 0. \tag{4.29}$$

Figure 4.7 shows $\mathcal{S}_{\text{inc}}^{\text{TR}}(q,\omega)$ for a hypothetical particle of radius $r_h = 36\,\text{Å}$ (circles) as well as the Lorentzian function $\mathscr{L}(\gamma,\omega)$ (dark blue solid line) and the two incoherent scattering functions $\mathcal{S}_{\text{inc}}^{\text{T}}(q,\omega)$ (green dashed lines) and $\mathcal{S}_{\text{inc}}^{\text{R}}(q,\omega)$ (pink short-dashed lines) for $q = 0.2$ and $1\,\text{Å}^{-1}$. Below the spectra, the residuals $\chi = \mathcal{S}_{\text{inc}}^{\text{TR}}(q,\omega) - \alpha\mathscr{L}(\gamma,\omega)$ of the fit in equation (4.25) as a function of $\hbar\omega$ confirm the goodness of the fit: a small, narrow peak centered in $\hbar\omega = 0$ at $q = 0.2\,\text{Å}^{-1}$ becomes a broader oscillation, but with even smaller amplitude, at $q = 1\,\text{Å}^{-1}$. Also χ^2 as a function of q (figure 4.8(B)) corroborates the validity of the fit with a single Lorentzian function, which becomes increasingly precise at higher q. $D^{(n)}\,(q, D_t, D_r)$ obtained from equation (4.29) with $n = 550$ for the same particle as before is shown in figure 4.8(A). We observe that $D^{(n)}\,(q, D_t, D_r)$ starts at D_t for $q = 0$ and converges rapidly to a constant value, such that in the q-range $0.2\,\text{Å}^{-1} \lesssim q \leqslant 2\ \text{Å}^{-1}$ accessible by backscattering experiments we can safely assume:

$$D\,(D_t, D_r) = \lim_{n\to\infty} D^{(n)}\,(q, D_t, D_r) = \text{const}\,. \tag{4.30}$$

Thus, equation (4.28) can be approximated by

$$\sum_{l=0}^{n} B_l(q) \frac{D_r l(l+1) + (D_t - D)q^2}{[D_r l(l+1) + (D_t + D)q^2]^2} = 0\,, \tag{4.31}$$

where n must be sufficiently larger than $q\,R$. The sum in equation 4.31 can be truncated at $n = 2qR$, since the spherical Bessel function of first kind $j_l(x)$, and similarly $B_l(q)$, decays fast for $n > x$, as follows:

$$j_l(x) \leqslant \sqrt{\pi} \frac{x^l \sqrt{\pi}}{2^{l+1}\Gamma[l + 3/2]} < \frac{x^l \sqrt{\pi}}{2^{l+1} l!}\ . \tag{4.32}$$

Finally, to solve the implicit relation, equation (4.31), we assume that D_r obeys the colloid model for the rotational diffusion [38]

$$D_r(\varphi) = D_{r,0}(1 - 1.3\,\varphi^2), \tag{4.33}$$

where $D_{r,0}$ is the rotational diffusion coefficient in the dilute limit. In this way, we obtain a method to separate $D_r(\varphi)$ and $D_t(\varphi)$ from the observable quantity $D(\varphi)$ based solely on the assumption that the colloid model for the rotational diffusion is valid, which is a rather robust assumption in the short-time limit where the angular displacement of a protein is of the order of only a small fraction of a full rotation and therefore its exact shape is of minor importance. We observe that in the q-range covered by IN16B and BASIS, the q-dependence of $\mathcal{S}_{\mathrm{inc}}^{\mathrm{TR}}(q,\omega)$ due to the rotational diffusion of a typical protein can be neglected (figure 4.8(A)).

With this Section, we conclude the discussion of all the steps required for the sample preparation and the data analysis.

The next Section is concerned with the details of the instruments used for our experiments.

4.4 Instruments

In this Section, we will present some components commonly employed in the design of neutron spectrometers. Hereto, we mainly refer to Refs. [177] and [178]. Subsequently, the neutron backscattering spectrometers, BASIS [171, 174] and IN16B [171], employed to gather the data presented in Chapters 5 and 6-8 will be described. In doing so, we will also briefly explain the basics of neutron production for research purposes, because of the crucial role of the neutron source in the construction of efficient instruments.

4.4.1 Common Concepts of Neutron Instruments

High-Flux Neutron Sources

Neutron sources are either natural, or artificial. Natural sources include rocks containing uranium, radon gas and cosmic ray spallation occurring in the atmosphere. Billions of years ago, when large amounts of active uranium had not decayed yet, the existence of natural nuclear fission reactors was possible. The Oklo natural reactor, for example, was active about 1.7 billion years ago in what is now known as Gabon, Africa [179]. Nowadays, the flux of natural neutron sources is however too low to perform experiments in a reasonable time. Therefore, high flux neutron sources need dedicated facilities and typically supply numerous instruments at the same time.

There exist two kinds of high-flux neutron sources, that is nuclear reactors and spallation neutron sources, which exploit different nuclear reactions. The way neutrons are produced affects the beam characteristics, and particularly its time structure. In Section 4.4.3, we will briefly describe the neutron production *via* nuclear spallation. The production of neutrons in a nuclear reactor will be discussed shortly in Section 4.4.4.

Neutron Moderator

Directly after their generation, both spallation and fission neutrons are too fast (the average energy is on the order of 2 MeV [36, 180]) for most research purposes. In order to obtain a neutron wavelength range suitable for experiments (most often on the atomic and molecular length scale), neutrons exiting the target or the core are moderated, i.e. they are passed through a material, typically with medium to large scattering cross-section and low absorption cross-section, the moderator, such that the neutrons easily collide and thermalize with it before being extracted with a nearly Maxwellian energy distribution [35, 178].

Depending on the type of source and desired energy range and time structure of the beam, moderators can be chosen with different characteristics.

Generally, in research reactors, the so-called primary source is composed of the core surrounded by a D_2O moderator. The moderator is maintained close to room temperature, such that, after thermalization, the neutron energy spectrum is rich in thermal neutrons, that is in the energy range from 10 to 100 meV and wavelength range from 2.8 to 0.9 Å [36]. Heavy water is used rather than H_2O to reduce neutron absorption (cf. Table 2.1). Part of the thermalized neutrons return to the core and sustain the nuclear fission in the fuel element while a small fraction of the produced thermal neutrons is collected by the beam guides. Additional moderators may be placed after the primary source, if hot, cold or ultra-cold neutrons are needed [178] (see also Sections 4.4.3 and 4.4.4).

Pulsed spallation sources do not need reflected neutrons to maintain the reaction, and can therefore employ small moderators, in which the duration of the moderation process is shorter [181]. Thereby, the pulsed structure of the beam can be retained and neutrons with a broad energy distribution are generated [181]. As an example, the emission time width of neutrons with a wavelength of 6.3 Å is about 60 μs for the moderator in front of the Beamline 2 at the SNS leading to BASIS [174].

Neutron Guides

In order to deliver the moderated neutrons to the instruments, neutron guides are employed. A neutron guide is a hollow tube constituted by an internal substrate (typically glass, silicon wafers or aluminum) and a nickel or a supermirror[2] coating [177, 178]. Only those neutrons reaching the inner surface with an glancing angle smaller than the critical angle $\theta_c = \lambda\sqrt{n\,b/\pi}$ (where n is the atomic density and b denotes the coherent scattering length, cf. Section 2.4) are totally reflected and propagate through the beam guide with very little loss [177, 182]. The specular reflectivity is between 98.5 and 99 % for nickel guides. For supermirror guides, at the critical θ of nickel θ_c(Ni) the reflectivity can also reach 98 % and is still above 90 % at the much higher θ_c of the supermirror [177].

Neutron guides can reach lengths of more than 100 m and can be straight or typically curved with a radius of curvature from 10 m to 30 km [178] needed e.g. to suppress the direct line of sight to γ-radiation from the source, to filter away small wavelengths λ, or to allow a sufficiently large flight path to produce the desired time structure of the beam, requiring to account for the gravitational force acting on neutrons. Moreover, the guide curvature, together with focusing optics such as mosaic graphite crystal deflectors, helps focusing the beam from the typical cross-section at the reactor end of $12 \times 6\,\mathrm{cm}^2$ to the typical beam size at the sample of $3 \times 3\,\mathrm{cm}^2$.

Disk Choppers

Choppers are devices that take advantage of the neutron time of flight to make a selection on the transported neutrons [177]. The two main types of choppers used in neutron instruments are disk and Fermi choppers. Fermi choppers will not be discussed here as they are not part of either of the instruments described below. Further information can be found, for instance, in Refs. [177] and [183] .

Disk choppers serve either to pulse the neutron beam, or to pulse and monochromatize it, or to reduce the background due to the overlapping of the direct and scattered beams. They are large disks made of a neutron absorbing material with one or more empty or neutron-transparent slits (see Figure 4.9). The choppers are placed along the beam guides and rotate about an axis that is parallel to the neutron beam at speeds up to 20000 rpm. At every turn, the beam is stopped by the chopper until the slit reaches the guide cavity and neutrons are free to pass.

---

[2] A supermirror is a Ni-Ti multilayer with varying stacking (the layer thickness is smaller close to the substrate), with a higher critical angle than a normal mirror.

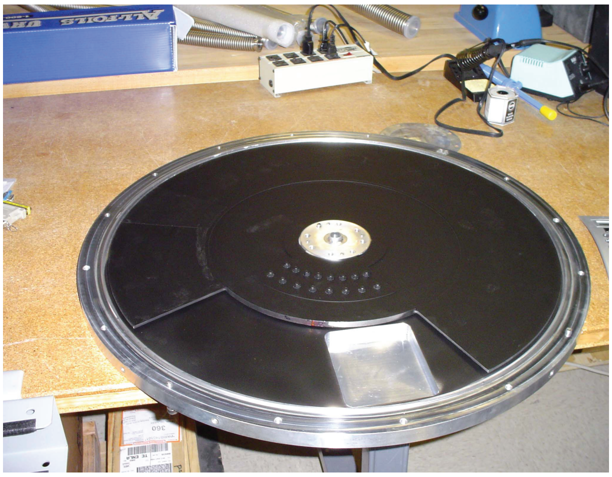

Figure 4.9: One of the BASIS choppers with the cover plate underneath. The aluminum (neutron-transparent) window at the position of the neutron guide is visible at the front. Figure from Ref. [174]

Therefore, one chopper can turn a continuous beam into a pulsed beam (at the expense of the neutron flux).

A second chopper placed at a well-defined distance and rotating with an optimized phase shift relative to the first one can be used to monochromate the beam: only those neutrons having the right velocity (and thus energy) to reach the second chopper while in the open position will pass through, so that after the second chopper the beam is composed of monochromated pulses. More than two choppers can be employed to avoid frame overlap (i.e. suppression of higher orders) of the incident and scattered beams.

Finally, choppers are also employed for the phase-space transformation technique presented in Section 4.4.4.

Monochromators

Several techniques require the neutron beam to be monochromated along its path to the detector. To this purpose, different components may be employed.

First, as mentioned above, Fermi choppers and a sequence of disk choppers may be used to monochromate the beam by exploiting the neutron flight time.

In addition to that, Bragg reflection from crystals with the appropriate lattice spacing can be used to select a well-defined wavelength band from a white beam. Examples of materials used for crystal monochromators are Si, Ge, Cu, Zn [177].

Analyzer Crystals

For certain techniques, notably those measuring inelastic neutron scattering spectra, it is crucial to determine the energy of the detected neutrons. Since energy-dispersive detectors do not exist for neutrons, such a determination is carried out by indirect means. In particular, in neutron backscattering, this requires a specific wavelength of the scattered beam to be selected (i.e. after the interaction with the sample; see Section 4.4.2). Such a selection is simply achieved by placing a monochromator crystal along the path of the scattered neutrons. Monochromator crystals selecting a wavelength of the scattered neutrons are known as analyzer crystals.

Neutron Detectors

This and the next two paragraphs are mainly based on Refs. [184] and [185], unless otherwise stated.

There exist numerous types of neutron detectors, all based on the measurement of electric currents. Since neutrons are obviously lacking an electric charge and do not interact directly with the electrons in matter, they can be detected only with indirect methods. The measured electrical signal is in fact generated when the interaction of neutrons with various nuclei leads to the release of charged particles.

Such interactions can be of two types. In the first, the neutron is scattered by a light nucleus, such as hydrogen or helium, to which some of the neutron energy is transferred. If the transferred energy is sufficiently high, the recoiling nucleus ionizes the surrounding material.

Under other circumstances, neutrons can cause a nuclear reaction, which in turn produces charged particles.

The most common types of detectors are gas-filled proportional counters, scintillators, fission chambers and ^{10}B-lined chambers. In particular, the instruments used in this work employ ^{3}He gas-filled counters, which will be described below. A detailed explanation of the design and principles of the other types of detectors can be found in Ref. [184] and references therein.

Importantly, there exist no energy-dispersive neutron detectors; the energy of the detected neutrons must be therefore quantified e.g. with time-of-flight techniques making use of choppers, backscattering (cf. Section 4.4.2) and triple-axis spectroscopy combining monochromators and analyzers, or also with spin-echo techniques relying on the spin-echo arising from the precession of neutron spins in magnetic fields.

^{3}He single detectors and ^{3}He position-sensitive detectors employed in the backscattering spectrometer IN16B are presented below.

^{3}He Single Detector (SD) A ^{3}He single detector is essentially a metal cylinder with typical wall thickness of about 0.5 mm and diameter typically ranging from 1.25 to 2.54 cm. Aluminum is the most widely used material for their fabrication because of its very low neutron absorption, but in some cases also stainless steel is employed [184].

In the center of the cylinder, a 0.03-mm-thick gold-plated tungsten wire is held in place by ceramic rings insulating it from the cylinder walls. In most cases, a voltage between 1200 and 1800 V is applied between the walls and the wire, which is connected at one end to the electric circuit and measurement devices. As an example, a 2.54-cm-diameter cylinder filled with ^{3}He gas at 4 atm, yields a 77% efficiency for thermal neutrons ($E \sim$25 meV) [184].

In order for a current to be detected the incoming neutron must break one ^{3}He nucleus into a tritium nucleus, ^{3}H, and a proton, ^{1}H, with total energy of 765 keV:

$$^{3}\mathrm{He} \ + \ \mathrm{n} \rightarrow \ ^{3}\mathrm{H} \ + \ ^{1}\mathrm{H} \ + \ 765 \ \mathrm{keV} \ .$$

After the nuclear reaction takes place, the charged particles ionize and excite the atoms along their path. Approximately 30 eV are needed for the creation of an ion pair. Therefore, the maximum number of ion pairs produced after one neutron absorption is about 25000, corresponding to approximately 8×10^{-15} C of total positive and negative charge released. These charges move then to the cathode or anode respectively, and a current is detected. Given the high applied voltage, the primary electrons can trigger an avalanche ionization by gaining sufficient energy to ionize other gas molecules (secondary ionization) and produce secondary electrons, which can in turn gain sufficient energy to ionize more molecules, and so on, up to amplification factors on the order of 10^{10}.

1D ^{3}He Position-Sensitive Detector (PSD) ^{3}He position-sensitive detectors are based on the same principle as SDs but are usually operated at a lower voltage than the SD, in the range from 200 to 800 V, known as proportional region. In such a voltage range, the avalanche ionization does not reach the saturation of generated secondary electrons, which allows to estimate the neutron interaction point with a much better accuracy. A ^{3}He one-dimensional PSD is analogous to the SD, besides the fact that the wire inside the gas-filled cylinder is connected at both ends to the electric circuit leading to the measurement device. The position of a neutron absorption along the cylinder can be determined by comparing the rise times for the pulses that come out at each end of the wire [186].

Primary and Secondary Spectrometer

Neutron spectrometers can be conceptually divided in two parts. The first, called primary spectrometer, is composed of all the elements leading from the moderator to the sample. Essentially, it includes the beam guide and all those components, such as choppers and velocity selectors, needed to obtain a neutron beam with characteristics suitable for the experiment.

When the beam meets the requirements for a given instrument, it enters the secondary spectrometer, where it interacts with the sample and, eventually, is detected. The secondary spectrometer includes the sample environment, possibly collimators and analyzer crystals and the detectors.

4.4.2 Principle of a Backscattering Spectrometer

Backscattering spectroscopy is a technique measuring the quasi-elastic spectrum of a sample i.e. small energy losses or gains – typically ranging from $\sim$ 1 to 100 μeV – of the neutrons scattered by the atoms in the sample. The theory of quasi-elastic neutron scattering (QENS) was presented in Section 2.5. In this paragraph we explain the principle of a backscattering spectrometer.

The setup of a backscattering spectrometer is best explained by following a neutron along its path to the detector. A schematic representation of a standard backscattering spectrometer is shown in Figure 4.10.

(i) First, the beam is prepared such that, its time-integrated energy spectrum is in a range $E_0 \pm \Delta E$, where E_0 is the energy selected by the analyzer crystals (i.e. the energy a neutron

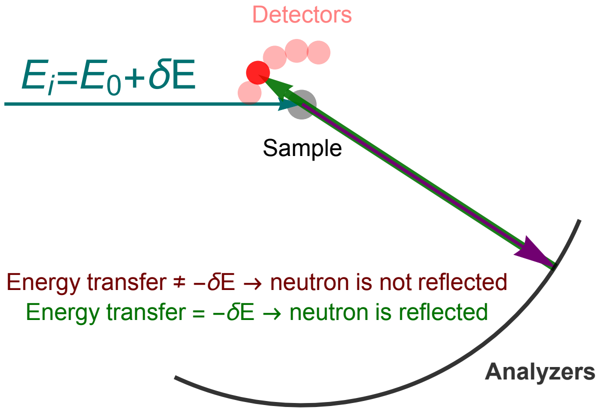
Detectors
E_i=E_0+δE
Sample
Energy transfer ≠ −δE → neutron is not reflected
Energy transfer = −δE → neutron is reflected
Analyzers

Figure 4.10: Schematic of the principle of a backscattering spectrometer. In the example, a neutron with energy $E_0 + \delta E$ is delivered to the sample. After scattering, if the energy transfer equals $-\delta E$ the neutron is reflected by the analyzers and detected; if the energy transfer differs from $-\delta E$ the neutron is not reflected and is usually absorbed by absorbing material placed behind the analyzers. The thickness of the sample is chosen such that the probability for a neutron to be scattered once is $\sim 10\%$ and that of being scattered twice is hence $\sim 1\%$.

must have in order to be reflected by the analyzer, cf. Section 4.4.1), and $\pm\Delta E$ defines the so-called dynamic range. An additional crucial feature of the beam is its time structure: neutrons with different energies must reach the sample at different, well-known times. This is achieved in different ways at BASIS and IN16B and will be explained in Sections 4.4.3 and 4.4.4, respectively. Typical ΔE for backscattering spectrometers range from $\sim 10 - 100\,\mu$eV.

(ii) When reaching the sample, some neutrons may be absorbed by the sample itself, and some others may be scattered in different directions. The remainder will be transmitted and absorbed by an absorbing material placed behind the sample, the beamstop. In typical experiments, the transmitted intensity amounts to $\geqslant 90\%$ of the incoming beam, while the scattered intensity is $\leqslant 10\%$, which also maintains the multiple scattering probability to $\leqslant 1\%$. After scattering, neutrons may have changed the wavevector $\mathbf{k_f} = \mathbf{k_i} + \mathbf{q}$ and the energy $E_f = E_i + \delta E$ (see Section 2.4).

(iii) The scattered neutrons reach the analyzer crystals. Only the neutrons with energy $E_f = E_0$ are reflected back (backscattered), towards the detectors situated behind or close to the sample, and are eventually detected. The backscattering condition is chosen because for Bragg angles close to 90° one can achieve with relaxed collimation a sharp energy resolution while maintaining a reasonable count rate [171]. In fact, by differentiation of the Bragg law, the contribution to the energy resolution arising from a backscattering analyzer yields

$$\frac{\delta E}{E} = \frac{\delta d}{d} + \cot(\theta)\,\delta\theta\,, \tag{4.34}$$

where d denotes the lattice interplanar distance. Hence, the highest energy resolution is obtained for $\theta = 90^\circ$, around which the contribution of the beam divergence is minimum.

The backscattering technique relies on the following requirements and concepts:

1. The energy of the neutrons reaching the sample position is well-defined and known (indirectly) at every moment. In other words, it is known that at a time t_0 the neutrons reaching the sample have an energy E_0 and at a time $t_1 = t_0 + \delta t$ the neutrons with an energy $E_1 = E_0 - \delta E$ have arrived to the sample position. This can be achieved in different ways. In the following Sections we will describe the methods used for BASIS and IN16B.

2. Only the neutrons reflected back by the analyzers are detected, and the analyzers – in the ideal case– only reflect neutrons with a given energy E_0 defined by the crystal lattice as predicted by the Bragg law. This means that a neutron reaching the sample with any energy must gain or lose in the scattering event exactly an energy such that the *final* energy matches the one defined by the analyzer properties, in order to be detected.

3. The sample-to-analyzer and analyzer-to-detector distance is well known and is the same for every detected neutron.

It follows from 2. and 3. that, since after scattering all the detected neutrons travel the same distance at the same velocity, it takes them the same time to reach the detector after the interaction with the sample. The energy of the detected neutrons can be therefore easily calculated: knowing the energy of the neutrons at the sample at a given time (as requested by 1.), the neutrons detected at that time plus the sample-analyzer-detector flight time will have the same energy. Thus, counting the neutrons as a function of time allows the acquisition of the energy spectra.

4.4.3 The Backscattering Spectrometer BASIS at the ORNL Spallation Neutron Source

The measurements reported in Chapters 7 and 8 were performed at the backscattering spectrometer BASIS [174] at the spallation neutron source (SNS) of the Oak Ridge National Laboratory (ORNL). At the SNS, the neutrons are produced in short pulses by nuclear spallation of target nuclei. They are subsequently moderated, guided to the sample placed in the secondary spectrometer, and finally detected. In the following, the SNS and BASIS will be described in further detail, mainly referring to Refs. [174, 187–189].

The Spallation Neutron Source (SNS)

Neutron production at the SNS is achieved in several steps. First, H^- ions are provided by an ion source. These are then bunched into pulses of 645 ns duration with 300 ns gaps and accelerated up to 2.5 MeV prior to being delivered to a sequence of three linear accelerators (linac) [189].

The drift-tube linac accelerates the beam to 87 MeV and is followed by a coupled-cavity linac accelerating the beam to 186 MeV [189]. Both are made of copper and operate at room temperature. In order to further accelerate the ions up to 1 GeV, a superconducting linac is employed. In this linac, Niobium cavities are cooled with liquid helium to an operating temperature of 2 K [187].

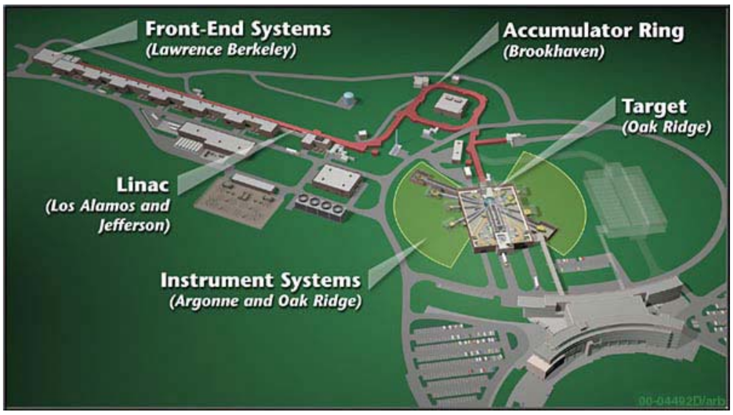

Figure 4.11: Three-dimensional scheme of the Spallation Neutron Source facility. Ions produced at the front-end system are accelerated in the linac, at the end of which protons are produced and stored in the accumulator ring. When the a proton bunch is ready, it is directed to the target, where neutrons are produced by spallation and delivered to the instruments. Figure created by John Jordan, Oak Ridge National Laboratory [190].

At the end of the superconducting linac, the beam is passed through a stripper foil, which strips off the ion's electrons, thus producing protons [187]. The protons are subsequently injected into an accumulator ring (see Figure 4.11), where they circulate and accumulate about 1200 pulses. When a bunch has gathered a sufficient amount of protons, it is extracted from the ring in a pulse less than 10^{-6} s in duration and 60 Hz frequency, and is delivered to a mercury target [191]. The SNS is hence a so-called short-pulse target station.

When the beam reaches the target, the protons hit the nuclei of mercury atoms with a kinetic energy much higher than the binding energy between their nucleons. In a semi-classical picture, the impact triggers a cascade of collisions between the nucleons inside the nucleus, thus bringing it to a highly exited state [178]. The excess energy is expelled by evaporation of 20 to 30 neutrons from the nucleus, as well as by the emission of γ radiation and some protons. Some of the escaped particles can then trigger the cascade in other target nuclei.

In order to obtain a suitable neutron wavelength range for experiments, neutrons are then passed through a moderator (see Section 4.4.1). On the beamline 2 at ORNL SNS, leading to BASIS, a supercritical hydrogen moderator is employed [174].

After being moderated, the pulsed neutrons are guided into beam guides to the instruments. The path of the neutrons from the source to the sample and BASIS detectors is described in the following paragraph.

The Time-of-Flight Backscattering Silicon Spectrometer BASIS

BASIS is a so-called inverted time-of-flight backscattering spectrometer ideally adapted to the time-structure of the short-pulse target station.

Given the pulsed nature of the neutron beam generated by the SNS, the energy of neutrons with known mass m can be conveniently determined from the time t needed for a neutron to travel over a known distance L. Relativistic corrections to the laws of motion for thermal and cold neutrons can be safely neglected, such that

$$E_{\text{kin}} = \frac{1}{2}\, m\, v^2 = \frac{1}{2}\, m \left(\frac{L}{t}\right)^2 , \tag{4.35}$$

where v is the neutron velocity. Thus, knowing the length of the path from the source to the detector, and measuring the time elapsed between the production of a bunch of neutrons and their detection, the energy of the neutrons can be easily calculated (as explained in Section 4.4.2, the time needed to cover the sample-analyzer-detector path is ideally the same for every detected neutron).

The construction of BASIS as a time-of-flight spectrometer is therefore a clever optimization to the pulsed structure of the neutron beam, allowing to exploit the highest possible neutron flux.

However, BASIS is a backscattering spectrometer, meaning that, in the secondary spectrometer, analyzer crystals reflect the neutrons at a given energy back to the detectors.

In general, in a backscattering time-of-flight instrument, the energy resolution can be estimated by [174, 182]

$$\delta E = 2\sqrt{\delta E_p^2 + \delta E_s^2} \tag{4.36}$$

where δE is intended as full width at half maximum of a Lorentzian-shaped resolution function, and δE_p and δE_s represent the contributions of the primary and of the secondary spectrometer, respectively.

The resolution of the primary spectrometer δE_p, reflects the uncertainty on the flight path length L_i and time t_i, from the moderator to the sample [174]:

$$\delta E_p = E_i \sqrt{\left(\frac{\delta L_i}{L_i}\right)^2 + \left(\frac{\delta t_0}{t_i}\right)^2} , \tag{4.37}$$

where E_i is the energy of the incident neutron, δt_0 is the moderator emission time at a specific wavelength, and δL_i is the path length uncertainty.

The resolution of the secondary spectrometer δE_s in equation (4.36) can be estimated by [174]:

$$\delta E_s = \sqrt{E_i^2 \left(\frac{\delta t_f}{t_i}\right)^2 + E_f^2 \left((\cot\theta\ \delta\theta)^2 + \left(\frac{\delta d}{d}\right)^2\right)} . \tag{4.38}$$

Herein, the first term under the square root accounts for the uncertainty on the time t_f needed for a neutron to travel from the sample to the analyzer and back to the detector, while the second term derives from the differentiation of the Bragg law with the scattering angle θ and the spacing d (cf. equation (4.34)).

Combining equations (4.36), (4.37) and (4.38) one can notice that, in order to improve the energy resolution, L_i must be reasonably large. At BASIS, $L_i = 84\,\text{m}$, which ensures $\delta E_p \sim 1\mu\text{eV}$, while keeping low neutron losses along the path. $\delta E_p > \delta E_s$ for $\theta = 90°$, i.e. in perfect backscattering geometry. Relaxing the backscattering condition and adopting a near-backscattering geometry by setting the Si(111) analyzer crystals at a Bragg angle of 88° allows to match the secondary to the primary spectrometer resolution. Thereby, the resolution is only slightly worsened, while significantly increasing the rate of the detected neutrons.

Due to the instrument characteristics, the energy resolution of BASIS is non-Gaussian and non-symmetric, with a FWHM of $\sim 3.5\mu$eV in the configuration with Si(111) analyzers [174]. Thanks to the time-of-flight setup, BASIS can easily reach the large dynamic range $-100\,\mu\text{eV} < \hbar\omega < 100\,\mu\text{eV}$. Hence, the accessible timescale τ can be estimated as $40\,\text{ps} \lesssim \tau = 2\pi\hbar/\Delta E \lesssim 1\,\text{ns}$. The probed length scale $l = 2\pi/q$ is set to $25\ \text{Å} \geqslant l \geqslant 3.22\ \text{Å}$ by the q-range $0.25\ \text{Å}^{-1} \leqslant q \leqslant 1.95\ \text{Å}^{-1}$.

4.4.4 The Backscattering Spectrometer IN16B at the ILL Reactor

The ILL Nuclear Reactor

In nuclear reactors neutrons are produced by nuclear fission. In a fission reaction a nucleus captures a neutron and becomes unstable. In a semi-classical picture, the neutron capture causes oscillations of the nucleus, which eventually lead to the splitting into smaller nuclei and the emission of neutrons and other radiation.

At the ILL, as in many research nuclear reactors, fuel elements of uranium highly enriched in the fissile U-235 isotope are employed. The ILL reactor is, with a full power of 58 MW generated by a single fuel element (containing about 9 kg of U-235), the brightest continuous thermal source for scientific purposes. As a consequence of the production technique, the flux of neutrons delivered to the neutron guides is continuous, i.e. it has no time structure.

In average, the fission of one uranium atom delivers 2.5 fast neutrons. The neutrons leaving the core are moderated with D_2O at 47°C. Some of the thermal neutrons are then collected by the beam tubes at about 40 cm from the center of the core, where the integrated flux of equilibrated neutrons has a maximum of $1.5 \times 10^{15}\,\text{n}\,\text{cm}^{-2}\,\text{s}^{-1}$, and led to the instruments [36]. Other neutrons are further moderated to colder temperatures before being delivered to the instruments, as in the case of IN16B. The cold source is placed in the region of the thermal flux maximum and consists of an aluminum cylinder with a diameter of 210 mm with two elliptical cavities containing about 6 l of boiling D_2 at $\sim 25\,\text{K}$ [36, 192].

The Backscattering Spectrometer IN16B

Here, we refer to the standard configuration of IN16B employing Si(111) monochromator and analyzer crystals, as used in this thesis.

After extraction from the source, the neutrons travel along the beam guide and reach the last components, which cut out all the energies apart from a narrow range of some $10 - 100\,\mu$eV around a given wavelength. At IN16B, for the time being, these components are a phase-space transformer (PST) and a Doppler monochromator, both of which will be explained below. IN16B is ideally adapted to the continuous neutron source at the ILL, where the use of the Doppler monochromator, combined with other components, allows to maintain a reasonable count rate

Figure 4.12: Photograph of the backscattering spectrometer IN16B at the Institut Laue-Langevin. (Courtesy Serge Claisse, ILL)

while achieving a dynamic range of $\pm\,30\,\mu$eV and a symmetric, Gaussian resolution function with FWHM $\sim 0.9\,\mu$eV. Hence, the timescale τ accessible by IN16B in the described configuration can be estimated as $300\,\mathrm{ps} \lesssim \tau \lesssim 5\,\mathrm{ns}$. The accessible q-range $0.2\ \text{Å}^{-1} \leqslant q \leqslant 2\ \text{Å}^{-1}$ results instead in a probed length scale $l = 2\pi/q$ of $30\ \text{Å} \gtrsim l \gtrsim 3\ \text{Å}$.

The operating principle of a backscattering spectrometer, once the beam is reflected by the Doppler monochromator towards the sample, is described in Section 4.4.2.

As a future development, given that IN16B has a dedicated beam guide and that the entire instrument (primary and secondary spectrometer) is about 140 meters long, a time-of-flight option is planned, employing a series of choppers along the guide, and allowing to reach larger energy transfers (i.e. a broader dynamic range), at the expense of a lower flux and a worse energy resolution (see Section 4.4.3).

In the following, we present the most peculiar components of IN16B in its standard configuration.

The phase-space transformer (PST) At the end of the beam guide dedicated to IN16B, the neutrons are reflected by a fast rotating chopper, the phase-space transformer (PST), with the aim of increasing the flux to the sample [172].

The PST technique is based on a non-relativistic transformation between the laboratory rest frame and the moving frame of a mosaic crystal (at IN16B, a graphite crystal).

The axis of rotation of the PST chopper forms an angle $\theta = 68^\circ$ with the incoming beam on the horizontal plane, such that neutrons hitting the chopper with the energy $E_0 = 2.08\,\mathrm{meV}$ are reflected towards the Doppler monochromator. E_0 is chosen to match the backscattering Bragg condition of a Si(111) crystal. Through the mosaicity of the PST, also neutrons hitting the chopper with energy up to some $100\,\mu$eV away from E_0 are reflected in the same direction [172].

In addition to this, the angular velocity of the chopper is chosen such that it optimally accelerates the neutrons with an energy smaller than E_0, and decelerates those with $E > E_0$, thus "compressing" the neutron energy distribution around E_0. It is clear that, by increasing the fraction of neutrons in the energy range reflected by the Doppler monochromator (see below), the PST increases the flux to the sample. In practice, the employment of the PST chopper at IN16B increases the flux to the sample by a factor between 2.5 and 3 at the expense of an acceptable increase of the beam divergence.

The Doppler monochromator The neutrons arriving from the PST reach the Doppler monochromator, a crystal moving back and forth with a given frequency and, usually, a sine velocity profile. In our experiments, the monochromator was composed of Si(111) single crystals. When not moving, these crystals backscatter neutrons with $E_0 = 2.08\,\mathrm{meV}$. For incoming neutrons, if the monochromator is moving, the effective lattice spacing changes depending on the velocity, due to the Doppler effect. Therefore, by moving the monochromator in a controlled manner, one can select with high accuracy the energy of the neutrons. Obviously, the energy range $E_0 \pm \Delta E$ the Doppler monochromator can reflect is limited by the maximum velocity the monochromator can reach (in both directions along the beam axis). ΔE is often referred to as dynamic range. At present, the most advanced Doppler drive, employed by IN16B, can reach 4.5 m/s, a maximum amplitude of $\pm 75\,\mathrm{mm}$ and a maximum jerk of 300 m/s^3, corresponding to a dynamic range of $\pm 30\,\mu\mathrm{eV}$.

In conclusion, the well-defined time structure and energy distribution of the neutron beam needed for the backscattering technique (cf. Section 4.4.2) is obtained after the reflection by the moving Doppler monochromator.

The remaining path of the neutrons leaving the Doppler monochromator is described in detail in Section 4.4.2.

For the detection of the neutrons, IN16B is equipped with 18 ^{3}He gas tubes (see Section 4.4.1). Two of these are single detectors and are placed at $2\theta \sim 10^\circ$ and $\sim 17^\circ$, that is $q \sim 0.2$ and $0.3\,\text{Å}^{-1}$. The other 16, at angles $2\theta \sim 25^\circ$ to 142°, i.e. $q \sim$0.4 to 1.9 Å^{-1}, are position-sensitive detectors.

Chapter 5

Overview of the Results

In Chapters 2 and 4, the theory of neutron backscattering, and the general procedure for data treatment were presented. In particular, it was mentioned in Sections 2.4 and 2.5 that NBS of proteins in solution yields a Lorentzian-shaped scattering function, corresponding to the quasi-elastic broadening of the elastic line due to diffusive dynamics. As a matter of fact, the different shape of the spectrum of the bare instrumental resolution (Gaussian-shaped, due to the bending of the crystals) compared to the scattering functions describing the physics of the samples (Lorentzian, due to diffusive motions) is one of the advantages of modern NBS, as it allows for a more effective decoupling of the resolution from the sample scattering intensity. Nevertheless, different types of protein dynamics contribute to the broadening of the scattering function, namely the center-of-mass diffusion, the rotational diffusion, and the internal dynamics (cf. Sections 2.6 and 4.3.4). Discerning between them in the scattering function is not trivial, and only few model-free conclusions can be drawn from QENS experiments. Instead, the quantitative analysis of QENS spectra requires in general careful modeling, which is inevitably linked to an evaluation of different assumptions and the related physical interpretation.

Obviously, in our experiments the observables are the scattering function $S(q, \omega)$, the temperature T, the protein concentration c_p and stoichiometric volume fraction φ (c_p and φ are obtained from the mass of the protein powder, and the volume of the solvent, which are easily and directly measurable) and the salt concentration. Other quantities, such as diffusion coefficients and relaxation times are obtained after the application of reasonable, physically justified models. Therefore, in many cases, a physical picture of the studied process is a prerequisite for QENS data analysis. Despite this limitation, the use of Lorentzian functions with HWHM γ to model the quasi-elastic scattering function of a diffusive motion is unquestionable from a theoretical point of view (cf. Sections 2.2.1 and 2.4) and the extraction of the apparent diffusion coefficient D of proteins in D_2O solution is remarkably robust: γ is usually found to increase quadratically with q without any forcing, which clearly indicates that the quasi-elastic broadening is largely produced by a diffusive process of the Fickian type, and D is not strongly affected by the number of Lorentzian functions in the model. Hence, these two parameters – γ and D – constitute, together with the observables, the basis for quantitative investigations of protein dynamics by NBS, and as such they are generally shown first in the presented studies. Moreover, the presence of additional faster dynamics associated with internal motions is routinely observed and reflected by the need of (at least) a second Lorentzian function with HWHM Γ to adequately fit $S(q,\omega)$.

There remain, however, some critical points in the data analysis and interpretation, which are elucidated below.

(i) As first pointed out by Perez et al. [56], both the center-of-mass diffusion D_t and the rotational diffusion D_r contribute to the broadening γ, and hence to D. It is not possible to separate the two contributions to $D = D(D_t, D_r)$ without the prior knowledge of one of the two (in addition to D, which is obtained experimentally, cf. Section 4.3.4) [29,56]. Namely, one needs to assume a value of D_r (D_t) in order to extract D_t (D_r) from the measurements. In previous studies, either the dilute limit rotational diffusion coefficient D_{r0}, or $D_r(\varphi)$ from the theory of colloids were used to obtain $D_t(\varphi)$. Once D_t is extracted, it can in turn be compared with the translational diffusion coefficient expected from the theory of colloid physics. It should be noted that, if on the one hand a rotational diffusion coefficient smaller than D_{r0} should be expected for finite protein concentrations, on the other hand it was observed that, for BSA, the particular choice of $D_r(\varphi)$ has little effect on $D_t(\varphi)$ (within the experimental accuracy) [29]. Moreover, it is important to point out that theoretical expressions for $D_r(\varphi)$ were shown to be valid at least up to $\varphi \approx 0.3$ [38]. At higher φ, the expression may not be strictly valid since higher order contributions to the many-body HI may become important. Furthermore, we note that these theories describe spherical particles. The rotation of non-spherical particles may be affected by HI in a different way due to the occurrence of an additional component of the solvent flow normal to the particle.

(ii) As mentioned in Chapter 3, when quantitatively comparing the experimentally obtained $D_t^{\mathrm{exp}}(\varphi)$ with colloid theories describing the slowing down of the diffusion of spherical particles with increasing φ_t, the volume fraction entering $D_t^{\mathrm{theo}}(\varphi_t)$ needs to be calculated from the stoichiometric volume fraction of the bare protein by accounting for the hydration layers moving with the protein. In this context, we pointed out already in Chapter 3 that data from distinct studies were interpreted in different ways leading to conflicting conclusions, which may be in part due to different assumptions on these hydration layers. In our work, we followed the approach by Roosen-Runge et al. [29], who found that the experimental $D_t^{\mathrm{exp}}(\varphi)$ of BSA agrees quantitatively with the theoretical $D_t^{\mathrm{theo}}(\varphi_t)$, if $\varphi_t = \varphi\,(R_h/R)^3$, where R_h and R denote the hydrodynamic and the dry radius of BSA, respectively.

(iii) At high concentrations, the effective volume fraction may become very large and go beyond the limits where the theory of colloids is well-defined (this may happen even if φ is below such limits). At these volume fractions, the application of expressions from the colloid theory might therefore not be rigorously valid.

(iv) Finally, we note that, although as seen above the extraction of the apparent diffusion coefficient is remarkably robust, systematic errors may affect D, depending on the instrument resolution. Other systematic errors may arise from the calibration of the effective volume fraction, especially through the factor $(R_h/R)^3$. However, diffusion coefficients measured with different resolutions at BASIS in this thesis and at IN16 in previous studies [29] were reasonably consistent. Hence, systematic effects should be rather limited in our studies.

Taking the points above into consideration, it is clear that there remain some open questions, which have just started to be addressed also thanks to the advent of new, improved instruments.

In this thesis, protein dynamics was studied as a function of three parameters: protein concentration, temperature, and the concentration of a multivalent salt (YCl_3). In the following, we summarize the results obtained in this work regarding the influence of the aforementioned parameters on the dynamics of proteins.

5.1 The Effect of Self-Crowding on the Dynamics of γ-Globulin

The influence of the concentration of γ-globulin (IgG) on both its diffusion and internal dynamics was investigated by neutron backscattering. The results of one of the first experiments performed on the new backscattering spectrometer IN16B are presented in Chapter 6 and were published in Ref. [28].

A systematic study was performed by measuring quasi-elastic spectra of solutions of IgG at volume fractions φ ranging from $\sim 6\%$ to $\sim 27\%$. The data were fitted with equation (4.17), where the sum of two Lorentzian functions models the quasi-elastic broadening due to the translation and the rotation of the protein, and that arising from internal motions. From the former component, the translational coefficient D_t was obtained as explained in Section 4.3.4 and in the Appendix A. As in several previous studies (cf. Section 3.11), we observed a decrease of D_t with increasing protein concentration.

Following the successful application of the theory of diffusion of colloidal hard spheres for the description of such a slowing down in BSA suspensions [29], the study presented in Chapter 6 was designed to test whether the same approach could be adopted for IgG, having a strongly branched structure (cf. Section 4.1.3). The comparison between experiment and theory requires the calculation of the effective volume fraction $\varphi_t = \varphi\,(R_h/R)^3$, where the scaling factor $(R_h/R)^3$ accounts for the effective hydrodynamic volume of the protein. The values $R \simeq 39\,\text{Å}$ and $R_h \simeq 55\,\text{Å}$ were obtained for an IgG monomer from HYDROPRO, yielding $R_h/R \simeq 1.4$. With this factor, the agreement of the experimental translational diffusion coefficient $D_t^{\text{exp}}(\varphi)$ with that from the theory of colloids $D_t^{\text{theo}}(\varphi_t)$ obtained from $D(\varphi)$ and $D_r(\varphi)$ was found to be remarkably good, and the discussion and conclusion is carried out consistently. However, the radius R provided by HYDROPRO corresponds to the dry protein volume *plus* the thickness of the hydration layer obtained with 0.3 g H_2O/g protein [151,193,194]. Hence, such a radius does *not* correspond to the dry protein volume. When using the actual dry radius $R \simeq 35.5\,\text{Å}$ without the hydration layer, $R_h/R \simeq 1.55$ and the agreement with the theory is lost, as the theoretical value drops significantly faster than the experimental data. This observation represents a challenge for the modeling of such a flexible protein, while maintaining a consistent physical picture. Since the renormalization of φ requires the cube of R_h/R, φ_t goes quickly beyond the maximum packing fraction and, at the highest concentrations, even beyond 1, which is clearly unphysical. Instead, in order to retrieve a quantitative agreement with the theory of colloids, one has to assume that the effective radius R_{eff} relevant for the hydrodynamic interactions on the accessible timescale lies in the range $R \leqslant R_{\text{eff}} \leqslant R_h$, and more precisely $R_{\text{eff}} \simeq 49.7\,\text{Å}$. From a physical point of view, this may be reasonable to suppose because of the following reasons. (a) As mentioned before, if $R_{\text{eff}} = R_h$, φ_t becomes quickly nonphysically large. In other words, if proteins are considered as hard spheres with a volume defined by their hydrodynamic radius, the maximum fraction $\varphi^{\max}$ of the total volume that can be occupied by these spheres is quickly reached and protein

dynamics should freeze. Nonetheless, $D \neq 0$, and it is observed to continuously decrease even for $\varphi\,(R_h/R)^3 > \varphi^{\max}$, which requires $R_{\text{eff}} < R_h$ to maintain a hard-sphere colloidal picture. (b) R_h is the hydrodynamic radius in the dilute limit. Although in this limit the short- and long-time diffusion coefficients converge to the same value (from which R_h is derived), it could be supposed that, when HI interactions become significant, the thickness of the water layer moving with the protein is smaller, at least in the short-time limit, when the flexibility of the protein domains may effectively reduce the drag. (c) An effective radius smaller than the hydrodynamic radius calculated from a rigid structure may be required to account for the fact that proteins are soft macromolecules and not hard spheres. Such an effect should become significant at high volume fractions [195].
Finally, the dynamics of the subunits of IgG could contribute to the quasi-elastic broadening of the QENS signal and lead to a larger apparent diffusion coefficient [30].

Since it was not clear if in our highly concentrated solutions IgG occurred in the monomeric form, the data were also analyzed assuming the sole presence of dimers, with the values reported in Appendix A. The resulting D_t was found to be inconsistent with the theory of colloids, suggesting that IgG monomers were the main component in the investigated samples.

In addition to the protein self-diffusion, information on the internal dynamics of the protein was self-consistently extracted from the scattering function. The EISF presented in Section 2.6 providing information on the geometry of the confinement of atoms in the protein was modeled by a combination of two types of confinement geometry and a fraction of immobile atoms. The first contribution describes the geometry of H-atoms in methyl groups (-CH_3) and was modeled by jumps between three sites fixed by the known atomic distances in the chemical group. The second, accounting for the average of the geometries of confinement of the remaining mobile H-atoms, was described by a model considering an atom diffusing inside an impermeable sphere. The radius R of the sphere as well as the fraction of immobile atoms were found to be, within the error bars, independent of φ.

The quasi-elastic broadening ascribable to the internal dynamics was modeled by a jump-diffusion model yielding a jump-diffusion coefficient D_j and a residence time τ (cf. Section 2.6). While D_j, as well as the geometrical parameters from the EISF, was constant within the error bars, τ was found to increase with rising volume fraction. This observation suggests a crowding-induced stabilization of the protein conformation.

5.2 The Dynamics of BSA upon Thermal Denaturation

In an attempt to gain a better understanding of the difference of the dynamics of BSA before and after denaturation, aqueous (D_2O) solutions at three protein concentrations (150, 200, and 500 mg/ml) were measured at BASIS at temperatures below and above the denaturation temperature.

Close to room temperature the analysis of the data *via* the conventional two-Lorentzian model yielded a q-dependence of the HWHM Γ_{int} attributed to the internal dynamics consistent with the jump-diffusion model used also in the study on IgG. On BASIS, at temperatures sufficiently close to denaturation, instead, an unusual non-monotonic behavior of $\Gamma_{\text{int}}(q)$ was obtained. Referring to the self-dynamics, such a behavior would suggest that it takes more time for an atom to explore a small volume than a large volume, which is clearly contradictory, and is therefore not consistent with a single process. Hence, the data indicate the occurrence of dynamical processes on at least three time scales.

We speculated that these three processes correspond to global diffusion of the entire protein, backbone dynamics and side-chain dynamics. We therefore applied a model in which the mobile side-chains continuously switch between two diffusive states (cf. Section 2.6.2). In one state the side-chain is blocked with respect to the backbone e.g. due to steric interactions with other side-chains. The backbone is however fluctuating, although at a lower rate, and with it also the bound side-chain. Consequently, in this state, the side-chain undergoes a diffusive motion reflecting that of the backbone. As time passes, an increasing number of local rearrangements takes place, and eventually the side-chain can move rather freely at a higher rate. Hence, considering that most of the detected signal derives from the side-chains, the backbone dynamics is measured only indirectly when the side-chains are in the "blocked state".

The model described above provided a consistent physical picture of the effect of temperature and thermal denaturation on both diffusion and internal dynamics. The short-time self-diffusion of BSA was confirmed to agree well with colloid theory at temperatures below denaturation. After unfolding, the diffusion coefficient dropped, consistent with the formation of a cross-linked protein network suppressing diffusion.

The dynamics of backbone atoms was found to undergo a transition at the denaturation temperature, above which the associated diffusion coefficients increase faster, probably reflecting the unfolding of secondary structure. The diffusion coefficient associated with the side-chains, instead, showed a change on denaturation only at the highest concentration, while at lower concentrations no clear transition was observed. By contrast, the time elapsed before the side-chains switch from one state to the other increased abruptly at the denaturation temperature.

Regarding the geometry of confinement, in addition to the effective radius accessible by the side-chains, a radius associated with the backbone fluctuations was derived from the EISF. The former radius remained constant, within the error bars, in the entire temperature range. This is consistent with the covalent bindings between side-chain atoms strongly influencing the accessible volume. Instead, the temperature dependence of the radius associated with the backbone fluctuations, could be interpreted in terms of atoms sitting in an effective elastic potential landscape. Under this assumption, an effective force constant was obtained and found consistent with literature values from EINS (see Table 3.1). Finally, the number of immobile atoms was observed to decrease with temperature, and the fraction of atoms participating in the "diffusion in a sphere" motion increased significantly at the denaturation temperature, consistent with a higher number of side-chains free to explore a large volume upon unfolding.

Several other hypothesis were made and tested to interpret the data, including the presence of populations of monomers and static clusters, or monomers and dynamic clusters (see Appendix B). Yet, none of these yielded consistent results.

In summary, a change of the pico- to nanosecond dynamics of BSA upon thermal denaturation was observed and a quantitative modeling of the unfolding dynamics in solution was attempted. A drop in the global diffusion was found consistent with the formation of a cross-linked protein network drastically reducing the center-of-mass mobility. A model was proposed to account for the internal dynamics, in accordance to the experimental data, describing the side-chain atoms alternating between a slow and a fast diffusive motion. The former was speculatively identified with the underlying backbone fluctuations. According to such a picture, the model tentatively applied here for the first time can grant access and discernment of the side-chain and the backbone dynamics.

5.3 The Diffusion of BSA in the Presence of the Trivalent Salt YCl_3

In order to understand the effect of the presence of YCl_3 on the dynamics of BSA, we performed systematic QENS measurements at the time-of-flight backscattering spectrometer BASIS at the Oak Ridge National Laboratory (ORNL). The apparent diffusion coefficients $D(c_s, c_p)$ obtained for series at several fixed protein concentrations c_p while increasing the salt concentration c_s were found to drop with rising c_s. Moreover, after plotting $D(c_p, c_s)$ of each salt concentration series normalized by the coefficient $D(c_s = 0, c_p)$ at the same c_p but no salt in solution as a function of c_s/c_p, a remarkably universal behavior was found. In mathematical terms, we found that $D(c_s, c_p) = D(c_s = 0, c_p)\, g(c_s/c_p)$, where $g(c_s/c_p)$ is a scalar function depending on the number of the number of Y^{3+} ions per protein in solution.

Consequently, $g(c_s/c_p)$ combined with the expressions from the theory of colloid mentioned in the previous Section fully characterizes the short-time dynamical properties of the system, at least within the investigated range of c_p and c_s/c_p.

We tried to explain the observation along with two physical pictures. Other more complex models may be successfully employed, nevertheless, we intentionally kept our description as simple as possible.

In a possible scenario, the addition of salt results in increased attractive interactions enhancing fluctuations of the local volume fraction φ. The proteins being locally more densely packed would damp their diffusion, as observed in the experiments. However, for the time being, this picture seems hard to justify for two reasons. (i) We were not able to reproduce the experimental data assuming a unimodal probability distribution of local densities $G(\varphi)$; yet, there is no obvious physical argument legitimizing the assumption of a well-separated bimodal distribution away from a phase separation. Furthermore, (ii) our analysis suggests that even when assuming such a $G(\varphi)$ the amplitude of the fluctuations should depend not solely on c_s/c_p, but rather on both c_s *and* c_p in a very specific manner, such that from non-universally scaling amplitudes a master dynamical behavior can be retrieved.

The second scenario we considered is inspired by the theory of colloidal suspensions of patchy hard spheres [24] (see also Section 2.3). In this picture, Y^{3+} ions are assumed to nearly quantitatively bind to specific sites on the surface of proteins and act as a bridge between them. In this case, the Flory-Stockmeyer theory provides an estimation of the number density distribution of n-clusters, which depends on the binding probability p_b. Hence, a shift of the distribution of the clusters towards larger sizes caused by the addition of salt would result in a slowing-down of the average diffusion measured by NBS.

In order to apply this model to our dynamics data, several assumptions had to be made to simplify the treatment, including that the used distribution of particle sizes does not significantly change the hydrodynamic interactions compared to a monodisperse system. Moreover, we assumed that the formed clusters are rigid. Although such an assumption may seem rather strong, it should be kept in mind that the instrument accesses only up to $\sim 1\,\mathrm{ns}$. On this timescale, clusters may still be stiff and move as a single particle.

Under the aforementioned assumptions, the Flory-Stockmeyer theory could be applied to the experimental data, providing a consistent physical explanation of the observed phenomenon, on condition that p_b, as $D(c_s, c_p)/D(c_s = 0, c_p)$, depends only on c_s/c_p, in line with a quantitative binding of Y^{3+} on the surface of BSA.

This result demonstrates the potential of patchy particle theories for the description of proteins. Moreover, if confirmed, this result could be of interest for tuning protein interactions for a controlled production of self-assembled particles.

Summarizing, a remarkably universal slowing down of the apparent short-time diffusion coefficient of BSA as a function of the number of Y^{3+} ions per protein in solution, c_s/c_p, was observed. The phenomenon could be interpreted in terms of a simplified model inspired by the theory of patchy particles with ion-activated patches. As a consequence of such a model, the observed universal dynamical behavior would be strictly related to the formation of clusters with a size distribution shifting towards larger clusters with increasing c_s/c_p. This is consistent with an almost quantitative binding of Y^{3+} ions on the protein surface in the explored (c_p, c_s)-range.

Chapter 6

The Effect of Self-Crowding on the Dynamics of γ-Globulin

This Chapter reproduces the article [28]:

Diffusion and dynamics of γ-globulin in crowded aqueous solutions. [1]

Marco Grimaldo,[a,b] **Felix Roosen-Runge,**[a] **Fajun Zhang,**[b] **Tilo Seydel,**[a] **Frank Schreiber**[b]

The Journal of Physical Chemistry B **2014** *118*, 7203–7209.

[a] Institut Max von Laue - Paul Langevin (ILL), CS 20156, F-38042 Grenoble, France
[b] Institut für Angewandte Physik, Universität Tübingen, D-72076 Tübingen, Germany

6.1 Abstract

Dynamics in protein solutions is essential for both protein function and cellular processes. The hierarchical complexity of global protein diffusion, side chain diffusion and microscopic motions of chemical groups renders a complete understanding challenging. We present results from quasi-elastic neutron scattering on protein solutions of γ-globulin over a wide range of volume fractions. Translational and rotational diffusion can be self-consistently separated from internal motions. The global diffusion is consistent with predictions for effective spheres, even though the branched molecular shape differs considerably from a colloidal sphere. The internal motions are characterized both geometrically and dynamically, suggesting a picture of methyl rotations and restricted diffusion of side chains. We show that the advent of new neutron spectrometers allows to address current questions including the coupling of intracellular dynamics and protein function.

---

[1] Author contributions: M. G., F. R.-R., T. S., F. Z., F. S. designed research; M. G., F. R.-R., T. S. performed research; M. G. analyzed data; M. G., F. R.-R., T. S., F. Z. and F. S. wrote the paper.

6.2 Introduction

Protein function in cellular processes is strongly influenced by the intracellular environment. The high volume occupancy of macromolecules of roughly 20-40 %, the so-called macromolecular crowding, affects biochemical reaction rates [18], slows down diffusive transport processes, and can cause compaction of protein conformations [196–198]. Recently, several publications have focused on protein dynamics in living cells [10], addressing diffusion of proteins in the nucleoplasm [11], in the mitochondrial lumen [12], and in the cytoplasm [13–16]. Generally, *in vivo* protein dynamics is found to be significantly slower than in dilute protein solutions.

In order to mimic the effect of crowding *in vivo*, several *in vitro* studies have addressed concentrated solutions of one protein (self-crowding), allowing systematic investigation of crowding effects on diffusion as well as a conceptual understanding along colloid theory [41, 123, 124, 199]. Brownian dynamics simulations [200] indicate that a major part of the diffusional slowing down in crowded protein solutions is due to hydrodynamic interactions. In this context, the short-time limit of self-diffusion is of particular interest, since hydrodynamic interactions are established quasi-instantaneously even on larger length scales, while other protein interactions become relevant near the interaction time $\tau_I \approx 400\,\mathrm{ns}$ for medium-sized globular proteins [38]. Recently, the protein self-diffusion on nanosecond time and nanometer length scales in aqueous solution has been found to be consistent with short-time predictions from colloid theory for the model globular protein BSA [29].

The successful modeling of global diffusion is promising for a better understanding of protein internal dynamics on a molecular level and possible effects of crowding. Numerous studies have focused on the protein internal dynamics on the sub-ns time scale – however, mainly in more or less hydrated powders [7, 201–205], since in this case global diffusion does not interfere with the internal dynamics during the data analysis. Only few of them have been performed on protein solutions [56, 96, 121] or *in vivo* [17, 112], but without systematically addressing the effect of crowding.

With the present article we report on a comprehensive study of diffusive dynamics in crowded aqueous γ-globulin protein solutions on a molecular length scale using quasi-elastic neutron spectroscopy. The measured spectra contain contributions from the global rotational D_r and translational D_t diffusion of the entire protein as well as from internal diffusive protein motions, and from the solvent water. We perform a self-consistent separation of these different contributions to quantitatively extract $D_t = D_t(\varphi)$ as well as information on the internal motions, thereby describing a wide range of volume fractions φ to reliably address dynamical effects of crowding. The results are consistent with short-time self-diffusion of the protein center of mass [2] superimposed with geometrically confined internal diffusive motions dominated by methyl rotations and restricted side chain motions.

We have carried out our investigation as one of the first experiments of the recently commissioned neutron backscattering spectrometer IN16B at ILL, Grenoble, with an energy range of $-30\mu\mathrm{eV} \leqslant \hbar\omega \leqslant +30\mu\mathrm{eV}$ at a Gaussian resolution of $0.9\mu\mathrm{eV}$ FWHM and the scattering vectors $0.2\text{Å}^{-1} \leqslant q \leqslant 1.9\text{Å}^{-1}$. IN16B provides an unprecedentedly high neutron flux at this energy resolution and range. We have measured on the native protonated proteins in heavy water (D_2O) solutions in order to reduce the solvent contribution to the measured signal. In this way, the recorded quasi-elastic neutron scattering (QENS) spectra are dominated by the incoherent scattering from the hydrogen ^1H nuclei of the proteins. Thus, to good approximation we obtain the incoherent scattering function $S(q,\omega)$ which, for our system, is proportional to the ensemble-averaged ^1H-single-atom self-correlation function. Importantly, given by the instrument characteristics, we unambiguously access self-diffusion and individual internal motions on nanosecond time scales and nanometer length scales.

---

[2] Provided that the volume fraction assumed for the theoretical D_t is renormalized accounting for additional water molecules diffusing with the protein, as defined by HYDROPRO [151, 193, 194]. See Section 5.1 for further discussion.

The article is organized as follows: In the next Section, we provide further details on the experiment, sample preparation, data reduction, and fits. Subsequently, we present and discuss our results regarding both the translational short-time self-diffusion $D_t(\varphi)$ of γ-globulin in aqueous solution as well as its internal molecular diffusive motions in detail. In the concluding Section, we outline the statements that can presently be made and we also point out possibilities for future continuations.

6.3 Experiments and Methods

Sample preparation. Bovine γ-globulin was purchased from Sigma-Aldrich (purity of 99%, G5009) and used without further purification. The samples at protein concentration $c_p = m_p/V_{D_2O}$ were prepared by dissolving the protein powder with mass m_p in a volume V_{D_2O} of D_2O. After complete dissolution, the solutions were filled in double-walled aluminum cylinders with outer diameter 23 mm and a gap of 0.16 mm, and sealed against vacuum. The volume fraction φ occupied by the bare proteins is given by

$$\varphi = \frac{\vartheta m_p}{V_{D_2O} + \vartheta m_p} , \tag{6.1}$$

where $\vartheta = 0.739$ ml/g is the specific volume of γ-globulin [157]. The samples were prepared to cover a φ-range of $\sim 10 - 28\%$. Using equation (6.1), we assume that the protein hydration shell volume does not depend on the crowding. Such small crowding effects of the hydration shell may occur [206], but it is difficult to quantify them for γ-globulin without a separate comprehensive volumetric study. In order to not introduce further experimental errors, we assume that equation (6.1) is valid with sufficient accuracy.

Quasi-elastic neutron backscattering. The experiments were carried out using the newly commissioned cold neutron backscattering spectrometer IN16B at the Institut Laue-Langevin (ILL) [171], achieving a Gaussian energy resolution of $0.9\,\mu$eV FWHM. The samples were inserted in a standard Orange cryofurnace mounted inside the evacuated secondary spectrometer chamber. The instrument was used with unpolished Silicon(111) crystal monochromator and analyzers and a vertically position-sensitive multidetector (PSD) consisting of 16 ^{3}He detector tubes covering the scattering vector range $0.57\text{Å}^{-1} < q < 1.94\text{Å}^{-1}$. In addition, two small-angle detectors with a slightly lower energy-resolution due to a small angular deviation from backscattering were placed at $q = 0.19\text{Å}^{-1}$ and 0.29Å^{-1}, respectively. The energy transfer $-30\,\mu\text{eV} < \hbar\omega < 30\,\mu\text{eV}$ was achieved in the so-called inverse geometry by Doppler-shifting the incident monochromatic neutrons using an AEROLAS Doppler drive operating with a sinus velocity profile with an amplitude of 75 mm and maximum velocity of 4.5 m/s. The flux at the sample was optimized by the Phase Space Transformer (PST) chopper disk [172] carrying graphite mosaic crystals at its circumference and spinning at 7100 rpm during the experiment, corresponding to a crystal velocity of 243 m/s. For every sample, we measured approximately 4 hours at full energy range, which results in similar or better statistics than when measuring on the predecessor instrument IN16 during 24h.

Measured spectra and fits, modeling of the contribution of D_2O. All data reductions and fits are carried out using MATLAB R2012b. We normalize the measured intensities by the incident neutron flux and detector efficiency, and we subtract the empty can signal from the protein solution spectra. The thus obtained scattering function $S(q,\omega)$ describing the protein solution spectra recorded on IN16B is modeled by the following expression [29]:

$$\begin{aligned} S(q,\omega) = \mathscr{R}\otimes\big\{\beta\,[A_0(q)\mathscr{L}_\gamma(\omega) + (1-A_0(q))\mathscr{L}_{\gamma+\Gamma}(\omega)]\ldots \\ \cdots + \beta_{\mathrm{D_2O}}\mathscr{L}_{\gamma_{\mathrm{D_2O}}}(\omega)\big\}\ . \end{aligned} \tag{6.2}$$

Therein, $\mathscr{L}$ denotes a Lorentzian function and the index to this symbol the respective half-width at half maximum. $\mathscr{R}$ is the nearly perfect Gaussian resolution function of IN16B determined from the spectrum of a Vanadium standard (width 0.9 μeV FWHM). In the fit of equation (6.2) to the IN16B spectra, the linewidths γ and Γ as well as the amplitudes β and A_0 are free to take any positive real value, and their physical meaning will become clear in the Results and Discussion Section. All other parameters are fixed, including $\beta_{\mathrm{D_2O}}$ and $\mathscr{L}_{\gamma_{\mathrm{D_2O}}}(\omega)$ as explained further below. The spectra for the individual q-values are fitted independently, i.e. no q-dependence is imposed on the fits. In the fit algorithm, $\mathscr{R}$ is described analytically by a sum of Gaussian functions, and the convolution $\mathscr{R}\otimes\{...\}$ is carried out analytically using Voigt functions built from $\mathscr{R}$ and $\mathscr{L}_{\{...\}}$. On the energy range $2\Delta\omega_{\mathrm{max}}$ accessible by IN16B, the line broadening $\mathscr{L}_{\gamma_{\mathrm{D_2O}}}(\omega)$ due to the D_2O solvent contribution is not flat, even though the half width at half maximum (HWHM) $\Delta\omega$ of the D_2O spectra with intensity $I_{\mathrm{D_2O}}(\omega)$ is bigger than $\Delta\omega_{\mathrm{max}}$. This may result in systematic uncertainties when subtracting the rescaled D_2O spectra $I^{(\varphi)}_{\mathrm{D_2O}}(q,\omega) = (1-\varphi)I_{\mathrm{D_2O}}(q,\omega)$ from the spectra of the solutions at protein volume fraction φ. In order to self-consistently quantify the contribution of heavy water and simultaneously reduce systematic errors, we combine D_2O measurements performed at the cold neutron time-of-flight spectrometer IN6 (ILL) and at the cold neutron backscattering spectrometer IN16B (see also Supporting Information). IN6 has the advantage of a substantially larger energy range (at the expense of energy resolution) and is thus better suited to measure the fast dynamics of D_2O and model the QENS line width $\gamma_{\mathrm{D_2O}}$ as a function of q^2. The D_2O spectra measured at IN16B and rescaled according to φ are then used to fit the amplitude $\beta_{\mathrm{D_2O}}$ of the modeled D_2O contribution $\mathscr{L}_{\gamma_{\mathrm{D_2O}}}(\omega)$. Finally, $\beta_{\mathrm{D_2O}}\mathscr{L}_{\gamma_{\mathrm{D_2O}}}(\omega)$ is added as a fixed term to equation (6.2), thus eliminating unnecessary free parameters in the fit.

Diffusion coefficients: separation of rotational and translational diffusion. The proteins in solution undergo both translational center-of-mass diffusion and rotational diffusion, which are convoluted in the measured signal, resulting in the observable apparent diffusion coefficient D. The fit parameter γ in equation (6.2) is associated with this apparent diffusion coefficient D of the proteins, as explained further in the following Section. In order to compare the experimental results with existing theories, the extraction of the translational part D_t and the rotational part D_r from D is performed following the method in Ref. [29] based on an implicit relation

$D(\varphi) = D(D_r(\varphi), D_t(\varphi))$ (see also Supporting Information). For this separation, we employ the colloid model for $D_r = D_r(\varphi)$. At the high q explored in our experiment, rotational diffusion contributes to a q-independent apparent diffusion coefficient [29], which enhances the robustness of the separation. The dilute limit translational $D_0 = 3.29\,\text{Å}^2/\text{ns}$ and rotational $D_{r,0} = 0.7 \times 10^{-3}\,\text{ns}^{-1}$ diffusion coefficients, as well as the molecular volume [3] $V_p = 251\,\text{nm}^3$, are calculated via HYDROPRO [151] using the crystal structure of murine immunoglobulin G (IgG) that can be identified with the γ-globulin in our samples except for some negligible amount of other immunoglobulins [154]. D_0 is in very good agreement with recent DLS measurements by Wang et al. [207] yielding $R_h = 55\,\text{Å}$, i.e. $D_0 = 3.3\,\text{Å}^2/\text{ns}$ in D_2O at $T = 295$ K.

6.4 Results and Discussion

6.4.1 Neutron Spectra

The inset of Fig. 6.1 depicts a typical QENS spectrum $S(q, \omega)$ (red circles) which can be well described by equation (6.2) (turquoise solid line). Here, the sum of three Lorentzian functions $\mathscr{L}(\omega)$ models a slower process with line broadening γ (blue dot-dashed line), a convoluted faster process with line broadening $\gamma + \Gamma$ (green dashed line), and the solvent contribution (magenta dotted line) with fixed values for both width γ_{D_2O} and intensity β_{D_2O} (see the previous Section for details on the data reduction and fits, and the Supporting Information for further example spectra). $A_0(q)$ in equation (6.2) is identified with the elastic incoherent structure factor (EISF). We emphasize that the processes occur on well-separated time scales, such that it is possible to distinguish between the different components in the measured spectra.

For the slower process, the relationship $\gamma = Dq^2$ (Fig. 6.1) indicates a simple diffusion with apparent diffusion coefficient $D(\varphi)$. Note that the slight deviation from this law for higher q-values is presumably due to a weakened signal, once the width of $S(q, \omega)$ exceeds the accessible energy range for higher q-values. In order to avoid artifacts, we restrict the fits for $D(\varphi)$ to $q^2 < 1.5\,\text{Å}^{-2}$, where $\gamma = Dq^2$ clearly holds for all samples.

The apparent diffusion coefficients $D(\varphi)$ are shown in the upper part of Fig. 6.2. The increase of φ causes a significant decrease of $D(\varphi)$, consistent with previous studies on bovine serum albumin [29,130]. The lower and higher temperature is used to test the robustness of the analysis against temperature effects, which might cause protein dynamics to exceed the accessible energy range.

6.4.2 Rotational and Translational Diffusion of the Proteins

The normalized translational self-diffusion coefficients $D_t(\varphi)/D_0$ (Fig. 6.2) are determined by the established deconvolution scheme [29] based on the implicit relation $D(\varphi) = D(D_r(\varphi), D_t(\varphi))$ (see the preceding Section on Experiments and Methods). Within this scheme, the proteins are modeled by effective spheres with the hydrodynamic radius of protein monomers as calculated

---

[3] The volume provided by HYDROPRO with $M_w = 157\,\text{kDa}$ and $\vartheta = 0.739\,\text{ml/g}$ contains also one hydration layer, corresponding to 0.3 g H_2O/g protein. Hence, this is not the dry volume of the protein. See Section 5.1 for further discussion.

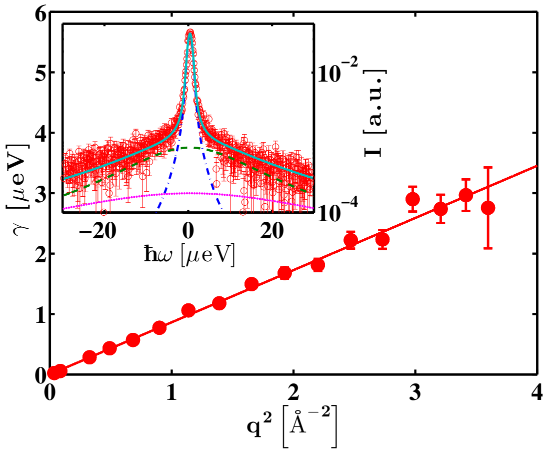

Figure 6.1: Inset: Typical $S(q,\omega)$ (red circles) recorded using cold neutron backscattering for γ-globulin in D_2O ($c_p = 300\,\mathrm{mg/ml}$, $T = 295\,\mathrm{K}$, individual detector at $q = 0.81\,\text{Å}^{-1}$). The lines depict the Lorentzian functions $\mathscr{L}_\gamma(\omega)$ (blue dot-dashed) $\mathscr{L}_{\gamma+\Gamma}(\omega)$ (green dashed) and $\mathscr{L}_{\gamma_{D_2O}}(\omega)$ (magenta dotted) in Eq. (6.2). The turquoise solid line superimposed on the data is the result of the complete fit using Eq. (6.2). Main figure: Fitted γ (red circles) vs. q^2 for the full accessible q-range. The fit $\gamma = Dq^2$ (solid red line) indicates a simple Brownian diffusive behavior. The fit range is restricted to $q^2 < 1.5\,\text{Å}^{-2}$ (see text).

by HYDROPRO [151]. The theoretical prediction for the translational short-time self-diffusion coefficients of these effective spheres (blue solid line) are in very good agreement with the experimental values for γ-globulin (symbols) (figure 6.2, bottom). Thus, the slower process can be identified and accurately modeled with the global self-diffusion of protein molecules. We stress that the dilute limit diffusion coefficient only enters for the normalization to D_0 in Fig. 6.2 and for the rather robust separation of the translational and rotational diffusion. Therefore, an uncertainty in D_0 will not alter the observed trend.

We point out that the data measured at $T = 280\,\mathrm{K}$ (blue triangle) and $T = 310\,\mathrm{K}$ (red square) are perfectly consistent with those measured at $T = 295\,\mathrm{K}$ (circles), thus confirming that the effect of crowding is largely temperature-independent. To consolidate the assumption of a mainly monomeric solution, we repeated the procedure for a hypothetical dimer of γ-globulin (see also Supporting Information). The resulting $D_t(\varphi)/D_0$ from dimers is not consistent with theoretical predictions, suggesting that the data analysis based on monomers is suitable, at least at nanosecond time and nanometer length scales.

We remark that the real protein shape specified by a crystal structure enters the analysis at two points only: first, for the calculation of the hydrodynamic radii with HYDROPRO and, second, for the calculation of the radial distribution function of hydrogen with respect to the protein center of mass (see the previous Section on Experiments and methods).

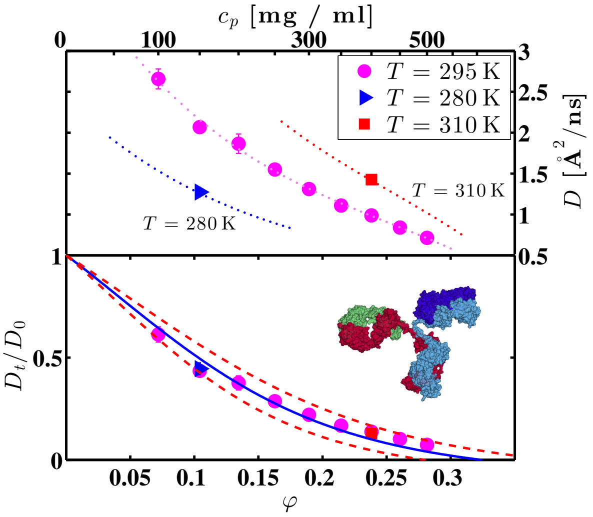

Figure 6.2: Apparent diffusion coefficient D (upper) and reduced translational short-time diffusion coefficient D_t/D_0 (lower) as a function of the protein volume fraction φ. The symbols represent the experimental data recorded at $T = 295$ K (circles), $T = 280$ K (triangles), and $T = 310$ K (squares). In the upper plot, the lines are guides to the eye (dotted). In the lower plot, the solid blue line depicts the normalized translational short-time self-diffusion from colloid theory for hard spheres [37]. The dashed red lines indicate the colloid model for a 5% relative error on R_h/R. When not visible, the experimental error bars are smaller than the symbols. The protein structure has been rendered using VMD.

6.4.3 Internal Diffusive Molecular Motions

The faster process observed in the neutron spectra (equation (6.2)) can be characterized both geometrically via the EISF $A_0(q)$ and dynamically via the line broadening Γ. The EISF provides information on the geometry of dynamical confinement of the hydrogen atoms within a protein molecule. Several theoretical models addressing confined diffusion provide analytical expressions for the EISF [34, 57, 208]. The most frequently used models describe either the diffusion of a particle within an impermeable sphere, or a jump diffusion between two or three definite sites [56]. The experimental EISF is most probably a rather complicated superposition of several diffusion mechanisms. Therefore, regarding all discussion in this subsection, we stress that the present modeling is far from final, and in what follows we chose one out of possibly various alternative approaches. We also note that the restricted dynamic range on which the spectra were recorded (i.e. the maximum energy transfer and energy resolution limits of IN16B) may pose systematic limitations to the conclusions on the internal motions. Further, we emphasize that the observable quantity in our experiment is the self-dynamics of the prevailing hydrogen atoms. Using neutron backscattering, we observe uncorrelated individual fluctuations of protein subunits on the nanometer length scale, such as e.g. the motions of methyl groups and other amino acid residues. Therefore, as opposed to neutron spin-echo experiments, our incoherent scattering experiment is not sensitive to correlated long-range inter-domain fluctuations within the proteins.

For the sake of simplicity, we assume the protein to be a dynamically heterogeneous system, so that the EISF is expected to be a simple sum of weighted contributions [208, 209]. It is well known that a large part of the hydrogen atoms within a protein form methyl groups (-CH$_3$), where the three hydrogens, located at an average distance $a_M = \sqrt{3} \cdot 0.99$ Å $\simeq 1.715$ Å from each other, perform 120°-jumps around the threefold axis [59,210]. Thus, one expects a significant component of the EISF due to three-sites jump diffusion [56, 59, 211]: $A_{\text{3-jump}}(q) = \frac{1}{3}\left[1 + 2j_0(qa)\right]$, where $j_0(x) = \sin(x)/x$ and $a \equiv a_M$ denotes the jump-distance of the atom. As a second component we choose the EISF of an atom diffusing freely within an impermeable sphere of radius R without any *a priori* physical interpretation [57, 211]: $A_{\text{sphere}}(q) = \left|\frac{3j_1(qR)}{qR}\right|^2$, where $j_1(x)$ is the first order spherical Bessel function of the first kind. The components are assumed to be uncorrelated such that the total EISF is modeled as

$$A_0(q) = P + (1 - P)\left[\Phi\ A_{\text{3-jump}}(q) + (1 - \Phi)\ A_{\text{sphere}}(q)\right]. \tag{6.3}$$

Here, Φ is the fraction of hydrogen atoms undergoing three-sites jump diffusion, and $(1 - \Phi)$ is the fraction of hydrogens diffusing in an impermeable sphere. P represents the fraction of hydrogen atoms that appear fixed on the accessible time-scale [212]. Fig. 6.3 shows the EISF as a function of q for three different c_p (symbols) along with fits using Eq. (6.3) (lines).

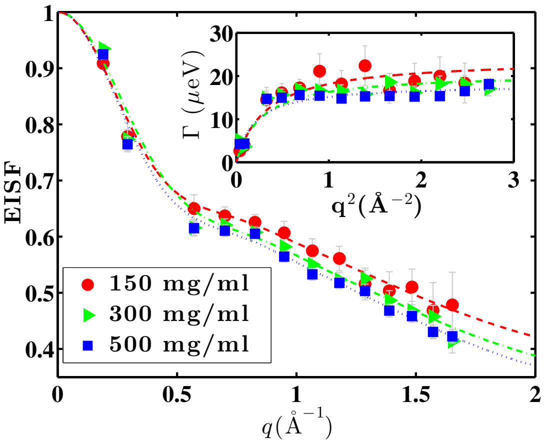

Figure 6.3: Main figure: Elastic incoherent structure factor as a function of q for three γ-globulin concentrations (symbols). The lines are the fits by Eq. (6.3). Inset: Γ as a function of q^2 for three protein concentrations. The symbols are the experimental data and the lines are the fits with Eq. (6.4).

The parameters obtained from the fit are listed in the Supporting Information. Within the error, they are constant and have error-weighted average values of $R = 6.7 \pm 0.27$Å, $P = 0.28 \pm 0.02$, and $\Phi = 0.55 \pm 0.02$. The fit results for R are also depicted in the inset of figure 6.4. These results are comparable to analogous parameters calculated in other studies [56, 96, 102].

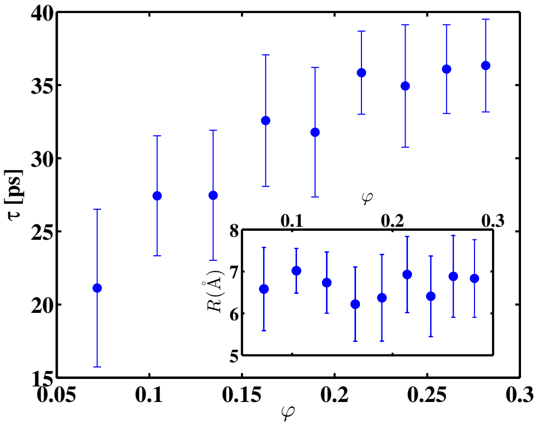

Figure 6.4: Main figure: Fit results for the residence time τ associated with the internal molecular motion of the proteins in terms of the jump diffusion model (Eq. (6.4)) as a function of the protein volume fraction φ in the aqueous solution. Inset: Fit result for the radius R of the impermeable sphere associated with the protein side chain motions in terms of the model for the EISF (Eq. (6.3)) as a function of the protein volume fraction φ.

From a rough estimation of the amount of CH_3 in γ-globulin we obtain $\Phi = 0.22$. The fit for this scenario of a fixed Φ (see Supporting Information) is less good compared to the situation with a free parameter Φ. This is reasonable, because the EISF does not allow to extract the number fractions of the different atoms corresponding to different internal diffusive processes on an absolute scale due to the restricted dynamic window on which the diffusion is sampled.

An increased thermal stability of proteins under crowding conditions has been reported in previous studies [213–215]. However, the anticipated effect of crowding on the thermal stability is small [196]. It is therefore not surprising that the fit parameters in the EISF, characterizing the geometrical confinement of internal motions, do not significantly vary with the protein concentration in our experiment. In particular, Stagg et al. [196] report an isotropic compaction of proteins of about 0.3% in the radius of gyration R_g in highly crowded solutions. The absence of a significant change of the geometry to which the internal motions are confined, as reflected by the radius R in the EISF (figure 6.4, inset), is consistent with such a small change in R_g.

In addition to the geometrical information via the EISF, Γ provides a dynamical signature of internal motions that occur in the time window defined by the resolution and the energy range of the instrument. For the three-sites jump-diffusion modeling methyl rotations, the residence time is of the order of 10^{-10} s, corresponding to a HWHM of the order of 100 μeV, well above the energy range of IN16B. Hence, the resulting signal is expected to be essentially flat [59] and will thus not contribute to Γ. For confined diffusion in a sphere, the dynamical signature should be present in Γ. In first approximation, we can use an expression for unrestricted jump-diffusion to fit our data. In the absence of a detailed microscopic dynamical picture, for simplicity we apply the model by Singwi and Sjölander [34, 60, 96]

$$\Gamma = \frac{D_{\mathrm{jump}}\, q^2}{1 + D_{\mathrm{jump}}\, q^2 \tau}\ , \tag{6.4}$$

where τ denotes the residence time before a jump, and D_{jump} is the jump-diffusion coefficient. The inset of Fig. 6.3 shows Γ as a function of q^2 for three c_p. The lines are the fits by Eq. (6.4). The fitted D_{jump} results in values around 150 Å^2/ns, while $\tau(\varphi)$ seems to follow an asymptotic behavior, monotonically increasing with c_p from $\tau \sim 20$ ps at $c_p = 100$ mg/ml to $\tau \sim 40$ ps at $c_p = 500$ mg/ml (see figure 6.4, main part). Within the errorbars, these values are consistent also with those obtained by fitting the data with the comparable model for unrestricted jump-diffusion by Hall and Ross [62]. However, at present our theoretical understanding is not yet sufficient to fully validate the picture of jump diffusion or a related model. Molecular dynamics simulations may in the future resolve this issue in combination with QENS experiments along the framework presented in this article.

From the geometrical and dynamical information on the internal motions, we obtain the picture of an insignificant change of the geometry of the confined motion with increasing crowding. By contrast, those hydrogen relaxations sampled on an excitation scale of some 10 μeV are subject to an increased residence time at higher crowding. Since crowding shifts the thermodynamic equilibrium of proteins towards a more folded state [196, 216], a small effect of crowding on the internal molecular fluctuations of proteins may be expected. It has been hypothesized that the structuring effect of water plays a role in this stabilization [216]. The trend in the residence time τ in terms of the jump diffusion model might be related to this stabilization. Perez et al. [56] have shown that internal motions in fully dissolved proteins are faster than in hydrated protein powders in the case of lysozyme and myoglobin. Since we use D_2O as solvent water, we assume that the contribution of the hydration shell itself to our measured signal is small, but we cannot yet make a conclusive statement on the role of the hydration shell water on the internal dynamics of γ-globulin. Nevertheless, the slower internal diffusion with increasing crowding observed in our experiment would be consistent with the trend towards even slower diffusion in hydrated powders, the latter being the “ultimately crowded" solution.

6.4.4 Further Discussion

The successful and self-consistent separation of global and internal motions using colloidal modeling of the protein is a central result of this study, since it not only describes the protein diffusion very well, but also allows for reliable access of the convoluted internal dynamics, which is promising for future applications of neutron backscattering. In this context, several questions deserve further discussion.

Protein solutions can, in general, not be considered as purely monodisperse solutions of monomers, but might also contain oligomers and clusters. Although previous studies have reported oligomerization of γ-globulin [135, 217] at concentrations up to $\sim$ 150 mg/ml, our data accessing high protein concentrations are fully consistent with a monomeric description. A tentative separation of motions using dimers results in inconsistent diffusion coefficients, indicating that oligomerization has a negligible effect at these short time scales. Large aggregates would not cause a quasi-elastic signal measurable by IN16B, but contribute only to the amplitude of the elastic line. Small oligomers would lead to an additional contribution to the quasi-elastic broadening. None of these effects is visible in our data. In addition, the good agreement of the experimental $D_t(\varphi)$ with the theoretical prediction from colloid theory based on the assumption of γ-globulin monomers is consistent with the picture that all our samples are predominately monomeric protein solutions. We remark, however, that we cannot rule out the presence of aggregates in some form. We also note that oligomerization or aggregation may depend on the type of antibody protein and we emphasize that our samples are not monoclonal.

Proteins can have different conformations [218] that coexist in solution or are switched due to environmental factors. In particular, pH-induced conformational changes of the protein can constitute a limitation to the applicability of colloid models to protein solutions [219]. Nevertheless, over the investigated concentration range the pH is expected to be sufficiently constant due to self-buffering ensuring a substantially unchanged protein conformation for our samples.

The strongly anisotropic shape of γ-globulin inspires the question whether inter-domain motions of the three branches of the protein may interfere with our analysis. In this context, we remark that on the observation time scale of our experiment, the measured D's correspond to a mean-squared displacement of the proteins by a few Ångströms. This length scale is much smaller than the radius of γ-globulin. Also, $D_{r,0}$ of γ-globulin corresponds to a root mean squared rotational displacement [32] of about 3°. Therefore, it is reasonable that the influence of the strongly branched shape of the protein does not lead to a deviation from the colloid hard-sphere model in the short-time limit. Stronger deviations may be expected to become significant at longer times. Even though the inter-domain motions are not visible in our experiment, we note that they may be affected by the change in the hydrodynamic interactions due to crowding.

The large energy range of the new backscattering spectrometer IN16B allows to access information on dynamics in the subnanosecond to nanosecond time scale which represents methodological challenges. Within this time window, water motions become visible, and the data analysis has to be reliably set up based on a physical picture. In our case, the scattering of the sample cylinder and instrumental background has been directly subtracted using a background measurement. The water contribution has been removed by a novel method employing results on D_2O from the time-of-flight spectrometer IN6 (see the Section on Experiments and Methods). With this method, we minimize effects of the water scattering on the determination of Γ.

Concerning the fit procedure, we emphasize that both γ and Γ in Eq. (6.2) are left completely free during the fit. The final result is very robust against variation of the initial values, meaning that both components are present and well-separated. The second component $\mathscr{L}_\Gamma(\omega)$ clearly does not follow a $\Gamma \propto q^2$ behavior, indicating *no* free diffusion, but diffusion in a confinement of some form. The data are at this stage not sufficient to further distinguish between different types of confined diffusion arising from processes such as rotational jump-diffusion of the methyl and amine groups, and diffusion of the tethered side chains of the amino acids, as well as confined diffusion of the hydration water. Nevertheless, the overall procedure is promising for allowing such a distinction also in view of future instrumental developments aimed at increasing the neutron flux to the sample. Further progress in the analysis of the component $\mathscr{L}_\Gamma(\omega)$ may be possible by comparison to molecular dynamics (MD) simulations and a complementary study on a wider energy range.

6.5 Conclusions and Outlook

In conclusion, using quasi-elastic neutron backscattering, we have successfully accessed self-diffusion and internal dynamics in aqueous solutions of γ-globulin on subnanosecond to nanosecond time and nanometer length scales. The study presents the results of one of the first experiments conducted at the newly commissioned backscattering spectrometer IN16B at the Institut Laue-Langevin. In order to minimize systematic errors, the data analysis has been reviewed carefully and extended by a newly developed procedure to account for solvent contributions. Due to the high data quality, it was possible to apply a self-consistent separation framework for the global translational and rotational diffusion and internal motions. The global diffusion is described with good agreement by predictions for effective spheres with the hydrodynamic radius of the strongly non-spherical protein monomers. The internal motions are characterized both geometrically and dynamically and consist of several contributions, including jump-like rotation of chemical endgroups and confined diffusion. The dynamical signature indicates a slowing down of the internal dynamics due to crowding, which might be related to the thermal stabilization of the protein conformation. Although the modeling of the internal diffusive motions is certainly far from complete yet, the presented framework allows for future experimental studies with various perspectives, and – in connection with accompanying instrumental, theoretical and computational advances – is promising for a comprehensive understanding of the hierarchical and complex dynamics in protein solutions. In the future, it will also be of interest to carry out a comparative study of internal fluctuations of a hydrated protein powder of γ-globulin in order to compare with the internal fluctuations observed on the proteins in solution.

Acknowledgment

We gratefully acknowledge the entire IN16B team including B. Frick, D. Bazzoli, R. Ammer, M. Appel (all ILL) for the successful commissioning of the new spectrometer, having made this pioneering experiment possible, and M. Hennig for software. We acknowledge financial support from the Deutsche Forschungsgemeinschaft (DFG).

Supporting Information

Appendix A contains the following contents. Details on the separation of rotational and translational diffusion and results of the separation assuming dimers in solution. Radial distribution of hydrogen atoms of IgG monomers, dimers and BSA. Summary of fit results of the EISF and Γ. Details on the treatment of the contribution of heavy water. Additional example spectra.

Chapter 7

The Dynamics of BSA upon Thermal Denaturation

This Chapter is based on the article [220]:

Hierarchical molecular dynamics of bovine serum albumin in concentrated aqueous solution below and above thermal denaturation. [1]

Marco Grimaldo,[a,b] **Felix Roosen-Runge,**[a] **Marcus Hennig,**[a,b] **Fabio Zanini,**[b] **Fajun Zhang,**[b] **Niina Jalarvo,**[c,e] **Michaela Zamponi,**[c,d] **Frank Schreiber,**[b] **Tilo Seydel**[a]

Physical Chemistry Chemical Physics **2015** *17*, 4645–4655.

[a] Institut Max von Laue - Paul Langevin (ILL), CS 20156, F-38042 Grenoble, France
[b] Institut für Angewandte Physik, Universität Tübingen, D-72076 Tübingen, Germany
[c] Jülich Centre for Neutron Science (JCNS), Forschungszentrum Jülich GmbH, D-52425 Jülich, Germany
[d] JCNS Outstation at the MLZ, Lichtenbergstraße 1, D-85747 Garching, Germany
[e] Chemical and Engineering Materials Division, Neutron Sciences Directorate, and JCNS Outstation at the Spallation Neutron Source (SNS), Oak Ridge National Laboratory, Oak Ridge, TN 37831, USA

7.1 Abstract

The dynamics of proteins in solution is a complex and hierarchical process, affected by the aqueous environment as well as temperature. We present a comprehensive study on nanosecond time and nanometer length scales below, at, and above the denaturation temperature T_d. Our experimental data evidence dynamical processes in protein solutions on three distinct time scales. We suggest a consistent physical picture of hierarchical protein dynamics: (i) Self-diffusion of the entire protein molecule is confirmed to agree with colloid theory for all temperatures where the protein is in its native conformational state. At higher temperatures $T > T_d$, the self-diffusion is strongly obstructed by cross-linking or entanglement. (ii) The amplitude of backbone fluctuations grows with increasing T, and a transition in its dynamics is observed above T_d. (iii) The number of mobile side-chains increases sharply at T_d while their average dynamics exhibits only little variations. The combination of quasi-elastic neutron scattering and the presented analytical framework provides a detailed microscopic picture of the protein molecular dynamics in solution, thereby reflecting the changes of macroscopic properties such as cluster formation and gelation.

7.2 Introduction

Proteins are an essential part of the molecular basis of life. Their function relies on a combination of structure and dynamics [7,221,222]. Therefore, a quantitative characterization of protein dynamics in their aqueous physiological environment on different length and time scales is an essential aspect for the understanding of the function of living systems. Most proteins possess a well-defined native globular structure, based on cooperative folding of the protein chain driven by an interplay of different intramolecular interactions of amino acid residues [223–226]. Importantly, protein conformations display several structural features in a hierarchical order: Starting from the sequence of amino acids—the primary structure—the protein chain builds structural elements such as α-helices, β-sheets or random coils—the secondary structure. These structural elements assemble into protein domains—the tertiary structure—that finally can arrange into multi-subunit proteins—the quaternary structure. As a consequence of the variety of typical time and length scales in such complex macromolecules, the dynamics of proteins is characterized by an extensive hierarchical nature.

Upon increasing the temperature, thermal denaturation of the protein occurs. In this process, a partial unfolding of the native protein structure is followed by a reorganization to a different globular structure or a random-coil-state sometimes leading to aggregation and gelation [223–225, 227–230]. Regarding a single protein molecule, unfolding is related to protein malfunction [231], and a better understanding of the driving factors has important implications from a biomedical perspective. In protein solutions, denaturation represents a pathway how microscopic structural changes can alter macroscopic properties. In this context, gelation and formation of aggregates is of general importance for soft condensed matter, nanotechnology, and food research.

---

[1] Author contributions: M. G., F. R.-R., M. H., T. S., F. Z., F. S. designed research; M. G., F. R.-R., M. H., T. S., F. Z., M. H. performed research; N. J. and M. Z. provided technical assistance; M. G. analyzed data; M. G., F. R.-R., T. S., F. Z., F. Z., F. S. wrote the paper.

The first step of denaturation, the unfolding, is related to the general question of protein folding and misfolding and is not understood in detail, although reasonable predictions for small proteins exist and general features such as dominant contributions to folding and influences from the environment have been identified [226, 231]. In this context, the funnel picture of protein folding has gained significant importance in the past years and creates a need for dynamic measurements on the molten globule state [232,233]. Mechanistically, Zimm and Bragg developed a theory for the first microscopic step of unfolding based on the helix-to-coil transition of a polypeptide chain as a result of which at low temperatures the polymer chain is dominated by helices, at high temperatures by random coils, with a rather narrow transition region where mixtures of these conformations may be found [223].

While the Zimm-Bragg model takes only the secondary structure into account, real proteins possess a well-defined tertiary structure. Starting from a protein model with a dense core without contact to solvent and a hydrated outer shell, Finkelstein and Shakhnovich developed a theory of denaturation of single protein molecules and derived a first-order phase transition between the folded and a slightly expanded form [234,235]. While this initial step of denaturation is independent of solvent, the further unfolding is dominated by the hydration-mediated interaction with the penetrating solvent [226], giving rise to a phase diagram for a single protein in dependence on solvent quality and temperature [234].

Leaving the level of individual molecules, denaturation is represented by processes of aggregation and cross-linking, i.e. clustering and gelation, which, depending on the protein, can be rationalized either along the arguments of vulcanization of polymers [67,236,237] or with colloidal gels with non-specific intermolecular attractive forces [238]. A higher absolute concentration of the proteins has on the one hand a stabilizing effect on the protein thermal stability [196], on the other hand promotes the formation of intermolecular β-structures at lower temperatures [239].

Numerous studies have focused on different aspects of the process of thermal denaturation by means of a variety of techniques [67, 238, 240–259]. In the following, we focus on the effect of thermal denaturation on the internal dynamics of globular proteins.

Quasi-elastic neutron scattering (QENS) has been proven to be a well-suited tool to investigate the dynamics of proteins in aqueous solution on pico- to nanosecond time scales [17, 28, 29, 64, 96]. Several elastic and quasi-elastic neutron scattering studies have compared the internal dynamics of proteins in native, molten (i.e. an intermediate equilibrium state between native and fully denatured), or denatured conformation, mostly in the picosecond time scale and mainly reflecting side-chain reorientations but in general not taking into account the global motion in solution [67, 78, 80, 82, 102–105, 107, 108, 255, 260–263]. As a general outcome, the conformation-dependent dynamics is characterized by the increase of the number of mobile H-atoms on picosecond time scales and a decrease of the confinement of restricted motions in non-native structures. Importantly, upon unfolding, internal protein fluctuations exhibit increased dynamical heterogeneities [105, 108]. In this context, Gibrat et al. suggested that the dynamics of atoms within the protein is more influenced by the distance to the backbone than by solvent exposure [108].

Importantly, thermal denaturation can lead to several steps of dynamical changes. Two characteristic temperatures for the denaturation of hydrated lysozyme were determined from the protein internal dynamics: above $T_b = 325\,\mathrm{K}$ the mobility of side chains starts to increase, while

$T_d = 346\,\mathrm{K}$ defines the limit for irreversible denaturation [258]. Murayama and Tomida [249] have shown that bovine serum albumin (BSA) in D_2O at protein concentration $c_p = 20\,\mathrm{mg/ml}$ undergoes two conformational transitions at $T = 330\,\mathrm{K}$ and around $T_d = 348\,\mathrm{K}$. The latter corresponds to the melting of α-helices and the formation of intermolecular β-sheets. Above T_d, the fraction of random coils, turns and connecting loops becomes at least as significant as that of α-helices and β-sheets [249]. This finding, together with the fact that backbone fluctuations are much smaller in α-helices and β-sheets, compared to the greater amplitudes in connecting loops and unstructured termini [105], is consistent with the experimental observation that the average internal mean-square displacement of 500 mg/ml BSA in D_2O increases faster for $T \gtrsim 343\,\mathrm{K}$ [67].

Reconsidering the hierarchical structure of proteins, a similar hierarchy in dynamics is expected, however, only partly suggested by the aforementioned studies on the average internal dynamics of entire proteins or labeled protein domains. In this article, we present a comprehensive study outlining the hierarchical protein dynamics before and after thermal denaturation. Using a high-quality data set recorded on the backscattering spectrometer BASIS [174] (SNS, ORNL), we access the dynamics of BSA at nanosecond time and nanometer length scales in a temperature range between 280 and 370 K. We propose and justify a model reflecting the complex dynamics of the proteins. In terms of this model, we obtain three self-diffusion coefficients which we attribute to three hierarchical levels of the dynamics of proteins: (i) entire-protein translation and rotation, (ii) backbone fluctuations and (iii) side-chain motion. Consistently, the elastic incoherent structure factor (EISF) can be fitted by an extension of the model in Ref. [28] accounting for the restricted dynamics of both side-chains *and* backbone. The analysis of the EISF, although more sensitive to the background treatment and to the fraction of coherent scattering, confirms an increase of mobile atoms and indicates a weaker restriction of the backbone with increasing temperature, while that of the side-chains is constant within the error. Both our new model and its physical interpretation may not be complete or unique, but we find that previous models of protein diffusive dynamics are not consistent with our observations at high temperatures.

In the following, subsequent to the experimental Section, we present our results as well as a new analytical framework. This framework provides a quantitative access to the internal motions of proteins during the changeover from freely diffusing molecules in solution at low temperatures to protein molecules incorporated in a gel at high temperatures. Following the results Section, we discuss our observations in terms of the aforementioned hierarchical levels and in the context of the reported previous findings. In the conclusions Section, we draw a comprehensive picture of the nanosecond self-dynamics observed on molecular length scales.

7.3 Experimental Section

Bovine serum albumin (BSA) was obtained from Sigma-Aldrich (product code A3059) as a lyophilized powder (99% purity) and used without further purification. The proteins were dissolved in water (D_2O) and filled in double-walled cylindrical Aluminum sample holders (outer diameter 22 mm, gap 0.25 mm) for the neutron scattering experiments. The cylinders where sealed against vacuum and inserted into a cryostat on the neutron spectrometer for temperature control.

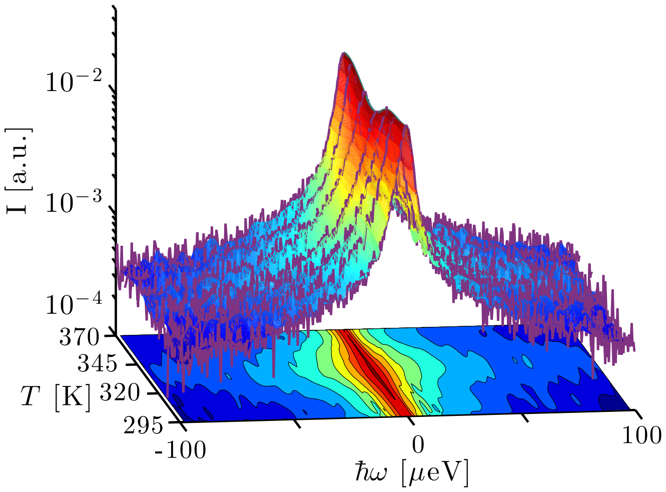

Figure 7.1: Example spectra (purple lines) recorded using the backscattering spectrometer BASIS, SNS, ORNL, on bovine serum albumin (BSA) at the scattering vector $q = 0.85\,\text{Å}^{-1}$ for different temperatures T at the protein concentration $c_p = 200\,\text{mg/ml}$ in heavy water (D_2O) subsequent to the subtraction of the empty can spectra. The surface interconnecting the 7 spectra is a spline interpolation of binned data (7 points per bin for $|\omega| > 10\,\mu\text{eV}$). The bottom projection displays the normalized scattering intensity $S(q,\omega)/S(q,\omega = 0)$ using spline interpolation and illustrates the T-dependent width of the spectra.

The neutron data were recorded on the backscattering spectrometer BASIS [174] (SNS, ORNL). Neutrons were analyzed using Si(111) single crystals, thus setting the analyzed energy to 2.08 meV. The integration time for each neutron spectrum amounted to approximately 4 hours per temperature. We have carried out the data reduction using the *Mantid* software provided by the SNS and subsequently analyzed the data using *MATLAB*, as reported in detail in Ref. [170].

Using neutron spectroscopy, we measure the scattering function $S(q,\omega)$ at scattering vectors q which are coupled to reciprocal intermolecular distances and at energy transfers ω which can be resolved, at BASIS, down to $\sim 3.5\,\mu\text{eV}$ FWHM. We have determined the spectrometer resolution function $\mathscr{R}$ by recording the scattering signal from a Vanadium standard and modeled it by a sum of 4 Gaussians. We have subsequently implemented the convolution of $\mathscr{R}$ with the fit functions in *MATLAB* analytically by building Voigt functions [170].

7.4 Results and Discussion

7.4.1 Model-Free Observations

Figure 7.1 depicts the evolution of the measured scattering function $S(q,\omega)$ in dependence of temperature. In general, two temperature regimes can be observed directly from visual inspection. Below $T_d \approx 345\,\text{K}$, the overall broadening of the spectra increases with rising temperature, indi-

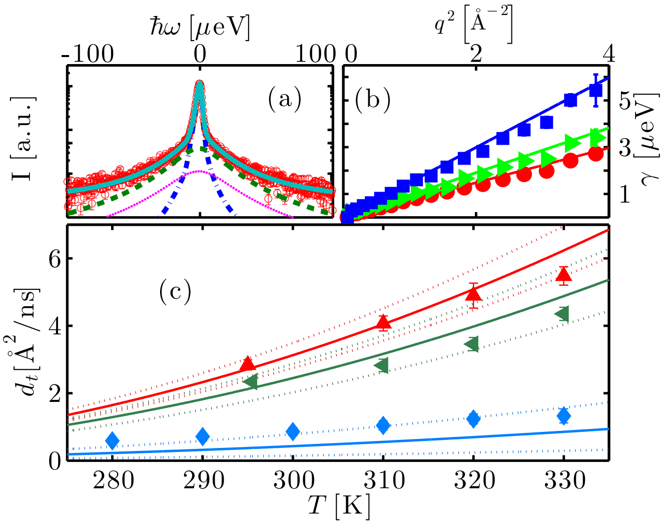

Figure 7.2: (a) Example spectrum (symbols) recorded using the neutron backscattering spectrometer BASIS, SNS, ORNL, on bovine serum albumin (BSA) at the concentration $c_p = 200\,\mathrm{mg/ml}$ in heavy water (D_2O) at the temperature $T = 295\,\mathrm{K}$. The displayed data have been detected at the scattering vector $q = 0.45\,\text{Å}^{-1}$. The solid line superimposed on the data is a fit of the model function (equation (4.17)) containing two Lorentzians accounting for the dynamics of the protein molecules (blue and green dashed lines) and a fixed contribution accounting for D_2O (magenta dotted line), convoluted with the resolution function. (b) Linewidth γ of the Lorentzian accounting for the translational and rotational diffusion of the entire protein as a function of q^2 for $c_p = 500\,\mathrm{mg/ml}$ at T =280, 290 and 310 K (red circles, green triangles and blue squares, respectively). The lines are the fits following the Fickian law $\gamma = dq^2$. (c) Translational self-diffusion coefficients d_t as a function of temperature for $c_p = 150\,\mathrm{mg/ml}$ (red pointing-up triangles), $200\,\mathrm{mg/ml}$ (green triangles), and $500\,\mathrm{mg/ml}$ (blue diamonds). The solid lines are the respective theoretical self-diffusion coefficients and the dotted lines indicate the confidence interval defined by a relative error of 5% on the ratio between hydrodynamic radius R_h and effective radius R.

cating increasingly faster dynamics. Around T_d, the spectral width decreases sharply. Finally, for $T > T_d$, the spectral width appears to remain constant or increase slightly with increasing temperature. The elastic scattering intensity ($\omega = 0$) decreases with rising T for $T < T_d$ and increases again for $T > T_d$, consistent with earlier observations focusing on the elastic signal only [67].

These model-free observations are consistent with the intuitive picture of denaturing. Before denaturing, the proteins diffuse freely in solution and global and internal dynamics become faster due to elevated temperatures. Upon denaturation, in particular the global dynamics irreversibly arrests due to unfolding and cross-linking between proteins, and the remaining dynamics again increases with rising temperature. This physical picture will be discussed further in the following subsections based on model fits that provide a consistent description of the observed dynamics.

7.4.2 Analysis via the Conventional Two-Lorentzian Model Below the Denaturation Temperature

The short-time self-diffusion of proteins in concentrated solutions and its dependence on crowding has been investigated earlier at temperatures well below denaturation [29, 130]. Advances in the performance of neutron backscattering spectrometers have made it possible only very recently to address both the global protein self-diffusion and its internal dynamics from solution samples, and to systematically investigate the effect of crowding on these two types of dynamics [28]. In that temperature range, the quasi-elastic scattering function has been shown to be well modeled by

$$\begin{aligned} S(q,\omega) = \mathscr{R}\otimes\big\{\beta(q)\,[A_0(q)\mathscr{L}_\gamma(\omega) + (1-A_0(q))\mathscr{L}_{\gamma+\Gamma}(\omega)]\ldots \\ \cdots + \beta_{\mathrm{D_2O}}\mathscr{L}_{\gamma_{\mathrm{D_2O}}}(\omega)\big\} \end{aligned} \tag{7.1}$$

where $\mathscr{R}$ denotes the instrumental resolution function, modeled by a combination of Gaussian functions, $\beta(q)$ is a scalar, and $A_0(q)$ represents the elastic incoherent structure factor (EISF). The two Lorentzians $\mathscr{L}_\gamma(\omega)$ and $\mathscr{L}_{\gamma+\Gamma}(\omega)$ account for two processes occurring at distinct time scales, where the faster process, responsible for a broadening of the elastic line of width Γ, is convoluted to the slower process with line broadening γ. Finally, the fixed term $\beta_{\mathrm{D_2O}}\mathscr{L}_{\gamma_{\mathrm{D_2O}}}$ models the solvent contribution. This fixed term is determined using time-of-flight spectroscopy data on pure D_2O for the linewidth $\gamma_{\mathrm{D_2O}} = \gamma_{\mathrm{D_2O}}(T)$ in combination with BASIS data on pure D_2O for the amplitude $\beta_{\mathrm{D_2O}} = \beta_{\mathrm{D_2O}}(T)$ as explained in detail in Ref. [170].

We have carried out the full analysis both with and without the assumption of an H/D-exchange of the labile H-atoms on the proteins with the solvent water. We estimate the magnitude of this exchange based on the number 776 of labile H-atoms [264] per BSA molecule obtained from the protein data base (PDB) file [145]. Taking into account the molar fraction of BSA in water and the scattering lengths of H and D, respectively, we obtain an increase of the amplitude of the solvent water signal compared to the assumption of an absent H/D-exchange by a factor of 1.08, 1.16, and 1.38, respectively, for the protein concentrations of 100, 200, and 500 mg/ml, respectively (resulting in 1, 2, and 5% H/D exchange in the solvent). Due to a remaining uncertainty in the exact number of exchangeable atoms, we display the figures without assuming the H/D-exchange in the article and the corresponding figures assuming the estimated exchange in Appendix B. The increase of the solvent scattering signal due to the H/D-exchange does not change the overall trend of the fit results, and we will report the essential fit results both with and without assumption of the exchange. In principle, the H/D-exchange does not only affect the solvent scattering amplitude, but also its dynamics. However, since the H/D-exchange amounts to only approximately 5% of the total number of hydrogens in the water for the case of the highest protein concentration, we assume that the effect of the modified solvent dynamics is small. The short-time dynamics of D_2O is essentially unaffected by the formation of a gel [265], therefore the treatment of its contribution is valid both in the solution and in the gel states of our samples. Having carefully handled the contribution of D_2O, we estimate that the incoherent fraction of the total scattering intensity is $\sim 88\,\%$, i.e. that of a dry protein powder, the coherent intensity varying only slightly in q. [266] In the following, we will thus carry out the analysis neglecting the coherent contribution, being aware that this might introduce a small systematic error, in particular in the EISF.

An example spectrum (symbols) fitted with equation (7.1) (solid line superimposed on the data) is shown in Figure 7.2(a). The two Lorentzians $\mathscr{L}_\gamma$ and $\mathscr{L}_\Gamma$ are depicted by the blue and the green dashed lines respectively, and $\beta_{\mathrm{D_2O}}\mathscr{L}_{\gamma_{\mathrm{D_2O}}}$ is represented by the magenta dotted line. In the physical picture established earlier [28], $\mathscr{L}_\gamma$ is associated with the global protein motions, and $\mathscr{L}_\Gamma$ is attributed to the internal molecular diffusive motions of the proteins. We find that the fitted γ are consistent with a Fickian process for the global self-diffusion, i.e. $\gamma = d\,q^2$ with the apparent diffusion coefficient d (cf. Figure 7.2(b)). Here, d is denoted 'apparent', because it contains contributions from both rotational and translational diffusion. The internal dynamics associated with the width Γ can be described by jump-diffusion for $T < 340\,\mathrm{K}$, i.e. $\Gamma = Dq^2/(1+\tau Dq^2)$ with a diffusion coefficient D and residence time τ. [60]

7.4.3 Analysis via a Model of Switching Diffusive States at Elevated Temperatures

At higher temperatures, the fit results for Γ are no longer consistent with a jump-diffusion process such as that by Singwi and Sjölander [60] or that by Hall and Ross [62]: a marked nonmonotonicity of the q-dependent Γ resulting for a single process (see Appendix B) cannot be interpreted in physical terms in a straight-forward way. By contrast, a multi-state process would be consistent with such an observation. Therefore, in order to extend the model given by equation (7.1), we substitute $\mathscr{L}_\Gamma(\omega)$ with the scattering function for a particle switching between two diffusive processes having rates $\Gamma_1 = D_1\,q^2$ and $\Gamma_2 = D_2\,q^2$ and residence times τ_1 and τ_2, respectively. D_1 and D_2 are thus the self-diffusion coefficients of the two states. Essentially, such a picture differs from that leading to the Singwi-Sjölander jump-diffusion model in that the (overdamped) particle vibration is substituted by a second diffusive state, and both diffusive states have a finite residence time. We have tested several other models as well, but these led to inconsistent results, as discussed in Appendix B. The scattering function for the two-state model reads [61]:

$$S_{\mathrm{sw}}(q,\omega) = \alpha\,\mathscr{L}_{\lambda_1}(\omega) + (1-\alpha)\,\mathscr{L}_{\lambda_2}(\omega) \tag{7.2}$$

with

$$\begin{aligned}\alpha =&(\lambda_2-\lambda_1)^{-1}\Bigg[\frac{\tau_1}{\tau_1+\tau_2}\left(\Gamma_2+\tau_1^{-1}+\tau_2^{-1}-\lambda_1\right)\dots\\ &\dots+\frac{\tau_2}{\tau_1+\tau_2}\left(\Gamma_1+\tau_1^{-1}+\tau_2^{-1}-\lambda_1\right)\Bigg]\end{aligned} \tag{7.3}$$

$$\lambda_{1,2} = \frac{\Gamma_1+\tau_1^{-1}+\Gamma_2+\tau_2^{-1}\pm\Lambda}{2} \tag{7.4}$$

$$\Lambda = \left[(\Gamma_1-\Gamma_2+\tau_1^{-1}-\tau_2^{-1})^2+4\,(\tau_1\,\tau_2)^{-1}\right] \tag{7.5}$$

Thus, the overall scattering function in this picture is:

$$\begin{aligned}&S(q,\omega) = \mathscr{R}\otimes\big\{\beta(q)\big[A_0(q)\mathscr{L}_\gamma(\omega)\dots\\ &\dots+\big(1-A_0(q)\big)\left(\alpha\,\mathscr{L}_{\gamma+\lambda_1}(\omega)+(1-\alpha)\,\mathscr{L}_{\gamma+\lambda_2}(\omega)\right)\big]\dots\\ &\dots+\beta_{\mathrm{D_2O}}\mathscr{L}_{\gamma_{\mathrm{D_2O}}}(\omega)\big\}\end{aligned} \tag{7.6}$$

Given the large number of free parameters, we set a priori $\Gamma_{1,2} = D_{1,2}\,q^2$ and $\gamma = d\,q^2$, where d represents the apparent self-diffusion coefficient of the entire protein. We are thus assuming that, at the short time and length scales accessible by the instrument, the dynamics of the entire protein corresponds to simple self-diffusion even at higher temperatures, having reliably confirmed this for physiological T [28,29]. We can then fit the model to the spectra in the entire q-range simultaneously with d, D_1, D_2, τ_1 and τ_2 as global parameters, while $A_0(q)$ and $\beta(q)$ are allowed to change at every q. The fixed term $\beta_{\mathrm{D_2O}}\mathscr{L}_{\gamma_{\mathrm{D_2O}}}$ models the solvent contribution [28,170], as explained in subsection 7.4.2. An example spectrum fitted with equation (7.6) as well as the global fit parameters as a function of T are plotted in Figure 7.3. The fits show a very good agreement of data and switching model for the full temperature range. Furthermore, the fit parameters show small error bars, evidencing a reasonable statistical representation of the data by the model. In this context it is important to emphasize that, due to the global fit parameters, the switching model has fewer free parameters than the two-Lorentzian fit function on the full q range.

In the following subsections we report the fit results, which we subsequently interpret in the context of a physical picture that has already been suggested in the model-free results. Generalizing the picture established for physiological temperatures [28], we will associate d with the global protein diffusion and the parameters D_1, D_2, τ_1 and τ_2 with internal dynamics.

7.4.4 Global Apparent Short-Time Self-Diffusion

Figure 7.3(a) shows the apparent self-diffusion coefficient d of the proteins at $c_p = 150, 200$ and $500\,\mathrm{mg/ml}$ as a function of T (symbols). As expected, a higher c_p causes a lower d due to the effect of crowding on the hydrodynamic interactions [29]. This difference aside, the three concentrations exhibit analogous behaviors, consistent with elastic neutron scattering measurements [67]: d increases for $T \lesssim 340\,\mathrm{K}$, decreases up to $T \approx 360\,\mathrm{K}$ and then increases again, with a smaller slope. As in Ref. [67], we fit the data with the function

$$d(T) = (m_1\,T + b_1)[1 - \Theta(T^*)] + (m_2\,T + b_2)\Theta(T^*) \ , \tag{7.7}$$

where $T^* = (T - T_d)/\Delta T$, with the denaturing temperature T_d and the transition width ΔT, and $\Theta(x) = [1 + \exp(-x)]^{-1}$. The indices 1 and 2 refer to the state of native proteins in solution and the gel-like state of denatured proteins, respectively. Despite the rather coarse temperature steps, we obtain an average transition temperature $T_d \approx 342\,\mathrm{K}$ consistent with earlier observations [67, 258, 259]. The fits are depicted by the lines in Figure 7.3(a). The solution at $c_p = 500\,\mathrm{mg/ml}$ has been measured at $300\,\mathrm{K}$ also after the formation of the gel-like state (open triangle). As expected, after the formation of the second state, the entire-protein dynamics does not return to its initial state even after cooling down the sample. In fact, after the transition, $(m_2\,T + b_2)$ from equation (7.7) seems to hold also at room temperature (dot-dashed line).

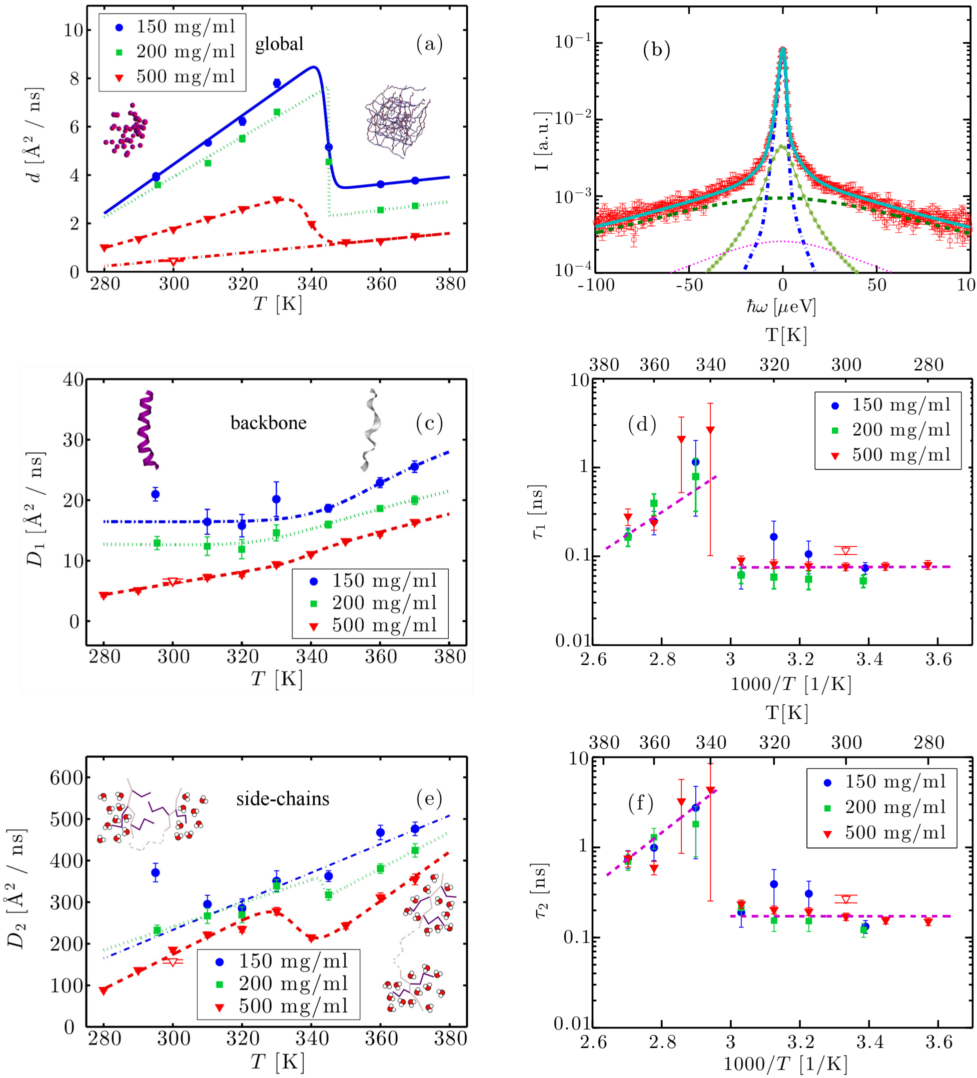

Figure 7.3: (a) Apparent self-diffusion coefficient d as a function of T for c_p = 150, 200 and 500 mg/ml (symbols) and fits with equation (7.7) (lines). The illustrations depict a colloidal suspension of native proteins (left) and a cross-linked network of denatured proteins (right). (b) Example spectrum (symbols) of aqueous BSA at c_p = 500 mg/ml, T = 370 K and q = 0.45 Å^{-1}. The solid line superimposed on the data is a fit of the model function (equation (7.6)). The blue dot-dashed line depicts the Lorentzian describing the protein global self-diffusion, while the light green asterisks and the dark green dashed line represent the Lorentzians attributed to backbone and side-chain dynamics, respectively. The magenta dots denote the contribution of D_2O. (c) D_1 as a function of T (symbols). D_1 is attributed to the dynamics of the backbone and sensitive to the secondary structure, part of which undergoes a transition from α-helix (left image) to disordered coil (right image). The illustration of a helix-to-coil transition was rendered with VMD [147]. The lines are guides to the eye. (d) Arrhenius plot of the residence time τ_1 between two jumps of the side-chains versus T for three c_p (symbols). The data above denaturation were fitted with an Arrhenius equation (line), while at low temperatures the line is a guide to the eye. (e) D_2 as a function of T for the concentrations reported in the legend (symbols). D_2 is associated with the dynamics of the side-chains. The lines are guides to the eye. The illustrations depict solvent-inaccessible side-chains in the folded protein (left) becoming solvent-exposed in the unfolded protein (right). (f) Arrhenius plot of the residence time τ_2 as a function of T (symbols). τ_2 is the time a side-chain needs to switch between two conformations during which they are considered immobile with respect to the backbone. The data above denaturation were fitted with an Arrhenius equation (line). The red open triangles in (a), (c)-(f) refer to the sample at 500 mg/ml cooled back to room temperature after denaturation.

7.4.5 Translational Short-Time Self-Diffusion Below the Transition Temperature T_d

Below the transition temperature T_d, d can be used to calculate the translational self-diffusion coefficient d_t once the structure of the protein is known [29]. As already observed both for BSA and gammaglobulins [28, 29], $d_t(\varphi, T)$ can be well described by the theory of colloidal hard spheres [37] (see Figure 7.2(c)). For $c_p = 500\,\mathrm{mg/ml}$, d_t is systematically higher than the curve of colloids. This is probably because at such high concentrations the determination of the effective protein volume fraction is less accurate. Also, at temperatures close to T_d, d_t becomes systematically lower than the theory for $c_p \leqslant 200\,\mathrm{mg/ml}$. The effect, although significant, is rather small and can be probably attributed to thermal expansion that is difficult to quantify. Note that such a deviation can be caused by an increase of the hydrodynamic radius R_H by only 3%, since the translational and rotational diffusion coefficients depend differently on R_H [29] (see also Appendix B).

7.4.6 Internal Dynamics

In addition to the global motion of the entire protein molecule, the wide energy range accessible at BASIS allows reliable fits of the parameters $D_{1,2}$ and $\tau_{1,2}$ in equation (7.6), which correspond to broader contributions in the spectra and in the physical picture are associated with internal motions. D_1 is plotted in Figure 7.3(c) as a function of T for the three investigated samples. Like d, also D_1 seems to decrease monotonically with protein concentration, probably due to a crowding-induced stabilization effect.

For all samples D_1 remains nearly constant or only slightly increases for $T < T_d$ and grows faster for higher temperatures resembling the high-temperature dynamical transition observed in other studies [67, 255]. The residence time τ_1 associated with this first internal diffusive state is, within the error bars, crowding-independent and is essentially constant at $\sim 100\,\mathrm{ps}$ for $T < T_d$ (Figure 7.3(d)). At $T \approx T_d$, τ_1 sharply increases by an order of magnitude to $\sim 1\,\mathrm{ns}$. The further decrease of τ_1 for $T > T_d$ can be modeled by an Arrhenius behavior with activation energy $E_a \sim 12\,\mathrm{kcal/mol} \simeq 0.5\,\mathrm{eV}$ (dashed line). (When assuming the increased amplitude of H-contaminated solvent water (subsection 7.4.2), $E_a \sim 18\,\mathrm{kcal/mol} \simeq 0.8\,\mathrm{eV}$, see Appendix B.) Note that the sample at $c_p = 500\,\mathrm{mg/ml}$ has been measured at $300\,\mathrm{K}$ both before and after denaturation. Although d at $300\,\mathrm{K}$ is, as expected, much lower in the denatured sample, D_1 is comparable before and after denaturation and τ_1 is only slightly higher in the gel (open triangle), indicating that, on the accessible time and length scales, the associated diffusive state is not strongly affected by the macroscopic structure.

D_2 linearly increases with T up to T_d, decreases stepwise for $c_p = 200$ and $500\,\mathrm{mg/ml}$ and then increases again with a similar slope (cf. Figure 7.3(e)). D_2 is crowding-dependent, being smaller for higher protein concentrations. The residence time τ_2 exhibits a behavior very similar to that of τ_1, with $\tau_2 > \tau_1$, and is independent of c_p within the error bars (Figure 3(f)). The activation energy calculated from τ_2 for $T > T_d$ is $E_a \sim 13\,\mathrm{kcal/mol} \simeq 0.6\,\mathrm{eV}$ ($E_a \sim 12\,\mathrm{kcal/mol} \simeq 0.5\,\mathrm{eV}$ assuming the H-contaminated solvent, see above). Similarly to D_1 and τ_1, the values of D_2 and τ_2 for $c_p = 500\,\mathrm{mg/ml}$ after denaturation at $T = 300\,\mathrm{K}$ are only slightly shifted to slower dynamics. In particular, D_2 is somewhat lower and τ_2 higher in the denatured sample, indicating a minute slowdown of this diffusive component. Thus, we obtain that the change of the overall internal dynamics on the investigated length and time scales varies only slightly for different folded protein structures, and more significantly for the unfolded structure, while being independent of the entire-protein dynamics. This result supports the validity of the decoupling of the global from the internal dynamics.

We note that we observe dynamics that is significantly faster than the surrounding water, as becomes apparent when comparing the fit results for D_2 with the published values for the diffusion coefficient of water [170, 176]. Dynamics on similar or even faster time scales has been observed in related systems and attributed to side chain dynamics [76, 267]. The fast time scale can be rationalized in this picture by the fact that the side chain motions partly consist of fast rotations or reorientations of the chain, or of smaller subgroups such as methyl groups.

7.4.7 Geometry of Confined Motions

The EISF $A_0(q)$ in equation (7.6) contains information on the geometry of localized motions within the protein. Figure 4(a) and (b) depicts the EISFs as a function of q for the temperatures given in the legend and $c_p = 200$ and $500\,\mathrm{mg/ml}$, respectively (symbols). At the lowest temperatures the EISF can be fitted well by the model proposed in a previous study on γ-globulins, i.e. a sum of two contributions from methyl-group rotations and diffusion in a sphere [28]. By contrast, this model does not adequately describe our data when approaching and overcoming T_d. Extending the aforementioned model, we fit the EISF with the function

$$\begin{aligned} A_0(q) = p + (1-p)\, A_{\mathrm{G}}(q\,, a)\big[s\ A_{\mathrm{sph}}(q\,, R) \ldots \\ \cdots + (1-s)\ A_{\text{3-j}}(q\,, a_{\mathrm{M}})\big] \end{aligned} \tag{7.8}$$

Here, s is the fraction of hydrogen atoms diffusing in an impermeable sphere, and $(1-s)$ is the fraction of hydrogens undergoing three-sites jump-diffusion attributed in the physical picture to methyl-group reorientations. p represents the fraction of H-atoms appearing fixed on the accessible time scale. Consequently, $(1-p)$ is the fraction of H-atoms moving on the accessible time scale. The three-sites jump diffusion is modeled by the term [56, 59]

$$A_{\text{3-j}}(q\,, a_{\mathrm{M}}) = \frac{1}{3}\left[1 + 2j_0(q a_{\mathrm{M}})\right] \ , \tag{7.9}$$

where $j_0(x) = \sin(x)/x$ and $a_M = 1.715\,\text{Å}$ denotes the jump-distance of the H-atoms in a methyl group. $A_{\mathrm{sph}}(q)$ describes an atom diffusing freely within an impermeable sphere of radius R [57]:

$$A_{\mathrm{sph}}(q\,, R) = \left|\frac{3j_1(qR)}{qR}\right|^2 \ , \tag{7.10}$$

where $j_1(x)$ is the first order spherical Bessel function of the first kind. $A_{\mathrm{sph}}(q)$ and $A_{\text{3-j}}(q)$ are assumed to be uncorrelated and are thus combined in a sum. Both components are multiplied by the term

$$A_{\mathrm{G}}(q) = \exp\left(-\frac{(qa)^2}{5}\right) \tag{7.11}$$

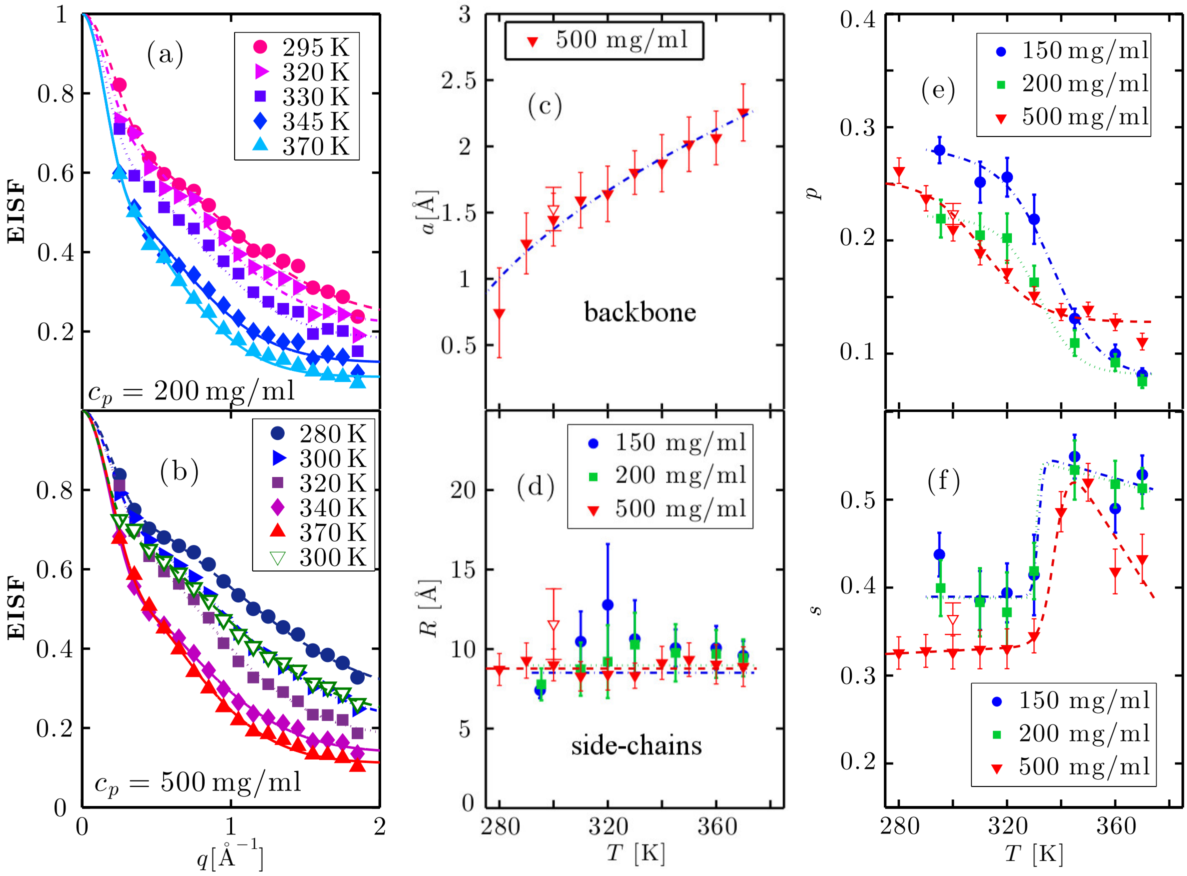

Figure 7.4: (a) and (b): EISF as a function of q at the temperatures given in the legend for $c_p = 200$ and $500\,\mathrm{mg/ml}$, respectively, (symbols) and fits following equation (7.8) (solid lines). (c) radius a (equation (7.11)) as a function of T for $c_p = 500\,\mathrm{mg/ml}$ (symbols) and fit with equation (7.12) (blue solid line). a is associated with the effective sphere accessible by backbone atoms. (d) Radius R (equation (7.10)) as a function of T (symbols). The lines are guides to the eye. This radius defines the sphere accessible by side-chain motions. (e) Fraction of immobile atoms p as a function of T (symbols). The lines are guides to the eye. (f) s as a function of T (symbols) defining the ratio of side-chains describable with a diffusion in a sphere model to the total amount of mobile side-chains. The line is a guide to the eye. The parameters in Figures 4(c)-(f) are obtained from the fit of the EISF with equation (7.8), and the open symbols in Figures 4(b)-(f) refer to the sample at $c_p = 500\,\mathrm{mg/ml}$ cooled down to room temperature after irreversible denaturation.

describing the diffusion of a particle in a potential with Gaussian radial profile around the equilibrium with effective radius a [58]. Anticipating the physical interpretation, this term may be understood as describing the geometry of confined fluctuations of the protein backbone on top of which the side-chains undergo their own motions in the geometries given by the combination of the other two components.

The fits with equation (7.8) are depicted by the lines in Figures 4(a)-(b). The open triangles measured in the gel-like sample at 300 K deviate slightly from those measured in solution before denaturation (full blue triangles) only in the lower q-range, reflecting a decrease of the confinement only for the largest accessible length scales in the denatured proteins. For $c_p = 500\,\mathrm{mg/ml}$, the radius a of the effective sphere accessible by the backbone is shown in Figure 4(c). If one assumes that backbone atoms sit in an elastic potential energy landscape, a can be fitted by

$$a = \sqrt{3k_{\mathrm{B}}(T - T_0)/\kappa}\ , \tag{7.12}$$

where k_{B} is the Boltzmann constant, κ represents the effective elastic constant, and T_0 is ideally the temperature above which the backbone starts fluctuating. We obtain an onset temperature $T_0 = 257 \pm 10\,\mathrm{K}$ ($T_0 = 241 \pm 20\,\mathrm{K}$ assuming the H-contaminated solvent, see above) for backbone fluctuations, comparable to the transition temperature between 260 and 270 K in the internal dynamics of bacteriorhodopsin (BR) [7, 89, 90]. Such a transition is probably related to solvent melting, since it only appeared with a hydration of $\gtrsim 93\%$ relative humidity [7, 89, 90]. The obtained force constant $\kappa = 0.09 \pm 0.01\,\mathrm{N/m}$ ($\kappa = 0.10 \pm 0.03\,\mathrm{N/m}$ assuming the H-contaminated solvent, see above) is of the same order of magnitude as that of highly hydrated BR above 270 K, $\kappa \sim 0.1\,\mathrm{N/m}$ [7, 89], and of that of BSA in solution [67] $\kappa \sim 0.041\,\mathrm{N/m}$, both averaged over the entire protein. For the lower concentrations, a follows a similar trend, but the statistical errors are larger. Therefore, in an attempt to reduce the error in the determination of the fit parameters for $c_p = 150$ and $200\,\mathrm{mg/ml}$, we set $a = \sqrt{3k_{\mathrm{B}}(T - 257\,\mathrm{K})/(0.09\,\mathrm{N\,m^{-1}})}$ in equation (7.8), thus reducing the number of free parameters to 3. Doing so, we assume that the geometry of the confined backbone fluctuations is essentially crowding-independent, although its dynamics varies with c_p as suggested by our previous study on γ-globulins [28].

The parameters R, s and p obtained from the fit of the EISF are plotted in Figures 4(d)-(f). The lines are guides to the eye. The radii R are roughly constant within the error bars, while as a general trend p decreases with temperature confirming earlier results [78, 80, 82, 102, 103, 105, 107, 108, 261]. Also the trend of s is similar for all protein concentrations: s remains essentially constant for $T < T_d$, reaches a sharp maximum about T_d and then decreases again, possibly reaching a plateau. All parameters indicate that, once the sample is cooled down back to 300 K (open triangles) only minor discrepancies with the system before denaturation have occurred.

7.5 Discussion of the General Physical Picture

While summarizing the results presented above, we discuss in the following a possible interpretation as an overall picture for the hierarchical protein dynamics measured here. Before going into detail, we note that our data are unequivocally characterized by a dynamical transition around $T_d \approx 342\,\mathrm{K}$, consistent with the literature [67, 259], probably coupled to the dynamical transition of hydration water [255, 258, 268]. Another slightly lower characteristic temperature around $T_b \sim 330\,\mathrm{K}$ is visible in the behavior of p (Figure 4(e)), above which structural changes are reported [259] and side-chains increase their mobility [258].

We assign the three diffusive processes in the model given by equation (7.6) (i.e. the processes associated with the diffusion coefficients d, D_1, and D_2, respectively) to three hierarchically distinct dynamics levels. The first of these is described by the short-time self-diffusion coefficient d and represents the dynamics of the entire protein. This process, although occurring at small time and length scales, is strictly related to macroscopic properties of the sample. It can be well described by the theory of colloids as long as the sample is still a solution, and becomes much slower when the gel is formed. When cooled down to room temperature after complete denaturation, the gel-like state is reflected in a much lower d than in the solution before heating up, indicating that the self-diffusion of entire proteins is strongly hindered e.g. through cross-linking or cluster formation.

The two-state model (equation (7.2)) describes a dynamical system that switches between two states with diffusion coefficients $D_{1,2}$ with constant switching rates $1/\tau_{1,2}$. Given the different magnitudes of D_1 and D_2 and comparable magnitudes of τ_1 and τ_2, we speculate that the two diffusive states correspond to two scenarios of side-chain confinement with respect to the protein backbone. (i) Side-chains are blocked in a certain position relative to the backbone atoms of the respective amino-acid (e.g. due to steric hindrance of close-by side-chains or fluctuating backbone segments). In this case the side-chains move together with the backbone with the diffusion coefficient D_1. (ii) The atoms of the side-chains are moving in a confined space limited mainly by the covalent bonds of the side-chain itself. These movements associated with the diffusion coefficient D_2 are one order of magnitude faster than the backbone motion that can be therefore neglected here. Mobile side-chains switch between the two states with residence times τ_1 and τ_2. We note that we cannot rule out a small contribution from interfacial water, which might occur at a similar time scale as the side chain motions. We neglect this possible effect due to the low scattering signal of the deuterated solvent, and attribute the two dynamical processes to backbone and side-chain diffusion.

This interpretation is consistent with the model for the EISF, where the geometry of confinement of the side-chains is "smeared-out" by that of the backbone on the order of $a \sim 1\,\text{Å}$. Therefore, in this picture, we account for the heterogeneity of protein internal dynamics by separating slower and smaller-amplitude backbone fluctuations from faster and greater-amplitude side-chain motions, coherently with previous findings [105, 108, 245, 246, 253].

The effect of temperature on the overall dynamics of proteins in solution at the observable time scales can be explained at different hierarchical levels as follows. For $T < T_d$ the proteins follow a center-of-mass diffusion in agreement with the theory of colloids. While the side-chain diffusivity increases linearly with T in this range, the effect on the dynamics of backbone fluctuations is rather limited. The effective radius a of the volume accessible to the backbone increases as a square-root, consistent with a spring model. The confinement radius R for the side chains remains constant within the errorbars, consistent with the length of a covalently bound side chain that determines the explored volume, rather than little fluctuations of atoms about its axis.

Around T_d, significant changes of the dynamics at all three levels are observed. The entire protein starts to slow down, probably because of cluster formation and cross-linking between proteins. At the same time, the backbone undergoes a dynamic crossover, similar to that reported for hydration water and for the backbone root mean-squared displacement (RMSD) of hydrated powders of lysozyme in NMR experiments [268] and simulations [255], and in the RMSD of BSA solutions from fixed window elastic neutron scattering [67]. Such an observation can be attributed to a Zimm-Bragg type structural transition of the α-helices to random coils [223]. The side-chain diffusivity follows a crowding-dependent behavior with a step-like reduction within a temperature range of $\sim 10\,\mathrm{K}$ for $c_p = 200$ and $500\,\mathrm{mg/ml}$, not discernible at the lowest concentration. This may be related to the increase of the exposed side-chains upon unfolding and a higher damping in the denser gel. The increase of τ_1 and τ_2 by an order of magnitude might be related to the higher solvent-accessible surface as well: the presence of water molecules might on the one hand prolong the average time needed for a side-chain getting solvent-exposed to “flip” between equilibrium positions, and on the other hand prevent it from moving for a longer time while waiting that D_2O density fluctuations allow it to escape the equilibrium position.

The geometry of confinement of both backbone and side-chains does not exhibit an equally pronounced transition, which is reasonable since the local confinement is mainly governed by the unaltered primary structure. The number of immobile atoms p decreases. The sharp increase of the fraction s of side-chains exploring an effective sphere with average radius R suggests that steric hindrance from other side chains decays due to changes of the secondary structure. We note that both fractions of mobile side-chains may include methyl-groups, but since $R \gg a_M$, their contribution can be neglected in a first approximation for the fraction s.

Further increasing T, proteins form bigger aggregates or become increasingly cross-linked into a gel-like state causing their global self-diffusion to decrease to a minimum. Proteins are now cross-linked through intermolecular β-sheets [249] and the global short-time self-diffusion is defined by the motion of the segments between two cross-links. At a certain point, either the clusters are too strongly charged to grow further or the cross-link number saturates, and protein global motion starts to increase again with T. The decrease of s is consistent with a stable structure with a constant number of side-chains free to diffuse in the effective sphere, while the increase of temperature unlocks the rotation of a higher number of methyl groups.

Finally, when cooling down the sample, although the system is now a gel, random coils undergo a partial refolding to α-helices or β-sheets. Even though refolding does not lead to the native structure, our data indicate that the dynamics of both backbone and side-chains of the non-native structure is similar to that of proteins in their native state on the nanometer length scale.

7.6 Conclusions

We present a comprehensive picture of hierarchical protein dynamics before and after thermal denaturation. Using high-quality data from the quasi-elastic neutron backscattering spectrometer BASIS in combination with novel and extended models for the scattering function, we provide a consistent interpretation of the data as a combination of contributions from three hierarchical dynamic levels: (i) entire-protein apparent self-diffusion, (ii) backbone fluctuations, and (iii) side-chain dynamics. As long as the protein is in its native conformation, i.e. below the transition temperature T_d, the translational self-diffusion is successfully described by colloid theory for hard spheres. The dynamics of the backbone is faster at lower protein concentration, and slows down for more crowded solutions at all temperatures. Increasing temperature results in accelerated dynamics and in a larger space accessible by backbone atoms, meaning that backbone dynamics becomes less confined. The side-chain dynamics also becomes slower with increasing protein concentration, while it becomes faster with increasing T. Below T_d, the geometrical confinement of the side-chains appears to be unaltered.

Above T_d, cross-links between the proteins and eventually a gel are formed. Connecting loops and random coils become at least as significant as intermolecular β-sheets and α-helices [249]. Consequentially, the center-of-mass protein dynamics decreases dramatically. By contrast, the average backbone fluctuations become faster. While the number of side-chains that can diffuse in their local environment increases, their average motion exhibits a sharp but limited crowding-dependent slowdown during denaturation, and subsequently continues its thermally-driven acceleration. Upon re-cooling, the denatured sample remains a gel. The global apparent self-diffusion in this case is significantly lower than in the solution at the same temperature, while the internal dynamics is comparable, probably due to partial refolding of proteins, although not in their native globular state.

The association of the model parameters with the three hierarchical dynamic levels, and in particular of the two linewidths $\Gamma_{1,2}$ with the backbone and side chain fluctuation, respectively, represents one consistent and physically justified interpretation. Although we cannot rule out other nontrivial models and interpretations of this complex system, the achieved picture of protein molecular dynamics during a complex process such as thermal denaturation is promising for future applications of quasi-elastic neutron scattering in complex systems with hierarchical dynamics down to the pico- and nanosecond time scale.

Acknowledgment

The research at Oak Ridge National Laboratory's Spallation Neutron Source was sponsored by the Scientific User Facilities Division, Office of Basic Energy Sciences, U.S. Department of Energy. The spectrometer BASIS is supported by the Jülich Center for Neutron Science (JCNS), Germany, via the partner user programme and M.G. and F.Za. acknowledge travel funding by JCNS to conduct the experiments as well as a student grant by the Institut Laue-Langevin (ILL). M.H., M.G. and T.S. have obtained travel funding by ILL. We acknowledge E. Mamontov, H. Schober and S. Da Vela for fruitful discussion and R. Moody for technical assistance. We further acknowledge financial support by the DFG.

Chapter 8

The Diffusion of BSA in the Presence of the Trivalent Salt YCl_3

This Chapter is based on the article [269]:

Salt-Induced Universal Slowing Down of the Short-Time Self-Diffusion of a Globular Protein in Aqueous Solution. [1]

Marco Grimaldo,[a,b] **Felix Roosen-Runge,**[a] **Marcus Hennig,**[a,b] **Fabio Zanini,**[b,f] **Fajun Zhang,**[b] **Michaela Zamponi,**[c,d] **Niina Jalarvo,**[c,e] **Frank Schreiber,**[b] **Tilo Seydel**[a]

The Journal of Physical Chemistry Letters **2015** *6*, 2577–2582.

[a] Institut Max von Laue - Paul Langevin (ILL), CS 20156, F-38042 Grenoble, France
[b] Institut für Angewandte Physik, Universität Tübingen, D-72076 Tübingen, Germany
[c] Jülich Centre for Neutron Science (JCNS), Forschungszentrum Jülich GmbH, D-52425 Jülich, Germany
[d] JCNS Outstation at the MLZ, Lichtenbergstraße 1, D-85747 Garching, Germany
[e] Chemical and Engineering Materials Division, Neutron Sciences Directorate, and JCNS Outstation at the Spallation Neutron Source (SNS), Oak Ridge National Laboratory, Oak Ridge, TN 37831, USA
[f] Present address: *Max-Planck Institute for Developmental Biology, Spemannstraße 35, D-72076 Tübingen, Germany*

8.1 Abstract

The short-time self-diffusion D of the globular model protein *Bovine Serum Albumin* (BSA) in aqueous (D_2O) solutions has been measured comprehensively as a function of the protein and trivalent salt (YCl_3) concentration, noted c_p and c_s, respectively. We observe that D follows a universal master curve $D(c_s, c_p) = D(c_s = 0, c_p)\, g(c_s/c_p)$, where $D(c_s = 0, c_p)$ is the diffusion coefficient in the absence of salt and $g(c_s/c_p)$ is a scalar function solely depending on the ratio of the salt and protein concentration. This observation is consistent with a universal scaling of the bonding probability in a picture of cluster formation of patchy particles. The finding corroborates the predictive power of the description of proteins as colloids with distinct attractive ion-activated surface patches.

8.2 Introduction

Diffusion is a ubiquitous process in a broad variety of condensed matter systems [32,270,271]. In the particular case of the biological cell, protein self-diffusion (i.e. the diffusion of single "tagged" protein macromolecules) governs e.g. transport processes, reaction kinetics and information exchange in the biological cell. Importantly, self-diffusion is affected by single-particle properties as well as by environmental factors. One well-known environmental control parameter for self-diffusion is macromolecular crowding, i.e. the dense packing fraction at which macromolecules such as proteins are usually found in the aqueous intracellular environment (Ref. [29, 272, 273] and references therein). The motion of proteins is affected by two kinds of interactions with surrounding macromolecules: direct interactions such as excluded volume and Coulomb interaction influence the dynamics on time scales of roughly microseconds and above. On shorter time scales, e.g. on the order of several nanoseconds, proteins interact only through quasi-instantaneous hydrodynamic interactions [32].

The presence of salts is another important control parameter that influences both structure and dynamics of protein solutions [41, 130] as well as e.g. DNA solutions [274], and may lead to the formation of protein aggregates [43, 134]. The interplay of macromolecular concentration and salts, physiological ones and others, to control condensation phenomena in protein solutions represents an important question with applications in medicine and biotechnology. Protein condensation is observed in several diseases [3], such as some forms of cataracts [4, 5], and neurodegenerative diseases [6]. In Parkinson's disease, raised levels of multivalent iron ions have been observed in sick neurons [275], pointing to a yet-to-be-explored role of salt. A deep understanding of the aggregation process of proteins is also of high interest for the tunable production of nanostructures through self-assembly [276]. Formation of clusters in dependence on protein concentration has been previously studied using small-angle scattering (SAS) [134,277,278], nuclear magnetic resonance (NMR) [279], dynamic light scattering (DLS) [280], and neutron spin-echo spectroscopy (NSE) [131].

Although studied since the pioneering work of Hofmeister more than a century ago [281],

---

[1] Author contributions: M. G., F. R.-R., M. H., T. S., F. Z., F. S. designed research; M. G., F. R.-R., M. H., T. S., F. Z., M. H. performed research; N. J. and M. Z. provided technical assistance; M. G. analyzed data; M. G., F. R.-R., T. S., F. Z., F. S. wrote the paper.

the effect of salt ions on the phase behavior of protein solutions presents still numerous questions. For the particular case of acidic proteins, trivalent salts such as $FeCl_3$ and YCl_3 induce complex reentrant phase diagrams depending on the protein concentration c_p and salt concentration c_s [161, 282], including macroscopic aggregation, liquid-liquid phase separation (LLPS) and protein crystallization [164, 282–285], and offer promising ways to manipulate the behavior of proteins. Based on the complex phase behavior, it is tempting to speculate that dynamic precursor processes of protein aggregation and crystallization occur already at lower trivalent salt concentrations. Such precursor processes may be the formation of small static or transient protein clusters. Indeed, our group has also explored the formation of clusters due to the presence of multivalent salts by SAS [284] and DLS [43].

Three factors render short-time self-diffusion a promising quantity to probe clustering of proteins as controlled by salt. First, the short-time self-diffusion of proteins can be described remarkably well by the theory of diffusion for effective hard spheres [28, 29], which links experimental results to a physical picture only based on the diffusional tensor of the single particle and an effective viscosity of the environment. In particular, the shift of structural correlation peaks due to a varying cluster size does not influence the interpretation. Second, the addition of salt efficiently alters direct interactions such as Coulomb repulsion, while hydrodynamic interactions remain comparable, which allows to study the non-trivial interplay of protein and salt concentration. Third, the short observation time scale much smaller than the collision time $\tau_i \approx 200\,\mathrm{ns}$ ensures that the effects of particle collisions and specific interactions with obstacles do not affect the observed diffusion. This short-time scale is routinely accessible by neutron spectroscopy as opposed to NMR, DLS, and fluorescence correlation (FCS) techniques.

In this context, incoherent quasi-elastic neutron backscattering (QENS) is an essential tool since it unambiguously accesses the self-diffusion of globular proteins on a nanometer length-scale and a nanosecond time-scale, even for crowded and possibly opaque samples [29]. Employing QENS to systematically investigate the protein short-time self-diffusion can hence provide crucial information on the presence or absence of clusters with a lifetime down to nanoseconds.

8.3 Results and Discussion

Spectra of protein solutions as a function of the energy transfer $\hbar\omega$ and the scattering vector q were recorded at the backscattering spectrometer BASIS [174] (SNS, ORNL) and fitted with the model described in detail elsewhere [29, 112, 170]

$$\begin{aligned} S(q,\omega) = \mathscr{R}(q,\omega) \otimes \Big\{ & \beta(q) \cdot \\ & \big[A_0(q)\, \mathscr{L}(\gamma(q),\omega) + \big(1 - A_0(q)\big)\, \mathscr{L}(\Gamma(q),\omega)\,\big] \\ & + \beta_{\mathrm{D_2O}}(q)\, \mathscr{L}(\gamma_{\mathrm{D_2O}}(q),\omega)\,\Big\}. \end{aligned} \tag{8.1}$$

Therein, $\mathscr{R}(q,\omega)$ represents the energy resolution function and $\mathscr{L}(\bullet,\omega)$ stand for Lorentzian functions with a linewidth related to dynamical processes in the sample. $\gamma(q)$ describes the global diffusion of the proteins, consisting of both translational and rotational contributions. $\Gamma(q)$ represents the internal relaxations accessed by the dynamic window of the spectrometer and convoluted with the global diffusion. $\beta(q)$ and $A_0(q)$ are scalars. The contribution of the solvent is modeled by the fixed term $\beta_{D_2O}\mathscr{L}(\gamma_{D_2O},\omega)$, as explained elsewhere [170]. In order to increase the contrast between the hydrogenated proteins and the surrounding solvent, we use D_2O rather than H_2O, as commonly done in neutron scattering by virtue of the large difference of the incoherent neutron scattering cross Sections of the two hydrogen isotopes.

An example spectrum is shown in the inset of Fig. 8.1. The red circles represent the recorded spectrum, the blue dot-dashed line depicts $\mathscr{L}(\gamma,\omega)$ and the green dashed line represents $\mathscr{L}(\Gamma,\omega)$. Finally, the turquoise solid line superimposed on the data is the result of the fit using equation (8.1). The widths $\gamma(q)$ obtained from the fit function in (8.1) are plotted in the main part of Fig. 8.1. The solid red line denotes the fit with the Fickian law $\gamma(q) = Dq^2$, where D is the global apparent self-diffusion coefficient of the proteins [28, 29].

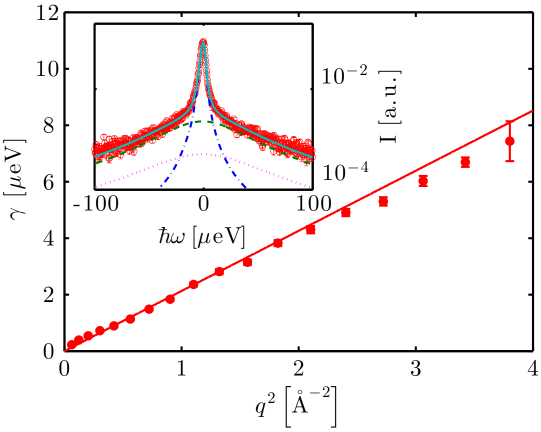

Figure 8.1: Inset: Example backscattering spectrum $I(q,\omega)$ (red circles) recorded at BASIS for BSA and YCl$_3$ in D_2O (c_p = 150 mg/ml, c_s = 8 mM, T = 295 K, individual detector at $q = 0.65$Å^{-1}). The blue dot-dashed line depicts $\mathscr{L}(\gamma,\omega)$ and the green dashed line pictures $\mathscr{L}(\Gamma,\omega)$ from Eq. (8.1). The turquoise solid line superimposed on the data is the result of the fit using Eq. (8.1). Main figure: Fitted γ (red circles) vs. q^2 for the full q-range of the example data. The fit $\gamma = Dq^2$ (solid red line) indicates a simple Brownian diffusive behavior with apparent self-diffusion coefficient D.

In this study, we explore the global diffusion coefficient D in solutions of the globular protein bovine serum albumin (BSA) depending on its concentration c_p and on the concentration c_s of the salt YCl$_3$ (cf. dots in Figure 8.2(b)). For several fixed protein volume fractions of approximately 7-20 %, we increase c_s, while remaining on an area of the phase diagram where no macroscopic aggregation or phase transition occur [161].

Strikingly, when plotting the reduced self-diffusion coefficient $D(c_s,c_p)/D(c_s = 0,c_p)$ as a function of the number of Y^{3+} ions per protein $N_s = c_s/c_p$ in Figure 8.2(a), we obtain a universal scaling for all measured protein concentrations. The master curve decreases continuously to 60% of the value with no added salt, when in the solution there are approximately 6 Y^{3+} ions per protein. Essentially, this curve characterizes the diffusion of BSA in the presence of YCl$_3$, in the

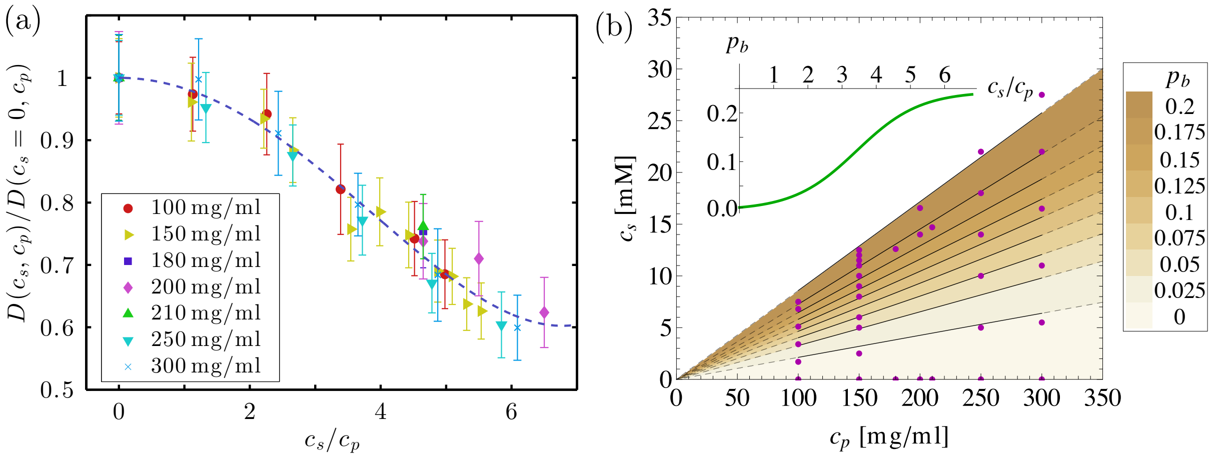

Figure 8.2: (a) Reduced short-time apparent self-diffusion coefficient $D(c_s, c_p)/D(c_s = 0, c_p)$ as a function of c_s/c_p (symbols). Independently from the protein concentration, all the points lie on a master curve which is parametrized by a polynomial function (dashed line, see text). (b) Contour plot of the bonding probability p_b as a function of c_p and c_s. The dots denote the coordinates where experimental data were recorded. The area with the solid lines corresponds to the range of protein concentrations measured in this study. The dashed lines are extrapolations to lower and higher protein concentrations. Inset: Bonding probability p_b as a function of the number of Y^{3+} ions per protein c_s/c_p as obtained from the experiment under the assumptions explained in the text, using equations (8.2) and (8.6) (see Methods Section).

entire explored range of c_p and c_s.

The dashed line in Figure 8.2(a) represents an empirical function for the master curve,

$$g(c_s/c_p) = 1 + a_2 \left(\frac{c_s}{c_p}\right)^2 + a_4 \left(\frac{c_s}{c_p}\right)^4 \tag{8.2}$$

with the parameters $a_2 = (-17.32 \pm 2.76) \times 10^{-3}$ and $a_4 = (18.86 \pm 8.93) \times 10^{-5}$.

Having established this rather remarkable universal behavior, we now turn to its possible origin. There may be several rather complex ways to model the salt dependence. In order to keep the model simple and limit the number of parameters, we consider a salt-induced cluster formation, inspired by the theory of ion-activated patchy particles [24,286], which was successfully used to semi-quantitatively describe the phase diagram of the system of BSA and YCl_3. In this physical picture, Y^{3+} ions bind to patches on the particle surface and thereby activate them for subsequent bridging between protein molecules. Thus, increasing the ions in solution increases the probability p_b of an ion-bridge between particles and so the formation of clusters.

The Flory-Stockmeyer theory provides a first-order estimation of the number density ρ_n^* of n-clusters [53, 54]:

$$\rho_n^* = (1 - p_b)^m \left[p_b (1 - p_b)^{m-2}\right]^{n-1} \frac{m(m\,n - n)!}{(m\,n - 2n + 2)!n!}\,, \tag{8.3}$$

where m is the maximum number of ion-bridges per particle, and n is the number of particles in the n-cluster. We chose $m = 4$ consistent with Ref. [24], inspired by the crystal structure displaying 4 ion bridges per monomer [283].

In order to compare our data with this theory we assume that, at the short-times probed with BASIS, the clusters are in good approximation rigid. Thus, movements of proteins within the clusters are neglected. Given the assumed strong bonds, these motions might occur on similar time scales as e.g. protein interdomain motions [121] beyond the observation time scale of our experiment. Moreover, we assume that each n-cluster diffuses according to the theory of colloidal hard-sphere suspensions as if they were in monodisperse suspensions at the actual volume fraction of the protein solution, i.e. for every cluster-size n

$$D_t^{(n)}(\phi) = D_t^{(1)}(\phi = 0)\, n^{-\nu}\, f_t(\phi) \tag{8.4}$$

$$D_r^{(n)}(\phi) = D_r^{(1)}(\phi = 0)\, n^{-\alpha}\, f_r(\phi)\,, \tag{8.5}$$

where $D_t^{(n)}$ and $D_r^{(n)}$ are the translational and rotational diffusion coefficients of the n-cluster, $D_t^{(1)}(\phi = 0) = k_B T/(6\pi\eta R_p)$, $D_r^{(1)}(\phi = 0) = k_B T/(8\pi\eta R_p^3)$ and R_p denote respectively the dilute limit diffusion coefficients and the effective hydrodynamic radius of the monomers. η represents the viscosity of the solvent and $f_{t,r}(\phi)$ is the theoretical reduced diffusion coefficient for hard-sphere suspensions [29, 37, 38]. Lacking a detailed description of the microscopic structure of clusters, we choose $\nu = 1/3$ and $\alpha = 1$, valid in the limit of low fractality. Thus, the hydrodynamic radius of an n-cluster scales as that of a hard sphere of volume nV_p, where V_p is the volume of a monomer.

The dynamic structure factor of the global diffusion is modeled for the cluster solution by

$$S_\gamma(q,\omega) = s\, \sum_n \rho_n^*(p_b)\, n\, S_n(q,\omega)\ . \tag{8.6}$$

Here, s is a scalar and the well-known scattering function for a single n-cluster $S_n(q,\omega)$ is provided in equation (8.7). Fitting of Eq. (8.6) to the experimental $\mathscr{L}(\gamma,\omega)$ obtained from equation (8.1) returns the two free parameters s and p_b. Interestingly, p_b for different protein concentrations, as derived from the master curve of the dynamics, follows itself a master curve (green line in inset of Figure 8.2(b)). Thus, the model reflects the damping of the diffusion, provided that the ion-bridge probability p_b depends only on c_s/c_p and not on ϕ. In other words, the observed universality of the dynamics would suggest that the contour lines of p_b in the explored area on the $c_p - c_s$ phase-diagram are straight lines with intercept 0 and increasing slope (cf. Figure 8.2(b)). A possible reason for the universality could be the nearly quantitative binding of cations to the protein due to a dominating ion binding energy. Such a result is important for a further refined picture along the model of ion-activated attractive patches in Ref. [24], also in connection with the generalized law of correspondent states for patchy interactions [287].

Importantly, this cluster picture could also explain previous results from light scattering in BSA solutions with lower volume fractions [43]. In these experiments, both reduced long-time collective diffusion and reduced isothermal compressibility showed a universal scaling with respect to c_s/c_p. With increasing c_s, the diffusion of both a monomer and a cluster fraction showed a substantial slowing down and the compressibility diverged. Using the ion-bridge probability derived from QENS, the DLS observations could be explained by the occurrence of increasingly large clusters with a size distribution universal in protein concentration, since the dynamics slows down and the total scattering power for light diverges once the clusters are large enough (cf. Fig. 3 in Ref. [24]).

We emphasize that our experiment does not allow to draw a conclusion whether the observed clusters are dynamic or transient (i.e. have a finite lifetime), or static.

On the nanosecond time scale explored by our experiment our model explains the measured short-time self-diffusion by at least temporarily “rigid” clusters, similar to NSE results on the formation of lysozyme clusters induced by the increase of the protein concentration (i.e. not by additional salt), where the lifetime of the observed clusters is longer than a few tens of nanoseconds [131, 288].

As an alternative scenario, the increase of attractive interactions between proteins due to bound Y^{3+} ions on the protein surface could enhance fluctuations of the local volume fraction φ of monomers and thus decrease the averaged apparent self-diffusion coefficient without the formation of bonds between particles, since most proteins would experience a denser packing. Under these assumptions, we would be able to describe our data assuming a well-separated bimodal distribution of φ. However, two points seem not to be consistent with a physical explanation along this scenario: (i) There is no obvious physical reason for a well-separated bimodal distribution $G(\varphi)$ away from a phase separation. (ii) There is no obvious physical reason why density fluctuations should produce a universal slowing down, since this implies a very specific relation between the fluctuation amplitude and the overall protein and salt concentration (see Figure SI1 in the Supporting Information).

8.4 Conclusion

In conclusion, we experimentally establish the existence of a remarkably universal slowing down of the short-time self-diffusion of the protein BSA as a function of the number of multivalent Yttrium ions per protein. The observation can be connected to earlier results [43] on a universal slowing down of the long-time collective diffusion of proteins in the same system (BSA + YCl_3 in solution) at lower protein concentration. In combination, the two results suggest that dynamics and thermodynamics in protein solutions can be tuned in a relatively universal manner for a broad range of protein concentration by the addition of multivalent cations.

Salt-induced cluster formation via ion-bridges renders a clear physical explanation for the universality and strength of the slowing down, provided that the ion-bridge probability depends only on the number of ions per protein, as e.g. expected for nearly quantitative binding of cations to the protein surface, embedding well into a general qualitative understanding of dynamics and thermodynamics in protein solutions with multivalent cations by assuming ion-activated attractive patches [24].

Such a result is promising in several respects. First, similar results might also be observed in other systems with strong crosslinking. Second, if the observations were indeed to be explained with the formation of clusters distributed according to a remarkably universal cluster distribution, the finding would be extremely relevant for a rational choice of pathways for self-assembly.

8.5 Experimental Methods

Sample preparation. BSA and YCl$_3$ were purchased from Sigma Aldrich with a purity of 98% (A3059) and 99.99% (451363), respectively. D$_2$O was purchased from Acros Organics with an indicated purity of 99.8%. Samples were prepared as described in Ref. [29]. After some hours on a roller mixer, all BSA powder was completely dissolved and the solutions appeared clear. For every protein concentration, a series of samples with increasing c_s were prepared. The solutions were filled into double-walled aluminum cylinders (23 mm outer diameter, 0.15 mm gap, i.e. difference between inner and outer radius), sealed against vacuum and kept at $T = 295$ K for the measurements.

Quasielastic Neutron Backscattering. We used the backscattering spectrometer BASIS [174] at the ORNL's Spallation Neutron Source in Oak Ridge, Tennessee, in the standard configuration with unpolished Si(111) analyzer crystals, which set the selected neutron wavelength to 6.27 Å. The energy resolution defined by the FWHM of the resolution function is approximately 3.5 µeV. The accessible energy transfer range is $-100 \leqslant \Delta E \leqslant +100$ µeV. The resulting accessible time range is thus

$$41\text{ps} \leqslant \tau = \frac{h}{\Delta E} \leqslant 1.2\text{ns} \; .$$

The q-range $0.25\ \text{Å}^{-1} \leqslant q \leqslant 1.95\ \text{Å}^{-1}$ sets the probed length scale $l = 2\pi/q$ to

$$25\ \text{Å} \geqslant l \geqslant 3.22\ \text{Å} \; .$$

The raw data were normalized to the incident neutron flux and relative detector efficiency. In order to remove the contribution of the sample holder from the spectra, the Paalman-Pings coefficients accounting for the q-dependent absorption of neutrons by the sample and the cell walls have been used. The details can be found in the Supporting Information.

Determination of p_b . The scattering function of a n-cluster is given by:

$$S_n(q,\omega) = \sum_{l=0}^{\infty} B_l(q) \frac{D_r^{(n)} l(l+1) + D_t^{(n)} q^2}{\omega^2 + [D_r^{(n)} l(l+1) + D_t^{(n)} q^2]^2} . \tag{8.7}$$

Therein, $D_t^{(n)}$ and $D_r^{(n)}$ are defined by the equations (8.4) and (8.5), respectively. $B_l(q)$ is defined as

$$B_l(q) = \int_0^{\infty} \mathrm{d}r \rho(r)(2l+1) j_l^2(qr),$$

where $\rho(r)$ describes the radial density distribution of the hydrogen atoms in the molecule and $j_l(x)$ denotes the lth-order spherical Bessel function of first kind. Under the assumption of homogeneously distributed H-atoms in effective hard spheres, $\rho(r) = 4\pi r^2$.

To obtain p_b, one can fit equations (8.6) and (8.7) to a Lorentzian function $\mathscr{L}(\gamma,\omega)$ with γ defined by

$$\gamma = D(c_s = 0, c_p)\, g(c_s/c_p)\, q^2 \, ,$$

where $g(c_s/c_p)$ denotes the master curve and $D(c_s = 0, c_p)$ is the apparent diffusion coefficient of the solution at protein concentration c_p and no added salt, which can be determined experimentally or calculated for an effective hard sphere by solving the equation [29]

$$\sum_{l=0}^{\infty} B_l(q) \frac{D_r l(l+1) + (D_t - D) q^2}{[D_r l(l+1) + (D_t + D) q^2]^2} = 0 \, ,$$

where $D_t \equiv D_t^{(1)}$ and $D_r \equiv D_r^{(1)}$, since at $c_s = 0$ the protein solution is a monodisperse suspension of monomers (i.e. n=1).

Supporting Information

A discussion of the alternative picture of dynamic density fluctuations can be found in Appendix C.

Acknowledgments

The research at Oak Ridge National Laboratory's Spallation Neutron Source was sponsored by the Scientific User Facilities Division, Office of Basic Energy Sciences, U.S. Department of Energy. The spectrometer BASIS is supported by the Jülich Center for Neutron Science (JCNS), Germany, via the partner user programme and M.G. and F.Za. acknowledge travel funding by JCNS to conduct the experiments as well as a student grant by the Institut Laue-Langevin (ILL). M.H., M.G. and T.S. have obtained travel funding by ILL to conduct the experiments. We acknowledge E. Mamontov, M. Oettel, R. Roth and H. Schober for fruitful discussions and R. Moody and V. Glenisson for assistance. We further acknowledge financial support by the DFG.

Chapter 9

Conclusion

In this Chapter, the main results of this thesis are summarized and possible impact of the results and developments are briefly discussed.

The aim of this thesis was the investigation of the diffusion and the internal dynamics of proteins in solution as a function of three parameters: the protein concentration, the solution temperature, and the concentration of multivalent ions. Effects related to these parameters on the dynamics of proteins are of interest for biology, colloid physics, chemical engineering and pharmacy. In order to obtain information on the picosecond to nanosecond timescale and nanometer length scale, we performed quasi-elastic neutron scattering experiments with a highly methodical approach consisting in the systematic variation of different parameters on simplified model systems. Importantly, all samples were aqueous solutions.

The study of a protein with a highly branched shape, γ-globulin (IgG), at various concentrations was performed in an attempt to understand the impact of the crowded environment found in living cells on protein diffusion and internal dynamics. Our results indicated that macromolecular crowding has a significant impact on both, as it induces both a significant slowing down of the diffusion of the protein, and an increase of the correlation times attributed to the side-chain motion, suggesting a stabilization of the protein structure, which may be of relevance for biological processes. Moreover, we showed that concepts of the physics of colloidal suspensions of hard spheres can be applied to describe the diffusion of the strongly anisotropic IgG on the nanosecond timescale, if the volume fraction assumed for the theoretical short-time translational diffusion coefficient is calculated with an effective particle radius, larger than that of the bare protein, but smaller than the hydrodynamic radius calculated from a rigid structure. An open challenge for future studies is the development of an improved model combining this outcome with recent results from NSE regarding the dynamics of the domains of IgG [30].

The performed investigation is, together with other works, a key step towards the understanding of the impact of the cellular environment on the dynamics of proteins. In this respect, neutron scattering studies of hydrogenated proteins in deuterated lysate [1] may provide additional information. Such a system is undoubtedly more complex than the aqueous solution of a single type of protein, but above all, it represents a more realistic model for mimicking the cellular environment. Moreover, as opposed to measurements in living cells, it allows for a systematic and controlled variation of diverse parameters (particularly crowding), similar to the experiments presented here.

Solutions of the globular protein BSA at three concentrations were used to investigate the impact of temperature and of thermal denaturation on protein dynamics. The diffusion of BSA was again found consistent with previous studies and colloid theories until when, due to the thermally induced unfolding of the protein, a gel-like network was formed and the protein mobility dropped. Especially at high temperatures, the data indicated the occurrence of two internal processes. In order to interpret the results, we developed a model describing an atom of the side-chain switching between two diffusive states, one where the side-chain motion is rather unhindered, the other where its dynamics is blocked with respect to the backbone. We obtained therewith a self-consistent physical picture of the internal dynamics before and after denaturation. Below denaturation, temperature has little or no effect on the diffusion coefficient associated with the backbone motion, while the diffusion coefficient assigned to the side-chains as well as the number of mobile atoms increase with rising temperature. After denaturation, the number of mobile atoms as well as the fraction of side-chains moving rather freely is significantly increased. Also, the diffusion coefficient attributed to the backbone fluctuations increased more markedly after denaturation, while that of the mobile side-chains was found be affected significantly only at the highest concentration, supposedly because of the vicinity of more side-chains of other proteins in the cross-linked network.

---

[1] Lysate is the product of the break of a cell by the rupture of the cellular membrane.

Besides being relevant in the processes of protein folding and unfolding, the discernment of backbone and side-chain dynamics may be of interest, for instance, to improve the understanding of allosteric regulation, in which the functionality of a protein is regulated by the binding of a specific molecule away from its active site, which may in turn imply some sort of "communication" mechanism along the protein.

In addition to this, we note that, from a mathematical point of view, the model used for the description of the internal dynamics can be applied also to a number of other processes where particles switch between two diffusive states, such as a protein diffusing for some time with a dynamical cluster, and then detaching and diffusing at a different rate, or also in fields different from soft-matter.

Finally, the effect of the trivalent salt YCl_3 on the diffusion of BSA in aqueous solution was investigated. Measurements at several protein and salt concentrations were performed, and a dampening of the diffusion was observed when increasing both the protein and the salt concentration. The influence of the concentration of BSA on its self-diffusion was thoroughly investigated in a previous backscattering study by Roosen-Runge et al. [29]. Interestingly, in addition to those results, we found that, at all measured concentrations c_p, the increase of the number of Y^{3+} ions per protein in solution caused, within the error bars, a universal slowing down relative to the diffusion at the same c_p but in the absence of salt. Inspired by Roosen-Runge et al. [24], the observation was interpreted in terms of colloidal suspensions of ion-activated patchy hard spheres predicting the formation of protein clusters through ion-bridges with a well-defined size distribution. A simplified scattering function derived for this scenario was fitted to the data and a binding probability p_b was obtained. We found that, within the error bars, p_b was itself following a universal behavior, which suggested an almost quantitative binding of the cations to specific sites on the protein surface. Therefore, the observed slowing down may be due to the presence in solution of clusters, the size distribution of which could be tuned by changing solely the ratio of the concentration of the salt and the concentration of the protein.

An interesting consequence of the suggested picture is the possibility of tuning the size distribution of the clusters also by changing the temperature of the system, thus without the need of modifying the sample composition. The observation and understanding of such a behavior may have important implications both in theoretical and applied fields, such as colloid physics and quantitative biology. For instance, it would be a good test for theories of colloid physics regarding patchy particles, it could lead to a rational choice of parameters for the production of self-assembling clusters, or even in the understanding of protein aggregation in biological cells, which is observed in several neurodegenerative diseases, where also multivalent salts seem to play a role.

Appendices

Appendix A

Supporting Information – Diffusion and dynamics of γ-globulin in crowded aqueous solutions[1]

A.1 Separation of Rotational and Translational Diffusion.

In order to compare the experimental results with existing theories, we have to extract the translational part D_t and the rotational part D_r from the measured apparent diffusion coefficient D. Following Ref. [29], we solve the expression

$$\sum_{l=0}^{\infty} B_l(q) \frac{D_r l(l+1) + (D_t - D)q^2}{[D_r l(l+1) + (D_t + D)q^2]^2} = 0, \tag{A.1}$$

for D_t. Here, D is determined experimentally, and $D_r(\varphi) = D_{r,0}(1 - 1.3\,\varphi^2)$ is assumed to correspond to the theoretical short-time rotational diffusion for charged spheres. Finally, $B_l(q)$ is defined as

$$B_l(q) = \int_0^{\infty} \mathrm{d}r \rho(r)(2l+1) j_l^2(qr)$$

where $\rho(r)$ describes the radial density distribution of the hydrogen atoms in the molecule and is calculated from the crystal structure of murine IgG – which can be identified with the γ-globulin in our samples except for some negligible amount of other immunoglobulins –, and $j_l(x)$ denotes the lth-order spherical Bessel function of first kind. Figure A.1 depicts $\rho(r)$ of IgG monomers and dimers and, for comparison, BSA.

The so-obtained D_t can be compared to the theoretical expression

$$D_t(\varphi) = D_0\, f(\varphi_t)\,,$$

with $\varphi_t = \varphi(R_h/R)^3$, where R is the radius of the effective sphere having the protein volume V_p. From the structure of IgG, we obtain for the monomer $R_h/R = 1.4$ and for the dimer $R_h/R = 1.5$. The structure of the dimer was obtained by simply combining two monomers as in the inset of Figure A.2.

---

[1] **Marco Grimaldo**[a,b], **Felix Roosen-Runge**[a], **Fajun Zhang**[b], **Tilo Seydel**[a] **and Frank Schreiber**[b]
[a] *Institut Laue-Langevin (ILL), B.P.156, F-38042 Grenoble, France.*
[b] *Institut für Angewandte Physik, Universität Tübingen, Auf der Morgenstelle 10, 72076 Tübingen, Germany.*

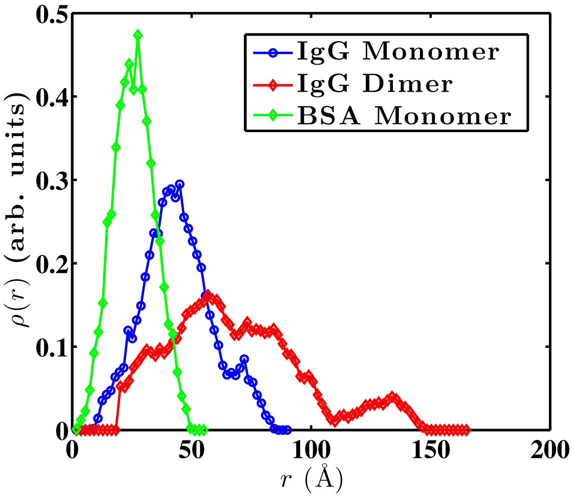

Figure A.1: Radial density distribution function $\rho(r)$ of hydrogen atoms in IgG monomers, dimers and, for comparison, BSA.

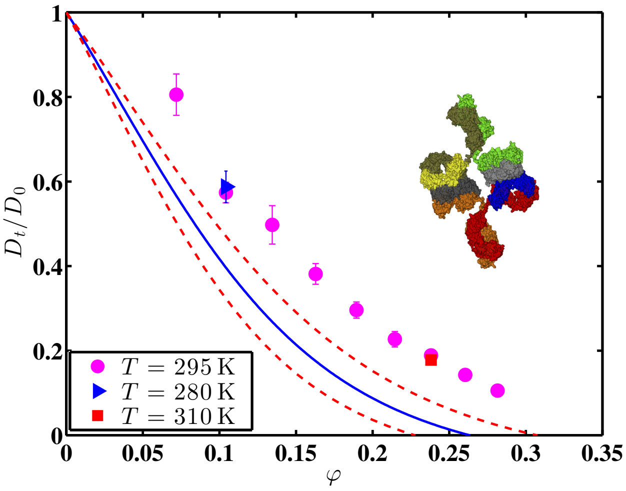

Figure A.2: Reduced short-time translational self-diffusion D_t/D_0 as a function of the volume fraction φ of γ-globulin in D_2O (symbols) when assuming dimers for the separation of rotation and translation from the apparent diffusion coefficient D. The calculation of both D_t and D_0, as well as of the factor $R_h/R = 1.5$ (R effective radius of a sphere with the protein volume V_p, R_h hydrodynamic radius) has thus been performed using the constructed dimer structure shown in the inset. The solid blue line indicates the normalized translational short-time self-diffusion from colloid theory for hard spheres [37] as a function of $\varphi_t = \varphi\,(R_h/R)^3$. The dashed lines indicate the colloid model for a 5% relative error on R_h/R.

A.2 Fit Results

We fit the EISF by:

$$A_0(q) = P + (1-P)\left[\Phi\ A_{\text{3-jump}}(q) + (1-\Phi)\ A_{\text{sphere}}(q)\right], \tag{A.2}$$

where [34]

$$A_{\text{3-jump}}(q) = \frac{1}{3}\left[1 + 2j_0(qa)\right] \ ,$$

and [57]

$$A_{\text{sphere}}(q) = \left|\frac{3j_1(qR)}{qR}\right|^2 \ .$$

In the three-site jump-diffusion model $j_0(x) = \sin(x)/x$, and $a \simeq 1.715$ Å denotes the jump-distance of the hydrogens in a methyl group. In the model for diffusion within a sphere, R is the radius and $j_1(x)$ is the first order spherical Bessel function of the first kind. In equation (A.2), Φ is the fraction of hydrogen atoms undergoing three-sites jump diffusion, and $(1-\Phi)$ is the fraction of hydrogens diffusing in an impermeable sphere. P represents the fraction of hydrogen atoms that appear fixed on the accessible time-scale [212]. The results of the fit are summarized in Table A.1.

Table A.1: Parameters of the fit of the EISF by equation (A.2).

c_p [mg/ml]	R [Å]	P	Φ
100	6.5 ± 1.6	0.32 ± 0.14	0.45 ± 0.18
150	6.83 ± 0.86	0.319 ± 0.041	0.571 ± 0.049
200	7.57 ± 1.46	0.292 ± 0.030	0.577 ± 0.037
250	5.7 ± 1.2	0.267 ± 0.067	0.584 ± 0.083
300	5.6 ± 1.3	0.259 ± 0.067	0.588 ± 0.085
350	5.9 ± 1.1	0.245 ± 0.053	0.586 ± 0.066
400	5.6 ± 1.1	0.256 ± 0.054	0.576 ± 0.072
450	6.1 ± 1.3	0.240 ± 0.046	0.581 ± 0.062
500	6.1 ± 1.2	0.241 ± 0.043	0.588 ± 0.060

The HWHM Γ are fitted with the model by Singwi and Sjölander citesingwisjolander1960

$$\Gamma = \frac{D_{\text{jump}}\; q^2}{1 + D_{\text{jump}}\; q^2 \tau} \;, \tag{A.3}$$

where τ denotes the residence time before a jump, and D_{jump} is the jump-diffusion coefficient. The results of the fit are summarized in Table A.2.

Table A.2: Parameters of the fit of Γ by equation (A.3).

c_p [mg/ml]	D_{jump} [Å^2/ns]	τ [ps]
100	160 ± 55	21 ± 5
150	113 ± 31	27 ± 4
200	121 ± 43	27 ± 4
250	140 ± 60	33 ± 4
300	117 ± 47	32 ± 4
350	187 ± 60	36 ± 3
400	135 ± 58	35 ± 4
450	168 ± 61	36 ± 3
500	142 ± 51	36 ± 3

A.3 Alternative Fits of the EISF

If one assigns the three-sites jump-diffusion component in

$$A_0(q) = P + (1 - P)\left[\Phi\; A_{\text{3-jump}}(q) + (1 - \Phi)\; A_{\text{sphere}}(q)\right] \tag{A.4}$$

to the methyl hydrogens in the protein, a rough estimate of the fraction $(1 - P)\,\Phi$ can be done by using the amino acid sequence in the PDB file, yielding $(1 - P)\,\Phi \simeq 0.22$. In this way, Φ can be fixed in (A.4). The results of the fit are shown in Figure A.3 and Table A.3.

Table A.3: Parameters of the fit of the EISF by equation (A.4) with $(1 - P)\,\Phi = 0.22$.

c_p [mg/ml]	R [Å]	P
100	6.63 ± 0.85	0.376 ± 0.024
150	6.55 ± 0.75	0.432 ± 0.016
200	6.2 ± 1.1	0.414 ± 0.018
250	5.65 ± 0.98	0.405 ± 0.021
300	5.8 ± 1.1	0.401 ± 0.023
350	6.2 ± 1.2	0.390 ± 0.024
400	5.6 ± 1.2	0.389 ± 0.023
450	6.1 ± 1.3	0.380 ± 0.023
500	6.0 ± 1.3	0.381 ± 0.023

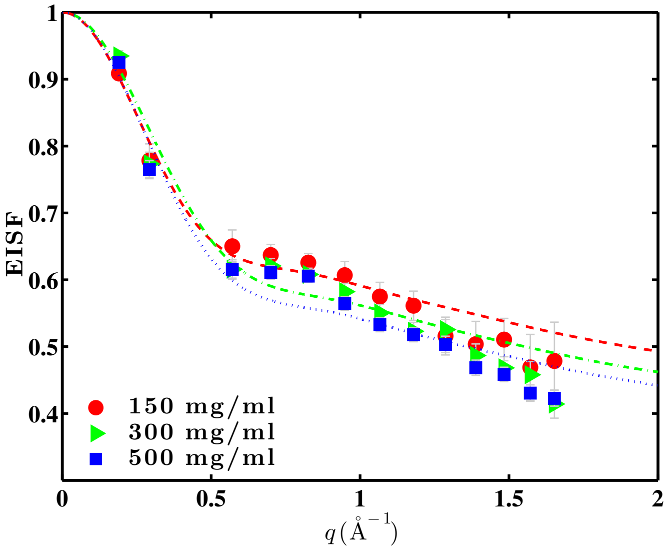

Figure A.3: Elastic incoherent structure factor (EISF) as a function of q for three γ-globulin concentrations (symbols). The lines are the fits by Eq. (A.4), with Φ fixed by $(1-P)\,\Phi \simeq 0.22$

A.4 Heavy Water (D_2O) Treatment

We apply the following procedure to quantitatively model the signal from D_2O.

1. Fit the heavy water measured using the time-of-flight spectrometer IN6 (ILL, incident wavelength $\lambda = 5.1\,\mathrm{\mathring{A}}$, resolution $\approx 90\,\mu$eV FWHM) with two Lorentz functions:

$$S(q,\omega) = A_\gamma \mathscr{L}_{\gamma_{\mathrm{D_2O}}}(\omega) + A_\Gamma \mathscr{L}_{\Gamma_{\mathrm{D_2O}}}(\omega) + B(q)\ ,$$

   where $\mathscr{L}_{\gamma_{\mathrm{D_2O}}}$ denotes the Lorentzian function describing the dynamics of the entire water molecule, and $\mathscr{L}_{\Gamma_{\mathrm{D_2O}}}(\omega)$ accounts for faster movements, the HWHM $\Gamma_{\mathrm{D_2O}}$ being a factor 3 or more larger than $\gamma_{\mathrm{D_2O}}$. A_γ and A_Γ are scalars. Only a slight curvature due to $\mathscr{L}_{\gamma_{\mathrm{D_2O}}}$ will be detectable within the dynamic range of IN16B.

2. Perform a polynomial fit of $\gamma_{\mathrm{D_2O}}$ as a function of q^2 (see Figure A.4).

3. For each protein concentration, scale the recorded water spectral intensity $I_{\mathrm{D_2O}}$ measured at IN16B by the protein volume fraction φ:

$$I^{(\varphi)}_{\mathrm{D_2O}}(q,\omega) = (1-\varphi) I_{\mathrm{D_2O}}(q,\omega)$$

4. Fit the scaled water spectra of IN16B (point 3.) with a single Lorentzian $\beta_{\mathrm{D_2O}} \mathscr{L}_{\gamma_{\mathrm{D_2O}}}(\omega)$ in order to determine the rescaled amplitude $\beta_{\mathrm{D_2O}}$. The width $\gamma_{\mathrm{D_2O}}$ of this Lorentzian is fixed from step 2. When the temperature of the protein solutions does not match the temperature of the D_2O spectra, an interpolation between the polynomial functions of the closest higher and lower temperatures is performed.

5. Add $\beta_{D_2O}\mathscr{L}_{\gamma_{D_2O}}(\omega)$ (fixed for every sample) to the fit function of the respective spectra:

$$S(q,\omega) = \mathscr{R} \otimes \{\beta \mathscr{L}_\gamma(\omega) \otimes [A_0(q)\delta(\omega) + (1 - A_0(q))\mathscr{L}_\Gamma(\omega)] + \\ + \beta_{D_2O}\mathscr{L}_{\gamma_{D_2O}}(\omega)\}$$

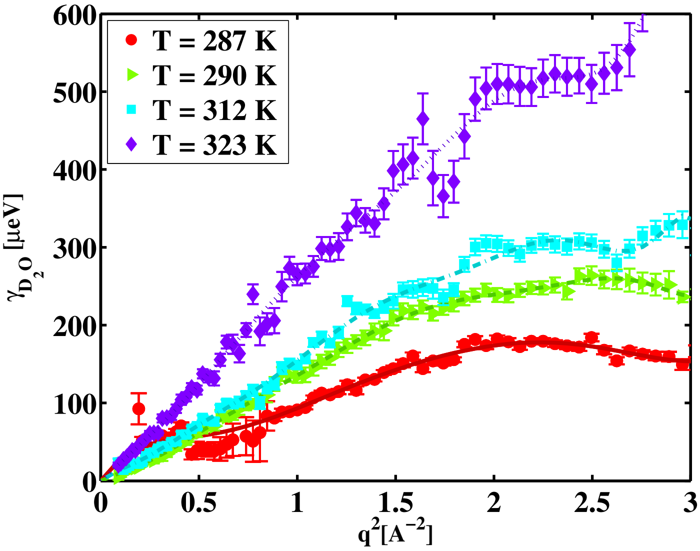

Figure A.4: Half width at half maximum γ_{D_2O} of the Lorentzian describing the quasi-elastic spectra of D_2O measured at IN6 at several temperatures (symbols). The lines superimposed to the data are polynomial fits.

A.5 Additional Examples of Measured Spectra.

In the following, additional examples of data collected at IN16B are shown. The inset depicts typical $S(q,\omega)$ (red circles) recorded using cold neutron backscattering for γ-globulin in D_2O at the concentrations and temperature indicated in the respective captions (individual detector at $q = 0.81\,\text{Å}^{-1}$). The lines depict the Lorentzian functions $\mathscr{L}_\gamma(\omega)$ (blue dot-dashed) $\mathscr{L}_{\gamma+\Gamma}(\omega)$ (green dashed) and $\mathscr{L}_{\gamma_{D_2O}}(\omega)$ (magenta dotted) in Eq. (5). The turquoise solid line superimposed on the data is the result of the complete fit using Eq. (5). Main figure: Fitted γ (red circles) vs. q^2 for the full accessible q-range. The fit $\gamma = Dq^2$ (solid red line) indicates a simple Brownian diffusive behavior. The fit range is restricted to $q^2 < 1.5\,\text{Å}^{-2}$.

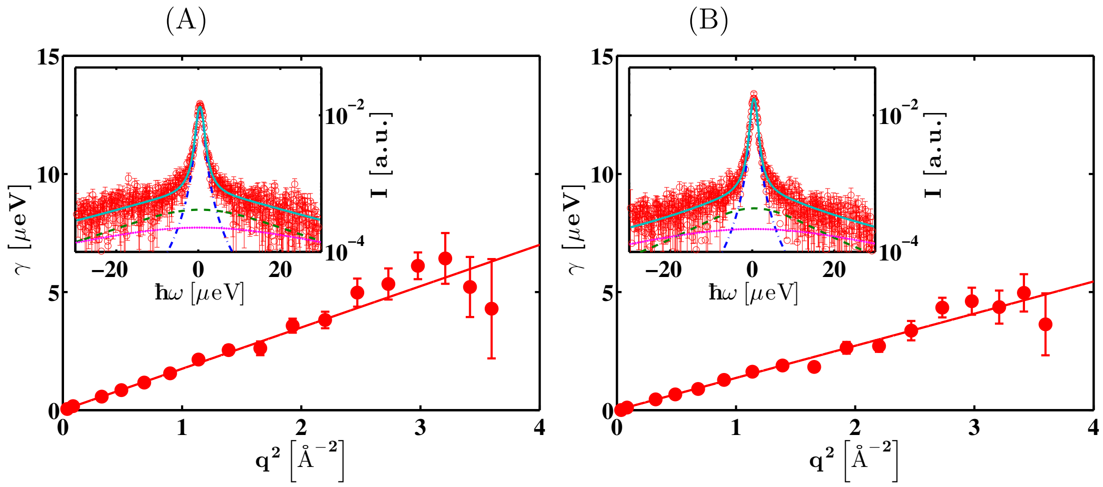
(A) (B)

Figure A.5: Example spectra and γ as a function of q^2 collected at IN16B for different IgG samples: (A) $c_p = 100\,\mathrm{mg/ml}$, $T = 295\,\mathrm{K}$, (B) $c_p = 150\,\mathrm{mg/ml}$, $T = 295\,\mathrm{K}$

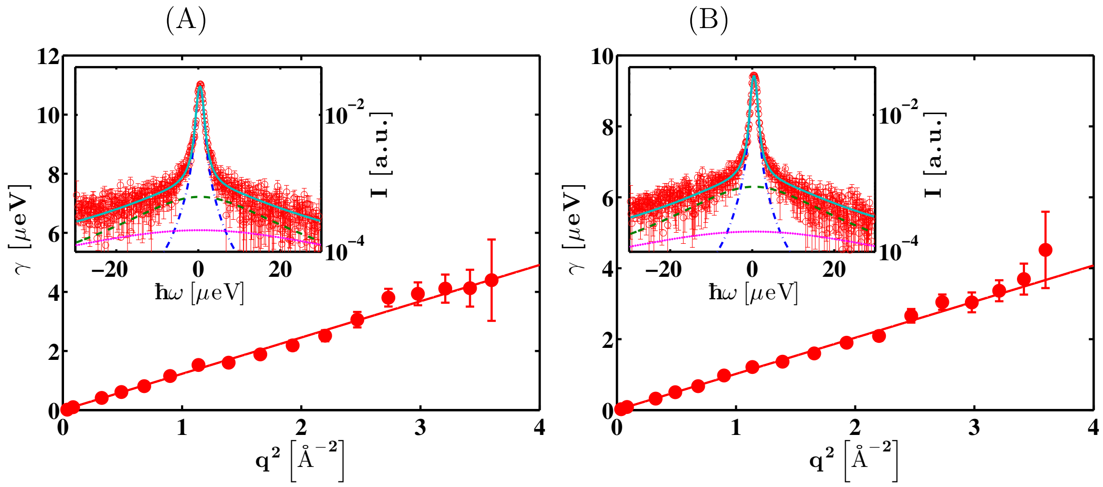
(A) (B)

Figure A.6: Example spectra and γ as a function of q^2 collected at IN16B for different IgG samples: (A) $c_p = 200\,\mathrm{mg/ml}$, $T = 295\,\mathrm{K}$, (B) $c_p = 250\,\mathrm{mg/ml}$, $T = 295\,\mathrm{K}$

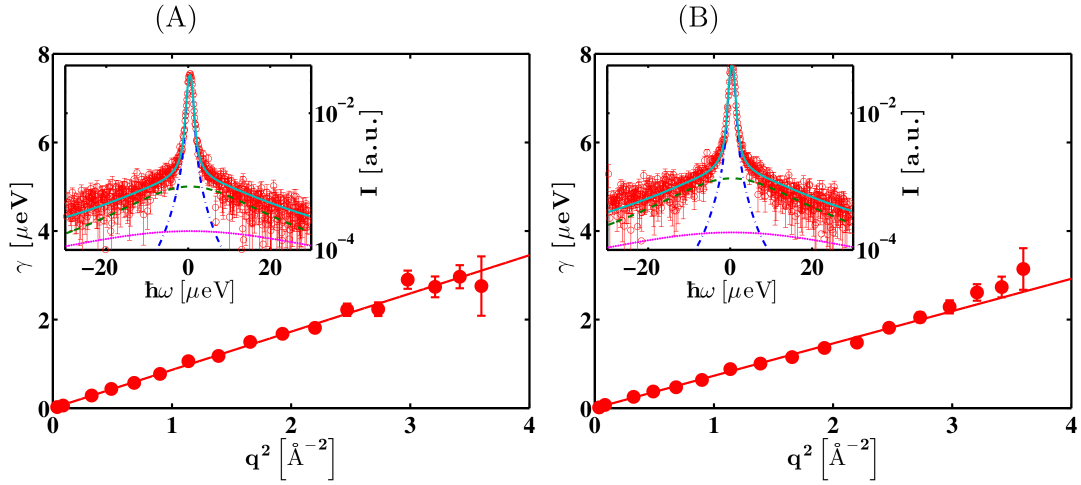

Figure A.7: Example spectra and γ as a function of q^2 collected at IN16B for different IgG samples: (A) $c_p = 300\,\mathrm{mg/ml}$, $T = 295\,\mathrm{K}$, (B) $c_p = 350\,\mathrm{mg/ml}$, $T = 295\,\mathrm{K}$

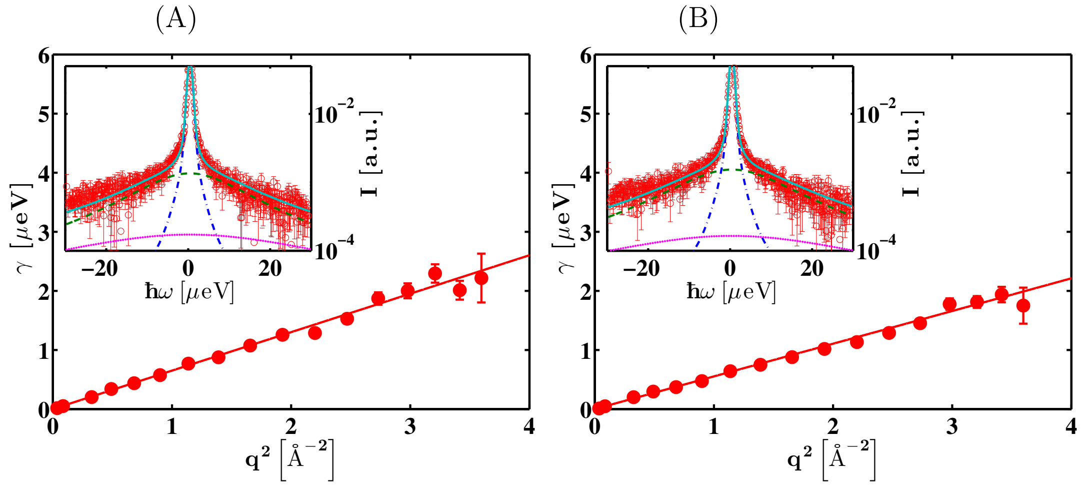

Figure A.8: Example spectra and γ as a function of q^2 collected at IN16B for different IgG samples: (A) $c_p = 400\,\mathrm{mg/ml}$, $T = 295\,\mathrm{K}$, (B) $c_p = 450\,\mathrm{mg/ml}$, $T = 295\,\mathrm{K}$

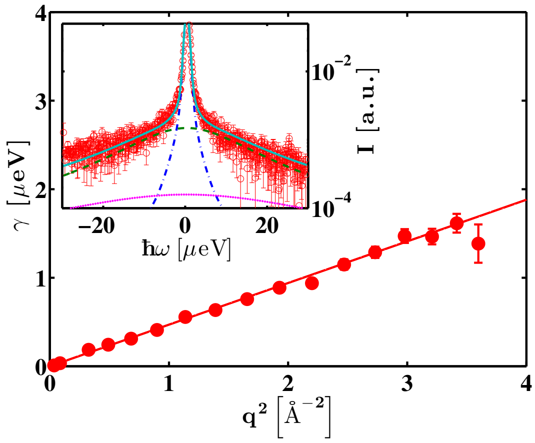

Figure A.9: Example spectrum and γ as a function of q^2 collected at IN16B the IgG sample at $c_p = 500\,\mathrm{mg/ml}$, $T = 295\,\mathrm{K}$

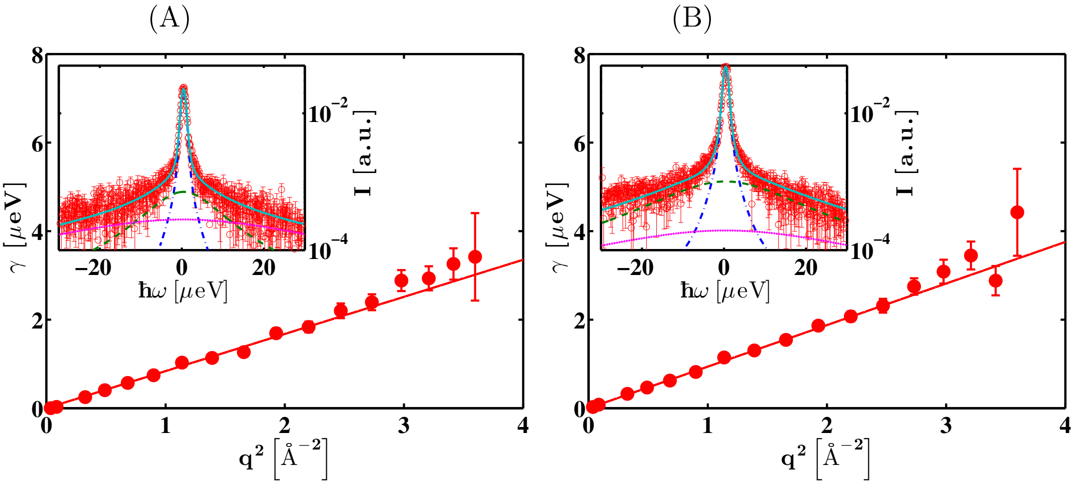

Figure A.10: Example spectra and γ as a function of q^2 collected at IN16B for different IgG samples: (A) $c_p = 150\,\mathrm{mg/ml}$, $T = 280\,\mathrm{K}$, (B) $c_p = 400\,\mathrm{mg/ml}$, $T = 310\,\mathrm{K}$

Appendix B

Supporting Information – Hierarchical molecular dynamics of bovine serum albumin in concentrated aqueous solution below and above thermal denaturation[1]

B.1 Effect of an Increase of the Hydrodynamic Radius on the Theoretical and Experimentally Determined Translational Diffusion Coefficients

The translational diffusion coefficient d_t becomes systematically lower than the value expected from the theory of colloids. The effect can be probably attributed to thermal expansion, which is however difficult to quantify. For example, as shown in Figure B.1 by the gray dashed lines a linear increase of the hydrodynamic radius R_H by 3% from 295 to 330 K lowers the theoretical translational diffusion coefficient, since the protein volume fraction is increased (even though there is a competing decrease of water density with T) and the dilute limit translational diffusion coefficient $d_0(T) = k_B T/(6\pi\, \eta(T)\, R_H)$ is decreased (k_B Boltzmann constant, $\eta(T)$ solvent viscosity) . The decrease of the rotational contribution

---

[1] **Marco Grimaldo,**[a,b] **Felix Roosen-Runge,**[a] **Marcus Hennig,**[a,b] **Fabio Zanini,**[b,f] **Fajun Zhang,**[b] **Niina Jalarvo,**[c,e] **Michaela Zamponi,**[c,d] **Frank Schreiber,**[b] **Tilo Seydel**[a]

Physical Chemistry Chemical Physics **2015** *17*, 4645–4655.

[a] Institut Max von Laue - Paul Langevin (ILL), CS 20156, F-38042 Grenoble, France
[b] Institut für Angewandte Physik, Universität Tübingen, D-72076 Tübingen, Germany
[c] Jülich Centre for Neutron Science (JCNS), Forschungszentrum Jülich GmbH, D-52425 Jülich, Germany
[d] JCNS Outstation at the MLZ, Lichtenbergstraße 1, D-85747 Garching, Germany
[e] Chemical and Engineering Materials Division, Neutron Sciences Directorate, and JCNS Outstation at the Spallation Neutron Source (SNS), Oak Ridge National Laboratory, Oak Ridge, TN 37831, USA
[f] Present address: *Max-Planck Institute for Developmental Biology, Spemannstraße 35, D-72076 Tübingen, Germany*

to the experimental apparent d yields slightly larger d_t (gray symbols).

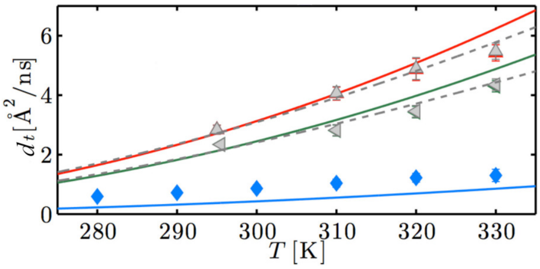

Figure B.1: Translational diffusion coefficients of BSA solutions as a function of temperature at three protein concentrations (from top to bottom, $c_p = 150, 200$ and $500\,\text{mg/ml}$). The solid lines are the values expected for a colloidal suspension at fixed R_H, while the gray symbols and dashed lines are the experimental and theoretical coefficients assuming a thermal expansion of R_H by 3%.

B.2 Alternative Models for the Analysis of the Scattering Function

In the following, we present the analysis of the data with a series of models for different physical pictures. In Section B.2.1 we show that the use of two components, one for the global and one for the internal dynamics, results in an unusual non-monotonicity of Γ as a function of q^2. In the following Sections we show that the models tested here yield unphysical or inconsistent results.

B.2.1 Single Lorentzian for the Global Protein motions and Single Lorentzian with HWHM Γ for the Internal Motions

The quasi-elastic scattering function can be modeled by [28, 29]

$$S(q,\omega) = \mathscr{R} \otimes \{\beta(q)\,[A_0(q)\mathscr{L}_\gamma(\omega) + (1 - A_0(q))\mathscr{L}_{\gamma+\Gamma}(\omega)] \ldots \\ \cdots + \beta_{\mathrm{D_2O}}\mathscr{L}_{\gamma_{\mathrm{D_2O}}}(\omega)\} \tag{B.1}$$

where $\mathcal{R}$ denotes the instrumental resolution function, modeled by a combination of Gaussian functions, $\beta(q)$ is a scalar, and $A_0(q)$ represents the elastic incoherent structure factor (EISF). The two Lorentzians $\mathcal{L}_\gamma(\omega)$ and $\mathcal{L}_{\gamma+\Gamma}(\omega)$ account for two processes occurring at distinct time scales. The HWHM Γ accounts for fast internal protein motions, while γ describes the apparent diffusion of the entire protein in solution. Finally, the fixed term $\beta_{\mathrm{D_2O}}\gamma_{\mathrm{D_2O}}$ models the solvent contribution as explained in Ref. [170]. Γ is plotted in Figure B.2 for three temperatures T (symbols), as indicated in the legend. At rather low temperatures, Γ can be well described by a jump-diffusion model as that by Singwi and Sjölander [60] (dotted blue line). However, at higher T, Γ has a peak at $q^2 \sim 0.4\,\text{Å}$, goes through a minimum and increases again at higher q^2. This non-monotonicity is inconsistent with a single process, since it would imply that a particle explores a larger area faster than a smaller. The jump-diffusion model mentioned above cannot describe such a behavior (cf. Figure B.2, green dot-dashed and red dashed lines), suggesting the presence of a multi-state diffusion.

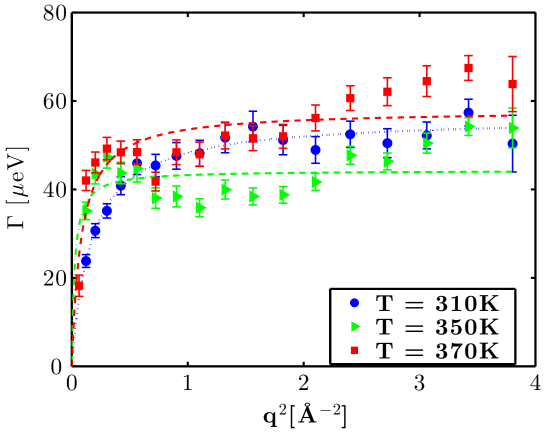

Figure B.2: HWHM Γ of the Lorentzian function describing the internal motions as a function of q^2 for the model in equation (B.1). Using only one Lorentzian function for the fit of global diffusion and one for the internal motions results in a non-monotonic Γ at higher temperatures, suggesting the presence of at least one additional diffusive process.

B.2.2 Static Distribution of Two Populations (Clusters and Monomers) - Homogeneous Internal Dynamics

Physical picture. There are two species in solution: clusters and monomers. Their volume fractions are ϕ_c and ϕ_m, respectively, with $\phi_m = 1 - \phi_c$. Proteins are thus either in a monomeric form or in a cluster, and do not exchange in the time-scale of the experiment. The overall internal dynamics can be described by a single effective Lorentzian function and is the same for the monomers and for the proteins in a cluster. The corresponding scattering function is:

$$S(q,\omega) = \beta(q)\{[\phi_c \mathscr{L}_{\gamma_c}(\omega) + (1-\phi_c)\mathscr{L}_{\gamma_m}(\omega)] \otimes [A_0\,\delta(\omega) + (1-A_0)\,\mathscr{L}_\Gamma(\omega)]\} \tag{B.2}$$

With the assumption that at such short time-scales the global dynamics can be described by a Fickian law, also at high temperatures, $\gamma_j = d_j\,q^2$ (d is the diffusion coefficient, $j = m, c$) and a global fit over all the spectra at different q can be performed.

Parameters. Cluster fraction ϕ_c and cluster apparent diffusion coefficient d_c and monomer apparent diffusion coefficient d_m are global parameters, $\beta(q)$, A_0 and Γ are q-dependent.

Expectations. ϕ_c should be ~ 0 at room temperature and up to the denaturation temperature; then, increase with T and become the main component. d_c should be considerably lower than d_m. On the other hand, d_m should not be higher than $d_0\,q^2$, and, as long as the cluster fraction is low, be consistent with colloid theory.

The obtained parameters are plotted as a function of T in Figure B.3.

- ϕ_c indicates that, even at temperatures well below denaturation, the main population is composed by clusters (Figure B.3(c)), and is thus inconsistent with previous findings [29].

- The faster diffusion coefficient d_m associated with monomers, is much higher than $d(c_p = 500mg/ml)$, while the slow component d_c which should account for clusters is closer to the value expected for monomers (cf. Figures B.3(a) and (b)).

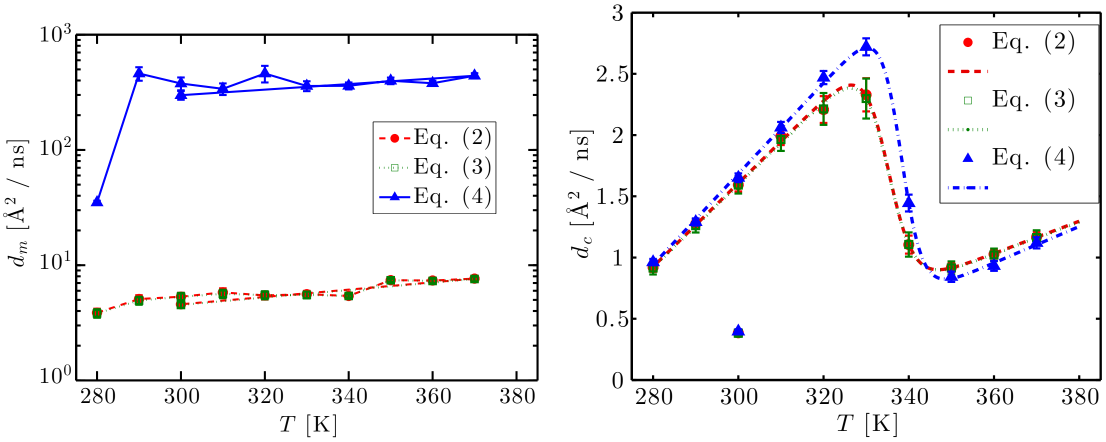

(a) Apparent diffusion coefficient d_m as a function of temperature T resulting from the models in equations (1)-(3), as reported in the legend, for $c_p = 500\,\mathrm{mg/ml}$. d_m is associated with the diffusion of monomers, since it is the faster global diffusive process in the respective models. In all cases shown here, and especially for the last model, d_m is significantly higher than the theoretical diffusion coefficient at $c_p = 500\,\mathrm{mg/ml}$, being thus inconsistent with the assumptions in the models.

(b) Apparent diffusion coefficient d_c as a function of temperature T resulting from the models in equations (1)-(3), as reported in the legend, for $c_p = 500\,\mathrm{mg/ml}$ (symbols). The lines are guides to the eye. d_c is associated with the diffusion of clusters, since it is the slower global diffusive process in the respective models. In all cases shown here, the extraction of the translational diffusion coefficient from the apparent coefficient d_c would be close to the theoretical translational diffusion coefficient of monomers at $c_p = 500\,\mathrm{mg/ml}$. Together with the values of d_m in Figure B.3(a), this suggests that our data are not consistent with the presence of monomers *and* clusters in solution.

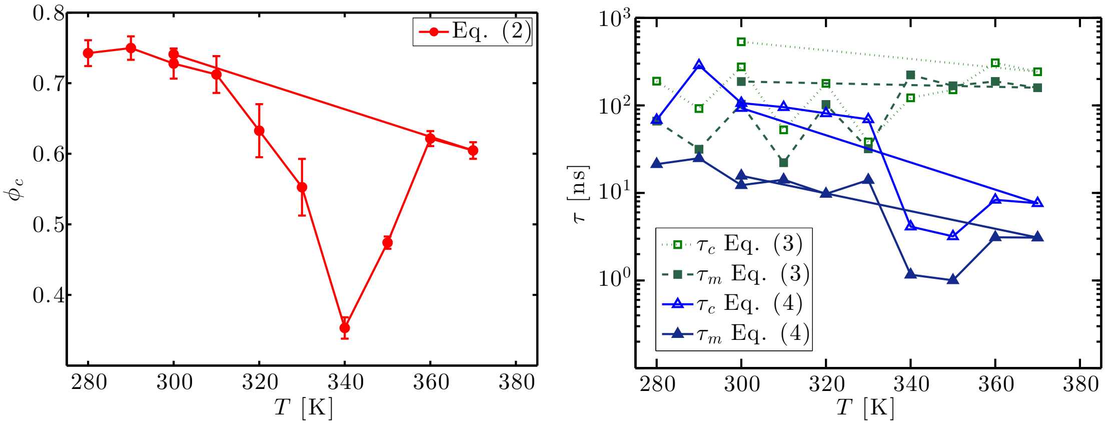

(c) Fraction ϕ_c of proteins in clusters calculated from model (B.2) as a function of T. This result would suggest a high amount of clusters in solution, even far away from denaturation, which seems highly unlikely, also combined with the results in Figures B.3(a) and (b).

(d) Residence times τ_m and τ_c as a function of T for $c_p = 500\,\mathrm{mg/ml}$, calculated from the fits of the scattering data by equations (3) and (4), as indicated in the legend. In general, their values are much higher than the time-range accessible by the instrument, and are thus inconsistent with the assumption made in the model that monomers bind and unbind from clusters on the time-scale sampled by the instrument. Furthermore, τ_c is always greater than τ_m, meaning that clusters are the main component, which is again inconsistent with expectations.

Figure B.3: Fit parameters d_m, d_c, ϕ_c, τ_m and τ_c from various models as discussed in the captions below the subfigures. These parameters are essentially unphysical or inconsistent with the assumptions made in the respective models.

- Having introduced the component $d_c\,q^2$ removes the "unusual" non-monotonicity of Γ discussed in the previous Section: Γ seems now rather consistent with a Singwi-Sjölander jump-diffusion model, as shown in Figure B.4, *left*.

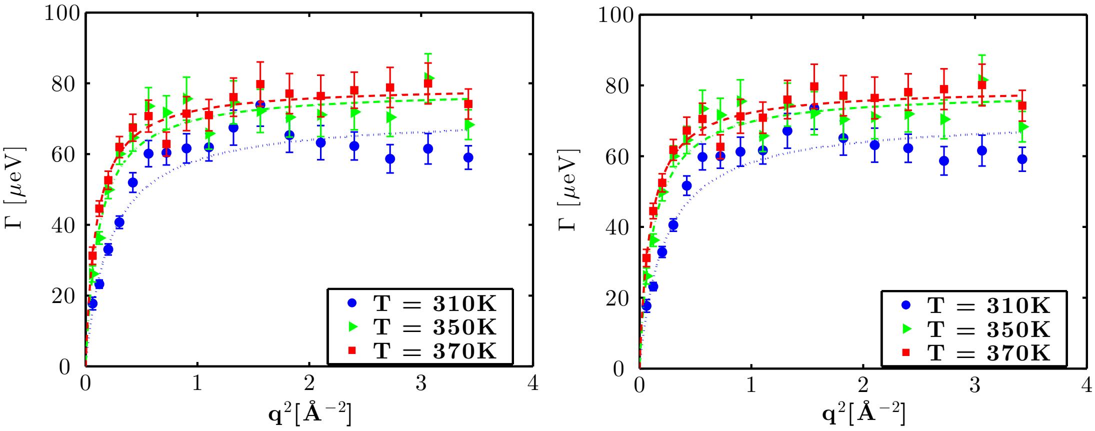

Figure B.4: HWHM Γ of the Lorentzian function describing the internal motions as a function of q^2 for the model in equation (B.2) (*left*) and that in equation (B.3) (*right*). Adding a component for the protein global diffusion essentially removes the non-monotonicity of Γ, although the diffusion coefficients obtained for the global diffusion are not consistent with the physical picture (see text).

B.2.3 Distribution of Dynamical Clusters and Monomers: Switching Mmodel for the Global Diffusion (2 Alternating Diffusive States) - Homogeneous Internal Dynamics

Physical picture. Proteins are alternating between a state diffusing with a cluster and a state diffusing as monomers. Such an exchange is visible on the time-scale of the experiment. The overall internal dynamics can be described by a single effective Lorentzian function and is the same for the monomers and for the proteins in a cluster. The corresponding scattering function is:

$$S(q,\omega) = \beta\{S_{\mathrm{sw}}(q,\omega)) \otimes [A_0\,\delta(\omega) + (1-A_0)\,\mathscr{L}_\Gamma(\omega)]\}\ , \tag{B.3}$$

where $S_{\mathrm{sw}}(q,\omega)$ is the scattering function of the switching model (Equation (2) in the article). Assuming that at such short time-scales the global diffusion of monomers and clusters follow a Fickian law, $\gamma_j = d_j\,q^2$ (d is the diffusion coefficient, $j = m, c$) and a global fit over all the spectra at different q can be done.

Parameters. The monomer d_m and cluster d_c apparent diffusion coefficients, and the residence times τ_m and τ_c in the two states are global parameters, β, A_0 and Γ are q-dependent.

Expectations. d_m and d_c should be consistent with the theoretical diffusion coefficients of monomers and clusters, respectively. Moreover, it is reasonable to expect that at low temperatures τ_c is ~ 0, meaning that clusters are almost completely absent.

The obtained parameters are plotted as a function of T in Figure B.3 and are almost exactly the same as for the previous model.

We observe that:

- d_m seems too big, at least at low T, and d_m and d_c are not consistent with a population of monomers and clusters.
- Both τ_c and τ_m are of the order of several hundreds of nanoseconds, which is not consistent with the assumption that the proteins are switching from one to the other diffusive state on the time-scale accessible by the instrument. Such a result would rather point back to a static picture (if it wasn't for the first observation). Note that $\tau(T)$ is plotted without the error bars, since these would be very large.
- As with the previous model, the addition of the Lorentzian with HWHM $d_c\, q^2$ removes the non-monotonicity of Γ, which is here consistent with jump-diffusion (see Figure B.4 *right*).

B.2.4 Distribution of Dynamical Clusters and Monomers: Switching Model for the Global Diffusion (2 Alternating Diffusive States) - Heterogeneous Internal Dynamics Modeled by 2 Alternating Diffusive States

Physical picture. Proteins are alternating between a state diffusing with a cluster and a state diffusing as monomers. Such an exchange happens within the time-scale of the experiment. Also the internal dynamics is modeled by two alternating diffusive states. The corresponding scattering function is:

$$S(q,\omega) = \beta\{S^{g}_{\mathrm{sw}}(q,\omega)) \otimes \left[A_0\, \delta(\omega) + (1-A_0)\, S^{i}_{\mathrm{sw}}(q,\omega))\right]\} \;, \tag{B.4}$$

where $S^{g}_{\mathrm{sw}}(q,\omega)$ and $S^{i}_{\mathrm{sw}}(q,\omega)$ are the scattering functions of the switching models for the global and internal motions respectively. Assuming that at such short time-scales the global dynamics can be described by a Fickian law, $\gamma_j = d_j\, q^2$ (d is the diffusion coefficient, $j = m, c$) and a global fit over all the spectra at different q can be done.
Parameters. d_m,d_c, τ_m, τ_c, D_1,D_2, $\tau_1^{(\mathrm{int})}$, $\tau_2^{(\mathrm{int})}$ are global parameters, β and A_0 are q-dependent.
Expectations. d_c and d_m should be consistent with the diffusion of a cluster and a monomer. Moreover, it is reasonable to expect that at low temperatures $\tau_c \ll \tau_m$, meaning that clusters are almost completely absent.

The obtained parameters are plotted as a function of T in Figure B.3.

- d_m is several hundreds Å^2 / ns . Not consistent with diffusion of monomers.
- Both τ_c and τ_m are of the order of some nanoseconds, which is not consistent with the assumption that the proteins are switching from one to the other diffusive state on the time-scale accessible by the instrument.

B.3 Effect of the H/D-Exchange Between the Native Proteins and the Deuterated Solvent Water

Labile H-atoms of the native proteins in solution may exchange with the deuterium from the solvent water. This exchange increases the amplitude of the solvent water in the contribution to the total scattering signal. In the following we estimate the maximum possible H/D-exchange and with the increased solvent amplitude repeat the fits reported in the article to which the present document is the Supplementary Information. We display the fit results assuming the H/D-exchange in the figures B.5,B.6, and B.7. Due to the remaining uncertainty on the actual magnitude of the H/D-exchange and the water structure factor, we do not display these figures in the article itself.

We obtain the number 776 of labile, i.e. exchangeable H-atoms per BSA protein from the protein data base (PDB) file [145], using VMD to determine the surface amino acids and a MATLAB script to count the number of exchangeable H-atoms according to Ref. [264]. Subsequently, we assume that all labile H-atoms actually exchange. The number density of exchangeable H-atoms then reads $n_H = 776 n_{BSA}$ where $n_{BSA} = c_{BSA}/M_{BSA}/(c_{BSA}\vartheta_{BSA} + 1\text{ml})$ is the number density of protein at the nominal concentration c_{BSA} (mg/ml). $\vartheta_{BSA} = 0.74\,\text{ml/g}$ is the specific volume and $M_{BSA} = 66500\,\text{g/mol}$ is the molecular weight of BSA. The number density of D-atoms from the water solvent is given by $n_D = 2 \cdot 55.5 M[1 - c_{BSA}\vartheta_{BSA}/(c_{BSA}\vartheta_{BSA} + 1\text{ml})]$. The contamination fraction of H-atoms α in the solvent is then simply calculated via $r_H = n_H/(n_H + n_D)$. Using this estimation, we obtain $\alpha \approx 1\,\%$, $2\,\%$, and $5\,\%$ H-contamination of the solvent water by atom number density, respectively, for the protein concentrations 100 mg/ml, 200 mg/ml, and 500 mg/ml, respectively.

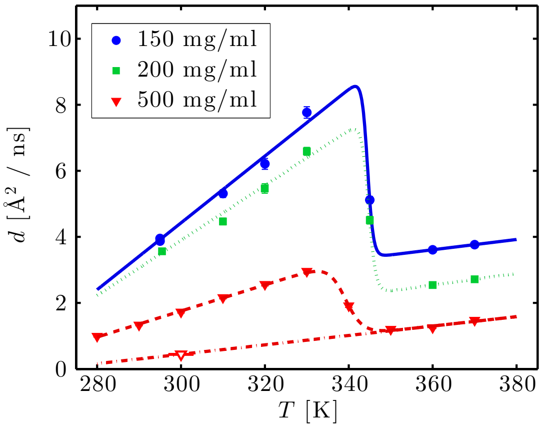

Figure B.5: Apparent self-diffusion coefficient d as a function of T for $c_p = 150$, 200 and 500 mg/ml (symbols) and fits with the two-state switching diffusion model (see article, lines), assuming an H/D-exchange between the proteins and the solvent water as outlined in Section B.3.

Assuming a similar dynamics of all atomic components in the water, the total scattering cross Section $\sigma_{tot}^{(X)}$ of the H/D-mixture $X = \alpha H + (1 - \alpha)D$ can then simply be calculated from the tabulated values for the total scattering cross Sections of H, D, and O:

$$\sigma_{tot}^{(X)} = 2\alpha\sigma_{tot}^{(H)} + 2(1-\alpha)\sigma_{tot}^{(D)} + \sigma_{tot}^{(O)} \tag{B.5}$$

With this expression, we obtain the following factors for the increase of the total scattering of the H-contaminated D_2O-solvent with respect to pure D_2O: 1.08 for 1 % contamination corresponding to 100 mg/ml BSA, 1.16 for 2 % contamination (200 mg/ml), 1.38 for 5 % contamination (500 mg/ml).

We have performed the analysis with these assumptions for the H/D-exchange, and the results are depicted in the Figures B.5, B.6 and B.7. We observe that the fit results are overall very similar to those obtained when not taking into account the H/D-exchange.

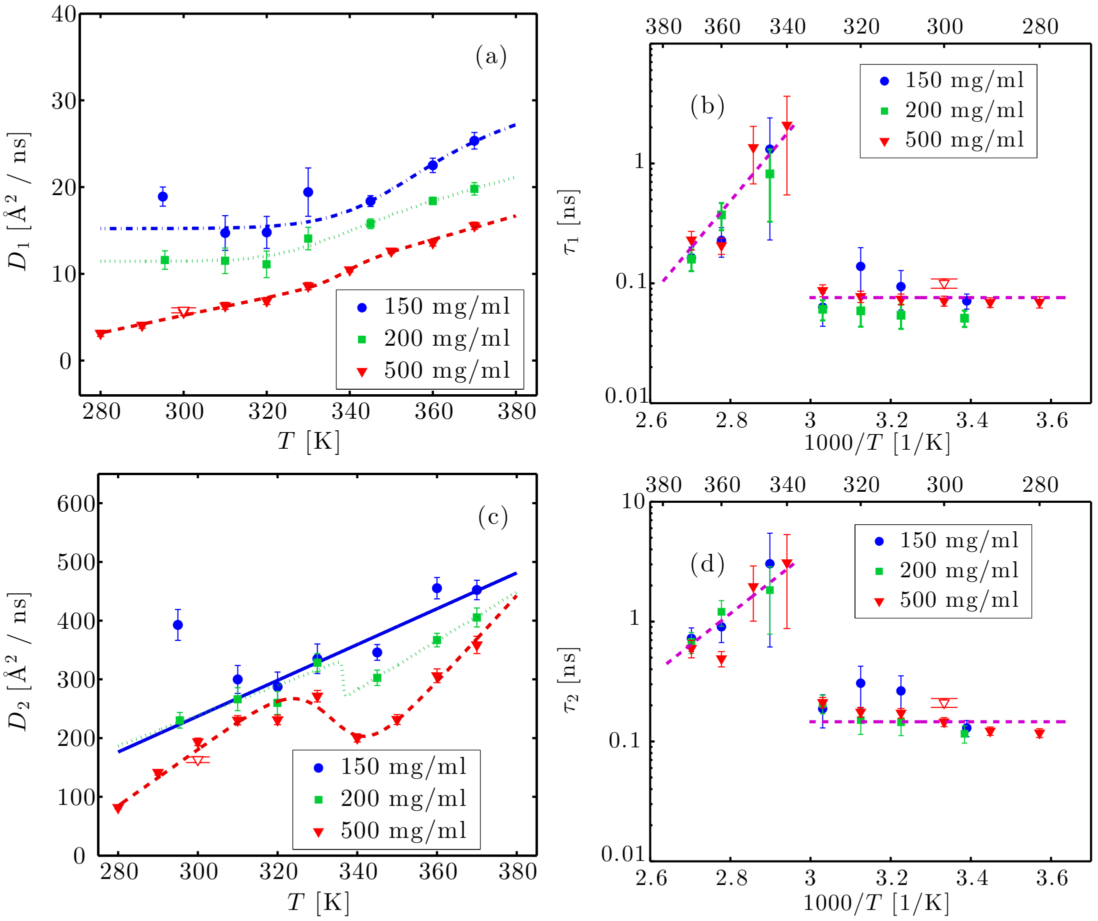

Figure B.6: Fit results for the two-state switching diffusion model assuming an H/D-exchange between the proteins and the solvent water as outlined in Section B.3: (a) D_1 as a function of T (symbols). The lines are guides to the eye. (b) Arrhenius plot of the residence time τ_1 between two jumps of the side-chains versus T for three c_p (symbols). The data above denaturation were fitted with an Arrhenius equation (line), while at low temperatures the line is a guide to the eye. (c) D_2 as a function of T for the concentrations reported in the legend (symbols). The lines are guides to the eye. The illustrations depict solvent-inaccessible side-chains in the folded protein (left) becoming solvent-exposed in the unfolded protein (right). (f) Arrhenius plot of the residence time τ_2 as a function of T (symbols). The data above denaturation were fitted with an Arrhenius equation (line). The red open triangles in (a), (c)-(f) refer to the sample at 500 mg/ml cooled back to room temperature after denaturation.

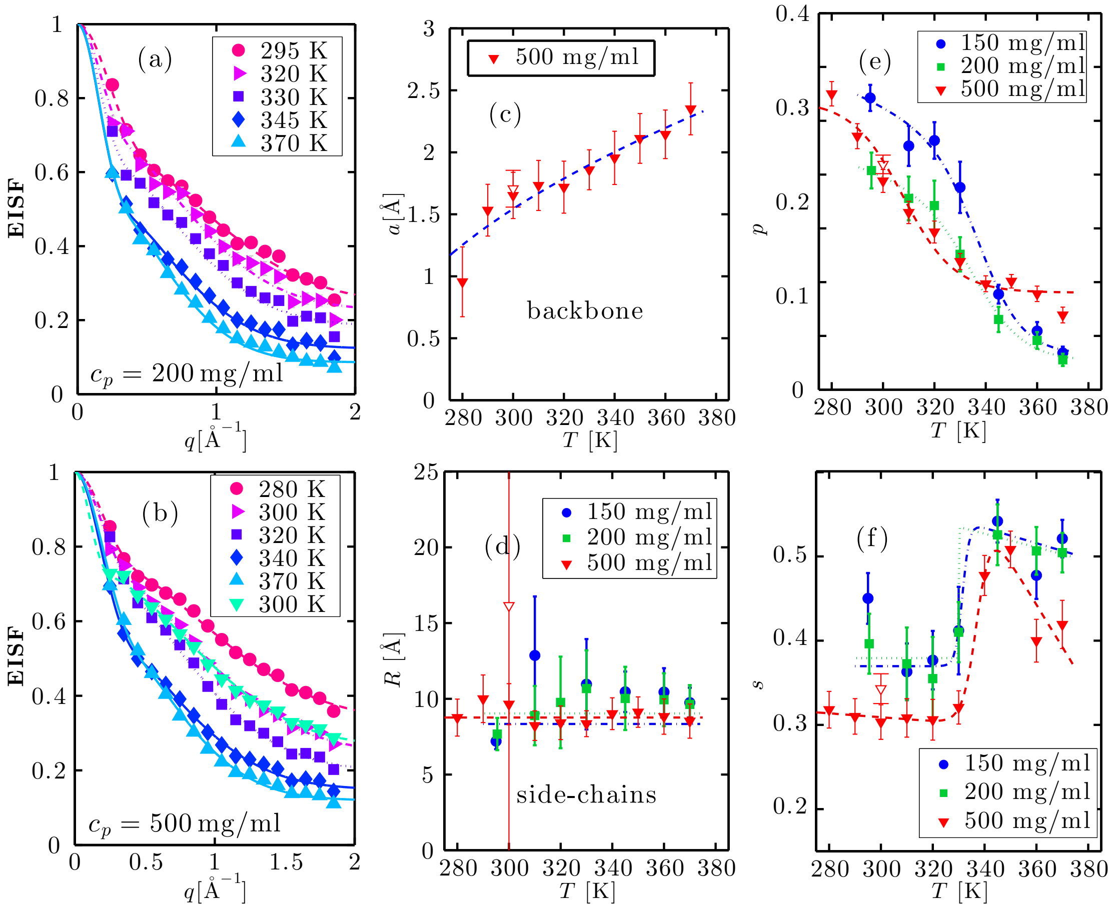

Figure B.7: Fit results for the EISF associated with the two-state switching diffusion model assuming an H/D-exchange between the proteins and the solvent water as outlined in Section B.3: (a) and (b): EISF as a function of q at the temperatures given in the legend for $c_p = 200$ and 500 mg/ml, respectively, (symbols) and fits as described in the article (solid lines). (c) radius a as a function of T for $c_p = 500$ mg/ml (symbols) and fit (blue solid line). a is associated with the effective sphere accessible by backbone atoms. (d) Radius R as a function of T (symbols). The lines are guides to the eye. This radius defines the sphere accessible by side-chain motions. (e) Fraction of immobile atoms p as a function of T (symbols). The lines are guides to the eye. (f) s as a function of T (symbols) defining the ratio of side-chains describable with a diffusion in a sphere model to the total amount of mobile side-chains. The line is a guide to the eye. The parameters in Figures 3(c)-(f) are obtained from the fit of the EISF, and the open symbols in Figures 3(b)-(f) refer to the sample at $c_p = 500$ mg/ml cooled down to room temperature after irreversible denaturation.

Appendix C

Supporting Information – Salt-induced universal slowing down of the short-time self-diffusion of a globular protein in aqueous solution[1]

C.1 Amplitudes of Density Fluctuations

Here we discuss a hypothetical picture of cluster formation via dynamic density fluctuations. The increase of attractive interactions between proteins due to bound Y^{3+} ions on the protein surface enhances fluctuations of the local volume fraction φ and thus leads to a density distribution $G(\varphi)$. Fluctuations in φ decrease the averaged apparent self-diffusion coefficient throughout the sample, since most proteins experience a denser packing.

The average diffusion coefficient can be written as:

$$D_{\mathrm{av}} = D_0 \int_0^{\phi^{\mathrm{max}}} G(\varphi)\, \varphi\, \beta(\varphi)\, \mathrm{d}\varphi, \tag{C.1}$$

where $G(\varphi)$ is the probability density function of the local volume fraction φ, ϕ^{max} is the maximum packing fraction, D_0 represents the dilute limit diffusion coefficient of a protein and $\beta(\varphi)$ is the theoretical reduced diffusion coefficient, such as that by Tokuyama and Oppenheim [37].

---

[1] **Marco Grimaldo,**[a,b] **Felix Roosen-Runge,**[a] **Marcus Hennig,**[a,b] **Fabio Zanini,**[b,f] **Fajun Zhang,**[b] **Michaela Zamponi,**[c,d] **Niina Jalarvo,**[c,e] **Frank Schreiber,**[b] **Tilo Seydel**[a]
The Journal of Physical Chemistry Letters **2015** *6*, 2577–2582.
[a] Institut Max von Laue - Paul Langevin (ILL), CS 20156, F-38042 Grenoble, France
[b] Institut für Angewandte Physik, Universität Tübingen, D-72076 Tübingen, Germany
[c] Jülich Centre for Neutron Science (JCNS), Forschungszentrum Jülich GmbH, D-52425 Jülich, Germany
[d] JCNS Outstation at the MLZ, Lichtenbergstraße 1, D-85747 Garching, Germany
[e] Chemical and Engineering Materials Division, Neutron Sciences Directorate, and JCNS Outstation at the Spallation Neutron Source (SNS), Oak Ridge National Laboratory, Oak Ridge, TN 37831, USA
[f] Present address: *Max-Planck Institute for Developmental Biology, Spemannstraße 35, D-72076 Tübingen, Germany*

We could not reproduce the experimental data assuming a unimodal probability distribution of local volume fractions. However, some well-separated bimodal distributions could explain the damping of the dynamics as e.g. in the limiting case of a distribution consisting of two delta functions

$$G(\varphi) = \delta(\varphi - (\phi - A)) + \delta(\varphi - (\phi + A)) \ ,$$

corresponding to square-wave-like fluctuations with an amplitude A around the average volume fraction ϕ (cf. Figure C.1).

At this point, two aspects seem difficult to reconcile with a physical explanation along this scenario: (i) There is no obvious physical reason for a well-separated bimodal distribution $G(\varphi)$ away from a phase separation. (ii) There is no obvious physical reason why density fluctuations should produce a universal scaling, since this implies a very specific relation between the fluctuation amplitude and the overall protein and salt concentration (see Figure C.1(c)).

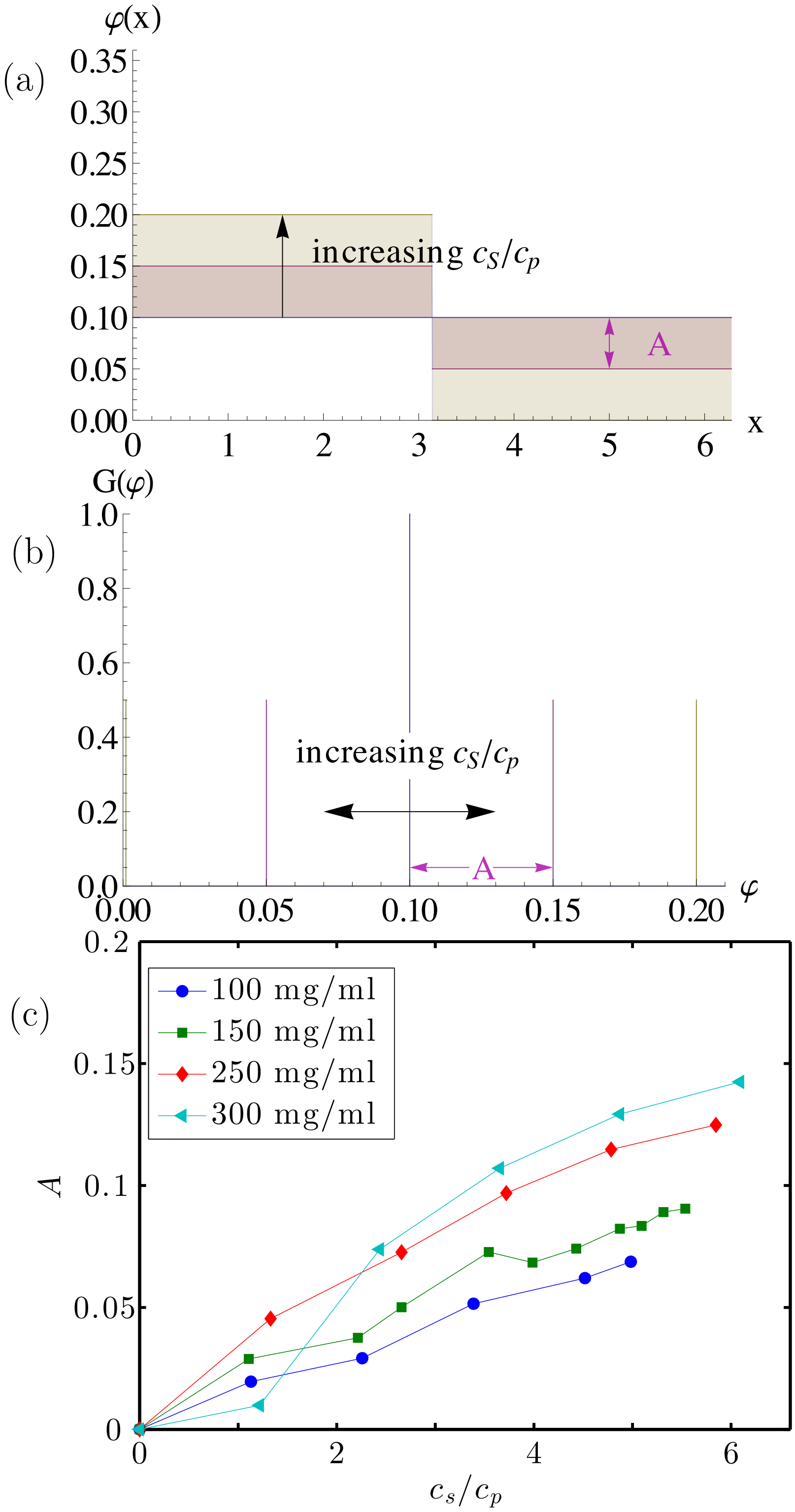

Figure C.1: (a) Local density $\varphi(x)$ as a function of the position x for a square-well-like fluctuation. Increasing salt concentration c_s/c_p increases the amplitude A of the fluctuation. (b) Probability density $G(\varphi)$ of local volume fractions φ as a function of φ, in the limiting case of Delta-functions (corresponding to the spatial profile shown in (a)). With increasing c_s/c_p, $G(\varphi)$ evolves from a single peak to two peaks at distance A from the average volume fraction ϕ. (c) Amplitude A of density fluctuations as a function of c_s/c_p obtained from the fit of experimental data under the assumption of square-well-like density fluctuations.

Appendix D

List of Performed Neutron Scattering Experiments

Table D.1: List of all the neutron scattering experiments carried out during the thesis including those not yet published in peer-reviewed journals. DOI denotes the persistent digital object identifier where the raw data, reduced data, log files, and experimental reports are available.

Experiment Title	Experiment Number / DOI	Instruments
Re-entrant condensation of proteins in electrolyte solution	IPTS-7787	BASIS (NBS)
Testing a general model for "local crowding" in protein solutions by approaching the liquid-liquid phase separation	IPTS-9987	BASIS (NBS)
Protein self-diffusion as a function of charge-screening in Ovalbumin solutions	9-13-477	IN16B (NBS)
Crowding in ternary protein solutions	9-13-526	IN16B (NBS)
Static versus dynamic protein clusters in solutions of bovine β-lactoglobulin	doi:10.5291/ILL-DATA.8-04-724	IN11 (NSE) IN16B (NBS)
Denaturation process in protein solutions studied by inelastic fixed window scans	doi:10.5291/ILL-DATA.8-04-752	IN16B (NBS)
Discerning static from transient clusters using neutron spin echo and backscattering	doi:10.5291/ILL-DATA.8-04-754	IN15 (NSE)
External crowding in protein solutions	doi:10.5291/ILL-DATA.8-04-759	IN16B (NBS)
Real-time study of protein dynamics during a one-step and a two-step crystallization process	doi:10.5291/ILL-DATA.8-04-760	IN11 (NSE) IN16B (NBS)
Real-time study of the dynamics of proteins throughout a one-step and a two-step crystallization process	doi:10.5291/ILL-DATA.8-05-420	IN16B (NBS)
Structure of arrested protein gel in the presence of a trivalent salt	doi:10.5291/ILL-DATA.9-13-565	D11 (SANS)
Kinetics of two-step nucleation in protein crystallization studied by real-time SANS	doi:10.5291/ILL-DATA.9-13-620	D11 (SANS)
Precursor behavior for protein crystallization	8471	KWS-1 (SANS)
Protein diffusion in aqueous solution	8635	TOFTOF (TOF)

Even when no DOI is assigned, the data are permanently curated by the respective facilities.

Bibliography

[1] Berg, J. M.; Tymoczko, J. L.; Stryer, L. *Protein Structure and Function* WH Freeman, New York **2002**.

[2] Griffiths, A. J.; Gelbart, W. M.; Miller, J. H.; Lewontin, R. C. *Modern Genetic Analysis* WH Freeman, New York **1999**.

[3] Gunton, J.; Shiryayev, A.; Pagan, D. *Protein Condensation: Kinetic Pathways to Crystallization and Disease* Cambridge University Press **2007**.

[4] Benedek, G. B. Cataract as a Protein Condensation Disease: The Proctor Lecture. *Invest. Ophth. Vis. Sci.* **1997** *38*, 1911–1921.

[5] Bloemendal, H.; De Jong, W.; Jaenicke, R.; Lubsen, N.; Slingsby, C.; Tardieu, A. Ageing and Vision: Structure, Stability and Function of Lens Crystallins. *Prog. Biophys. Mol. Biol.* **2004** *86*, 407–485.

[6] Ross, C.; Poirier, M. Protein Aggregation and Neurodegenerative Disease. *Nat. Med.* **2004** *10 Suppl*, S10–S17.

[7] Zaccai, G. How Soft Is a Protein? A Protein Dynamics Force Constant Measured by Neutron Scattering *Science* **2000** *288*, 1604–1607.

[8] Henzler-Wildman, K. A.; Lei, M.; Thai, V.; Kerns, S. J.; Karplus, M.; Kern, D. A Hierarchy of Timescales in Protein Dynamics Is Linked to Enzyme Catalysis *Nature* **2007** *450*, 913–916.

[9] Teague, S. J. Implications of Protein Flexibility for Drug Discovery *Nat. Rev. Drug Discov.* **2003** *2*, 527–541.

[10] Lippincott-Schwartz, J.; Snapp, E.; Kenworthy, A. Studying Protein Dynamics in Living Cells *Nat. Rev. Mol. Cell Biol.* **2001** *2*, 444–456.

[11] Phair, R. D.; Misteli, T. High Mobility of Proteins in the Mammalian Cell Nucleus *Nature* **2000** *404*, 604–609.

[12] Partikian, A.; Ölveczky, B.; Swaminathan, R.; Li, Y.; Verkman, A. Rapid Diffusion of Green Fluorescent Protein in the Mitochondrial Matrix *J. Cell Biol.* **1998** *140*, 821–829.

[13] Swaminathan, R.; Hoang, C.; Verkman, A. Photobleaching Recovery and Anisotropy Decay of Green Fluorescent Protein GFP-S65T in Solution and Cells: Cytoplasmic Viscosity Probed by Green Fluorescent Protein Translational and Rotational Diffusion *Biophys. J.* **1997** *72*, 1900 – 1907.

[14] Wojcieszyn, J. W.; Schlegel, R. A.; Wu, E.-S.; Jacobson, K. A. Diffusion of Injected Macromolecules Within the Cytoplasm of Living Cells *Proc. Natl. Acad. Sci. USA* **1981** *78*, 4407–4410.

[15] Arrio-Dupont, M.; Foucault, G.; Vacher, M.; Devaux, P. F.; Cribier, S. Translational Diffusion of Globular Proteins in the Cytoplasm of Cultured Muscle Cells *Biophys. J.* **2000** *78*, 901–907.

[16] Verkman, A. S. Solute and Macromolecule Diffusion in Cellular Aqueous Compartments *Trends Biochem. Sci.* **2002** *27*, 27–33.

[17] Jasnin, M.; Moulin, M.; Haertlein, M.; Zaccai, G.; Tehei, M. *In Vivo* Measurement of Internal and Global Macromolecular Motions in Escherichia Coli *Biophys. J.* **2008** *95*, 857–864.

[18] Ellis, R. Macromolecular Crowding: An Important but Neglected Aspect of the Intracellular Environment *Curr. Opin. Struct. Biol.* **2001** *11*, 114–119.

[19] Tehei, M.; Franzetti, B.; Madern, D.; Ginzburg, M.; Ginzburg, B. Z.; Giudici-Orticoni, M.-T.; Bruschi, M.; Zaccai, G. Adaptation to Extreme Environments: Macromolecular Dynamics in Bacteria Compared *In Vivo* by Neutron Scattering *EMBO Rep.* **2004** *5*, 66–70.

[20] Tehei, M.; Madern, D.; Franzetti, B.; Zaccai, G. Neutron Scattering Reveals the Dynamic Basis of Protein Adaptation to Extreme Temperature *J. Biol. Chem.* **2005** *280*, 40974–40979.

[21] Tehei, M.; Zaccai, G. Adaptation to Extreme Environments: Macromolecular Dynamics in Complex Systems *Biochim. Biophys. Acta* **2005** *1724*, 404–410.

[22] Stadler, A. M.; Garvey, C.; Bocahut, A.; Sacquin-Mora, S.; Digel, I.; Schneider, G.; Natali, F.; Artmann, G.; Zaccai, G. Thermal Fluctuations of Haemoglobin From Different Species: Adaptation to Temperature via Conformational Dynamics *J. R. Soc. Interface* **2012** *9*, 2845–2855.

[23] Tzeng, S.-R.; Kalodimos, C. G. Protein Activity Regulation by Conformational Entropy *Nature* **2012** *488*, 236–240.

[24] Roosen-Runge, F.; Zhang, F.; Schreiber, F.; Roth, R. Ion-Activated Attractive Patches as a Mechanism for Controlled Protein Interactions *Sci. Rep.* **2014** *4*, 07016.

[25] Ilari, A.; Savino, C. Protein Structure Determination by X-Ray Crystallography in *Bioinformatics* pages 63–87 Springer **2008**.

[26] Congreve, M.; Murray, C. W.; Blundell, T. L. Keynote Review: Structural Biology and Drug Discovery *Drug Discov. Today* **2005** *10*, 895–907.

[27] Hardy, L. W.; Malikayil, A. The Impact of Structure-Guided Drug Design on Clinical Agents *Curr. Drug. Discov.* **2003** *3*, 15–20.

[28] Grimaldo, M.; Roosen-Runge, F.; Zhang, F.; Seydel, T.; Schreiber, F. Diffusion and Dynamics of γ-Globulin in Crowded Aqueous Solutions *J. Phys. Chem. B* **2014** *118*, 7203–7209.

[29] Roosen-Runge, F.; Hennig, M.; Zhang, F.; Jacobs, R. M. J.; Sztucki, M.; Schober, H.; Seydel, T.; Schreiber, F. Protein Self-Diffusion in Crowded Solutions *Proc. Natl. Acad. Sci. USA* **2011** *108*, 11815–11820.

[30] Stingaciu, L. R.; Ivanova, O.; Ohl, M.; Biehl, R.; Richter, D. Fast Antibody Fragment Motion: Flexible Linkers Act as Entropic Spring *Scientific Reports* **2016** *6*, 22148.

[31] Hennig, M. *Dynamics of Globular Proteins in Crowded Electrolyte Solutions Studied by Neutron Scattering* Ph.D. thesis Institut Für Angewandte Physik - Eberhard Karls University of Tübingen, Institute Laue Langevin **2011**.

[32] Dhont, J. K. *An Introduction to Dynamics of Colloids* Elsevier Science, Amsterdam, Netherlands **1996**.

[33] Nägele, G. *The Physics of Colloidal Soft Matter* Centre of Excellence for Advanced Materials and Structures, Warsaw, Poland **2004**.

[34] Bee, M. Quasielastic Neutron Scattering: Principles and Applications in Solid State Chemistry, Biology and Material Science *Adam Hilger, Bristol* **1988**.

[35] Squires, G. L. *Introduction to the Theory of Thermal Neutron Scattering* Cambridge University Press **2012**.

[36] Schober, H. An Introduction to the Theory of Nuclear Neutron Scattering in Condensed Matter *J. Neutron Res.* **2014** *17*, 109–357.

[37] Tokuyama, M.; Oppenheim, I. Dynamics of Hard-Sphere Suspensions *Phys. Rev. E* **1994** *50*, 16–19.

[38] Banchio, A. J.; Nägele, G. Short-Time Transport Properties in Dense Suspensions: From Neutral to Charge-Stabilized Colloidal Spheres *J. Chem. Phys.* **2008** *128*, 104903.

[39] Piazza, R. Interactions and Phase Transitions in Protein Solutions *Curr. Opin. Colloid Interface Sci.* **2000** *5*, 38–43.

[40] Ianeselli, L.; Zhang, F.; Skoda, M. W.; Jacobs, R. M.; Martin, R. A.; Callow, S.; Prévost, S.; Schreiber, F. Protein- Protein Interactions in Ovalbumin Solutions Studied by Small-Angle Scattering: Effect of Ionic Strength and the Chemical Nature of Cations *J. Phys. Chem. B* **2010** *114*, 3776–3783.

[41] Heinen, M.; Zanini, F.; Roosen-Runge, F.; Fedunova, D.; Zhang, F.; Hennig, M.; Seydel, T.; Schweins, R.; Sztucki, M.; Antalik, M.; Schreiber, F.; Nägele, G. Viscosity and Diffusion: Crowding and Salt Effects in Protein Solutions *Soft Matter* **2012** *8*, 1404–1419.

[42] Wolf, M.; Roosen-Runge, F.; Zhang, F.; Roth, R.; Skoda, M. W.; Jacobs, R. M.; Sztucki, M.; Schreiber, F. Effective Interactions in Protein–Salt Solutions Approaching Liquid–Liquid Phase Separation *J. Mol. Liq.* **2014** *200*, 20–27.

[43] Soraruf, D.; Roosen-Runge, F.; Grimaldo, M.; Zanini, F.; Schweins, R.; Seydel, T.; Zhang, F.; Roth, R.; Oettel, M.; Schreiber, F. Protein Cluster Formation in Aqueous Solution in the Presence of Multivalent Metal Ions–a Light Scattering Study *Soft Matter* **2014** *10*, 894–902.

[44] Sear, R. P. Phase Behavior of a Simple Model of Globular Proteins *J. Chem. Phys.* **1999** *111*, 4800–4806.

[45] Kern, N.; Frenkel, D. Fluid–Fluid Coexistence in Colloidal Systems With Short-Ranged Strongly Directional Attraction *J. Chem. Phys.* **2003** *118*, 9882–9889.

[46] Gögelein, C.; Nägele, G.; Tuinier, R.; Gibaud, T.; Stradner, A.; Schurtenberger, P. A Simple Patchy Colloid Model for the Phase Behavior of Lysozyme Dispersions *J. Chem. Phys.* **2008** *129*, 085102.

[47] Whitelam, S. Nonclassical Assembly Pathways of Anisotropic Particles *J. Chem. Phys.* **2010** *132*, 194901.

[48] Whitelam, S. Control of Pathways and Yields of Protein Crystallization Through the Interplay of Nonspecific and Specific Attractions *Phys. Rev. Lett.* **2010** *105*, 088102.

[49] Bianchi, E.; Blaak, R.; Likos, C. Patchy Colloids: State of the Art and Perspectives. *Phys. Chem. Chem. Phys.* **2011** *13*, 6397–6410.

[50] Haxton, T. K.; Whitelam, S. Design Rules for the Self-Assembly of a Protein Crystal *Soft Matter* **2012** *8*, 3558–3562.

[51] Fusco, D.; Charbonneau, P. Crystallization of Asymmetric Patchy Models for Globular Proteins in Solution *Phys. Rev. E* **2013** *88*, 012721.

[52] Fusco, D.; Headd, J. J.; De Simone, A.; Wang, J.; Charbonneau, P. Characterizing Protein Crystal Contacts and Their Role in Crystallization: Rubredoxin as a Case Study *Soft Matter* **2014** *10*, 290–302.

[53] Flory, P. J. Molecular Size Distribution in Three Dimensional Polymers. I. Gelation1 *J. Am. Chem. Soc.* **1941** *63*, 3083–3090.

[54] Bianchi, E.; Tartaglia, P.; Zaccarelli, E.; Sciortino, F. Theoretical and Numerical Study of the Phase Diagram of Patchy Colloids: Ordered and Disordered Patch Arrangements *J. Chem. Phys.* **2008** *128*, 144504.

[55] Sears, V. F. Neutron Scattering Lengths and Cross Sections *Neutron News* **1992** *3*, 26–37.

[56] Pérez, J.; Zanotti, J.; Durand, D. Evolution of the Internal Dynamics of Two Globular Proteins From Dry Powder to Solution *Biophys. J.* **1999** *77*, 454–469.

[57] Volino, F.; Dianoux, A. Neutron Incoherent Scattering Law for Diffusion in a Potential of Spherical Symmetry: General Formalism and Application to Diffusion Inside a Sphere *Mol. Phys.* **1980** *41*, 271–279.

[58] Volino, F.; Perrin, J.-C.; Lyonnard, S. Gaussian Model for Localized Translational Motion: Application to Incoherent Neutron Scattering *J. Phys. Chem. B* **2006** *110*, 11217–11223.

[59] Bée, M. A Physical Insight Into the Elastic Incoherent Structure Factor *Phys. B* **1992** *182*, 323 – 336.

[60] Singwi, K. S.; Sjölander, A. Diffusive Motions in Water and Cold Neutron Scattering *Phys. Rev.* **1960** *119*, 863–871.

[61] Roosen-Runge, F.; Bicout, D. Self-Diffusion Through Heterogeneous Media *in preparation* .

[62] Hall, P. L.; Ross, D. Incoherent Neutron Scattering Functions for Random Jump Diffusion in Bounded and Infinite Media *Mol. Phys.* **1981** *42*, 673–682.

[63] Zaccai, G. Proteins as Nano-Machines: Dynamics–Function Relations Studied by Neutron Scattering *J. Phys. Condens. Matter* **2003** *15*, S1673.

[64] Gabel, F.; Bicout, D.; Lehnert, U.; Tehei, M.; Weik, M.; Zaccai, G. Protein Dynamics Studied by Neutron Scattering *Q. Rev. Biophys.* **2003** *35*, 327–367.

[65] Rahman, A.; Singwi, K.; Sjölander, A. Theory of Slow Neutron Scattering by Liquids. I *Phys. Rev.* **1962** *126*, 986.

[66] Boon, J. P.; Yip, S. *Molecular Hydrodynamics* Courier Corporation **1980**.

[67] Hennig, M.; Roosen-Runge, F.; Zhang, F.; Zorn, S.; Skoda, M. W.; Jacobs, R. M.; Seydel, T.; Schreiber, F. Dynamics of Highly Concentrated Protein Solutions Around the Denaturing Transition *Soft Matter* **2012** *8*, 1628–1633.

[68] Cusack, S.; Doster, W. Temperature Dependence of the Low Frequency Dynamics of Myoglobin. Measurement of the Vibrational Frequency Distribution by Inelastic Neutron Scattering. *Biophys. J.* **1990** *58*, 243.

[69] Smith, J.; Kuczera, K.; Karplus, M. Dynamics of Myoglobin: Comparison of Simulation Results With Neutron Scattering Spectra. *Proc. Natl. Acad. Sci. USA* **1990** *87*, 1601–1605.

[70] Diehl, M.; Doster, W.; Petry, W.; Schober, H. Water-Coupled Low-Frequency Modes of Myoglobin and Lysozyme Observed by Inelastic Neutron Scattering. *Biophys. J.* **1997** *73*, 2726.

[71] Joti, Y.; Kitao, A.; Go, N. Protein Boson Peak Originated From Hydration-Related Multiple Minima Energy Landscape *J. Am. Chem. Soc.* **2005** *127*, 8705–8709.

[72] Ciliberti, S.; De Los Rios, P.; Piazza, F. Glasslike Structure of Globular Proteins and the Boson Peak *Phys. Rev. Lett.* **2006** *96*, 198103.

[73] Wood, K.; Caronna, C.; Fouquet, P.; Häußler, W.; Natali, F.; Ollivier, J.; Orecchini, A.; Plazanet, M.; Zaccai, G. A Benchmark for Protein Dynamics: Ribonuclease a Measured by Neutron Scattering in a Large Wavevector-Energy Transfer Range *Chem. Phys.* **2008** *345*, 305–314.

[74] Zaccai, G.; Tehei, M.; Scherbakova, I.; Serdyuk, I.; Gerez, C.; Pfister, C. Incoherent Elastic Neutron Scattering as a Function of Temperature: a Fast Way to Characterise In-Situ Biological Dynamics in Complex Solutions *J. Phys. IV* **2000** *10*, Pr7–283.

[75] Tehei, M.; Madern, D.; Pfister, C.; Zaccai, G. Fast Dynamics of Halophilic Malate Dehydrogenase and BSA Measured by Neutron Scattering Under Various Solvent Conditions Influencing Protein Stability *Proc. Natl. Acad. Sci. USA* **2001** *98*, 14356–14361.

[76] Stadler, A. M.; Garvey, C. J.; Embs, J. P.; Koza, M. M.; Unruh, T.; Artmann, G.; Zaccai, G. Picosecond Dynamics in Haemoglobin From Different Species: A Quasielastic Neutron Scattering Study *Biochim. Biophys. Acta* **2014** *1840*, 2989–2999.

[77] Dee, D. R.; Myers, B.; Yada, R. Y. Dynamics of Thermodynamically Stable, Kinetically Trapped, and Inhibitor-Bound States of Pepsin *Biophys. J.* **2011** *101*, 1699–1709.

[78] Receveur, V.; Calmettes, P.; Smith, J. C.; Desmadril, M.; Coddens, G.; Durand, D. Picosecond Dynamical Changes on Denaturation of Yeast Phosphoglycerate Kinase Revealed by Quasielastic Neutron Scattering *Proteins: Struct., Funct., Bioinf.* **1997** *28*, 380–387.

[79] Tehei, M.; Smith, J. C.; Monk, C.; Ollivier, J.; Oettl, M.; Kurkal, V.; Finney, J. L.; Daniel, R. M. Dynamics of Immobilized and Native Escherichia Coli Dihydrofolate Reductase by Quasielastic Neutron Scattering *Biophys. J.* **2006** *90*, 1090–1097.

[80] Gaspar, A. M.; Appavou, M.-S.; Busch, S.; Unruh, T.; Doster, W. Dynamics of Well-Folded and Natively Disordered Proteins in Solution: a Time-of-Flight Neutron Scattering Study *Eur. Biophys. J.* **2008** *37*, 573–582.

[81] Monkenbusch, M.; Stadler, A.; Biehl, R.; Ollivier, J.; Zamponi, M.; Richter, D. Fast Internal Dynamics in Alcohol Dehydrogenase *J. Chem. Phys.* **2015** *143*, 075101.

[82] Kataoka, M.; Ferrand, M.; Goupil-Lamy, A.; Kamikubo, H.; Yunoki, J.; Oka, T.; Smith, J. Dynamical and Structural Modifications of Staphylococcal Nuclease on C-Terminal Truncation *Physica B Condens. Matter* **1999** *266*, 20–26.

[83] Gall, A.; Seguin, J.; Robert, B.; Bellissent-Funel, M.-C. Membrane Proteins in Bulk Solution Can Be Used for Quasi-Elastic Neutron Scattering Studies: The Case for the Photochemical Reaction Center *J. Phys. Chem. B* **2002** *106*, 6303–6309.

[84] Appavou, M.-S.; Busch, S.; Doster, W.; Gaspar, A.; Unruh, T. The Influence of 2 Kbar Pressure on the Global and Internal Dynamics of Human Hemoglobin Observed by Quasielastic Neutron Scattering *Eur. Biophys. J.* **2011** *40*, 705–714.

[85] Stadler, A. M.; Van Eijck, L.; Demmel, F.; Artmann, G. Macromolecular Dynamics in Red Blood Cells Investigated Using Neutron Spectroscopy *J. R. Soc. Interface* **2010** page Rsif20100306.

[86] Daniel, R. M.; Dunn, R. V.; Finney, J. L.; Smith, J. C. The Role of Dynamics in Enzyme Activity *Annu. Rev. Biophys. Biomol. Struct.* **2003** *32*, 69–92.

[87] Parak, F.; Knapp, E.; Kucheida, D. Protein Dynamics: Mössbauer Spectroscopy on Deoxymyoglobin Crystals *J. Mol. Biol.* **1982** *161*, 177–194.

[88] Fitter, J.; Ernst, O.; Hauß, T.; Lechner, R.; Hofmann, K.; Dencher, N. Molecular Motions and Hydration of Purple Membranes and Disk Membranes Studied by Neutron Scattering *Eur. Biophys. J.* **1998** *27*, 638–645.

[89] Lehnert, U.; Réat, V.; Weik, M.; Zaccai, G.; Pfister, C. Thermal Motions in Bacteriorhodopsin at Different Hydration Levels Studied by Neutron Scattering: Correlation With Kinetics and Light-Induced Conformational Changes *Biophys. J.* **1998** *75*, 1945–1952.

[90] Réat, V.; Patzelt, H.; Ferrand, M.; Pfister, C.; Oesterhelt, D.; Zaccai, G. Dynamics of Different Functional Parts of Bacteriorhodopsin: H-2H Labeling and Neutron Scattering *Proc. Natl. Acad. Sci. USA* **1998** *95*, 4970–4975.

[91] Tournier, A. L.; Xu, J.; Smith, J. C. Translational Hydration Water Dynamics Drives the Protein Glass Transition *Biophys. J.* **2003** *85*, 1871–1875.

[92] He, Y.; Ku, P. I.; Knab, J.; Chen, J.; Markelz, A. Protein Dynamical Transition Does Not Require Protein Structure *Phys. Rev. Lett.* **2008** *101*, 178103.

[93] Schiro, G.; Caronna, C.; Natali, F.; Koza, M. M.; Cupane, A. The "Protein Dynamical Transition" Does Not Require the Protein Polypeptide Chain *J. Phys. Chem. Lett.* **2011** *2*, 2275–2279.

[94] Marconi, M.; Cornicchi, E.; Onori, G.; Paciaroni, A. Comparative Study of Protein Dynamics in Hydrated Powders and in Solutions: A Neutron Scattering Investigation *Chem. Phys.* **2008** *345*, 224–229.

[95] Russo, D.; Teixeira, J.; Ollivier, J. The Impact of Hydration Water on the Dynamics of Side Chains of Hydrophobic Peptides: From Dry Powder to Highly Concentrated Solutions *J. Chem. Phys.* **2009** *130*, 235101.

[96] Stadler, A.; Digel, I.; Embs, J.; Unruh, T.; Tehei, M.; Zaccai, G.; Büldt, G.; Artmann, G. From Powder to Solution: Hydration Dependence of Human Hemoglobin Dynamics Correlated to Body Temperature. *Biophys. J.* **2009** *96*, 5073–5081.

[97] Russo, D.; Hura, G. L.; Copley, J. R. Effects of Hydration Water on Protein Methyl Group Dynamics in Solution *Phys. Rev. E* **2007** *75*, 040902.

[98] Ball, P. Water as an Active Constituent in Cell Biology *Chem. Rev.* **2008** *108*, 74–108.

[99] Daniel, R. M.; Finney, J. L.; Réat, V.; Dunn, R.; Ferrand, M.; Smith, J. C. Enzyme Dynamics and Activity: Time-Scale Dependence of Dynamical Transitions in Glutamate Dehydrogenase Solution *Biophys. J.* **1999** *77*, 2184–2190.

[100] Réat, V.; Dunn, R.; Ferrand, M.; Finney, J. L.; Daniel, R. M.; Smith, J. C. Solvent Dependence of Dynamic Transitions in Protein Solutions *Proc. Natl. Acad. Sci. USA* **2000**.

[101] Chu, X.-q.; Mamontov, E.; O'Neill, H.; Zhang, Q. Apparent Decoupling of the Dynamics of a Protein From the Dynamics of Its Aqueous Solvent *J. Phys. Chem. Lett.* **2012** *3*, 380–385.

[102] Bu, Z.; Neumann, D. A.; Lee, S.-H.; Brown, C. M.; Engelman, D. M.; Han, C. C. A View of Dynamics Changes in the Molten Globule-Native Folding Step by Quasielastic Neutron Scattering *J. Mol. Biol.* **2000** *301*, 525 – 536.

[103] Bu, Z.; Cook, J.; Callaway, D. J. Dynamic Regimes and Correlated Structural Dynamics in Native and Denatured Alpha-Lactalbumin *J. Mol. Biol.* **2001** *312*, 865–873.

[104] Russo, D.; Pérez, J.; Zanotti, J.-M.; Desmadril, M.; Durand, D. Dynamic Transition Associated With the Thermal Denaturation of a Small Beta Protein *Biophys. J.* **2002** *83*, 2792–2800.

[105] Tarek, M.; Neumann, D. A.; Tobias, D. J. Characterization of Sub-Nanosecond Dynamics of the Molten Globule State of α-Lactalbumin Using Quasielastic Neutron Scattering and Molecular Dynamics Simulations *Chem. Phys.* **2003** *292*, 435–443.

[106] Fitter, J. Conformational Dynamics of a Protein in the Folded and the Unfolded State *Chem. Phys.* **2003**.

[107] Fitter, J. A Measure of Conformational Entropy Change During Thermal Protein Unfolding Using Neutron Spectroscopy *Biophys. J.* **2003** *84*, 3924–3930.

[108] Gibrat, G.; Assairi, F.; Blouquit, Y.; Craescu, C.; Bellissentfunel, M. Biophysical Study of Thermal Denaturation of Apo-Calmodulin: Dynamics of Native and Unfolded States *Biophys. J.* **2008** *95*, 5247–5256.

[109] Caronna, C.; Natali, F.; Cupane, A. Incoherent Elastic and Quasi-Elastic Neutron Scattering Investigation of Hemoglobin Dynamics *Biophys. Chem.* **2005** *116*, 219 – 225.

[110] Marion, J.; Trovaslet, M.; Martinez, N.; Masson, P.; Schweins, R.; Nachon, F.; Trapp, M.; Peters, J. Pressure-Induced Molten Globule State of Human Acetylcholinesterase: Structural and Dynamical Changes Monitored by Neutron Scattering *Phys. Chem. Chem. Phys.* **2015** *17*, 3157–3163.

[111] Erlkamp, M.; Marion, J.; Martinez, N.; Czeslik, C.; Peters, J.; Winter, R. Influence of Pressure and Crowding on the Sub-Nanosecond Dynamics of Globular Proteins *J. Phys. Chem. B* **2015** *119*, 4842–4848.

[112] Stadler, A.; Digel, I.; Artmann, G.; Embs, J.; Zaccai, G.; Büldt, G. Hemoglobin Dynamics in Red Blood Cells: Correlation to Body Temperature *Biophys. J.* **2008** *95*, 5449 – 5461.

[113] Callaway, D. J.; Farago, B.; Bu, Z. Nanoscale Protein Dynamics: A New Frontier for Neutron Spin Echo Spectroscopy *Eur. Phys. J. E* **2013** *36*, 1–8.

[114] Monkenbusch, M.; Richter, D. High Resolution Neutron Spectroscopy – a Tool for the Investigation of Dynamics of Polymers and Soft Matter *C. R. Phys.* **2007** *8*, 845–864.

[115] Monkenbusch, M.; Richter, D.; Biehl, R. Observation of Protein Domain Motions by Neutron Spectroscopy *ChemPhysChem* **2010** *11*, 1188–1194.

[116] Bu, Z.; Biehl, R.; Monkenbusch, M.; Richter, D.; Callaway, D. J. Coupled Protein Domain Motion in Taq Polymerase Revealed by Neutron Spin-Echo Spectroscopy *Proc. Natl. Acad. Sci. USA* **2005**.

[117] Inoue, R.; Biehl, R.; Rosenkranz, T.; Fitter, J.; Monkenbusch, M.; Radulescu, A.; Farago, B.; Richter, D. Large Domain Fluctuations on 50-ns Timescale Enable Catalytic Activity in Phosphoglycerate Kinase *Biophys. J.* **2010** *99*, 2309–2317.

[118] Smolin, N.; Biehl, R.; Kneller, G.; Richter, D.; Smith, J. C. Functional Domain Motions in Proteins on The 1–100 Ns Timescale: Comparison of Neutron Spin-Echo Spectroscopy of Phosphoglycerate Kinase With Molecular-Dynamics Simulation *Biophys. J.* **2012** *102*, 1108–1117.

[119] Farago, B.; Li, J.; Cornilescu, G.; Callaway, D. J.; Bu, Z. Activation of Nanoscale Allosteric Protein Domain Motion Revealed by Neutron Spin Echo Spectroscopy *Biophys. J.* **2010** *99*, 3473–3482.

[120] Stadler, A. M.; Stingaciu, L.; Radulescu, A.; Holderer, O.; Monkenbusch, M.; Biehl, R.; Richter, D. Internal Nanosecond Dynamics in the Intrinsically Disordered Myelin Basic Protein *J. Am. Chem. Soc.* **2014** *136*, 6987–6994.

[121] Biehl, R.; Hoffmann, B.; Monkenbusch, M.; Falus, P.; Préost, S.; Merkel, R.; Richter, D. Direct Observation of Correlated Interdomain Motion in Alcohol Dehydrogenase *Phys. Rev. Lett.* **2008** *101*, 138102.

[122] Stadler, A.; Monkenbusch, M.; Biehl, R.; Richter, D.; Ollivier, J. Neutron Spin-Echo and TOF Reveals Protein Dynamics in Solution *J. Phys. Soc. Jpn.* **2013** *82*, SA016.

[123] Doster, W.; Longeville, S. Microscopic Diffusion and Hydrodynamic Interactions of Hemoglobin in Red Blood Cells *Biophys. J.* **2007** *93*, 1360 – 1368.

[124] Longeville, S.; Doster, W.; Kali, G. Myoglobin in Crowded Solutions: Structure and Diffusion *Chem. Phys.* **2003** *292*, 413 – 424.

[125] Longeville, S.; Doster, W.; Diehl, M.; Gaehler, R.; Petry, W. Neutron Resonance Spin Echo: Oxygen Transport in Crowded Protein Solutions in *Neutron Spin Echo Spectroscopy* pages 325–335 Springer **2003**.

[126] Le Coeur, C.; Longeville, S. Microscopic Protein Diffusion at High Concentration by Neutron Spin-Echo Spectroscopy *Chem. Phys.* **2008** *345*, 298–304.

[127] Busch, S.; Doster, W.; Longeville, S.; Sakai, V. G.; Unruh, T.; Maier-Leibnitz, F.-N. H. Microscopic Protein Diffusion at High Concentration *MRS Bulletin* **2006** pages 116–117.

[128] Häussler, W. Neutron Spin Echo Studies on Ferritin: Free-Particle Diffusion and Interacting Solutions *Eur. Biophys. J.* **2008** *37*, 563–571.

[129] Häußler, W.; Farago, B. Diffusive Dynamics of Ordered Solutions of Apoferritin Near the Structure Factor Peak *J. Phys. Condens. Matter* **2003** *15*, S197.

[130] Roosen-Runge, F.; Hennig, M.; Seydel, T.; Zhang, F.; Skoda, M.; Zorn, S.; Jacobs, R.; Maccarini, M.; Fouquet, P.; Schreiber, F. Protein Diffusion in Crowded Electrolyte Solutions *BBA-Proteins Proteom.* **2010** *1804*, 68 – 75.

[131] Porcar, L.; Falus, P.; Chen, W.-R.; Faraone, A.; Fratini, E.; Hong, K.; Baglioni, P.; Liu, Y. Formation of the Dynamic Clusters in Concentrated Lysozyme Protein Solutions *J. Phys. Chem. Lett.* **2009** *1*, 126–129.

[132] Liu, Y.; Porcar, L.; Chen, J.; Chen, W.-R.; Falus, P.; Faraone, A.; Fratini, E.; Hong, K.; Baglioni, P. Lysozyme Protein Solution With an Intermediate Range Order Structure *J. Phys. Chem. B* **2010** *115*, 7238–7247.

[133] Godfrin, P. D.; Hudson, S. D.; Hong, K.; Porcar, L.; Falus, P.; Wagner, N. J.; Liu, Y. Short-Time Glassy Dynamics in Viscous Protein Solutions With Competing Interactions *Phys. Rev. Lett.* **2015** *115*, 228302.

[134] Stradner, A.; Sedgwick, H.; Cardinaux, F.; Poon, W. C.; Egelhaaf, S. U.; Schurtenberger, P. Equilibrium Cluster Formation in Concentrated Protein Solutions and Colloids *Nature* **2004** *432*, 492–495.

[135] Yearley, E. J.; Godfrin, P. D.; Perevozchikova, T.; Zhang, H.; Falus, P.; Porcar, L.; Nagao, M.; Curtis, J. E.; Gawande, P.; Taing, R.; Zarraga, I. E.; Wagner, N. J.; Liu, Y. Observation of Small Cluster Formation in Concentrated Monoclonal Antibody Solutions and Its Implications to Solution Viscosity *Biophys. J.* **2014** *106*, 1763–1770.

[136] Erlkamp, M.; Grobelny, S.; Faraone, A.; Czeslik, C.; Winter, R. Solvent Effects on the Dynamics of Amyloidogenic Insulin Revealed by Neutron Spin Echo Spectroscopy *J. Phys. Chem. B* **2014** *118*, 3310–3316.

[137] Nemethy, G.; Scheraga, H. A. Structure of Water and Hydrophobic Bonding in Proteins. IV. The Thermodynamic Properties of Liquid Deuterium Oxide *J. Chem. Phys.* **1964** *41*, 680–689.

[138] Conway, B. E. *Ionic Hydration in Chemistry and Biophysics* volume 12 Elsevier Science Ltd **1981**.

[139] Lide, D. R. *CRC Handbook of Chemistry and Physics* CRC Press **2004**.

[140] Cho, C.; Urquidi, J.; Singh, S.; Robinson, G. W. Thermal Offset Viscosities of Liquid H2O, D2O, and T2O *J. Phys. Chem. B* **1999** *103*, 1991–1994.

[141] Bonneté, F.; Madern, D.; Zaccai, G. Stability Against Denaturation Mechanisms in Halophilic Malate Dehydrogenase "Adapt" to Solvent Conditions *J. Mol. Biol.* **1994** *244*, 436–447.

[142] Peters Jr, T. *All About Albumin: Biochemistry, Genetics, and Medical Applications* Academic Press **1995**.

[143] Carter, D. C.; Ho, J. X. Structure of Serum Albumin *Adv. Protein Chem.* **1994** *45*, 153–203.

[144] Figge, J.; Rossing, T.; Fencl, V. The Role of Serum Proteins in Acid-Base Equilibria. *J. Lab. Clin. Med.* **1991** *117*, 453–467.

[145] Bujacz, A. Structures of Bovine, Equine and Leporine Serum Albumin *Acta Crystallogr. Sect. A* **2012** *68*, 1278–1289.

[146] Majorek, K. A.; Porebski, P. J.; Dayal, A.; Zimmerman, M. D.; Jablonska, K.; Stewart, A. J.; Chruszcz, M.; Minor, W. Structural and Immunologic Characterization of Bovine, Horse, and Rabbit Serum Albumins *Mol. Immunol.* **2012** *52*, 174–182.

[147] Humphrey, W.; Dalke, A.; Schulten, K. VMD – Visual Molecular Dynamics *J. Mol. Graphics* **1996** *14*, 33–38.

[148] Böhme, U.; Scheler, U. Effective Charge of Bovine Serum Albumin Determined by Electrophoresis NMR *Chem. Phys. Lett.* **2007** *435*, 342–345.

[149] Tanford, C.; Buzzell, J. G. The Viscosity of Aqueous Solutions of Bovine Serum Albumin Between pH 4.3 and 10.5. *J. Phys. Chem.* **1956** *60*, 225–231.

[150] Gasteiger, E.; Hoogland, C.; Gattiker, A.; Duvaud, S.; Wilkins, M. R.; Appel, R. D.; Bairoch, A. *Protein Identification and Analysis Tools on the ExPASy Server* Springer **2005**.

[151] Ortega, A.; Amorós, D.; García De La Torre, J. Prediction of Hydrodynamic and Other Solution Properties of Rigid Proteins From Atomic- and Residue-Level Models. *Biophys. J.* **2011** *101*, 892–898.

[152] Hunter, M. J. A Method for the Determination of Protein Partial Specific Volumes *J. Phys. Chem.* **1966** *70*, 3285–3292.

[153] Junqueira, L. C.; Carneiro, J. *Basic Histology Text and Atlas* London: McGraw Hill, 2005 **2005**.

[154] Harris, L.; Larson, S.; Hasel, K.; A, M. Refined Structure of an Intact IgG2a Monoclonal Antibody. *Biochemistry (Mosc.)* **1997** *36*, 1581–1597.

[155] Sigma-Aldrich Antibody Basics *http://www.sigmaaldrich.com/technical-documents/articles/biology/antibody-basics.html.*

[156] Gorga, J. C.; Dong, A.; Manning, M. C.; Woody, R. W.; Caughey, W. S.; Strominger, J. L. Comparison of the Secondary Structures of Human Class I and Class II Major Histocompatibility Complex Antigens by Fourier Transform Infrared and Circular Dichroism Spectroscopy *Proc. Natl. Acad. Sci. USA* **1989** *86*, 2321–2325.

[157] Jøssang, T.; Feder, J.; Rosenqvist, E. Photon Correlation Spectroscopy of Human IgG. *J. Protein Chem.* **1988** *7*, 165–171.

[158] Chemicool *http://www.chemicool.com/elements/.*

[159] Sigma-Aldrich *http://www.sigmaaldrich.com/.*

[160] Heck, B. S. *Reentrant Phase Behavior of Proteins in Solution Induced by* Fe^{3+} *and* Al^{3+} *Ions* Diplom thesis Institut Für Angewandte Physik - Eberhard Karls University of Tübingen **2010**.

[161] Zhang, F.; Skoda, M. W. A.; Jacobs, R. M. J.; Zorn, S.; Martin, R. A.; Martin, C. M.; Clark, G. F.; Weggler, S.; Hildebrandt, A.; Kohlbacher, O.; Schreiber, F. Reentrant Condensation of Proteins in Solution Induced by Multivalent Counterions *Phys. Rev. Lett.* **2008** *101*, 148101.

[162] Zhang, F.; Weggler, S.; Ziller, M. J.; Ianeselli, L.; Heck, B. S.; Hildebrandt, A.; Kohlbacher, O.; Skoda, M. W.; Jacobs, R. M.; Schreiber, F. Universality of Protein Reentrant Condensation in Solution Induced by Multivalent Metal Ions *Proteins* **2010** *78*, 3450–3457.

[163] Zhang, F.; Zocher, G.; Sauter, A.; Stehle, T.; Schreiber, F. Novel Approach to Controlled Protein Crystallization Through Ligandation of Yttrium Cations *J. Appl. Crystallogr.* **2011** *44*, 755–762.

[164] Zhang, F.; Roth, R.; Wolf, M.; Roosen-Runge, F.; Skoda, M. W.; Jacobs, R. M.; Stzucki, M.; Schreiber, F. Charge-Controlled Metastable Liquid–Liquid Phase Separation in Protein Solutions as a Universal Pathway Towards Crystallization *Soft Matter* **2012** *8*, 1313–1316.

[165] Grimaldo, M. *Protein Self-Diffusion Studied by Quasi-Elastic Neutron Scattering: the Effect of Charge Tuning Using a Trivalent Salt* Diplom thesis Institut Für Angewandte Physik - Eberhard Karls University of Tübingen, Institute Laue Langevin, and University of Trento **2013**.

[166] Appel, M. *Ring Rotation in Ferrocene and Ferrocene-Containing Polymers.* Ph.D. thesis Technische Universität, Darmstadt **2015**.

[167] Paalman, H.; Pings, C. Numerical Evaluation of X-Ray Absorption Factors for Cylindrical Samples and Annular Sample Cells *J. Appl. Phys.* **1962** *33*, 2635–2639.

[168] NIST http://www.ncnr.nist.gov/resources/sldcalc.html.

[169] Kamal, M.; Malik, S.; Rorer, D. Neutron Incoherent Elastic Scattering Study of the Temperature Dependence of the Debye-Waller Exponent in Vanadium *Phys. Rev. B* **1978** *18*, 1609.

[170] Grimaldo, M.; Roosen-Runge, F.; Jalarvo, N.; Zamponi, M.; Zanini, F.; Hennig, M.; Zhang, F.; Schreiber, F.; Seydel, T. High-Resolution Neutron Spectroscopy on Protein Solution Samples in *EPJ Web of Conferences* volume 83 EDP Sciences **2015** page 02005.

[171] Frick, B.; Mamontov, E.; Eijck, L. V.; Seydel, T. Recent Backscattering Instrument Developments at the ILL and SNS *Z. Phys. Chem.* **2010** *224*, 33–60.

[172] Hennig, M.; Frick, B.; Seydel, T. Optimum Velocity of a Phase-Space Transformer for Cold-Neutron Backscattering Spectroscopy *J. Appl. Crystallogr.* **2011** *44*, 467–472.

[173] Frick, B.; Gonzalez, M. Five Years Operation of the Second Generation Backscattering Spectrometer IN16 – a Retrospective, Recent Developments and Plans *Physica B Condens. Matter* **2001** *301*, 8–19.

[174] Mamontov, E.; Herwig, K. W. A Time-of-Flight Backscattering Spectrometer at the Spallation Neutron Source, BASIS *Rev. Sci. Instrum.* **2011** *82*, 085109.

[175] *The ILL Yellow Book* **2008** http://www.ill.eu/fr/instruments-support/instruments-groups/yellowbook/.

[176] Qvist, J.; Schober, H.; Halle, B. Structural Dynamics of Supercooled Water From Quasielastic Neutron Scattering and Molecular Simulations. *J. Chem. Phys.* **2011** *134*, 144508.

[177] Dianoux, A.-J.; Lander, G. *Neutron Data Booklet* Old City Philadelphia **2003**.

[178] Filhol, A. *Exploring Matter With Neutrons* iMediaSoft & Nanopolis **2005**.

[179] Gauthier-Lafaye, F.; Holliger, P.; Blanc, P.-L. Natural Fission Reactors in the Franceville Basin, Gabon: A Review of the Conditions and Results of a "Critical Event" in a Geologic System *Geochim. Cosmochim. Acta* **1996** *60*, 4831–4852.

[180] Liyuan, L.; Rinaldi, R.; Schober, H. *Neutron Applications in Earth, Energy and Environmental Sciences* Springer Science & Business Media **2008**.

[181] Bauer, G. S. Physics and Technology of Spallation Neutron Sources *Nucl. Instr. Meth. Phys. Res. Sect. A* **2001** *463*, 505–543.

[182] Frick, B. Neutron Backscattering Spectroscopy in *Neutron and X-Ray Spectroscopy* pages 483–527 Springer **2006**.

[183] Hippert, F.; Geissler, E.; Hodeau, J. L.; Lelièvre-Berna, E.; Regnard, J.-R. *Neutron and X-Ray Spectroscopy* Springer Science & Business Media **2006**.

[184] Crane, T.; Baker, M. Neutron Detectors *Passive Nondestructive Assay of Nuclear Materials* **1991** pages 379–406.

[185] Baruchel, J.; Hodeau, J.-L.; Lehmann, M. S.; Regnard, J.-R.; Schlenker, C. *Neutron and Synchrotron Radiation for Condensed Matter Studies* Springer **1993**.

[186] Scherm, R.; FAk, B. VL Properties and Production of Neutrons *Neutron and Synchrotron Radiation for Condensed Matter Studies: Theory, Instruments and Methods* **1993** *1*, 113.

[187] Oak Ridge National Laboratory - Spallation Neutron Source
http://neutrons2.ornl.gov/facilities/SNS/works.shtml.

[188] Herwig, K.; Keener, W. Design and Performance of the Spallation Neutron Source Backscattering Spectrometer *Applied Physics A* **2002** *74*, S1592–s1594.

[189] Henderson, S.; Abraham, W.; Aleksandrov, A.; Allen, C.; Alonso, J.; Anderson, D.; Arenius, D.; Arthur, T.; Assadi, S.; Ayers, J.; Bach, P.; Badea, V.; Battle, R.; Beebe-Wang, J.; Bergmann, B.; Bernardin, J.; Bhatia, T.; Billen, J.; Birke, T.; Bjorklund, E.; Blaskiewicz, M.; Blind, B.; Blokland, W.; Bookwalter, V.; Borovina, D.; Bowling, S.; Bradley, J.; Brantley, C.; Brennan, J.; Brodowski, J.; Brown, S.; Brown, R.; Bruce, D.; Bultman, N.; Cameron, P.; Campisi, I.; Casagrande, F.; Catalan-Lasheras, N.; Champion, M.; Champion, M.; Chen, Z.; Cheng, D.; Cho, Y.; Christensen, K.; Chu, C.; Cleaves, J.; Connolly, R.; Cote, T.; Cousineau, S.; Crandall, K.; Creel, J.; Crofford, M.; Cull, P.; Cutler, R.; Dabney, R.; Dalesio, L.; Daly, E.; Damm, R.; Danilov, V.; Davino, D.; Davis, K.; Dawson, C.; Day, L.; Deibele, C.; Delayen, J.; DeLong, J.; Demello, A.; DeVan, W.; Digennaro, R.; Dixon, K.; Dodson, G.; Doleans, M.; Doolittle, L.; Doss, J.; Drury, M.; Elliot, T.; Ellis, S.; Error, J.; Fazekas, J.; Fedotov, A.; Feng, P.; Fischer, J.; Fox, W.; Fuja, R.; Funk, W.; Galambos, J.; Ganni, V.; Garnett, R.; Geng, X.; Gentzlinger, R.; Giannella, M.; Gibson, P.; Gillis, R.; Gioia, J.; Gordon, J.; Gough, R.; Greer, J.; Gregory, W.; Gribble, R.; Grice, W.; Gurd, D.;

Gurd, P.; Guthrie, A.; Hahn, H.; Hardek, T.; Hardekopf, R.; Harrison, J.; Hatfield, D.; He, P.; Hechler, M.; Heistermann, F.; Helus, S.; Hiatt, T.; Hicks, S.; Hill, J.; Hill, J.; Hoff, L.; Hoff, M.; Hogan, J.; Holding, M.; Holik, P.; Holmes, J.; Holtkamp, N.; Hovater, C.; Howell, M.; Hseuh, H.; Huhn, A.; Hunter, T.; Ilg, T.; Jackson, J.; Jain, A.; Jason, A.; Jeon, D.; Johnson, G.; Jones, A.; Joseph, S.; Justice, A.; Kang, Y.; Kasemir, K.; Keller, R.; Kersevan, R.; Kerstiens, D.; Kesselman, M.; Kim, S.; Kneisel, P.; Kravchuk, L.; Kuneli, T.; Kurennoy, S.; Kustom, R.; Kwon, S.; Ladd, P.; Lambiase, R.; Lee, Y.; Leitner, M.; Leung, K.-N.; Lewis, S.; Liaw, C.; Lionberger, C.; Lo, C.; Long, C.; Ludewig, H.; Ludvig, J.; Luft, P.; Lynch, M.; Ma, H.; MacGill, R.; Macha, K.; Madre, B.; Mahler, G.; Mahoney, K.; Maines, J.; Mammosser, J.; Mann, T.; Marneris, I.; Marroquin, P.; Martineau, R.; Matsumoto, K.; McCarthy, M.; McChesney, C.; McGahern, W.; McGehee, P.; Meng, W.; Merz, B.; Jr., R. M.; Sr., R. M.; Miller, B.; Mitchell, R.; Mize, J.; Monroy, M.; Munro, J.; Murdoch, G.; Musson, J.; Nath, S.; Nelson, R.; Nelson, R.; O'Hara, J.; Olsen, D.; Oren, W.; Oshatz, D.; Owens, T.; Pai, C.; Papaphilippou, I.; Patterson, N.; Patterson, J.; Pearson, C.; Pelaia, T.; Pieck, M.; Piller, C.; Plawski, T.; Plum, M.; Pogge, J.; Power, J.; Powers, T.; Preble, J.; Prokop, M.; Pruyn, J.; Purcell, D.; Rank, J.; Raparia, D.; Ratti, A.; Reass, W.; Reece, K.; Rees, D.; Regan, A.; Regis, M.; Reijonen, J.; Rej, D.; Richards, D.; Richied, D.; Rode, C.; Rodriguez, W.; Rodriguez, M.; Rohlev, A.; Rose, C.; Jr., T. R.; Rowton, L.; Roybal, W.; Rust, K.; Salazer, G.; Sandberg, J.; Saunders, J.; Schenkel, T.; Schneider, W.; Schrage, D.; Schubert, J.; Severino, F.; Shafer, R.; Shea, T.; Shishlo, A.; Shoaee, H.; Sibley, C.; Sims, J.; Smee, S.; Smith, J.; Smith, K.; Spitz, R.; Staples, J.; Stein, P.; Stettler, M.; Stirbet, M.; Stockli, M.; Stone, W.; Stout, D.; Stovall, J.; Strelo, W.; Strong, H.; Sundelin, R.; Syversrud, D.; Szajbler, M.; Takeda, H.; Tallerico, P.; Tang, J.; Tanke, E.; Tepikian, S.; Thomae, R.; Thompson, D.; Thomson, D.; Thuot, M.; Treml, C.; Tsoupas, N.; Tuozzolo, J.; Tuzel, W.; Vassioutchenko, A.; Virostek, S.; Wallig, J.; Wanderer, P.; Wang, Y.; Wang, J.; Wangler, T.; Warren, D.; Wei, J.; Weiss, D.; Welton, R.; Weng, J.; Weng, W.-T.; Wezensky, M.; White, M.; Whitlatch, T.; Williams, D.; Williams, E.; Wilson, K.; Wiseman, M.; Wood, R.; Wright, P.; Wu, A.; Ybarrolaza, N.; Young, K.; Young, L.; Yourd, R.; Zachoszcz, A.; Zaltsman, A.; Zhang, S.; Zhang, W.; Zhang, Y.; Zhukov, A. The Spallation Neutron Source Accelerator System Design *Nucl. Instr. Meth. Phys. Res. Sect. A* **2014** *763*, 610–673.

[190] Paquit, V. C.; Wendel, M. W.; Felde, D. K.; Riemer, B. W. Quantitative measurement by artificial vision of small bubbles in flowing mercury in *IS&T/SPIE Electronic Imaging* International Society for Optics and Photonics **2011** pages 78770L–78770L.

[191] Mansur, L.; Gabriel, T.; Haines, J.; Lousteau, D. R&D for the Spallation Neutron Source Mercury Target *J. Nucl. Mater.* **2001** *296*, 1–16.

[192] Ageron, P. Cold Neutron Sources at ILL *Nucl. Instr. Meth. Phys. Res. Sect. A* **1989** *284*, 197–199.

[193] Ortega, A.; Amorós, D.; García De La Torre, J. HYDROPRO User Guide *http://leonardo.inf.um.es/macromol/programs/hydropro/hydropro10.pdf.*

[194] Ortega, A.; García de la Torre, J. Equivalent Radii and Ratios of Radii from Solution Properties as Indicators of Macromolecular Conformation, Shape, and Flexibility *Biomacromolecules* **2007** *8*, 2464–2475.

[195] Senff, H.; Richtering, W. Temperature sensitive microgel suspensions: Colloidal phase behavior and rheology of soft spheres *The Journal of chemical physics* **1999** *111*, 1705–1711.

[196] Stagg, L.; Zhang, S.; Cheung, M.; Pernilla, W. Molecular Crowding Enhances Native Structure and Stability of Alpha/beta Protein Flavodoxin. *Proc. Natl. Acad. Sci. USA* **2007** *104*, 18976–18981.

[197] Hong, J.; Gierasch, L. M. Macromolecular Crowding Remodels the Energy Landscape of a Protein by Favoring a More Compact Unfolded State *J. Am. Chem. Soc.* **2010** *132*, 10445–10452.

[198] Dhar, A.; Samiotakis, A.; Ebbinghaus, S.; Nienhaus, L.; Homouz, D.; Gruebele, M.; Cheung, M. S. Structure, Function, and Folding of Phosphoglycerate Kinase Are Strongly Perturbed by Macromolecular Crowding *Proc. Natl. Acad. Sci. USA* **2010** *107*, 17586–17591.

[199] Nesmelova, I. v.; Skirda, V. D.; Fedotov, V. D. Generalized Concentration Dependence of Globular Protein Self-Diffusion Coefficients in Aqueous Solutions *Biopolymers* **2002** *63*, 132–140.

[200] Ando, T.; Skolnick, J. Crowding and Hydrodynamic Interactions Likely Dominate *In Vivo* Macromolecular Motion. *Proc. Natl. Acad. Sci. USA* **2010** *107*, 18457–18462.

[201] Doster, W.; Cusack, S.; Petry, W. Dynamical Transition of Myoglobin Revealed by Inelastic Neutron Scattering *Nature* **1989** *337*, 754 – 756.

[202] Cornicchi, E.; Marconi, M.; Onori, G.; Paciaroni, A. Controlling the Protein Dynamical Transition With Sugar-Based Bioprotectant Matrices: A Neutron Scattering Study *Biophys. J.* **2006** *91*, 289 – 297.

[203] Paciaroni, A.; Cinelli, S.; Onori, G. Effect of the Environment on the Protein Dynamical Transition: A Neutron Scattering Study *Biophys. J.* **2002** *83*, 1157 – 1164.

[204] Paciaroni, A.; Cornicchi, E.; Francesco, A.; Marconi, M.; Onori, G. Conditioning Action of the Environment on the Protein Dynamics Studied Through Elastic Neutron Scattering *Eur. Biophys. J.* **2006** *35*, 591–599.

[205] Chen, S.-H.; Liu, L.; Fratini, E.; Baglioni, P.; Faraone, A.; Mamontov, E. Observation of Fragile-To-Strong Dynamic Crossover in Protein Hydration Water *Proc. Natl. Acad. Sci. USA* **2006** *103*, 9012–9016.

[206] Murphy, L. R.; Matubayasi, N.; Payne, V. A.; Levy, R. M. Protein Hydration and Unfolding–Insights From Experimental Partial Specific Volumes and Unfolded Protein Models *Fold. Des.* **1998** *3*, 105–118.

[207] Wang, Y.; Lomakin, A.; Latypov, R. F.; Laubach, J. P.; Hideshima, T.; Richardson, P. G.; Munshi, N. C.; Anderson, K. C.; Benedek, G. B. Phase Transitions in Human IgG Solutions *J. Chem. Phys.* **2013** *139*, 121904.

[208] Bicout, D. Influence of Environment Fluctuations on Incoherent Neutron Scattering Functions *Phys. Rev. E* **2001** *64*, 011910.

[209] Bicout, D. Incoherent Neutron Scattering Functions for Combined Dynamics *Proceedings of the ILL Millennium Symposium and European User Meeting* **2001**.

[210] Fitter, J. Confined Molecular Motions of Globular Proteins Studied in Powder Samples and in Solution *J. Phys. IV* **2000** *10*, 265–270.

[211] Damay, P.; Leclercq, F. Diffusion Quasiélastique De Neutrons; Étude Des Mouvements Localisés *J. Phys. IV* **2000** *10*, Pr1–105.

[212] Bellissent-Funel, M.-C.; Teixeira, J.; Bradley, K.; Chen, S. Dynamics of Hydration Water in Protein *J. Phys. I* **1992** *2*, 995–1001.

[213] Makowski, L.; Rodi, D.; Mandava, S.; Minh, D.; Gore, D.; Fischetti, R. Molecular Crowding Inhibits Intramolecular Breathing Motions in Proteins. *J. Mol. Biol.* **2008** *375*, 529–546.

[214] Cheung, M. S.; Klimov, D.; Thirumalai, D. Molecular Crowding Enhances Native State Stability and Refolding Rates of Globular Proteins *Proc. Natl. Acad. Sci. U. S. A.* **2005** *102*, 4753–4758.

[215] Minh, D. D.; Chang, C.-E.; Trylska, J.; Tozzini, V.; McCammon, J. A. The Influence of Macromolecular Crowding on HIV-1 Protease Internal Dynamics *J. Am. Chem. Soc.* **2006** *128*, 6006–6007.

[216] Politi, R.; Harries, D. Enthalpically Driven Peptide Stabilization by Protective Osmolytes *Chem. Commun.* **2010** *46*, 6449–6451.

[217] Lilyestrom, W.; Yadav, S.; Shire, S.; Scherer, T. Monoclonal Antibody Self-Association, Cluster Formation, and Rheology at High Concentrations. *J. Phys. Chem. B* **2013** *117*, 6373–6384.

[218] Lilyestrom, W. G.; Shire, S. J.; Scherer, T. M. Influence of the Cosolute Environment on IgG Solution Structure Analyzed by Small-Angle X-Ray Scattering *J. Phys. Chem. B* **2012** *116*, 9611–9618.

[219] Sarangapani, P. S.; Hudson, S. D.; Migler, K. B.; Pathak, J. A. The Limitations of an Exclusively Colloidal View of Protein Solution Hydrodynamics and Rheology *Biophys. J.* **2013** *105*, 2418–2426.

[220] Grimaldo, M.; Roosen-Runge, F.; Hennig, M.; Zanini, F.; Zhang, F.; Jalarvo, N.; Zamponi, M.; Schreiber, F.; Seydel, T. Hierarchical Molecular Dynamics of Bovine Serum Albumin in Concentrated Aqueous Solution Below and Above Thermal Denaturation *Phys. Chem. Chem. Phys.* **2015** *17*, 4645–4655.

[221] Whisstock, J. C.; Lesk, A. M. Prediction of Protein Function From Protein Sequence and Structure *Q. Rev. Biophys.* **2003** *36*, 307–340.

[222] Karplus, M.; Kuriyan, J. Molecular Dynamics and Protein Function *Proc. Natl. Acad. Sci. USA* **2005** *102*, 6679–6685.

[223] Zimm, B. H.; Bragg, J. K. Theory of the Phase Transition Between Helix and Random Coil in Polypeptide Chains *J. Chem. Phys.* **1959** *31*, 526–535.

[224] Kauzmann, W. Some Factors in the Interpretation of Protein Denaturation *Adv. Protein Chem.* **1959** *14*, 1–63.

[225] Tanford, C. Protein Denaturation *Adv. Protein Chem.* **1968** *23*, 121–282.

[226] Dill, K. A. Dominant Forces in Protein Folding *Biochemistry (Mosc.)* **1990** *29*, 7133–7155.

[227] Lumry, R.; Eyring, H. Conformation Changes of Proteins *J. Phys. Chem.* **1954** *58*, 110–120.

[228] Tanford, C. Protein Denaturation: Part C. Theoretical Models for the Mechanism of Denaturation *Adv. Protein Chem.* **1970** *24*, 1–95.

[229] Gosal, W. S.; Ross-Murphy, S. B. Globular Protein Gelation *COCIS* **2000** *5*, 188–194.

[230] Clark, A.; Kavanagh, G.; Ross-Murphy, S. Globular Protein Gelation – Theory and Experiment *Food Hydrocolloids* **2001** *15*, 383–400.

[231] Dobson, C. M. Protein Folding and Misfolding *Nature* **2003** *426*, 884–890.

[232] Onuchic, J. N.; Wolynes, P. G.; Luthey-Schulten, Z.; Socci, N. D. Toward an Outline of the Topography of a Realistic Protein-Folding Funnel. *Proc. Natl. Acad. Sci. USA* **1995** *92*, 3626–3630.

[233] Dill, K. A.; Chan, H. S. From Levinthal to Pathways to Funnels *Nat. Struct. Biol.* **1997** *4*, 10–19.

[234] Finkelstein, A. v.; Shakhnovich, E. I. Theory of Cooperative Transitions in Protein Molecules. II. Phase Diagram for a Protein Molecule in Solution *Biopolymers* **1989** *28*, 1681–1694.

[235] Shakhnovich, E. I.; Finkelstein, A. V. Theory of Cooperative Transitions in Protein Molecules. I. Why Denaturation of Globular Protein Is a First-Order Phase Transition *Biopolymers* **1989** *28*, 1667–1680.

[236] De Gennes, P. Critical Behaviour for Vulcanization Processes *J. Phys. Lett. Paris* **1977** *38*, 355–358.

[237] San Biagio, P.; Bulone, D.; Emanuele, A.; Palma, M. Self-Assembly of Biopolymeric Structures Below the Threshold of Random Cross-Link Percolation *Biophys. J.* **1996** *70*, 494–499.

[238] Le Bon, C.; Nicolai, T.; Durand, D. Kinetics of Aggregation and Gelation of Globular Proteins After Heat-Induced Denaturation *Macromolecules* **1999** *32*, 6120–6127.

[239] Wetzel, R.; Becker, M.; Behlke, J.; Billwitz, H.; Böhm, S.; Ebert, B.; Hamann, H.; Krumbiegel, J.; Lassmann, G. Temperature Behaviour of Human Serum Albumin *Eur. J. Biochem.* **1980** *104*, 469–478.

[240] Lin, V.; Koenig, J. Raman Studies of Bovine Serum Albumin *Biopolymers* **1976** *15*, 203–218.

[241] Oakes, J. Thermally Denatured Proteins. Nuclear Magnetic Resonance, Binding Isotherm and Chemical Modification Studies of Thermally Denatured Bovine Serum Albumin *J. Chem. Soc. Faraday Trans. I* **1976** *72*, 228–237.

[242] Hayakawa, I.; Kajihara, J.; Morikawa, K.; Oda, M.; Fujio, Y. Denaturation of Bovine Serum Albumin (BSA) and Ovalbumin by High Pressure, Heat and Chemicals *J. Food Sci.* **1992** *57*, 288–292.

[243] Tobitani, A.; Ross-Murphy, S. B. Heat-Induced Gelation of Globular Proteins. 1. Model for the Effects of Time and Temperature on the Gelation Time of BSA Gels *Macromolecules* **1997** *30*, 4845–4854.

[244] Wilkins, D. K.; Grimshaw, S. B.; Receveur, V.; Dobson, C. M.; Jones, J. A.; Smith, L. J. Hydrodynamic Radii of Native and Denatured Proteins Measured by Pulse Field Gradient NMR Techniques *Biochemistry (Mosc.)* **1999** *38*, 16424–16431.

[245] Dellerue, S.; Petrescu, A.-J.; Smith, J. C.; Bellissent-Funel, M.-C. Radially Softening Diffusive Motions in a Globular Protein *Biophys. J.* **2001** *81*, 1666–1676.

[246] Lee, A. L.; Sharp, K. A.; Kranz, J. K.; Song, X.-J.; Wand, A. J. Temperature Dependence of the Internal Dynamics of a Calmodulin-Peptide Complex *Biochemistry (Mosc.)* **2002** *41*, 13814–13825.

[247] Militello, V.; Vetri, V.; Leone, M. Conformational Changes Involved in Thermal Aggregation Processes of Bovine Serum Albumin *Biophys. Chem.* **2003** *105*, 133–141.

[248] Militello, V.; Casarino, C.; Emanuele, A.; Giostra, A.; Pullara, F.; Leone, M. Aggregation Kinetics of Bovine Serum Albumin Studied by FTIR Spectroscopy and Light Scattering *Biophys. Chem.* **2004** *107*, 175–187.

[249] Murayama, K.; Tomida, M. Heat-Induced Secondary Structure and Conformation Change of Bovine Serum Albumin Investigated by Fourier Transform Infrared Spectroscopy *Biochemistry (Mosc.)* **2004** *43*, 11526–11532.

[250] Ding, F.; Jha, R. K.; Dokholyan, N. V. Scaling Behavior and Structure of Denatured Proteins *Structure* **2005** *13*, 1047–1054.

[251] Pouzot, M.; Nicolai, T.; Visschers, R.; Weijers, M. X-Ray and Light Scattering Study of the Structure of Large Protein Aggregates at Neutral pH *Food Hydrocolloids* **2005** *19*, 231–238.

[252] Vetri, V.; Librizzi, F.; Leone, M.; v. Militello Thermal Aggregation of Bovine Serum Albumin at Different pH: Comparison With Human Serum Albumin *Eur. Biophys. J.* **2007** *36*, 717–725.

[253] Song, X.-J.; Flynn, P. F.; Sharp, K. A.; Wand, A. J. Temperature Dependence of Fast Dynamics in Proteins *Biophys. J.* **2007** *92*, L43–L45.

[254] Adel, A.; Nadia, M.; Mohamed, O.; Abdelhafidh, G. Study of Thermally and Chemically Unfolded Conformations of Bovine Serum Albumin by Means of Dynamic Light Scattering *Mater. Sci. Eng. C* **2008** *28*, 594–600.

[255] Zhang, Y.; Lagi, M.; Liu, D.; Mallamace, F.; Fratini, E.; Baglioni, P.; Mamontov, E.; Hagen, M.; Chen, S.-H. Observation of High-Temperature Dynamic Crossover in Protein Hydration Water and Its Relation to Reversible Denaturation of Lysozyme *J. Chem. Phys.* **2009** *130*, 135101.

[256] Meersman, F.; Atilgan, C.; Miles, A. J.; Bader, R.; Shang, W.; Matagne, A.; Wallace, B. A.; Koch, M. H. Consistent Picture of the Reversible Thermal Unfolding of Hen Egg-White Lysozyme From Experiment and Molecular Dynamics *Biophys. J.* **2010** *99*, 2255–2263.

[257] Fu, L.; Villette, S.; Petoud, S.; Fernandez-Alonso, F.; Saboungi, M.-L. H/D Isotope Effects in Protein Thermal Denaturation: The Case of Bovine Serum Albumin *J. Phys. Chem. B* **2011** *115*, 1881–1888.

[258] Corsaro, C.; Mallamace, D. A Nuclear Magnetic Resonance Study of the Reversible Denaturation of Hydrated Lysozyme *Phys. A* **2011** *390*, 2904 – 2908.

[259] Das, N. K.; Ghosh, N.; Kale, A. P.; Mondal, R.; Anand, U.; Ghosh, S.; Tiwari, V. K.; Kapur, M.; Mukherjee, S. Temperature Induced Morphological Transitions From Native to Unfolded Aggregated States of Human Serum Albumin *J. Phys. Chem. B* **2014** *118*, 7267–7276.

[260] Jansson, H.; Swenson, J. Dynamical Changes of Hemoglobin and Its Surrounding Water During Thermal Denaturation as Studied by Quasielastic Neutron Scattering and Temperature Modulated Differential Scanning Calorimetry *J. Chem. Phys.* **2008** *128*, 245104.

[261] Ortore, M. G.; Spinozzi, F.; Mariani, P.; Paciaroni, A.; Barbosa, L. R.; Amenitsch, H.; Steinhart, M.; Ollivier, J.; Russo, D. Combining Structure and Dynamics: Non-Denaturing High-Pressure Effect on Lysozyme in Solution *J. R. Soc. Interface* **2009** *6*, S619.

[262] Mamontov, E.; O'Neill, H.; Zhang, Q. Mean-Squared Atomic Displacements in Hydrated Lysozyme, Native and Denatured *J. Biol. Phys.* **2010** *36*, 291–297.

[263] Perticaroli, S.; Nickels, J. D.; Ehlers, G.; Mamontov, E.; Sokolov, A. P. Dynamics and Rigidity in an Intrinsically Disordered Protein, β-Casein *J. Phys. Chem. B* **2014** *118*, 7317–7326.

[264] Jacrot, B. The Study of Biological Structures by Neutron Scattering From Solution *Rep. Prog. Phys.* **1976** *39*, 911.

[265] Seydel, T.; Wiegart, L.; Juranyi, F.; Struth, B.; Schober, H. Unaffected Microscopic Dynamics of Macroscopically Arrested Water in Dilute Clay Gels *Phys. Rev. E* **2008** *78*, 061403.

[266] Gaspar, A. M.; Busch, S.; Appavou, M.-S.; Haeussler, W.; Georgii, R.; Su, Y.; Doster, W. Using Polarization Analysis to Separate the Coherent and Incoherent Scattering From Protein Samples *BBA-Proteins Proteom.* **2010** *1804*, 76–82.

[267] Tehei, M.; Perlmutter, J.; Giusti, F.; Sachs, J.; Zaccai, G.; Popot, J.-L. Thermal Fluctuations in Amphipol A8-35 Particles: A Neutron Scattering and Molecular Dynamics Study *J. Membr. Biol.* **2014** *247*, 897–908.

[268] Mallamace, F.; Chen, S.-H.; Broccio, M.; Corsaro, C.; Crupi, V.; Majolino, D.; Venuti, V.; Baglioni, P.; Fratini, E.; Vannucci, C.; Stanley, H. E. Role of the Solvent in the Dynamical Transitions of Proteins: The Case of the Lysozyme-Water System *J. Chem. Phys.* **2007** *127*, 045104.

[269] Grimaldo, M.; Roosen-Runge, F.; Hennig, M.; Zanini, F.; Zhang, F.; Zamponi, M.; Jalarvo, N.; Schreiber, F.; Seydel, T. Salt-Induced Universal Slowing Down of the Short-Time Self-Diffusion of a Globular Protein in Aqueous Solution *J. Phys. Chem. Lett.* **2015** *6*, 2577–2582.

[270] Heitjans, P.; Kärger, J., editors *Diffusion in Condensed Matter: Methods, Materials, Models* Springer, Heidelberg **2006**.

[271] Crank, J. *The Mathematics of Diffusion* Clarendon Press Oxford **1975**.

[272] Dix, J. A.; Verkman, A. Crowding Effects on Diffusion in Solutions and Cells *Annu. Rev. Biophys.* **2008** *37*, 247–263.

[273] Höfling, F.; Franosch, T. Anomalous Transport in the Crowded World of Biological Cells *Rep. Prog. Phys.* **2013** *76*, 046602.

[274] Grosberg, A. Y.; Nguyen, T.; Shklovskii, B. Colloquium: The Physics of Charge Inversion in Chemical and Biological Systems *Rev. Mod. Phys.* **2002** *74*, 329–345.

[275] Oakley, A.; Collingwood, J.; Dobson, J.; Love, G.; Perrott, H.; Edwardson, J.; Elstner, M.; Morris, C. Individual Dopaminergic Neurons Show Raised Iron Levels in Parkinson Disease *Neurology* **2007** *68*, 1820–1825.

[276] Whitesides, G. M.; Grzybowski, B. Self-Assembly at All Scales *Science* **2002** *295*, 2418–2421.

[277] Stradner, A.; Cardinaux, F.; Schurtenberger, P. A Small-Angle Scattering Study on Equilibrium Clusters in Lysozyme Solutions. *J. Phys. Chem. B* **2006** *110*, 21222–21231.

[278] Kowalczyk, P.; Ciach, A.; Gauden, P.; Terzyk, A. Equilibrium Clusters in Concentrated Lysozyme Protein Solutions *J. Colloid Interface Sci.* **2011** *363*, 579–584.

[279] Barhoum, S.; Yethiraj, A. NMR Detection of an Equilibrium Phase Consisting of Monomers and Clusters in Concentrated Lysozyme Solutions *J. Phys. Chem. B* **2010** *114*, 17062–17067.

[280] Johnston, K. P.; Maynard, J. A.; Truskett, T. M.; Borwankar, A. U.; Miller, M. A.; Wilson, B. K.; Dinin, A. K.; Khan, T. A.; Kaczorowski, K. J. Concentrated Dispersions of Equilibrium Protein Nanoclusters That Reversibly Dissociate Into Active Monomers *Acs Nano* **2012** *6*, 1357–1369.

[281] Hofmeister, F. Zur Lehre Von Der Wirkung Der Salze *N-S Arch. Pharmacol.* **1888** *24*, 247–260.

[282] Zhang, F.; Roosen-Runge, F.; Sauter, A.; Wolf, M.; Jacobs, R. M.; Schreiber, F. Reentrant Condensation, Liquid–Liquid Phase Separation and Crystallization in Protein Solutions Induced by Multivalent Metal Ions *Pure Appl. Chem.* **2014** *86*, 191–202.

[283] Zhang, F.; Zocher, G.; Sauter, A.; Stehle, T.; Schreiber, F. Novel Approach to Controlled Protein Crystalization Through Ligandation of Yttrium Cations *J. Appl. Cryst.* **2011** *44*, 755.

[284] Zhang, F.; Roosen-Runge, F.; Sauter, A.; Roth, R.; Skoda, M. W.; Jacobs, R. M.; Sztucki, M.; Schreiber, F. The Role of Cluster Formation and Metastable Liquid–Liquid Phase Separation in Protein Crystallization *Faraday Discuss.* **2012** *159*, 313–325.

[285] Sauter, A.; Roosen-Runge, F.; Zhang, F.; Lotze, G.; Jacobs, R. M. J.; Schreiber, F. Real-Time Observation of Nonclassical Protein Crystallization Kinetics *J. Am. Chem. Soc.* **2015** *137*, 1485–1491 pMID: 25569484.

[286] Wertheim, M. Fluids With Highly Directional Attractive Forces. I. Statistical Thermodynamics *J. Stat. Phys.* **1984** *35*, 19–34.

[287] Foffi, G.; Sciortino, F. On the Possibility of Extending the Noro-Frenkel Generalized Law of Correspondent States to Nonisotropic Patchy Interactions *J. Phys. Chem. B* **2007** *111*, 9702–9705.

[288] Cardinaux, F.; Zaccarelli, E.; Stradner, A.; Bucciarelli, S.; Farago, B.; Egelhaaf, S. U.; Sciortino, F.; Schurtenberger, P. Cluster-Driven Dynamical Arrest in Concentrated Lysozyme Solutions *J. Phys. Chem. B* **2011** *115*, 7227–7237.

Acknowledgments

The results in this thesis would not have been achieved without the contribution, in different forms, of a large number of people.

First, I would like to thank my P.h.D. supervisor at the University of Tübingen, Prof. Dr. Frank Schreiber, for his patience, firmness, and calmness in the key moments of this thesis and for his pinpoint advice. At the Institut Laue-Langevin, I am particularly thankful to Dr. Tilo Seydel for his unparalleled mentoring, as well as to Dr. Felix Roosen-Runge for his priceless advice. I thank both of them for their constant availability and their countless hints and explanations, as well as for so much scientific discussion and the curiosity and knowledge they have shared with me in these years, and for proofreading.

I am very thankful to Prof. Dr. Helmut Schober, Prof. Dr. Frank Schreiber, Dr. Tilo Seydel and Dr. Felix Roosen-Runge for the confidence they have accorded to me. Moreover, I would like to thank them, as well as Prof. Dr. Martin Oettel, Prof. Dr. Roland Roth, Dr. Niina Jalarvo, Dr. Eugene Mamontov, Dr. Marcell Wolf and Dr. Andrea Sauter for fruitful discussion. Furthermore, I am thankful to Dr. Bernhard Frick, Dr. Markus Appel, Dr. Orsolya Czakkel, Dr. Bela Farago, Dr. Ingo Hoffman, Dr. Ralf Schweins for discussion and advice before, during, and after experiments.

I am grateful also to Dr. Marcus Hennig, Richard Ammer, Dr. David Hess, Rhonda Moody, and Richard Goyette for assistance in several matters. Moreover, I would like to thank the EMBL/ILL D-Lab, including Prof. Dr. Trevor Forsyth, Dr. Michael Haertlein, Dr. Juliette Devos, and Dr. Martine Moulin for the availability and enthusiasm as well as the Tübinger Werkstatt for the production of so many Aluminum sample holders.

I thank very much Simon and Joseph for proofreading, as well as Christian Beck, Michal Braun, Stefano Da Vela, Olga Matsarskaia, and PD Dr. Fajun Zhang for proofreading and fruitful and enthusiastic discussion.

This PhD thesis was however the result of many steps of personal growth. An uncountable number of people has contributed in this respect, and I thank but cannot cite all of them. Voglio comunque ringraziare in primis la mia famiglia, in particolare mamma e papà, Barbara, Alessandro ed Emanuele per avermi sempre supportato ed aiutato, come anche i miei zii per la loro vicinanza. Ringrazio enormemente anche Francesca, per avermi accompagnato e sorretto in questi tre anni, e avermi sempre spronato a migiorarmi. Un grande grazie anche ai gruppi P.A.R.V., 21.45 da Subito, così come al gruppo doppia laurea, e alla S.A.F. Bolzano, dalla quale ho ricevuto tanto.

Dedico poi un ringraziamento particolare al Prof. Franco Criscuolo, che piú di ogni altro mi ha insegnato a non desistere fin *dopo* il traguardo, e a Don Roberto Lorenzon per la sua impronta e per essermi sempre stato tanto vicino.

Finally, I would like to thank: The storm in Geneva and the *protection civile* for letting me sleep in a fallout shelter (20/06/2013); The MVV for making me run in the night through dark fields to take a flight (28/10/2013); The ORNL for the coyote standing in front of me right after breakfast (10/04/2014); The ILL for giving me the best office to see the meteorite on Grenoble (17/02/2016) and for letting me be in the middle of a S.W.A.T. exercise while going home (07/04/2016); All the ILL PhD students, and in particular the best office, for being so awesome.